NASA CR-134286
R-9270

FINAL REPORT

NONCIRCULAR ORIFICE HOLES AND ADVANCED FABRICATION TECHNIQUES FOR LIQUID ROCKET INJECTORS

PHASE III: ANALYTICAL AND COLD-FLOW EXPERIMENTAL EVALUATION OF RECTANGULAR CONCENTRIC TUBE INJECTOR ELEMENTS FOR GAS/LIQUID APPLICATION

PHASE IV: ANALYTICAL AND EXPERIMENTAL EVALUATION OF NONCIRCULAR INJECTOR ELEMENTS FOR GAS/LIQUID AND LIQUID/LIQUID APPLICATION

NAS9-9528

by

R. M. McHale

May 1974

ROCKETDYNE DIVISION/ROCKWELL INTERNATIONAL
6633 CANOGA AVENUE, CANOGA PARK, CALIFORNIA

prepared for

NASA LYNDON B. JOHNSON SPACE CENTER
Mr. Merlyn F. Lausten: Project Manager

Unclassified

SECURITY CLASSIFICATION OF THIS PAGE (*When Data Entered*)

REPORT DOCUMENTATION PAGE

READ INSTRUCTIONS
BEFORE COMPLETING FORM

1. REPORT NUMBER CR-	2. GOVT ACCESSION NO.	3. RECIPIENT'S CATALOG NUMBER
4. TITLE (*and Subtitle*) NONCIRCULAR ORIFICE HOLES AND ADVANCED FABRICATION TECHNIQUES FOR LIQUID ROCKET INJECTORS (PHASES III AND IV)		5. TYPE OF REPORT & PERIOD COVERED Final 6. PERFORMING ORG. REPORT NUMBER R-9270
7. AUTHOR(*s*) R. M. McHale		8. CONTRACT OR GRANT NUMBER(*s*) NAS9-9528
9. PERFORMING ORGANIZATION NAME AND ADDRESS Rocketdyne Division/Rockwell International 6633 Canoga Ave. Canoga Park, California		10. PROGRAM ELEMENT, PROJECT, TASK AREA & WORK UNIT NUMBERS
11. CONTROLLING OFFICE NAME AND ADDRESS Lyndon B. Johnson Space Center Houston, Texas		12. REPORT DATE May 1974 13. NUMBER OF PAGES 230
14. MONITORING AGENCY NAME & ADDRESS(*if different from Controlling Office*) NASA Lyndon B. Johnson Space Center Houston, Texas		15. SECURITY CLASS. (*of this report*) Unclassified 15a. DECLASSIFICATION/DOWNGRADING SCHEDULE

16. DISTRIBUTION STATEMENT (*of this Report*)

17. DISTRIBUTION STATEMENT (*of the abstract entered in Block 20, if different from Report*)

18. SUPPLEMENTARY NOTES

19. KEY WORDS (*Continue on reverse side if necessary and identify by block number*)

Noncircular orifices, orifices, rectangular elements, concentric tube, unlike doublets, triplets, mixing, atomization, LOX/GH$_2$.

20. ABSTRACT (*Continue on reverse side if necessary and identify by block number*)

This report contains the results (Phases III and IV) of a cold-flow and hot-fire experimental study of the mixing and atomization characteristics of injector elements incorporating noncircular orifices. Both liquid/liquid and gas/liquid element types are discussed. Unlike doublet and triplet elements (circular orifices only) were investigated for the liquid/liquid case while concentric tube elements were investigated for the gas/liquid case. It is concluded that noncircular shape can be employed to significant advantage in injector design for liquid rocket engines.

DD FORM 1 JAN 73 1473 EDITION OF 1 NOV 65 IS OBSOLETE

Unclassified

SECURITY CLASSIFICATION OF THIS PAGE (*When Data Entered*)

NASA CR-
R-9270

FINAL REPORT

NONCIRCULAR ORIFICE HOLES AND ADVANCED FABRICATION TECHNIQUES FOR LIQUID ROCKET INJECTORS

PHASE III: ANALYTICAL AND COLD-FLOW EXPERIMENTAL EVALUATION OF RECTANGULAR CONCENTRIC TUBE INJECTOR ELEMENTS FOR GAS/LIQUID APPLICATION

PHASE IV: ANALYTICAL AND EXPERIMENTAL EVALUATION OF NONCIRCULAR INJECTOR ELEMENTS FOR GAS/LIQUID AND LIQUID/LIQUID APPLICATION

NAS9-9528

by

R. M. McHale

ROCKETDYNE DIVISION/ROCKWELL INTERNATIONAL
6633 CANOGA AVENUE, CANOGA PARK, CALIFORNIA

prepared for

NASA LYNDON B. JOHNSON SPACE CENTER
Mr. Merlyn F. Lausten: Project Manager

FOREWORD

This report was prepared for the NASA Lyndon B. Johnson Space Center, Houston, Texas, by the Rocketdyne Division of Rockwell International. The study was conducted under contract NAS9-9528, Mr. M. F. Lausten, Project Manager. Phases III and IV of a four-phase effort are reported.

ABSTRACT

This report contains the results (Phases III and IV) of a cold-flow and hot-fire experimental study of the mixing and atomization characteristics of injector elements incorporating noncircular orifices. Both liquid/liquid and gas/liquid element types are discussed. Unlike doublet and triplet elements (circular orifices only) were investigated for the liquid/liquid case while concentric tube elements were investigated for the gas/liquid case. It is concluded that noncircular shape can be employed to significant advantage in injector design for liquid rocket engines.

CONTENTS

Appendix F

Appendix G

Appendix H

ILLUSTRATIONS

TABLES

SYMBOLS

A = area, in.^{2}
AR = orifice aspect ratio, x_1/y_1
B, b = larger dimension for noncircular orifice, inches
c^* = characteristic velocity, ft/sec
CCTE = circular concentric tube element
C_p = specific heat, Btu/lbm-R
D, d = diameter or characteristic length, inches
$\overline{D}$ = mass median diameter, usually microns
D_H = hydraulic diameter, inches
E_m = mixture ratio uniformity parameter, Eq. F-4
f( ) = function of ( )
$f_{H.L.}$ = heat loss correction factor, Eq. 3-16
GCC = gas/liquid circular concentric element code
GCR = gas/liquid rectangular concentric element code
G/L = gas/liquid
GST = gas/liquid multishowerhead triplet element code
h = heat transfer coefficient, Btu/in.^{2}-sec-R
K = general constant, or bulk compressibility, lbm/ft-sec^2
K, k = thermal conductivity, Btu/in.-sec-R
L = orifice length, or general dimension-length
M = momentum flux, ρu^2, or general dimension-mass
mff = mass fraction flux
MR = mixture ratio, $\dot{w}_o/\dot{w}_f$

P, Δp = pressure, psia, and delta pressure, psid

Pr = Prandtl number

$\dot{Q}$ = heat flux, Btu/in.^{2}-sec

R = centerpost recess depth, inches

Re, Rey = Reynolds number

RCTE = rectangular concentric tube element

S = wall thickness, inches

St = Stanton number

STE = showerhead triplet element

T = temperature, R, or general dimension-time

U, u = velocity, ft/sec

U.D. = unlike doublet code

U.T. = unlike triplet code

V, v = velocity, ft/sec

w = smaller dimension for noncircular orifice, inches

$\dot{w}$ = flowrate, lbm/sec

We = Weber number

x = larger dimension for rectangles, inches

y = smaller dimension for rectangles, inches

Greek

ε_c = contraction ratio

η_{c^*} = characteristic velocity efficiency

μ = viscosity, lbm/ft-sec, or microns

ρ = density, lbm/ft^3

σ = surface tension, lbf/ft

ϕ = centerline momentum ratio $\rho_1 V_1^2 d_1 / \rho_2 V_2^2 d^2$

Subscripts

0 = stagnation properties

1 = liquid orifice dimensions, concentric element - smaller orifice, doublets - outer orifices, triplets

2 = centerpost dimensions, concentric element - larger orifice, doublets - center orifice, triplets

3 = gas port dimensions, concentric element

b = bulk properties

B.C. = coolant bulk

C = coolant

C.F. = cold flow

E = environment properties

f, F = fuel side properties

g, G = gas side properties

H.F. = hot fire

i = general index for ith quantity

j = jet properties

L = liquid side properties

mix = mixing process limited

o = oxidizer side properties

opt = optimum condition

s = static properties

sat = saturation properties

T = total or stagnation properties, also throat conditions

vap = vaporization process limited

w = wall properties

wc = coolant side wall

wg = gas side wall

1.0 SUMMARY

This report contains the results of a 27-month applied research program. This program constituted the final two phases (Phases III and IV) of an overall 4-year program. The objectives of Phases III and IV were: (1) to determine the effect of shape upon the mixing and atomization characteristics of concentric tube injector elements of rectangular shape for gas/liquid propellant system applications, (2) to characterize the atomization and mixing performance of liquid/liquid unlike triplet elements, and (3) to investigate, parametrically, the effect of area ratio and orifice aspect ratio upon the mixing characteristics of liquid/liquid unlike-doublet elements with rectangular orifices. (The results of Phases I and II of this program may be found in Ref. 1 and 2, respectively, and a comprehensive overall program summary may be found in Ref. 3.)

The chronology of Phases III and IV effort is presented in Fig. 1-1. Phase III was divided into three tasks (all devoted to gas/liquid studies: Task I. Design of Gas/Liquid Model Hardware and Definition of the Gas/Liquid Cold-Flow Test Plan; Task II. Gas/Liquid Cold-Flow Mixing and Atomization Experimentation; and Task III. Design and Fabrication of a Single-element Thrust Chamber for Gas/Liquid Hot-Fire Testing Planned for Phase IV.

Phase IV was divided into five tasks (both gas/liquid and liquid/liquid studies): Task I. Hot-Fire Evaluation of the Gas/Liquid Elements Characterized in Phase III Cold Flow; Task IA. Evaluation of the Mixing and Atomization Characteristics of Unlike Triplets (liquid/liquid cold flow); Task II. Additional Gas/Liquid Cold-Flow Mixing Tests; Task III. Evaluation of the Mixing Characteristics of Rectangular Unlike Doublets (liquid/liquid cold flow); and Task IV. Final Analysis of results and Final Report Preparation.

1.1 GAS/LIQUID RESULTS

Concentric tube injector elements of rectangular cross section were investigated employing cold-flow techniques. Elements of different aspect ratio, x_1/y_1 (width to height of the central liquid jet), were compared at a fixed set of nominal operating conditions. Additional comparisons made included the effects of element size,

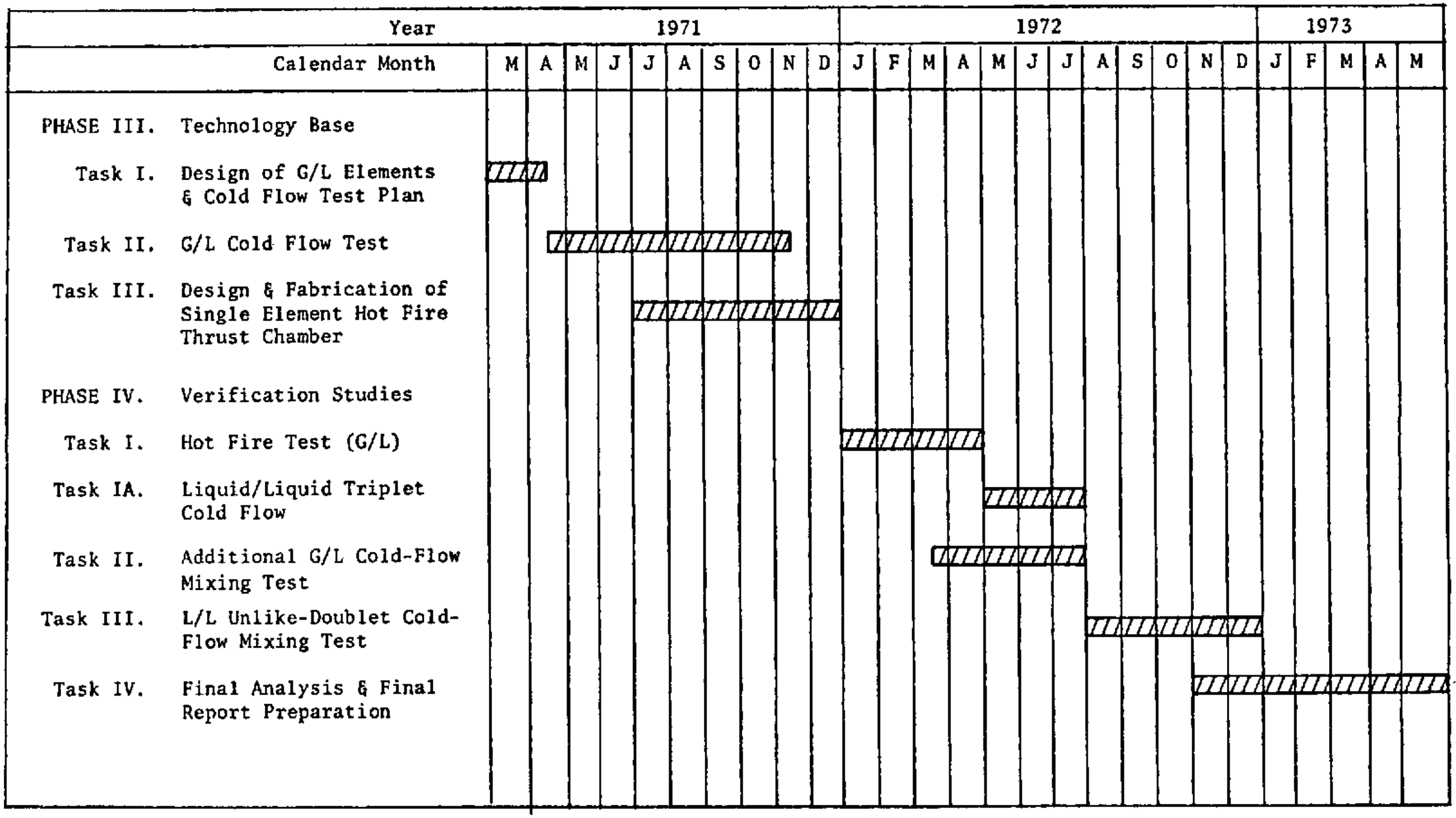

Figure 1-1. Noncircular Orifice, Phases III and IV Program Schedule

distribution of gas annulus area, gas-to-liquid area ratio, and center-post recess. Results obtained with the rectangular elements were compared with those for a circular element of equivalent injection areas.

Results showed that the mixing uniformity improved markedly with increased aspect ratio. For zero center-post recess, the value of E_m increased from 47 percent at aspect ratio unity (the circular element) to 65.6 percent at aspect ratio 6 (for the nominal conditions). The improvements provided by aspect ratio were even more striking with recessed posts; an E_m of 85 percent was obtained with the aspect ratio 6 element at a relative recess, $R/y_1 = 1.0$.*

Element size was found to have no effect upon mixing when the flow per unit area was maintained.

Variation of gas port aspect ratio, x_3/y_3 (gas annulus area distribution about the center-post) showed that the characteristics of the flowfield could be altered significantly. It was concluded that high levels of mixing could be achieved employing this parameter as an independent variable.

A factor of 2 reduction of the gas-to-liquid area ratio (i.e., an increase in the gas-to-liquid velocity ratio by a factor of 2) produced an increase in E_m of 15 percentage points (60 to 75 percent). Similar performance trends were noted for the circular element.

It was concluded that the most detrimental parameter to concentric tube mixing is high liquid velocity (i.e., high mixture ratio at fixed area ratio). Liquid velocities above 10 to 20 ft/sec at mixture ratio 6:1 produce significant reductions in E_m.

---

*Post recess also improved performance of the circular element. However, the improvements were greater for the rectangular elements.

The effect of liquid jet aspect ratio, x_1/y_1 = AR, upon mass median droplet diameter (frozen wax atomization technique) may be summarized as follows:

$$\frac{\bar{D}}{y_1} = K\left[\frac{AR^2}{3 + AR^2}\right], \text{ turbulent jets}$$

where

$K = f$ (center-post recess) = 0.31 for zero recess

$\bar{D}$ = mass median droplet diameter

y_1 = height of liquid jet ($y_1 < x_1$)

$AR = x_1/y_1$

The aspect ratio was varied in such a manner that the liquid port area was maintained constant (i.e., x_1/y_1 was varied with $x_1 y_1$ = const). Under this restriction, the dropsize varied in the following manner:

$$\bar{D} = K\sqrt{\frac{A_L}{\sqrt{AR}}}\left[\frac{AR^2}{3 + AR^2}\right]$$

where A_L = liquid area - const. This relationship shows dropsize increasing with aspect ratio to a value of $AR \approx 3$, and then decreasing with further increase in aspect ratio.

The effect of a reduction of element size, y_1, by 41 percent produced a 70 percent reduction in dropsize at zero recess. This suggests that the variation of dropsize with characteristic element dimension is a complex phenomenon and requires more than the relative droplet diameter, $\bar{D}/y_1$, for description.

The redistribution of gas annulus area from uniform gap to nonuniform gap around the central liquid post produced a reduction in dropsize. It is expected that this is not a general trend but depends upon the degree and the direction of the redistribution of annular gap.

Gas/liquid hot fire results (4-inch long, $\varepsilon_c = 2.3$ single-element chamber) were shown to be nearly mixing limited with the vaporization efficiency being approximately unity under the design and operating conditions tested. The extremely high vaporization efficiency are presently attributed to secondary droplet breakup. This effect was not included in predicted vaporization efficiencies. The hot valuesare, therefore, higher than those calculated. The trends of the hot-fire results confirmed most of the mixing trends suggested by the cold-flow results.

It was generally concluded that the rectangular concentric tube element could most advantageously be employed to improve mixing efficiency for high mixture ratio, and/or low gas momentum injector applications. The rectangular elements showed no particular atomization advantage. This result suggests that the atomization process is strictly governed by the energetics of the shearing process and is little effected by the relative shape of the flow field.

1.2 LIQUID/LIQUID STUDIES

Triplet mixing results (circular orifices) showed that E_m optimized for a given element at a value of centerline momentum ratio of unity for diameter ratio $d_1/d_2 = 1.0$. (d_1 is the outer orifice diameter and d_2 is the central orifice diameter.) Optimum mixing occurred at $\phi = 0.7$ for $d_1/d_2 < 1.0$. The parameter ϕ has the following definition for triplets:

$$\phi \equiv \frac{\rho_1 V_1^2 d_1}{\rho_2 V_2^2 d_2/2} \equiv \text{centerline momentum ratio}$$

It was also noted that the value of $E_{m_{opt}}$ dropped as the value of d_1/d_2 was decreased from unity.

Only laminar jet atomization data were correlated for the triplet elements. The data were shown to follow a functional relationship of the form:

$$\frac{\overline{D}}{D_j} = f(\text{Weber number x } \frac{L}{D})$$

where

$\overline{D}$ = mass median droplet diameter

D_j = given orifice diameter

Weber number = $\dfrac{\rho V_j^2 D_j}{\sigma}$

L/D $\equiv$ orifice length-to-diameter ratio

The functional relationship between dropsize and physical parameters was found to be:

$$\overline{D} = K V_j^{-.77} \sqrt{(L/D)^{-.39} \quad D_j^{.62}}$$

where K is a constant. It was concluded that the relatively strong influence of L/D was due to its affect on jet velocity profile development as suggested by the results of Zajac (Ref. 9).

Results of the investigation of the mixing characteristics of unlike-doublet elements with rectangular orifices suggested the following design criteria for optimum mixing:

$$\phi = 1$$

and

$$\left(\frac{b_o}{W}\right) \left(\frac{b_o}{b_f}\right)^3 = 8$$

where

$$\phi \equiv \frac{\rho_f V_f^2 b_f}{\rho_o V_o^2 b_o}$$

with the following definition of geometrical parameters for a rectangular unlike doublet:

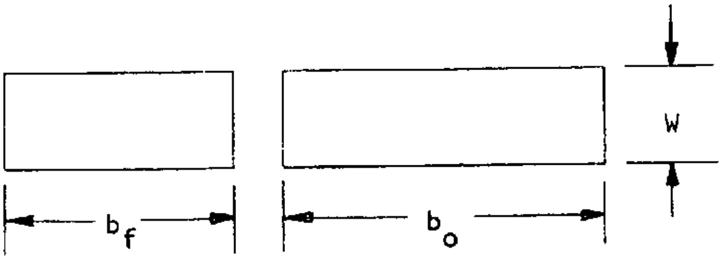

These results are based upon cold flow and are not directly indicative of the impingement characteristics of hypergolic reactants that can be dominated by reactive stream separation or "blowapart."

2.0 INTRODUCTION

The study of the influence of orifice and element shape upon rocket engine injector performance was initiated under the Noncirucular Orifice Program in June of 1969 under NASA funding from the Manned Spacecraft Center (now the Lyndon B. Johnson Spacecraft Center), Houston, Texas. In Phase I of this program (Ref. 1) the flow characteristics of individual orifices of noncircular shape and the mixing and atomization characteristics of unlike-doublet injector elements with noncircular orifices were investigated. The scope of Phase I was limited to liquid/liquid propellant systems, primarily of the storable, hypergolic variety. It was discovered that the noncircular shape offered greater design flexibility for the unlike-doublet element by providing high levels of mixing uniformity over a broad range of propellant density and mixture ratio. This flexibility had, heretofore, been unavailable with circular orifices.

The scope of the program was expanded in Phase II to include gas/liquid propellant combinations (Ref. 2) with emphasis upon the LOX/GH_2 system. Phase II consisted of an analytical screening analysis of candidate gas/liquid elements to select interesting elements for further research and a preliminary experimental investigation of a concentric tube injector element of rectangular shape. The screening study indicated that the concentric tube element type had the greatest potential for improvement with the adaptation of noncircular shape, and had the largest data base for comparison. Preliminary cold-flow experimental results suggested that improvements in both atomization and mixing could be achieved with rectangular shape. The atomization results were quite straightforward. However, the mixing uniformity trends with physical parameters were unclear.

Results obtained under both Phases I and II stimulated interest in further investigation of noncircular orifices for both liquid/liquid and gas/liquid propellant systems. Rocketdyne was subsequently funded to conduct a Phase III and Phase IV effort. The scope of the additional research was formulated to include extensive cold-flow mixing and atomization studies for gas/liquid concentric tube elements, hot-fire investigation of gas/liquid concentric tube elements, and further cold-flow mixing and atomization studies with (liquid/liquid) unlike doublets and triplets.

This volume is a presentation of the results of the Phase III and IV portion of the Noncircular Orifice Program. A comprehensive summary of the entire program is contained in Ref. 3.

3.0 GAS/LIQUID STUDIES

The gas/liquid studies reported herein are composed primarily of cold-flow mixing, cold-flow atomization, and hot-fire experimental investigations of the effect of geometrical parameters upon the performance of rectangular concentric tube injector elements. (A small amount of cold-flow data was obtained for another element type, a showerhead triplet. Reporting of the results of that element is limited to a discussion at the end of the gas/liquid section to avoid confusion of the concentric tube presentation with another type of geometry.) To avoid unnecessary repetition of certain lengthy terms, a list of abbreviations to be employed throughout this report is presented in Table 3-1.

TABLE 3-1. LIST OF ABBREVIATIONS FOR GAS/LIQUID INJECTOR ELEMENT STUDIES

Term	Abbreviation
Gas/Liquid	G/L
Rectangular Concentric Tube Element	RCTE
Circular Concentric Tube Element	CCTE
Showerhead Triplet Element	STE

3.1 TECHNICAL APPROACH

The technical approach adopted for the G/L study is outlined in block diagram form in Fig. 3-1. The objective of the program was to determine experimentally the influence of element geometry upon injector performance employing rectangular concentric tube elements (RCTE), and, as a result, to answer the question, *"Exactly what can a noncircular element accomplish that cannot be accomplished by a circular element?"* To attack this problem, the concept of "performance" had to be broken down into fundamental components; one related to the quality of mixing provided by a given element, and one related to the degree to which that element is capable of atomizing the liquid propellant. This was accomplished

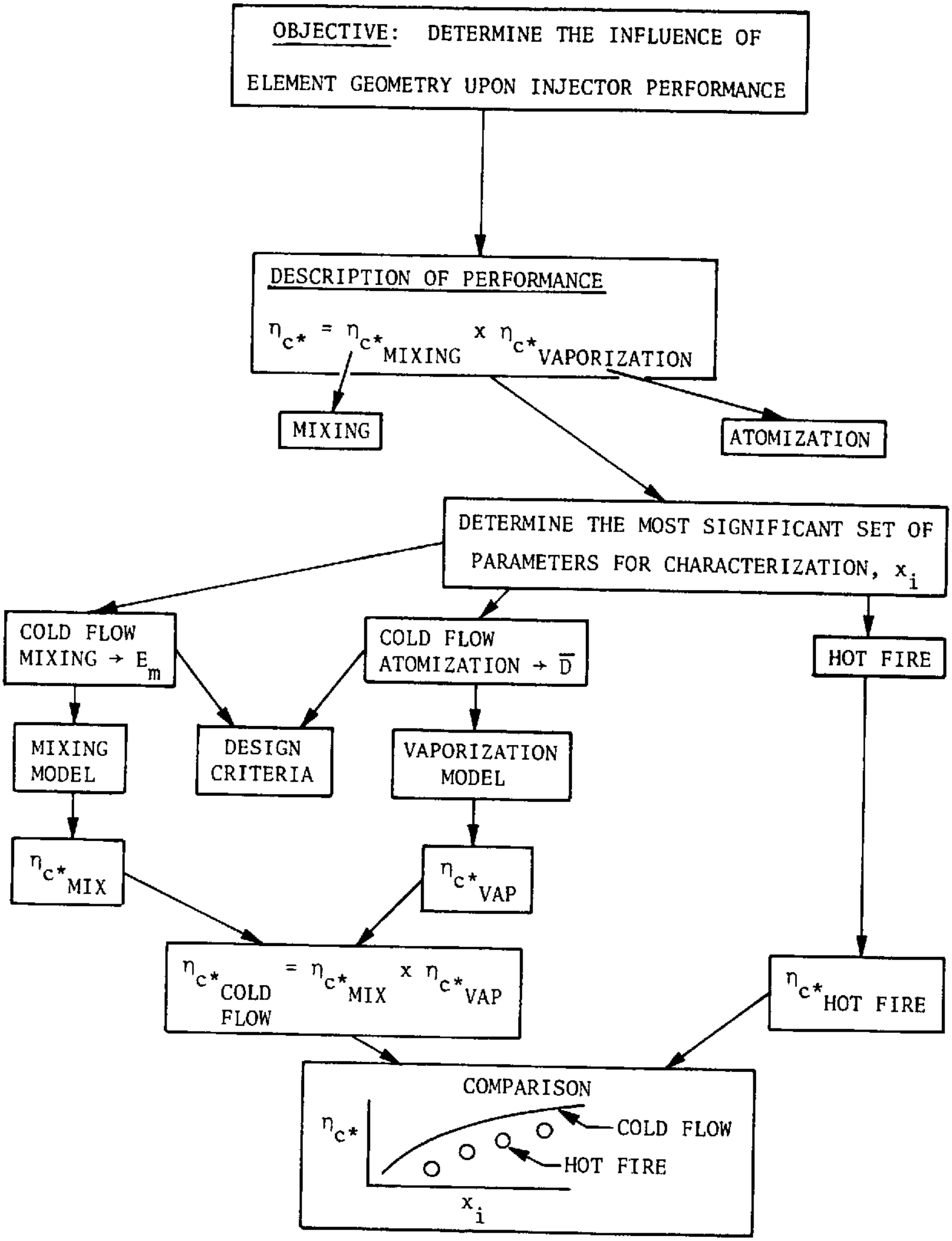

Figure 3-1. Technical Approach for the Characterization of Gas/ Liquid Rectangular Concentric Tube Injector Elements

by assuming that thrust chamber c* efficiency is approximated, to the first order, by the product of a mixing-limited and a vaporization-limited c* efficiency (Fig. 3-1 and Appendix F). Under this assumption, the performance problem is greatly simplified and can be investigated along two essentially independent paths.

The next step in the approach was to single out those geometrical and operational parameters that, (1) most influence the mixing and atomization processes, and (2) could be varied over significant ranges employing practical experimental techniques within the scope of the program. This was accomplished by the application of dimensional analysis.

With the selected parameters as guidelines, a set of model hardware and an experimental approach were formulated. The model hardware was designed to allow variation of the selected geometrical parameters. The experimental plan included independent cold-flow mixing, cold-flow atomization, and hot-fire experimentation.

Primary element comparisons and design criteria are obtained from the cold-flow results. The hot-fire experimentation was performed to ensure that the trends indicated by the cold-flow results were essentially correct.

To be able to compare cold-flow and hot-fire performance trends, the cold-flow results were converted to equivalent mixing-limited and vaporization-limited c* efficiencies (see Appendix F). The product of these efficiencies was termed $\eta_{c*C.F.}$ and was compared to the hot-fire efficiency, $\eta_{c*H.F.}$.

It was not the objective of this study to "predict" performance. However, the hot-fire trends must serve as a yardstick for the credibility of the cold-flow design criteria.

A CCTE was carried along throughout the program to serve as a basis of comparison for the RCTE results. It should be emphasized that the comparisons between circular and rectangular elements made in this report are not intended to imply that circular elements are either "worse" or "better" than noncircular over all ranges of injector design. These results should be viewed in the light of changes in performance (at the conditions and over the ranges stipulated in this document) produced by variations of shape, alone.

3.2 DEFINITION OF SIGNIFICANT PARAMETERS AND TEST PLAN FORMULATION

3.2.1 Dimensional Analysis

As could be envisioned, intuitively, the mixing and atomization processes associated with concentric tube injector elements are highly complex. To single out the individual parameters that should most influence these processes, the method of dimensional analysis was applied to the problem. This method, attributed to Buckingham, stipulates that if there are M physical parameters involving N dimensions, then there are M-N dimensionless groups that will completely characterize the physical problem.

The first task in the development of a dimensional analysis is to identify all of the parameters that are involved in the problem. Great care must be taken to ensure that all of the parameters are included. At this point, a discussion of the flowfield and the physics associated with concentric-tube element mixing and atomization is appropriate.

Injector face geometries for both a CCTE and a RCTE are shown in Fig. 3-2, and a cross section of a concentric tube element with physical processes identified is presented in Fig. 3-3. The standard concentric-tube element (often called coaxial element) is composed of a single tube within a larger orifice. Liquid, usually oxidizer, is injected through this central tube while gas, usually fuel, is injected through the annulus between the central post and the orifice (Fig. 3-3). Atomization of the liquid and subsequent mixing of the gas and liquid is produced by shear between the gas and liquid. The bulk of the energy required for the mixing and atomization processes is provided in the gas component in the form of velocity head.

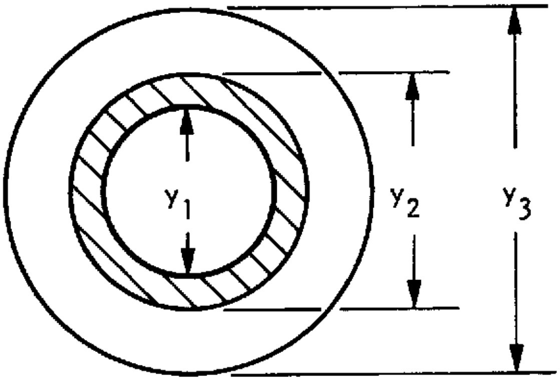

(a) CIRCULAR

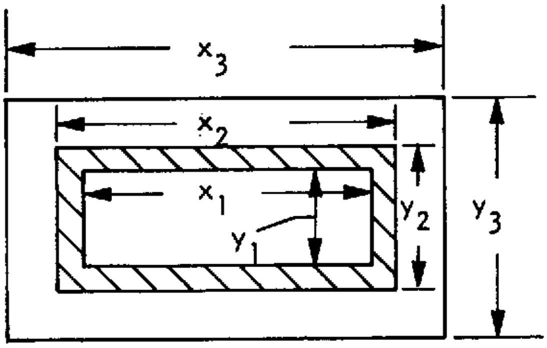

(b) RECTANGULAR

Figure 3-2. Typical Face Geometry for Circular and Rectangular Concentric Tube Elements

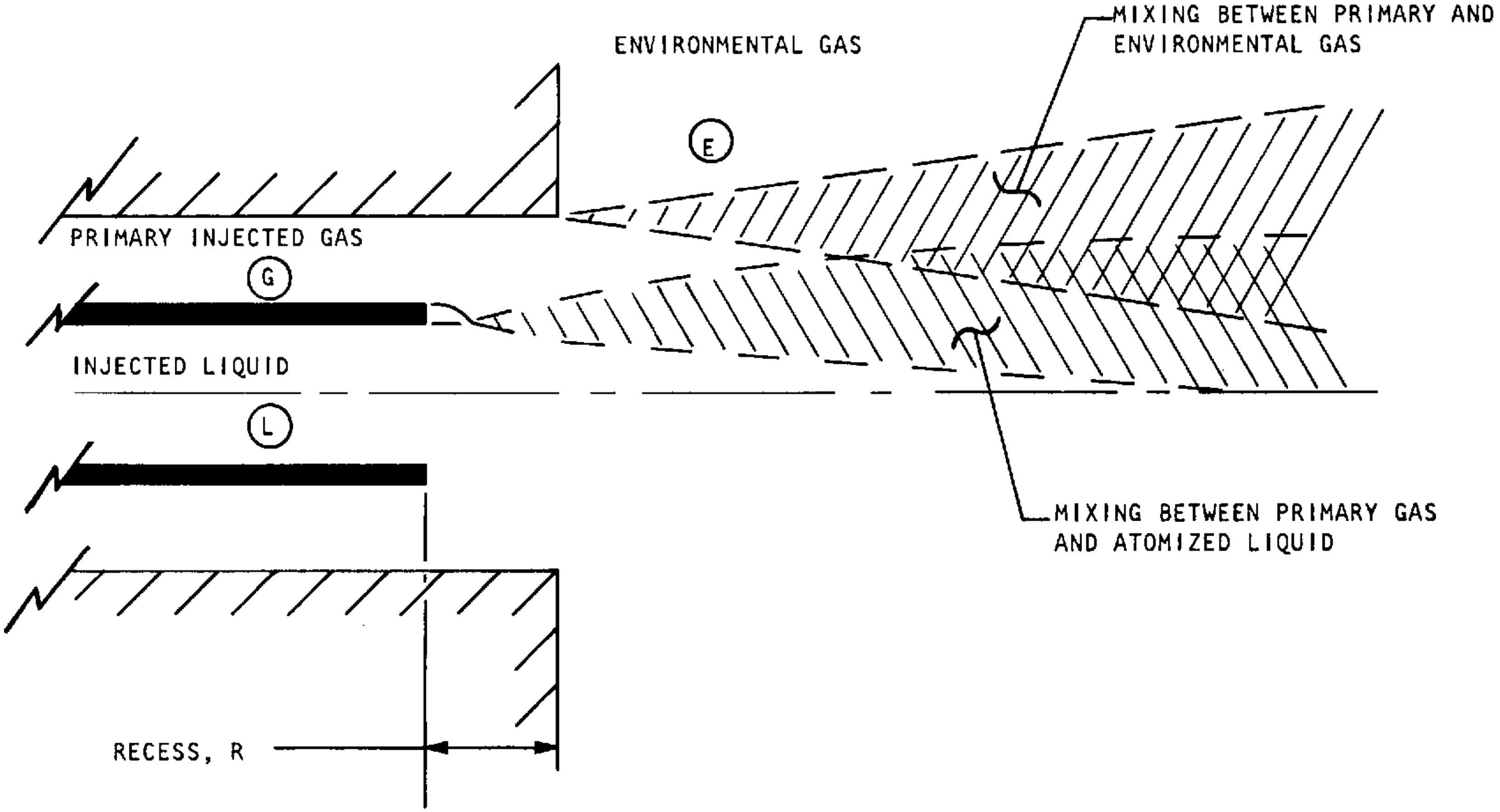

Figure 3-3. Typical Concentric Tube Element Flowfield

In many cases, the performance of the elements may be improved by recessing the central tube (Fig. 3-3) to allow more efficient momentum (or energy) exchange between the two fluids. There are situations, however, in which recess can be detrimental either from a performance or a hardware compatibility standpoint.

With the physical processes in mind, it is very important to note that there is a significant difference between a cold-flow model of these processes and the actual operation of an element with chemically reactive propellants. In the cold-flow situation, there is no vaporization of the liquid component and there is no energy release due to combustion. Thus, cold-flow results should not be expected to "predict" levels of performance exactly. However, cold-flow trends in performance with the geometrical and operational variables should be representative of actual trends. These modeling restrictions are not as important in the cold-flow modeling of liquid/liquid injector processes due to the fact that the majority of the mixing and atomization of liquid/liquid propellants occurs before significant combustion interaction.

In addition to the primary mixing of the injected liquid and gas components, there is a competitive mixing of the environmental gas with the injected gas. This secondary mixing is detrimental to the performance of the element as it severely degrades the momentum of the primary gas jet. The importance of the secondary mixing is diminished, however, with increased central tube recess.

The variables that were selected as representative of the concentric-tube element performance are listed in Table 3-2, along with their basic physical dimensions. (Note must be taken that many variables have been eliminated from the analysis. For example, the compressibility of the liquid has been assumed to be constant, gravitational forces have been neglected, and all temperatures, specific heats and, thus heat transfer, have been neglected.) There are 19 variables considered, having a total of three dimensions. According to the Buckingham Π theorem (see, e.g., Ref. 4), with $M = 19$ variables and $N = 3$ dimensions, there are $19 - 3 = 16$ dimensionless groups that will completely characterize the problem.

TABLE 3-2. PHYSICAL VARIABLES AND THEIR DIMENSIONS

Variable	Liquid	Gas	Environment	Dimensions*
Geometry	$X_1, X_2, X_3, y_1, y_2, y_3, R$			L
Density	ρ_L	ρ_G	ρ_E	ML^{-3}
Velocity	V_L	V_G	V_E	LT^{-1}
Compressibility		K_G	K_E	$ML^{-1} T^{-2}$
Viscosity	μ_L	μ_G	μ_E	$ML^{-1} T^{-1}$
Surface Tension	σ_L			MT^{-2}

* M = mass
L = length
T = time

The results of the dimensional analysis are presented in Table 3-3. These groups are the fundamental groups. More meaningful combinations can be obtained by combining two or more groups and replacing one of the variables employed in the new group. For example, the mixing of the primary gas with the environment is a free turbulent mixing process and is little dependent upon the viscosity of the gases (Reynolds No.). A better group may be $(\rho_G V_G - \rho_E V_E)/\rho_G V_G$ to replace V_E/V_G. However, no attempt has been made in this report to regroup the variables, *a priori*. Rather, the quantities which appear in the groups that could be varied were studied, and the results used to suggest which dimensionless groups would be most appropriate.

TABLE 3-3. DIMENSIONLESS GROUPS REQUIRED FOR THE DESCRIPTION OF GAS/ LIQUID CONCENTRIC-TUBE ELEMENT MIXING AND ATOMIZATION

Group No.	Group	Name and Type
1	x_1/y_1 (Aspect Ratio)	Geometry
2	x_2/y_2	
3	x_3/y_3	
4	y_2/y_1	
5	y_3/y_2	
6	R/y_1 (Relative Recess)	
7	ρ_g/ρ_L	Density Ratio
8	ρ_E/ρ_G	
9	V_G/V_L	Velocity Ratio
10	V_E/V_G	
11	$\rho_G V_G (y_3-y_2)/\mu_G$	Reynolds Number
12	$\rho_L V_L (y_1)/\mu_L$	
13	$\rho_E (V_G-V_E) y_3/\mu_E$	
14	$V_G/\sqrt{K_G/\rho_G}$	Mach Number
15	$V_E/\sqrt{K_E/\rho_E}$	
16	$\rho_G (V_G-V_L)^2 y_1/\sigma_L$	Weber Number

It is obvious upon inspection of the results shown in Table 3-3 that the task of investigating the concentric-tube flowfield is formidable. Therefore, the next task in the formulation of the experimental approach was to significantly reduce the number of variables for further study.

Since most of the basic results to be generated under this contract would come from cold flow, it was natural, first, to examine which of the parameters involved in the problem could be varied over a significant range and yet maintain the study within the scope of the contract.

Realistically, the only parameters that could be varied included the geometry, the gas density, the gas velocity, and the liquid velocity. Therefore, these parameters were selected as the primary experimental variables. Since all the dimensionless groups could not be varied independently, it was decided that presentation of the results in terms of any of these groups would be inappropriate unless sound justification could be presented. Thus, only in the case of certain of the geometric groups are results presented in dimensionless form. However, where possible, the results are employed to suggest which terms should be investigated in more detail.

In addition to these restrictions, it was also decided that the scope of the program did not allow an independent variation of all of the geometrical groups. The rationale employed to limit the experimental scope and the basis of the test plan are presented in the next section.

3.2.2 Test Plan Formulation

In formulating the test plan, the most important consideration was the original objective of the study: determine the influence of shape upon the performance of concentric-tube injector elements. Therefore, the question that one should ask is: "Exactly what does a rectangular concentric-tube element accomplish that a circular element cannot?"

Study of Table 3-3 will show that all of the dimensionless groups can be varied equally well by either a CCTE or a RCTE except groups No. 1, 2, and 3. It is clear, upon reference to Fig. 3-2 that these groups are available only to RCTE's. Thus, these three groups embody the only possible advantages or disadvantages available with noncircular (rectangular) shape.

The experimental plan, therefore, was limited to a parametric variation of these geometrical groups at a nominal baseline set of operating conditions. Some variations about the nominal conditions were selected to show relative sensitivity of the various elements. However, the restriction to baseline conditions was necessary, again, to meet scope.

Operating conditions selected as baseline are those of an 800-psia chamber pressure, liquid oxygen, gaseous hydrogen (LOX/GH_2) rocket engine with contraction ratio approximately 2.3:1, and nominal flow per element of 0.43 lb/sec. A list of the baseline conditions is presented in Table 3-4.

TABLE 3-4. BASELINE OPERATIONAL PARAMETERS

Parameter	Symbol	Nominal Value
Chamber Pressure	P_c	800 psia
Propellant Properties		LOX/GH_2
Mixture Ratio	MR	6
Gas Density	ρ_G	0.27 lbm/ft^3
Liquid Density	ρ_L	70 lbm/ft^3
Chamber Contraction Ratio	ε_c	≈2.3
Flow per Element	$\dot{w}_T$	0.432 lbm/sec
Fuel Injection Velocity (gas)	V_G	≈1000 ft/sec
Oxidizer Injection Velocity (liquid)	V_L	≈50 ft/sec

The set of concentric-tube elements selected for experimental evaluation is shown in Fig. 3-4 to relative scale. (Letters and numbers appearing under each element are element code numbers.)

The element comparison was accomplished in two stages: (1) comparison between a CCTE and "baseline" RCTE's, and (2) a comparison of one baseline RCTE with three variations of geometrical parameters about this baseline (Fig. 3-4).

The primary geometrical variable selected for comparison is the liquid orifice dimension ratio, X_1/y_1 termed the element aspect ratio (AR), (Fig. 3-2). Values of 1.5, 3.0, and 6.0 were chosen for this ratio. Certain ground rules were established for the primary baseline comparison; all baseline liquid areas were equal, all baseline gas annulus areas were equal, gas annulus gap was uniform, and all central tube wall thicknesses were equal. This was stipulated to ensure that all baseline elements would produce respectively equal gas velocities and liquid velocities at the baseline operating conditions. The equivalence of post tube-wall thickness was a fabrication consideration.

Under these ground rules, all the geometrical dimensionless groups become directly related to the aspect ratio, X_1/y_1.

The central post aspect ratio of 3.0 was selected for further parametric study. These additional elements are labeled "variations about AR = 3," in Fig. 3-4. One of these elements, GCR-7 is a direct scale model of the baseline AR = 3 element, reduced by a factor of $1/\sqrt{2}$. This reduces all of the areas by a factor of two. The other two variations (GCR-4 and GCR-3) employ the exact center post of GCR-2 (basic AR = 3 element) and have, respectively, one-half the gas annulus area (uniform gap) and a nonuniform gas gap (same gas area as GCR-2, Fig. 3-4).

These latter three variations were designed to test the effects of element size, velocity ratio, and nonuniform gas annulus distribution.

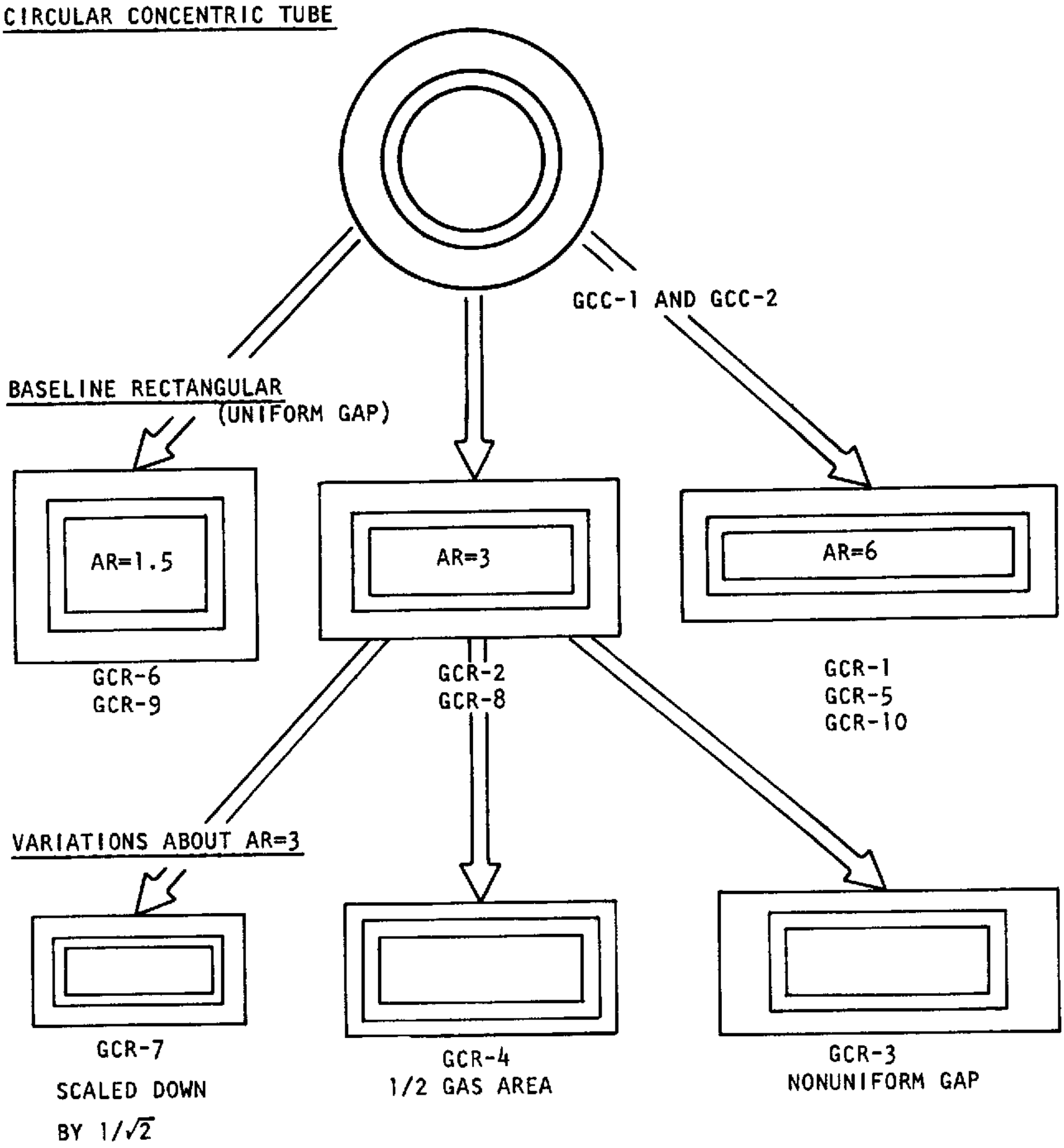

Figure 3-4. Rectangular Concentric Tube Element Comparisons

A complete list of all of the elements, their dimensions, and the objective of each is presented as Table 3-5. Two additional elements (GST-1 and GST-2) appear in Table 3-5. These are the "showerhead triplet elements" and are discussed in a separate section at the end of major section 3.0. The code number meaning is explained in Table 3-5.

In the next section, the hardware designed to implement the test plan is described followed by the presentation of the experimental results. The test plan described in this section has been general in nature. The exact test plan and method of presentation are detailed in Section 3.4.

3.3 TEST HARDWARE

The discussion of the test hardware is divided into two sections: injectors and hot-fire thrust chamber. The injectors were designed for use in both the cold-flow and the hot-fire portions of the program; therefore, there is further discussion of injectors directly in the thrust chamber section.

3.3.1 Injectors

Detailed injector face geometry descriptions and rationale for geometry selection have been presented and are summarized in Fig. 3-4 and Table 3-5. Only the hardware aspect of the injectors is presented in this section.

As mentioned, the injector models were designed to serve both the cold-flow and the hot-fire tasks. Each injector is composed of four pieces (Fig. 3-5)--a body, a clamp (or retaining ring), a post, and a port. The body and the clamp were employed for all of the models, only the port and/or post were changed to achieve a different configuration. A photograph of the individual components for a typical element is presented in Fig. 3-6 (element GCR-5 is shown; Table 3-5).

The body holds the entire assembly together and serves as a manifold for the gaseous component. The post is held into the body by means of the retaining clamp ring that bolts to the body. The post is maintained "concentric" with the port

TABLE 3-5. GAS/LIQUID ELEMENT GEOMETRY

(See Fig. 3-2 and 3-4)

Element* Code No.	x_1 (in.)	x_2 (in.)	x_3 (in.)	y_1 (in.)	y_2 (in.)	y_3 (in.)	Aspect Ratio x_1/y_1	Gas Area $(x_3/y_3 - x_2/y_2)$	Liquid Area x_1/y_1	Element Description
GCC-1	0.160	0.200	0.305	0.160	0.200	0.305	1.0	0.0416	0.0201	Circular concentric tube from Phase II
GCC-2	0.1604	0.2005	0.292	0.1604	0.2005	0.292	1.0	0.0354	0.0202	Circular concentric tube from Phase III
GCR-1	0.346	0.386	0.450	0.058	0.098	0.162	5.97	0.0351	0.0201	Rectangular concentric tube from Phase II, AR=6
GCR-2	0.245	0.286	0.3592	0.0825	0.1211	0.1936	2.97	0.0349	0.0202	Baseline RCTE, uniform gap, AR=3
GCR-3	0.245	0.286	0.4039	0.0825	0.1211	0.1721	2.97	0.0349	0.0202	Nonuniform gas gap, AR=3
GCR-4	0.245	0.286	0.3249	0.0825	0.1211	0.1615	2.97	0.0178	0.0202	1/2 baseline gas area, AR=3
GCR-5	0.350	0.3876	0.4518	0.0595	0.0981	0.1625	5.88	0.0354	0.0208	Baseline RCTE, uniform gap, AR=6
GCR-6	0.1735	0.2122	0.2922	0.1165	0.1611	0.2333	1.49	0.0340	0.0202	Baseline RCTE, uniform gap, AR=1.5
GCR-7	0.1750	0.2020	0.2535	0.058	0.0851	0.1379	3.02	0.0178	0.0101	$1/\sqrt{2}$ scale model of GCR-2
GCR-8	0.2450	0.286	0.3590	0.0825	0.1211	0.1950	2.97	0.0354	0.0202	Remake of GCR-2 with copper gas port for hot fire
GCR-9	0.1735	0.2122	0.2903	0.1165	0.1611	0.2350	1.49	0.0340	0.0202	Remake of GCR-6 with copper gas port for hot fire
GCR-10	0.350	0.3876	0.450	0.0595	0.0981	0.1620	5.88	0.0349	0.0208	Remake of GCR-5 with copper gas port for hot fire
	x_1 (in.)			y_1 (in.)	D_j (in.)					
GST-1	0.320	---	---	0.055	0.020	---	5.82	0.0352	0.0088	Showerhead triplet with 28 each 0.020 in. dia. orifices
GST-2	0.320	---	---	0.055	0.030	---	5.82	0.0352	0.0088	Showerhead triplet with 12 each 0.030 in. dia. orifices

*Code No. Definition

GCC ≡ Gas/Liquid Concentric Tube - Circular
GCR ≡ Gas/Liquid Concentric Tube - Rectangular
GST ≡ Gas/Liquid Showerhead Triplet

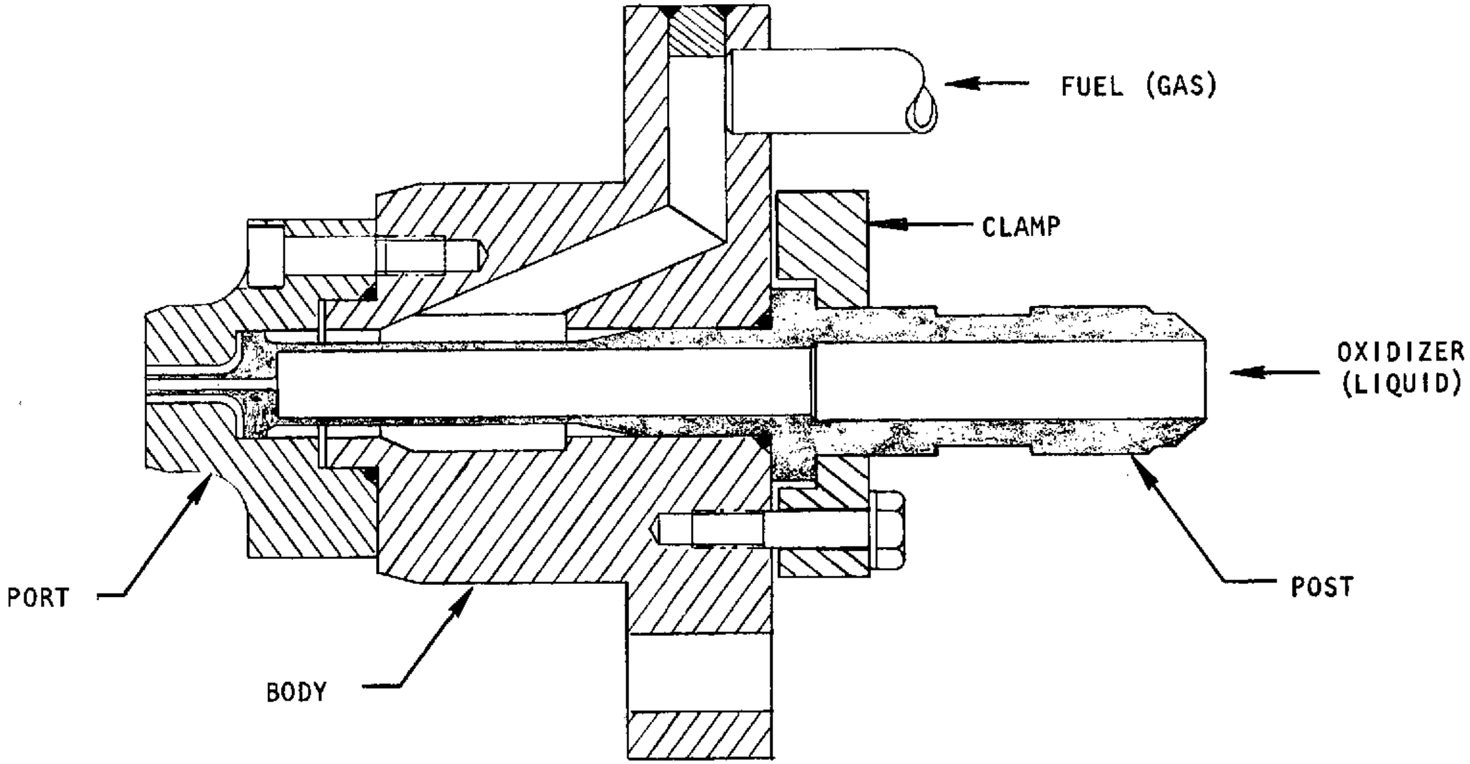

Figure 3-5. Single-Element Injector Assembly--Element GCR-5 Shown

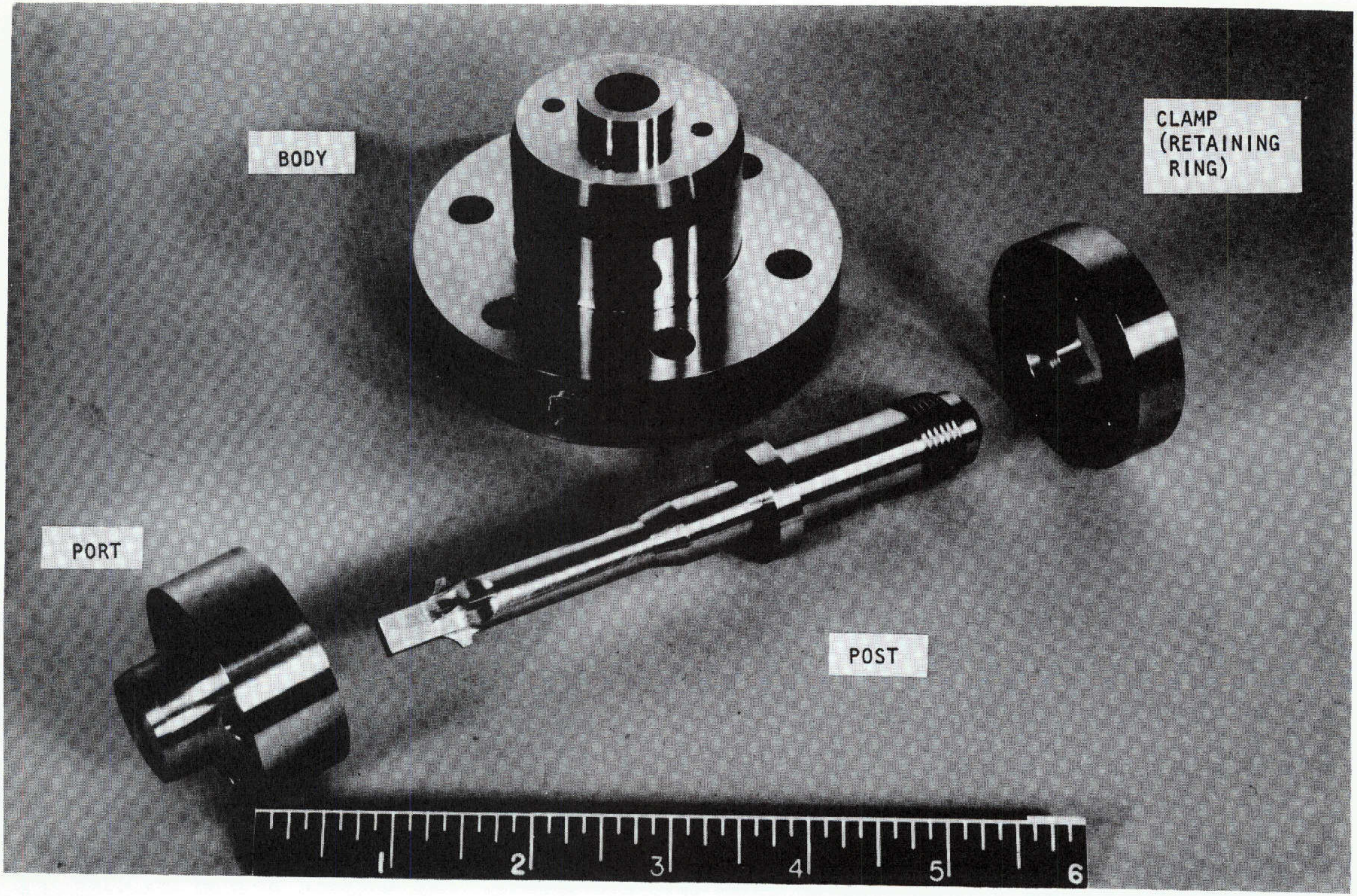

1DZ36-6/21/71-S1C

Figure 3-6. Injector Components (Element GCR-5 Shown) means of the alignment tabs, which may be seen in Fig. 3-5 and 3-6 toward the downstream end of the post. These tabs are relatively far from the gas annulus in a low-velocity region and did not pose a significant wake problem in the gas flow. The port is bolted to the body.

Sealing of the liquid, which is injected straight through the post, is accomplished by means of standard AN type B-nut fitting (not shown). Sealing of the gas is accomplished by two O-ring seals (Fig. 3-5). The gas is injected through two tubes that were brazed to the gas inlet orifices in the body. (Only one tube is shown in Fig. 3-5 due to the manner in which the section was taken.)

Center-post recess capability was provided by placing spacers between the body and the ring on the posts.

The liquid orifices were provided with rounded inlets to avoid flow separation and cavitation and were designed with a length to minimum dimension (y_1) ratio of 10:1. The gas annulus gaps were designed with a length-to-gap height ratio of 5:1 at zero recess conditions.

The rectangular orifices in the ports and posts were produced by the electrical discharge machining (EDM) method. This process yields an orifice with very accurate dimensions but with a rather rough (sand-blasted-like) surface.

All components of the injectors were made of series 321 stainless steel except the port pieces employed in the hot-fire experiments. These were made from OFHC copper for improved heat transfer capability.

Front and back views of the injector assembly are shown in Fig. 3-7 and 3-8, respectively (element GCR-2 shown). The two gas inlet orifices can be seen in Fig. 3-8 before brazing of the inlet tubes.

A comparative photograph of the three baseline RCTE's (Table 3-5) is presented in Fig. 3-9, wherein only the ports and posts are shown.

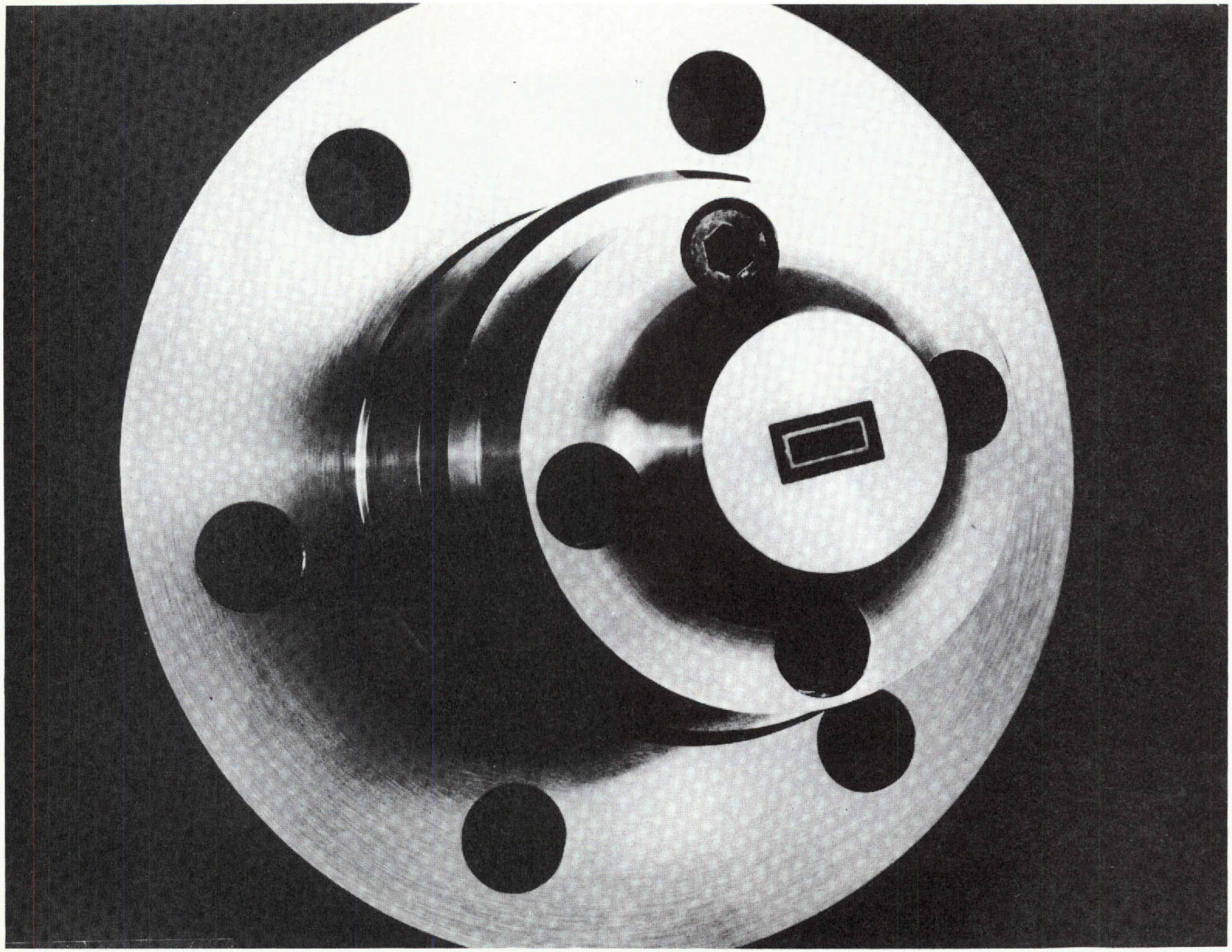

1DZ36-6/21/71-S1A

Figure 3-7. Injector Assembly, Front View (Element GCR-2 Shown)

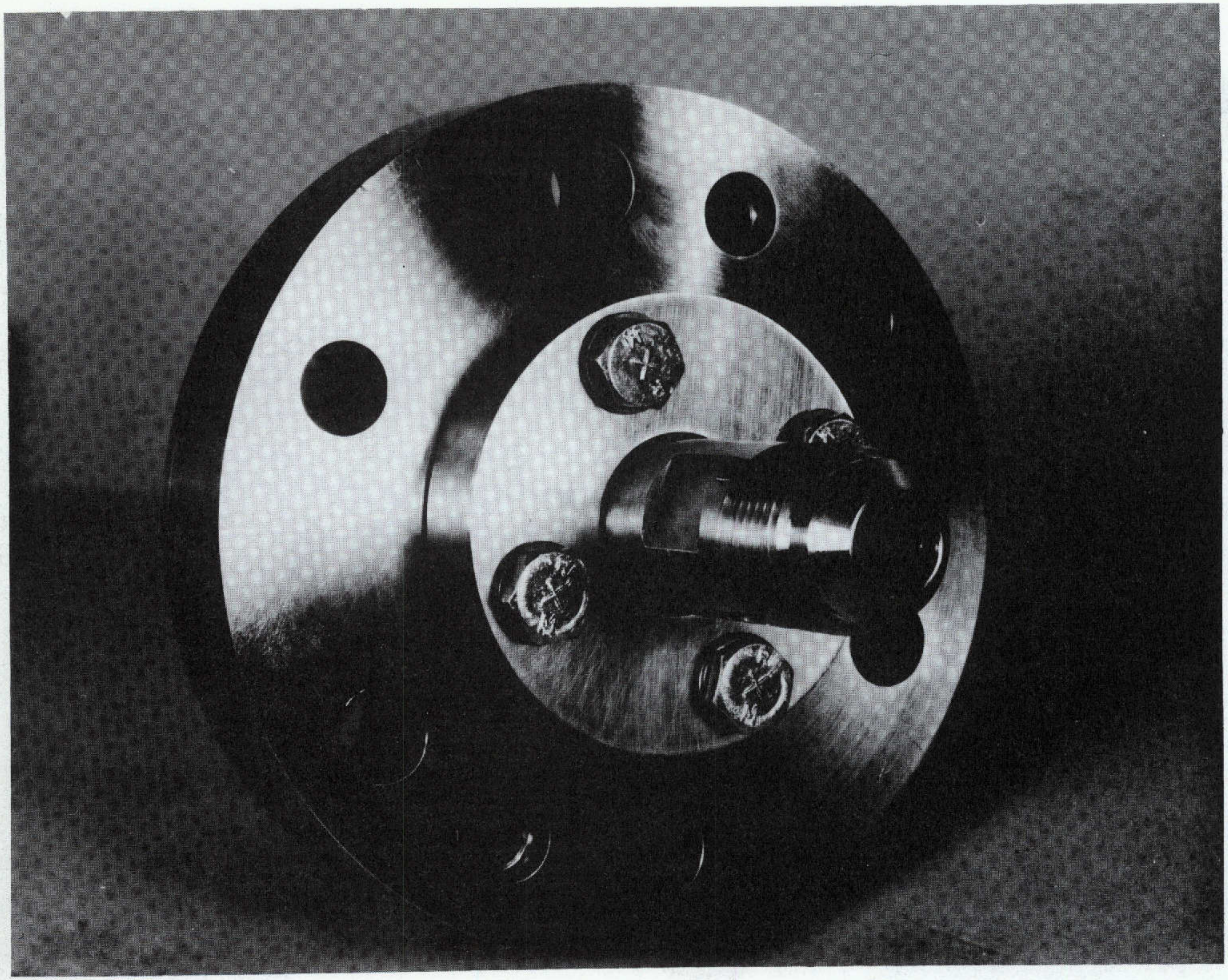

1DZ36-6/21/71-S1B

Figure 3-8. Injector Assembly, Rear View (Element GCR-2 Shown)

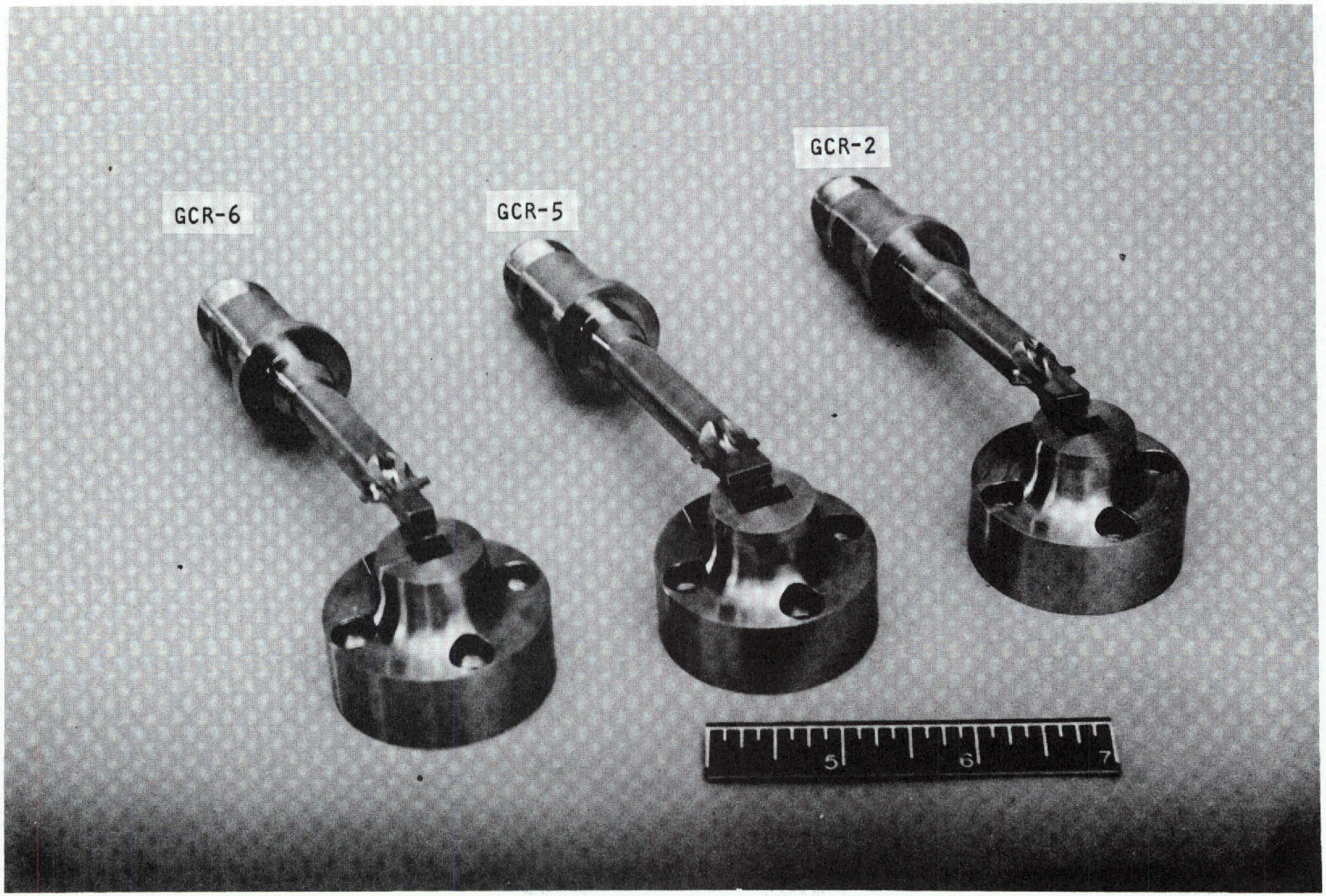

5AA34-7/6/71-S1A

Figure 3-9. Comparison of the Three Baseline Rectangular Concentric-Tube Elements

A face detail of element GCR-2 is shown in Fig. 3-10, at high magnification, to illustrate the dimensional control which was achieved with the EDM process and the concentricity between the port and post provided by the alignment tabs on the post.

The showerhead triplet injector models (GST-1 and GST-2) employ the same body and retaining clamp as the RCTE's and the CCTE. However, instead of a liquid post, a manifolding piece is used to introduce the liquid to the injection orifices. A cross section of this element is shown in Fig. 3-11 and a photograph of the face of GST-1 is shown in Fig. 3-12. The liquid is injected through many small showerhead orifices (circular), while the gas is injected through two orifices directed at the liquid jets with an included angle between the gas jet orifice centerlines of 60 degrees. The gas orifices are rectangular with aspect ratio of 5.82:1. Gas is supplied to these orifices through the same manifold employed with concentric tube elements. There is an additional O-ring seal between the liquid and the gas at the tip of the center-post manifold (Fig. 3-11).

All injector models were designed to adapt to the pressurized cold-flow mixing facility (Appendix A), the cold-flow atomization facility (Appendix B), and the hot-fire thrust chamber (Section 3.3.2).

For documentation, all Phase III gas/liquid element hardware is keyed to Rocketdyne drawing numbers in Table 3-6. It will be noted that elements GCC-1 and GCR-1 do not appear. These elements were employed in Phase II and were of different design (Ref. 2).

3.3.2 Hot-Fire Thrust Chamber

The discussion of the single-element, hot-fire thrust chamber design is presented in two sections--a summary of the heat transfer analysis for the chamber followed by a discussion of the chamber design itself.

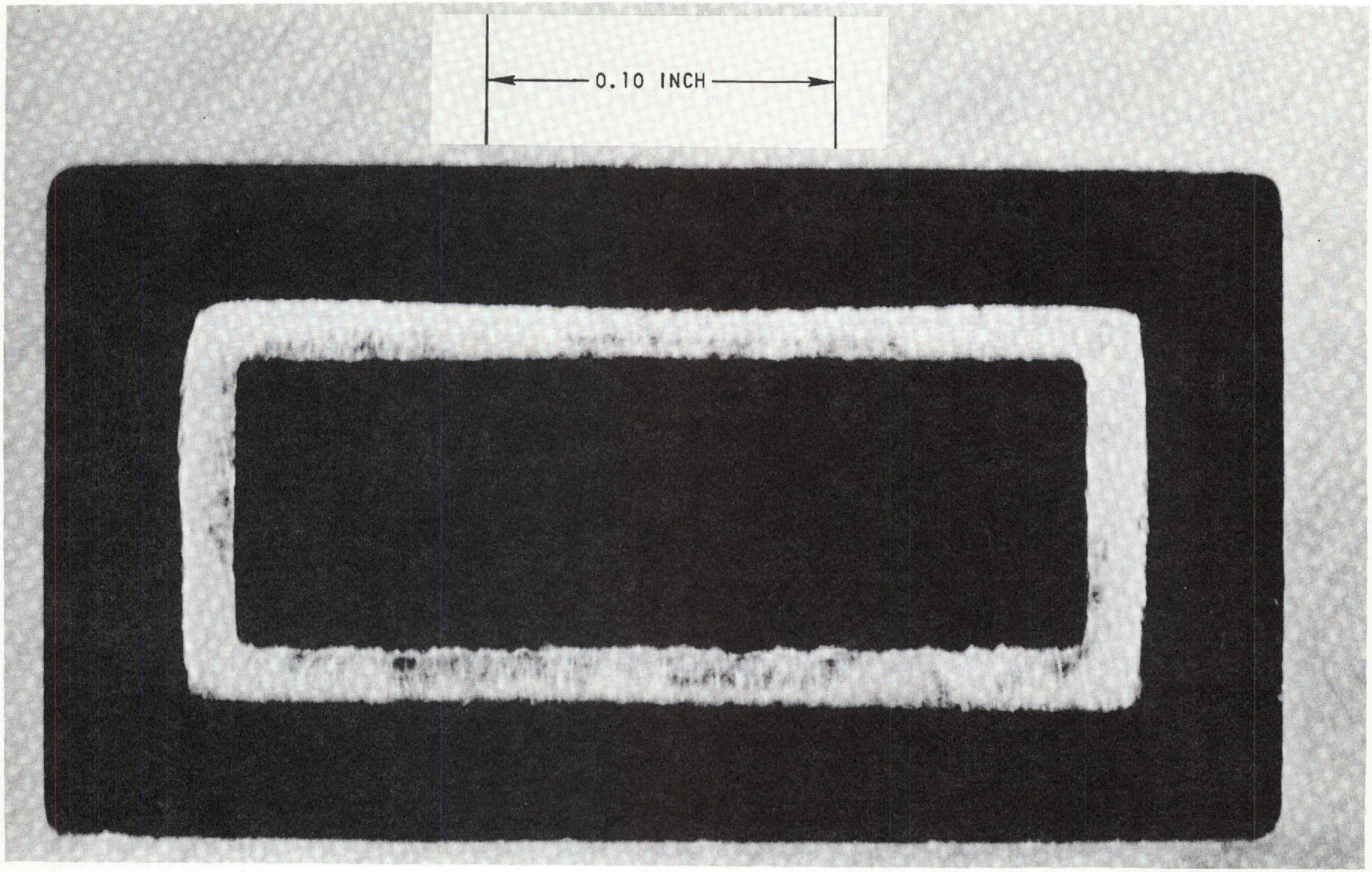

5AA32-8/20/71-S1

Figure 3-10. Element Face Detail (Element GCR-2 Shown)

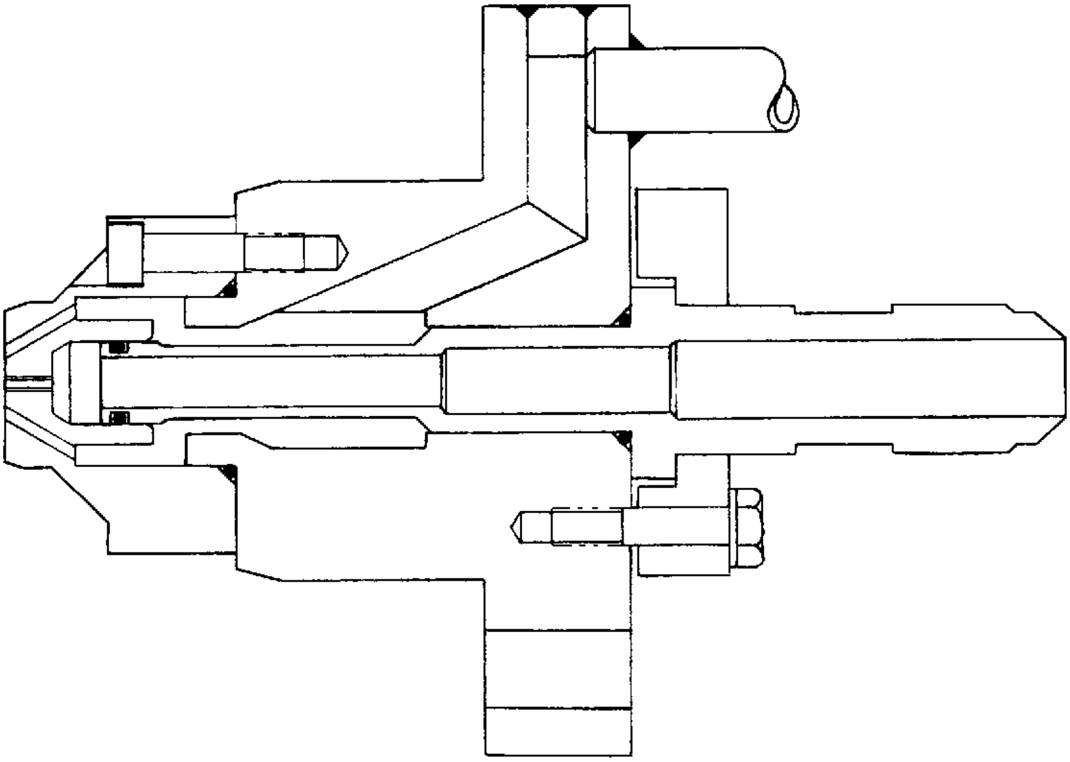

Figure 3-11. Single-Element Injector Assembly (Element GST-2 Shown)

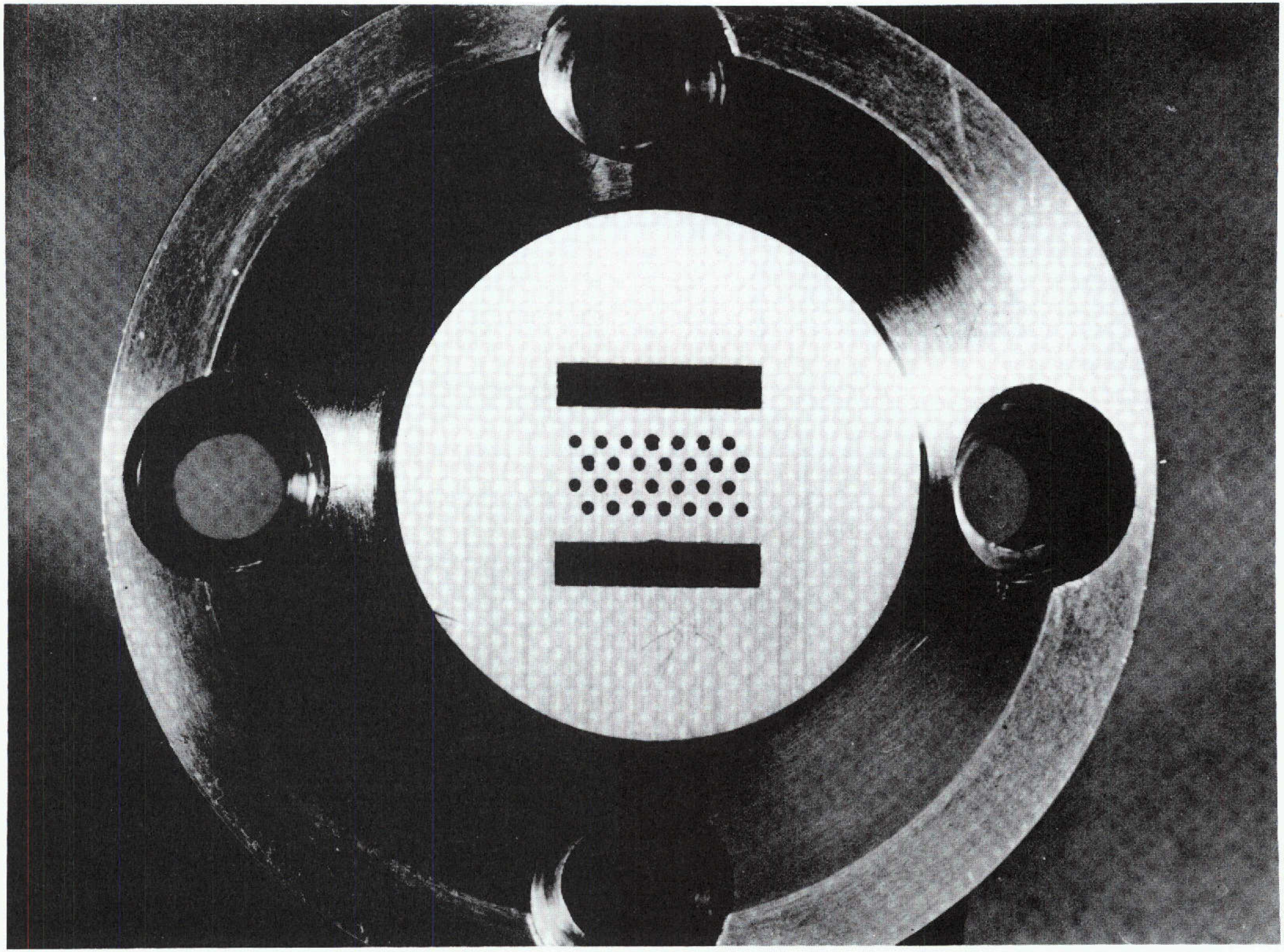

5AA34-8/2/71-S1

Figure 3-12. Multishowerhead Triplet Face Pattern (Element GST-1 Shown)

TABLE 3-6. PHASE III ELEMENT HARDWARE DRAWING NUMBER KEY

Element Code	Drawing Numbers			
	Body	Clamp	Port	Post
GCC-2	R1C2928	R1B2930	R1B2960	R1C2961
GCR-2	↓	↓	R1B2927	R1C2929
GCR-3	↓	↓	R1B2954	R1C2929
GCR-4	↓	↓	R1B2955	R1C2929
GCR-5	↓	↓	R1B2935	R1C2933
GCR-6	↓	↓	R1B2934	R1C2931
GCR-7	↓	↓	R1B2957	R1C2958
GCR-8	↓	↓	R1B2927-3	R1C2929
GCR-9	↓	↓	R1B2934-3	R1C2933
GCR-10	↓	↓	R1B2935-3	R1C2933
GST-1	↓	↓	R1B2937	R1C2938
GST-2	↓	↓	R1B2948	R1C2938

3.3.2.1 Chamber Heat Transfer Analysis. The chamber heat transfer analysis was based upon the nominal operating conditions listed in Table 3-4. With the assumption of 100-percent c* efficiency, these conditions yield the chamber design parameters listed in Table 3-7.

A chamber length (injector to throat) of 4 inches was selected based upon a preliminary droplet vaporization calculation that indicated that vaporization would be incomplete at the throat. Thus, performance variations due to dropsize variations were expected to be clearly evident within the accuracy of the experimental apparatus.

A heat transfer analysis of the chamber was conducted with Rocketdyne's integral-momentum turbulent boundary layer computer program. The chamber wall temperature was assumed to be a constant 1560 R. The results of that analysis are presented in Table 3-8.

A copper chamber liner of the type shown in Fig. 3-13 with axial coolant channels was selected for the chamber design. Subcooled water was chosen for the coolant.

The design of the copper chamber liner was based upon four heat transfer correlations and/or fundamental equations plus a stress analysis of the liner wall at the thinnest section. These design equations are listed in Table 3-9.

A great deal of judgment and experience was applied to the design in addition to the equations listed in Table 3-9. Many of the variables appearing in the equations are either known or can be estimated to the first order.

The following is a brief discussion of the logic employed to reduce the number of variables in the design equations. It is arranged in list form for clarity of presentation.

TABLE 3-7. PRELIMINARY CHAMBER DESIGN PARAMETERS

Parameter	Value
Maximum Adiabatic Temperature	6374 R
Throat Diameter	0.395 inch
Chamber Diameter	0.600 inch
ρu at Throat	3.525 $\mathrm{lbm/in.^2}$-sec
ρu in Chamber	1.528 $\mathrm{lbm/in.^2}$-sec
Throat Reynolds Number	2.62×10^6
Chamber Reynolds Number	1.72×10^6
Specific Heat Ratio	
Frozen	1.202
Shifting	1.138
Specific Heat (c_p)	
Frozen	0.890 Btu/lbm-R
Shifting	2.417 Btu/lbm-R
Prandtl Number	0.826

TABLE 3-8. RESULTS OF THE TURBULENT BOUNDARY LAYER ANALYSIS
(P_c = 800 psi; T_o = 6374 R; T_w = 1560 R)

Parameter	Value
Throat Heat Flux	33 to 35 $\mathrm{Btu/in.^2}$-sec
Chamber Heat Flux	19 to 20 $\mathrm{Btu/in.^2}$-sec
Gas-Side Film Coefficient	
Throat	0.00685 $\mathrm{Btu/in.^2}$-sec-R
Chamber	0.00414 $\mathrm{Btu/in.^2}$-sec-R

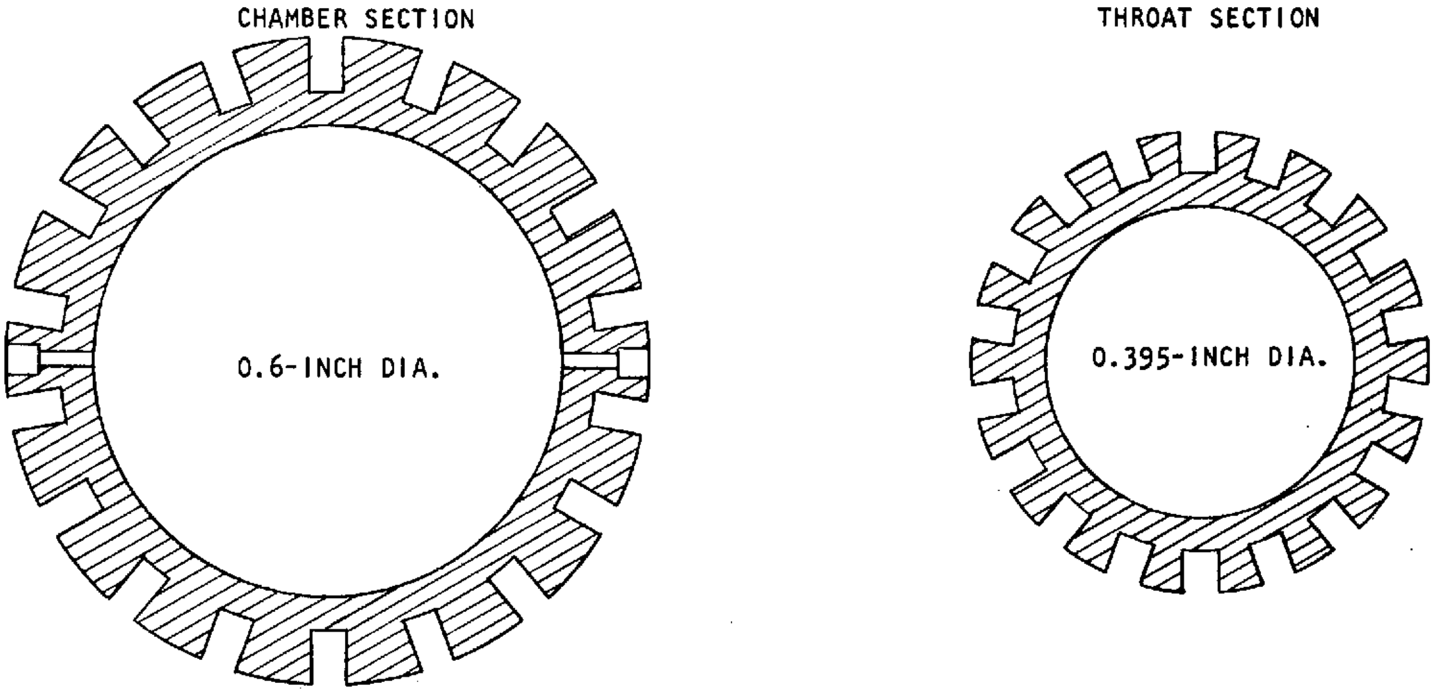

Figure 3-13. Cross-Sectional View of Hot-Fire Chamber Liner

TABLE 3-9. HEAT TRANSFER RELATIONSHIPS EMPLOYED FOR THE DESIGN OF THE COPPER CHAMBER LINER (ONE-DIMENSIONAL CONDUCTION ASSUMED)

Relationship	Equation*	Eq. No.	Reference
Heat Flow Continuity	$\frac{k}{s}(T_{wg} - T_{wc}) = \frac{\dot{Q}}{A}$	3-1	Basic Definition
	$h_c(T_{wc} - T_{BC}) = \frac{\dot{Q}}{A}$	3-2	
Burn Out Heat Flux	$.01\sqrt{V_c}(T_{SAT} - T_{BC}) = \left(\frac{\dot{Q}}{A}\right)_{B.O.}$	3-3	Ref. 5
Coolant Side Heat Transfer Coefficient	$S_t = .005\,(R_e)^{-.05}\,(P_r)^{-.6}$	3-4	Ref. 6

* $k \equiv$ Conductivity of Liner Wall, BTU/in-sec-°R
$s \equiv$ Liner Wall Thickness, inch
$h_c \equiv$ Coolant Side Coefficient, BTU/in^2-sec-°R
$\dot{Q}/A$ = Actual Estimated Heat Flux, BTU-in^2-sec
$(\dot{Q}/A)_{B.O.}$ = Burnout Heat Flux, BTU/in^2-sec.
V_c = Coolant Velocity, Ft/Sec

$T_{wg} \equiv$ Gas Side Wall Temp., °R
$T_{wc} \equiv$ Coolant Side Wall Temp., °R
$T_{BC} \equiv$ Coolant Bulk Temp., °R
$T_{SAT} \equiv$ Coolant Saturation Temp., °R
$S_t = h_c/\rho v c_p$ (Stanton)
$R_e = \rho v d/\mu$ (Reynolds)
$P_r = c_p \mu / k$ (Prandtl)

1. The value of $\dot{Q}/A$ maximum was given by the gas-side heat transfer solution $\dot{Q}/A_{max}$ = 35 Btu/in.^{2}-sec.
2. The burnout heat flux was computed by multiplying the maximum heat flux by an assumed cooling margin. A value of 1.25 was selected for a cooling margin; therefore $(\dot{Q}/A)_{B.O.}$ = 1.25 x 35 = 44 Btu/in.^{2}-sec.
3. With copper liners, it is reasonable to limit the gas-side wall temperature to 800 F or 1260 R; therefore T_{wg} = 1260 R.
4. The saturation temperature for water is shown plotted as a function of static pressure in Fig. 3-14. It is desirable to maintain a high saturation temperature while limiting the pressure to reasonable values. For pressures of the order of 600 psia, the saturation temperature is of the order of 500 F; therefore T_{SAT} = 500 F = 960 R.
5. For added yield strength, at elevated temperature and pressure difference, NARloy was selected for the chamber liner material rather than OFHC copper. Thus, the thermal conductivity was established, K = 0.005 Btu/in.-sec-R.
6. The facility for hot-fire experimentation could be expected to supply coolant water at temperatures around the ambient temperature. Actually, a subsequent analysis, which is presented later in this section, indicated that a coolant water temperature of the order of 120 F was superior to ambient temperatures; thus, T_{BC} = 580 R.
7. The scale of the liner dictates that the hydraulic diameter of the channels should be of the order of 0.1 inch. Reasonable coolant velocities could be expected to be roughly 150 ft/sec. These approximate values yield a coolant Reynolds number of the order of 2 x 10^5.
8. Around 100 F, the Prandtl number for water is about 4.0; Pr = 4.0.

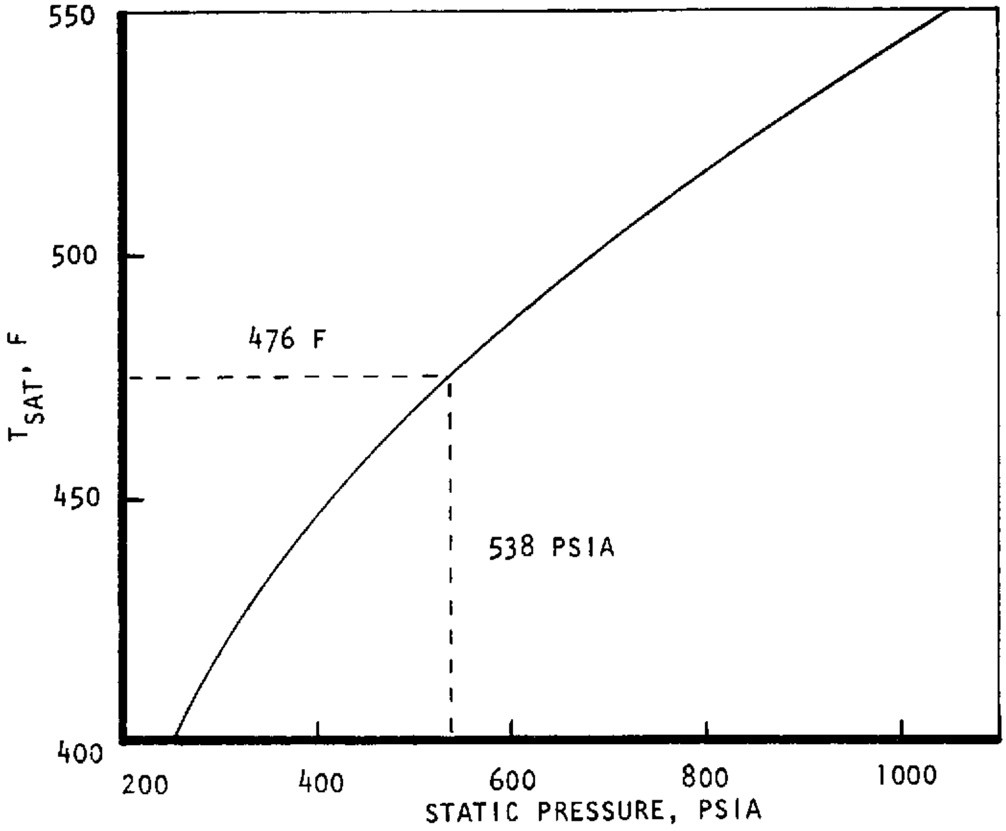

Figure 3-14. Saturation Temperature of Water as a Function of Pressure

These approximate values are listed in Table 3-10. Substitution of the values from Table 3-10 into the equations in Table 3-9 yields the following set of simplified equations. The coefficient in Eq. 3-4 was reduced by 60 percent for safety margin, and C_p for water was assumed to be 1 Btu/lbm-R. (S is the wall thickness in inches.)

$$T_{WC} = 1260 - 7000\ S \tag{3-1}$$

$$h_c\ (T_{WC} - 580) = 35 \tag{3-2}$$

$$V_c = 134 \tag{3-3}$$

$$h_c = 0.000307\ V_c \tag{3-4}$$

Solution of these equations gave the first-order liner design parameters:

V_c = 134 ft/sec

h_c = 0.0411 Btu/in.^{2}-sec-R

T_{WC} = 1432 R

S = 0.0246 inch

These numbers are, obviously, not physical. The problem rests with allowing the wall thickness to vary, arbitrarily, with the rough-order-of-magnitude estimates for the other variables.

If the wall thickness, S, is selected from structural considerations, it can be seen that the set of design equations is overdetermined. That is, there are two criteria for selection of the coolant velocity; one from burnout considerations, and one from coolant-side heat transfer conditions. If the velocity required to achieve the coolant-side coefficient is greater than the burnout velocity, then the design parameters are acceptable to the first order.

TABLE 3-10. APPROXIMATE VALUES EMPLOYED FOR "FIRST-TRIAL" CHAMBER LINER DESIGN

Variable	Approximate Value
$\dot{Q}/A$	35 Btu/in.^{2}-sec
$(\dot{Q}/A)_{B.O.}$	44 Btu/in.^{2}-sec
T_{wg}	1260 R
T_{sat}	960 R
K	0.005 Btu/in.-sec-R
T_{BC}	580 R
Re	2×10^5
Pr	4

A structural analysis of the liner wall was conducted and it was concluded that a minimum liner wall thickness equal to 0.046 inch was acceptable. Setting S equal to 0.046 inch in Eq. 3-1 and solving the set of design equations gave the following results:

T_{WC} = 938 R = 478 F

h_c = 0.0978 Btu/in.^{2}-sec-R

(V_c) = 134 burnout

(V_c) = 318 coolant-side coefficient

Based upon these preliminary results, it was concluded that coolant-side coefficients of the order of 0.09 Btu/in.^{2}-sec-R and coolant velocities of the order of at least 200 ft/sec at the throat must be employed. A chamber liner design was configured to meet these criteria. The liner is shown in cross section in Fig. 3-13. Eighteen evenly spaced axial coolant channels were selected, having a total flow area of 0.0591 in.^{2} in the chamber section and 0.04536 in.^{2} at the throat. A coolant velocity of 200 ft/sec was selected, which gave a total water flowrate of approximately 4 lbm/sec and a coolant velocity of 153 ft/sec in the chamber section. Wall thickness at the channel roots, S, was set at 0.046 inch.

The liner is shown in cross section in Fig. 3-15, along with the heat fluxes, coolant velocities, and coolant-side pressures chosen. The task remained to perform a final analysis of this design configuration to ensure that the desired features had been achieved. Before this analysis is discussed, however, a brief mention of the logic behind selection of water bulk temperature is presented. A study was conducted employing Eq. 3-4 (Table 3-9) to estimate the cooling effectiveness of water. The following values were assumed:

$V_c = 200$ ft/sec

$T_{WC} = 400$ F

$d_{channel} \approx 0.06$ inch

$(Rey)^{0.05} \approx const \approx 2.21$

$C_p = 1$ Btu/lbm-R

With these values, Eq. 3-4 becomes:

$$h_c = \frac{0.1961}{(Pr)^{0.6}} \tag{3-5}$$

The cooling effectiveness, $\dot{Q}/A$, may be written:

$$\dot{Q}/A = h_c \, (T_{WC} - T_{BC}) \tag{3-6}$$

Combining Eq. 3-5 and 3-6 and introducing the value of $T_{WC} = 400$ F yields:

$$\dot{Q}/A = \frac{0.239}{(Pr)^{0.6}} \, (400 - T_{BC}) \tag{3-7}$$

It can be seen from Eq. 3-7 that, as T_{BC} is increased, the effective driving potential is decreased. However, for water, the reduction of the Prandtl number with increased temperature overrides the loss in ΔT up to roughly, 200 to 250 F. Equation 3-7 is plotted in Fig. 3-16. It is evident that it is beneficial to heat the coolant water to at least 120 to 140 F.

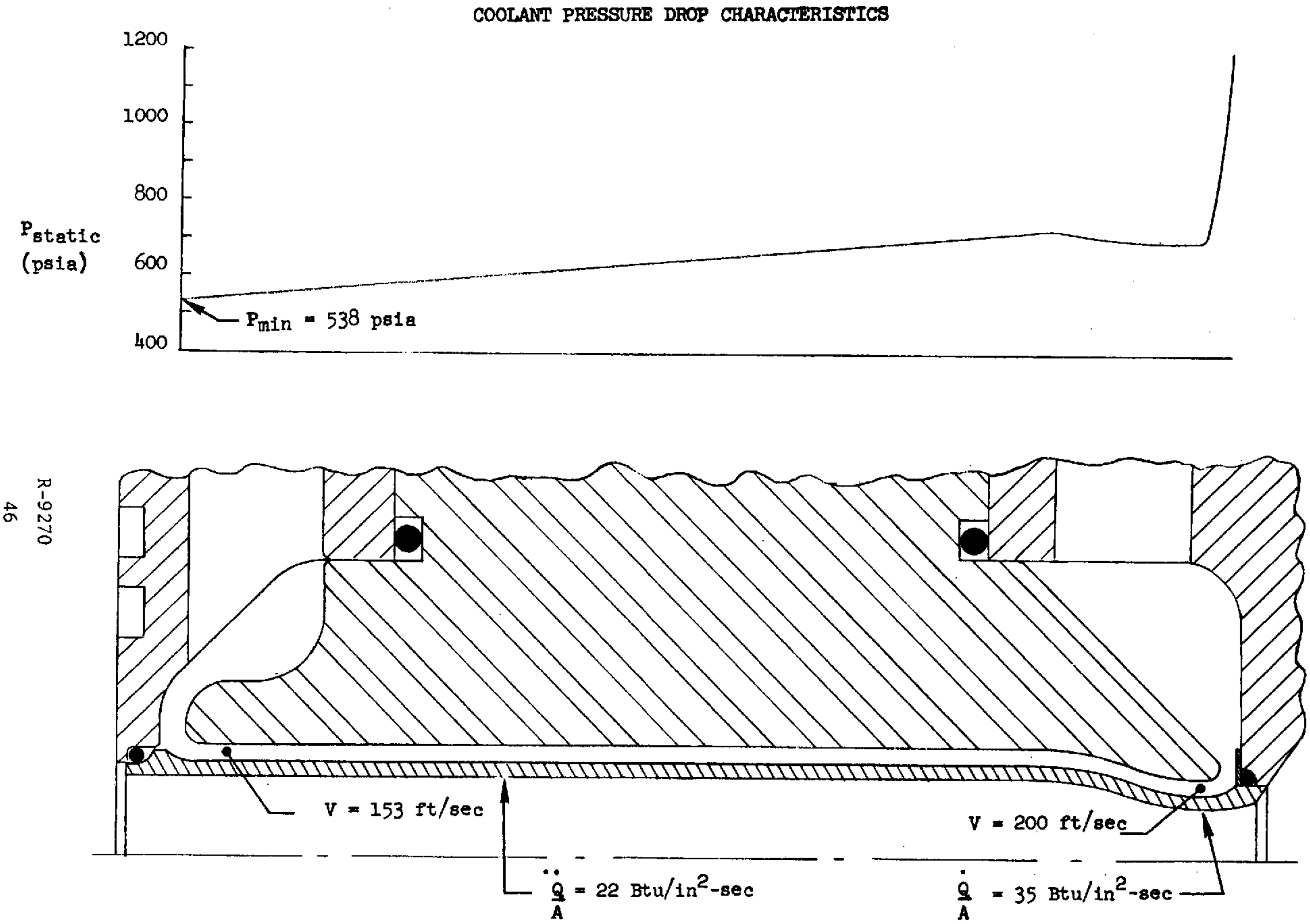

Figure 3-15. Chamber Liner Coolant Passage

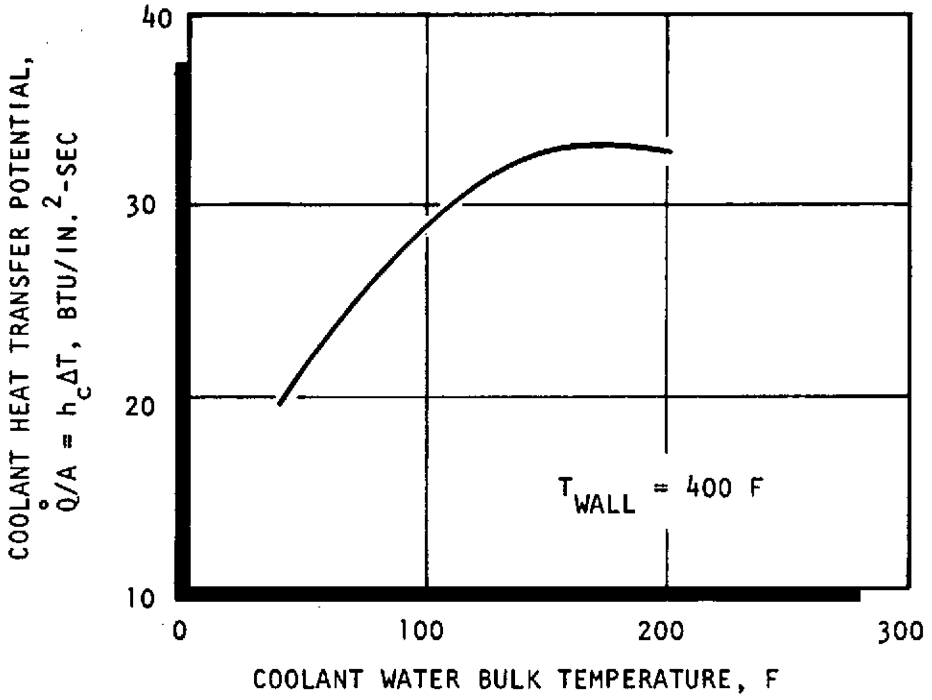

Figure 3-16. Effect of Bulk Temperature Upon the Effectiveness of Water for Cooling

A final analysis of the chamber liner was conducted assuming the coolant parameters shown in Fig. 3-15 and with T_{BC} = 120 F. A two-dimensional conduction model was employed in place of Eq. 3-1 and 3-2. The results of that analysis are presented in Table 3-11. These results indicated that the first design for the chamber liner was more than adequate. The temperatures were quite acceptable and the cooling margins were greater than 50 percent.

TABLE 3-11. FINAL CHAMBER HEAT TRANSFER RESULTS

($T_{BC} \approx 120$ F)

	Throat	Chamber
$\dot{Q}/A$, Btu/in.^{2}-sec	35	20
T_{WG}, F	800	680
$T_{WC(Root)}$, F	400	430
h_g, Btu/in.^{2}-sec-R	0.00685	0.00414
h_c, Btu/in.^{2}-sec-R	0.090	0.060
V_c, ft/sec	200	153
P_{STATIC}, psia	700	538
T_{SAT}, F	500	
$(\dot{Q}/A)_{B.O.}$, Btu/in.^{2}-sec	53.7	43.9
Cooling Margin, $(\dot{Q}/A)_{B.O.}/(\dot{Q}/A)$	1.53	2.20

3.3.2.2 Hardware Design Description. The entire thrust chamber assembly is shown in Fig. 3-17, including the injector assembly previously discussed. Figure 3-17 is the actual chamber top assembly drawing and contains all of the Rocketdyne drawing numbers for each part. The detail drawing of the chamber liner (presented as Fig. 3-18) shows all of the critical chamber dimensions (the -013 chamber was fabricated).

FOLDOUT FRAME

FOLDOUT FRAME

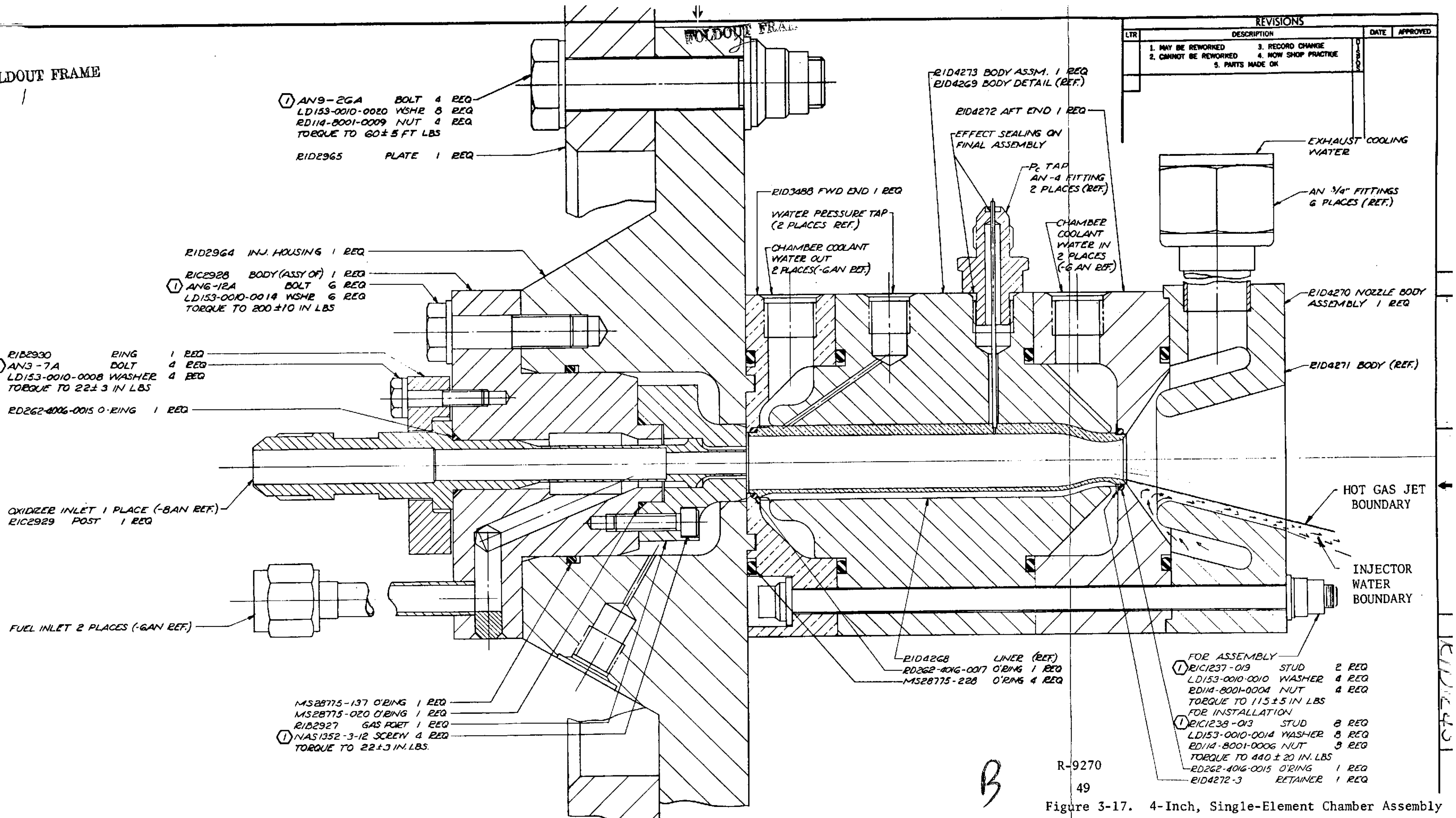

REVISIONS

LTR	DESCRIPTION	DISPOS	DATE	APPROVED
	1. MAY BE REWORKED 3. RECORD CHANGE 2. CANNOT BE REWORKED 4. NOW SHOP PRACTICE 5. PARTS MADE OK			

B

Figure 3-17. 4-Inch, Single-Element Chamber Assembly

A

① INSTALL ALL FASTENERS PER RA0101-002

NOTE: UNLESS OTHERWISE SPECIFIED

HEAT TREAT NONE	UNLESS OTHERWISE SPECIFIED: DIMENSIONS ARE IN INCHES AND APPLY PRIOR TO FINISH. 125/ MACH. SURF. ROUGHNESS	DR BY RussD DATE 12-21-71 CHK BY DATE	**ROCKETDYNE** A DIVISION OF NORTH AMERICAN ROCKWELL CORPORATION CANOGA PARK, CALIFORNIA • McGREGOR, TEXAS
FINISH NONE	TOLERANCES ON: ANGLES ± 0° 30' DECIMALS .XX ± .03 .XXX ± .010 HOLES NOTED "DRILL" OVER THRU TOLERANCE .0000 .0400 + .0015 — .0010 .0400 .1300 + .0030 — .0010 .1300 .2290 + .0045 — .0010 .2290 .5000 + .0060 — .0010 .5000 .7500 + .0070 — .0010 .7500 1.0000 + .0090 — .0010 1.0000 2.0000 + .0120 — .0010	DSGN MATL STR	CHAMBER ASSY, 4 INCH SINGLE ELEMENT-NON-CIRC ORIFICE PROGRAM
MAT'L NONE	DO NOT SCALE PRINT	DESIGN ACTIVITY APPD DATE	SIZE D CODE IDENT NO. 02602 R1D1243 SCALE 2/1 SHEET

FOLDOUT FRAME 1

FOLDOUT FRAME 2

DASH NO.	"U"	"V"	
-003	3.210	2.964	
-005	6.410	6.164	
-007	9.610	9.364	
-009	12.810	12.564	
-013	4.221	3.975	(A1)

LTR	DESCRIPTION	DISPOS	DATE	APPROVED
	1. MAY BE REWORKED 2. CANNOT BE REWORKED 3. RECORD CHANGE 4. NOW SHOP PRACTICE 5. PARTS MADE OK			
A	1.) ADD -13 LENGTH 2) ADDED NOTE '9' 3.) REVISED P. TAPS		11/15/71	Russ
B	1) REVISED NOTE 2) .005R MAX WAS .060R		11/18/71	Russ
C	1.) 030R MAX WAS .060R. 2.) 030R MAX WAS .060		12/16/71	Russ
D	TOLERANCE $^{+.000}_{-.002}$ WAS $^{+.000}_{-.010}$		12/20/71	Russ

(A3) DRILL #76 (.020) DIA THRU ONE WALL FLAT BOTTOM C'DRILL NOMINAL #57 (.043)

(B1) SEE DRAWING RID4273 FOR CLEARANCE WITH RID3490-3 TUBE 2 PLACES EQUALLY SPACED 180° APART, LOCATED AS SHOWN.

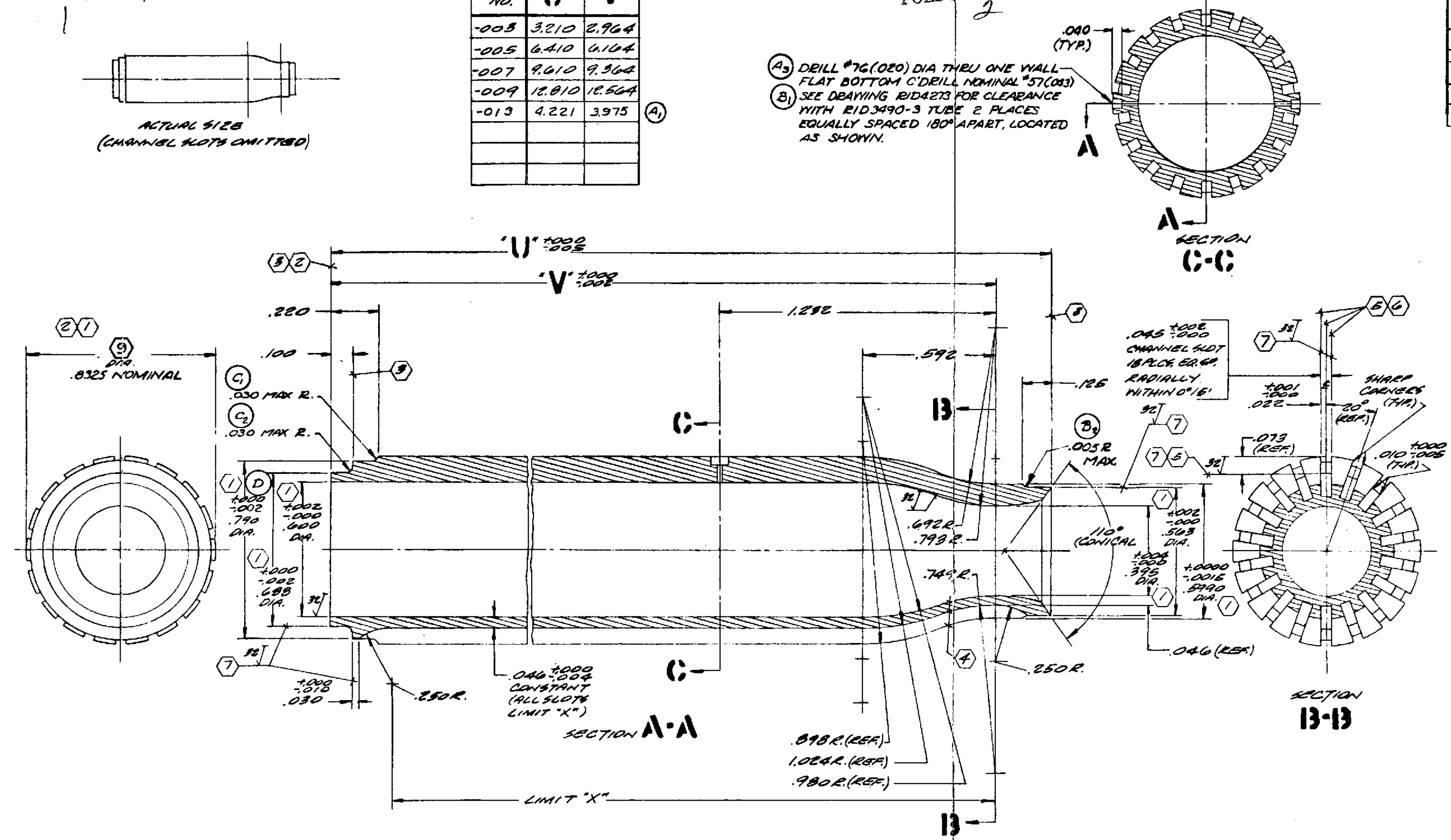

(A2) ⟨9⟩ TO HAVE .0035 TO .0045 DIAMETRAL CLEARANCE WITH RID4269 BODY

8. IDENTIFY PER RA0104-008. DO NOT IMPRESSION STAMP. TAG ONLY.

⟨7⟩ THIS SURFACE IS A SEALING SURFACE. IT SHALL BE FREE OF ALL NICKS, SCRATCHES OR OTHER IMPERFECTIONS WHICH WOULD IMPAIR ITS SEALING FUNCTION.

⟨6⟩ PARALLEL WITHIN .002

⟨5⟩ PERPENDICULAR WITHIN .002

⟨4⟩ SURFACE CONTINUITY SHALL BE SMOOTH THROUGHOUT ENTIRE .592 TRANSITION LENGTH.

⟨3⟩ PARALLEL WITHIN .002

⟨2⟩ PERPENDICULAR WITHIN .002

⟨1⟩ CONCENTRIC WITHIN .002 T.I.R.

NOTE: UNLESS OTHERWISE SPECIFIED

Figure 3-18. Nozzle Section Liner, Single-Element Chamber

A

B

HEAT TREAT

FINISH

MAT'L: "NARLOY" BAR

UNLESS OTHERWISE SPECIFIED: DIMENSIONS ARE IN INCHES AND APPLY PRIOR TO FINISH.
125√ MACH. SURF. ROUGHNESS
TOLERANCES ON: ANGLES ± 0° 30' DECIMALS .XX ± .03 .XXX ± .010
HOLES NOTED "DRILL"

OVER	THRU	TOLERANCE	
.0000	.0400	+ .0015	— .0010
.0400	.1300	+ .0030	— .0010
.1300	.2290	+ .0045	— .0010
.2290	.5000	+ .0060	— .0010
.5000	.7500	+ .0070	— .0010
.7500	1.0000	+ .0090	— .0010
1.0000	2.0000	+ .0120	— .0010

DO NOT SCALE PRINT

DR BY G. JANSON 10-4-71
CHK BY
DES
SUP
MAT
STR
DEV

ROCKETDYNE
A DIVISION OF NORTH AMERICAN AVIATION, INC.
CANOGA PARK, CALIFORNIA • McGREGOR, TEXAS

LINER, NOZZLE SECTION, NON-CIRCULAR ORIFICE PROGRAM, SINGLE ELEMENT CHAMBER

SIZE D
CODE IDENT NO. 02602
RID4268
SCALE 4X
SHEET

RID4268

The chamber liner was fabricated from NARloy (a special copper alloy) rather than OFHC copper to gain a high yield strength (Fig. 3-18). The chamber diameter is 0.6 inch and the throat diameter is 0.395 inch, giving a contraction ratio $\varepsilon_c = 2.307$.

The liner is retained in the thrust chamber body (R1D4273, Fig. 3-17) between the forward closure (R1D3488) and the aft closure (R1D4272). The liner is restricted from moving downstream by retainer R1D4272-3 but is free to move upstream by sliding in the forward closure R1D3488. This was required to allow for thermal expansion of the liner to avoid upset yielding. All pieces, except the liner, were fabricated from series 321 stainless steel.

Cooling water is introduced through two inlets in the aft closure, R1D4272 (only one shown due to section) into a manifold formed between the aft closure and the body. The coolant enters the axial channels between the liner and the body and travels upstream to a manifold between the body and the forward closure (Fig. 3-17). The coolant exits from two outlets in the forward closure (only one shown due to section). In operation, the inlets and outlets were actually oriented at 90 degrees to one another to prevent preferential circulation.

A pressure tap was provided in the body (R1D4273) at the downstream end of the cooling channels to ensure that the minimum static pressure in the cooling system was sufficiently high during firing to maintain the high values of T_{SAT} required.

Two chamber pressure taps were provided (at 180 degrees apart; only one shown due to section) 1.232 inches upstream of the throat.

A simple exhaust nozzle (R1D4270) was clamped to the aft closure. The actual expansion contour was composed of an annular water jet that was injected around the hot-gas jet. This was done to reduce the cost of the chamber and was justified due to the fact that thrust data were not to be taken with this chamber.

The chamber assembly is bolted together by the studs (R1C1237-019) shown in Fig. 3-17. With these studs in place, the chamber could be removed from the injector housing plate (R1D2964) and transported separately as an assembly. The chamber assembly is installed on the housing plate by studs R1C1238-013 (not shown due to section), which screw into holes in the housing and protrude all the way through the chamber and are secured on the downstream end of the nozzle with nuts.

The housing (R1D2964) was the only piece of hardware that was attached directly to the test stand (on plate R1D2965). The thrust chamber or the injector could be removed, independently, without removing the other. The injectors mount to the housing as an assembly so that they can be "made up" ahead of a test in the work shop.

Photographs of selected components are presented in Fig. 3-19 through 3-23 and photographs of the body assembly (R1D4273), showing the liner in place, are presented as Fig. 3-24 and 3-25. The entire thrust chamber assembly is shown mounted on the test stand (Appendix E) in Fig. 3-26.

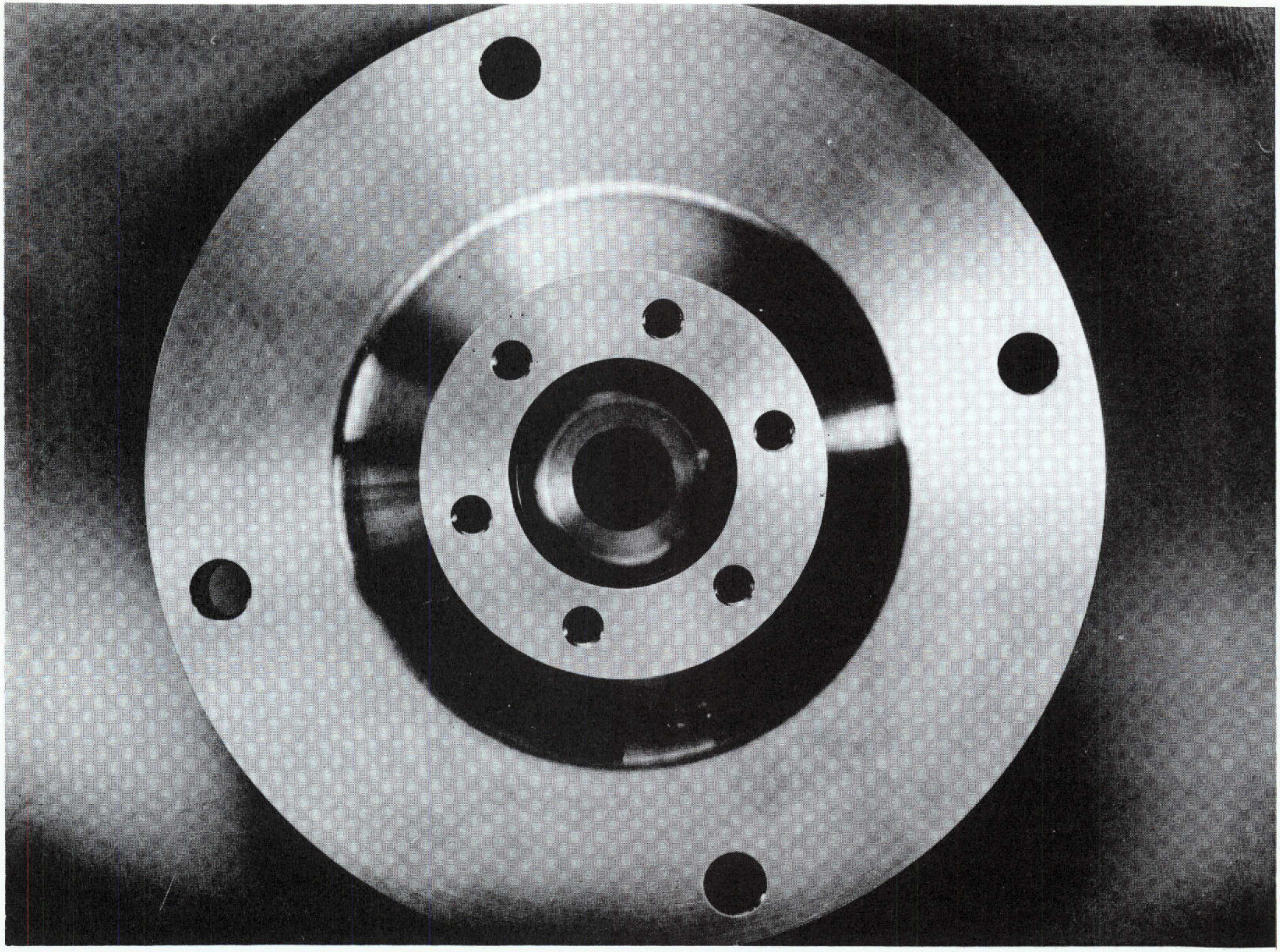

5AA34-1/7/72-S1B

Figure 3-19. Housing (Injector End), R1D2964

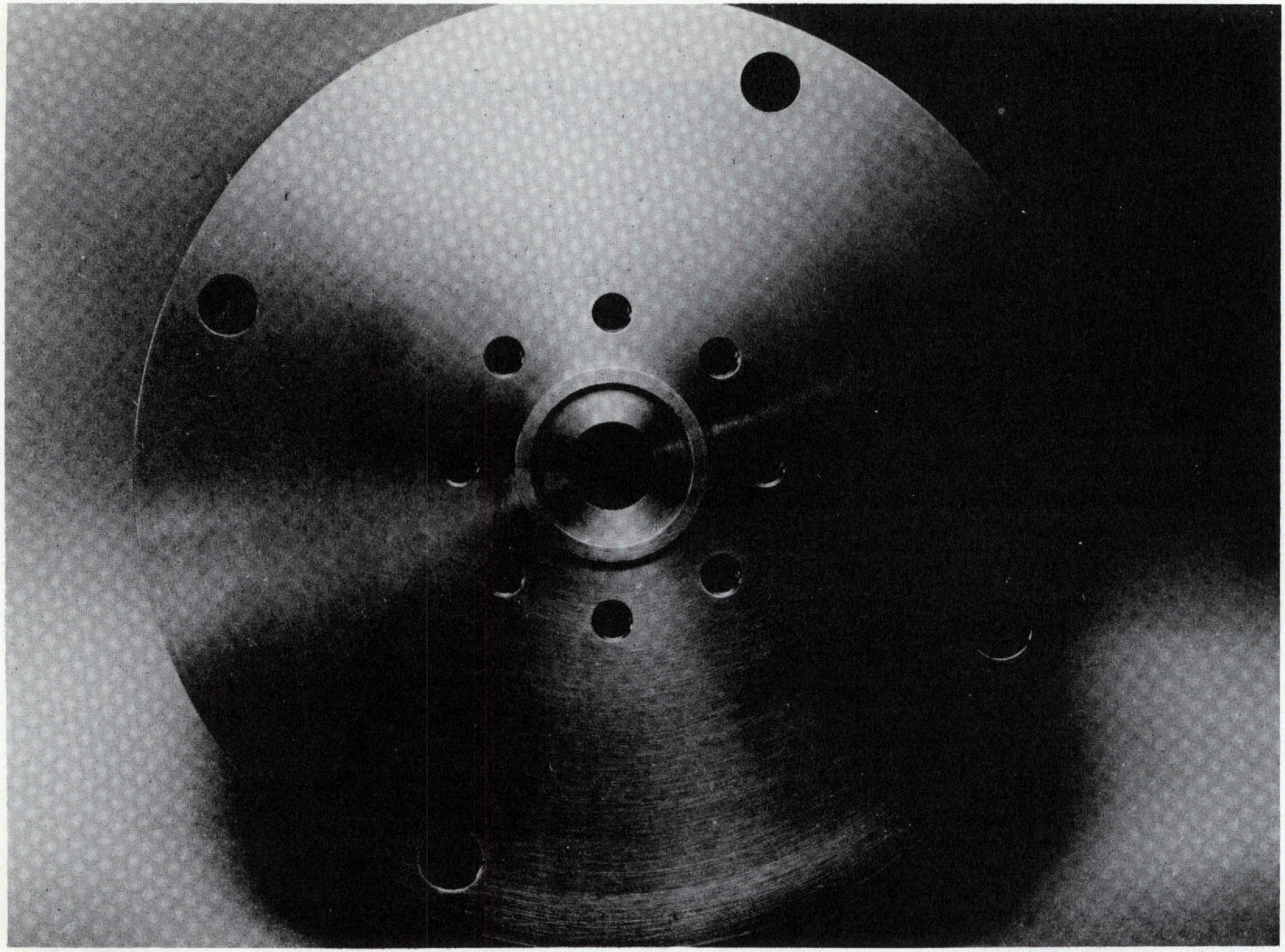

5AA34-1/7/72-S1A

Figure 3-19. (Concluded) (Chamber End)

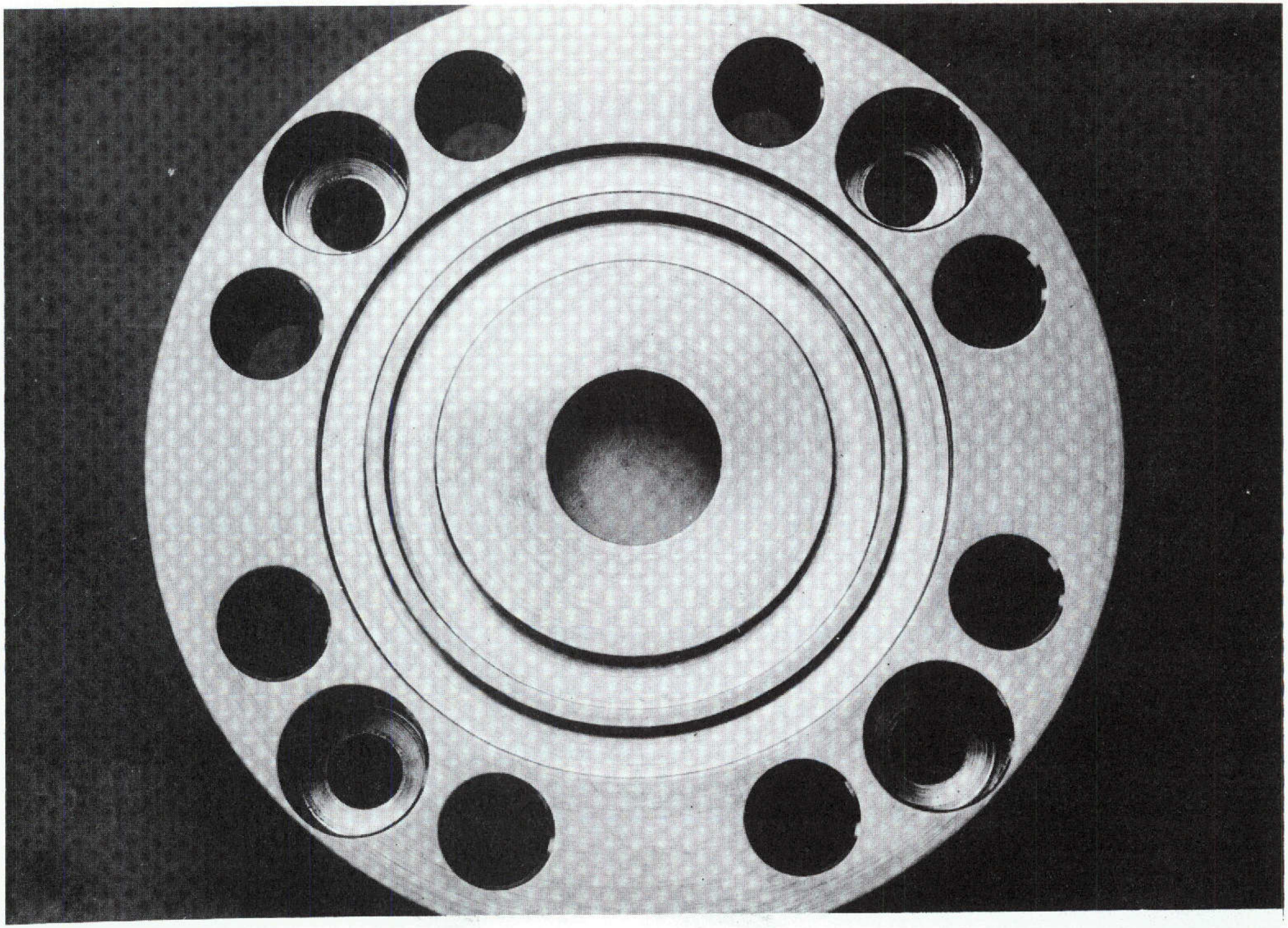

5AA34-1/7/72-S1F

Figure 3-20. Forward Closure (Forward End), R1D3488

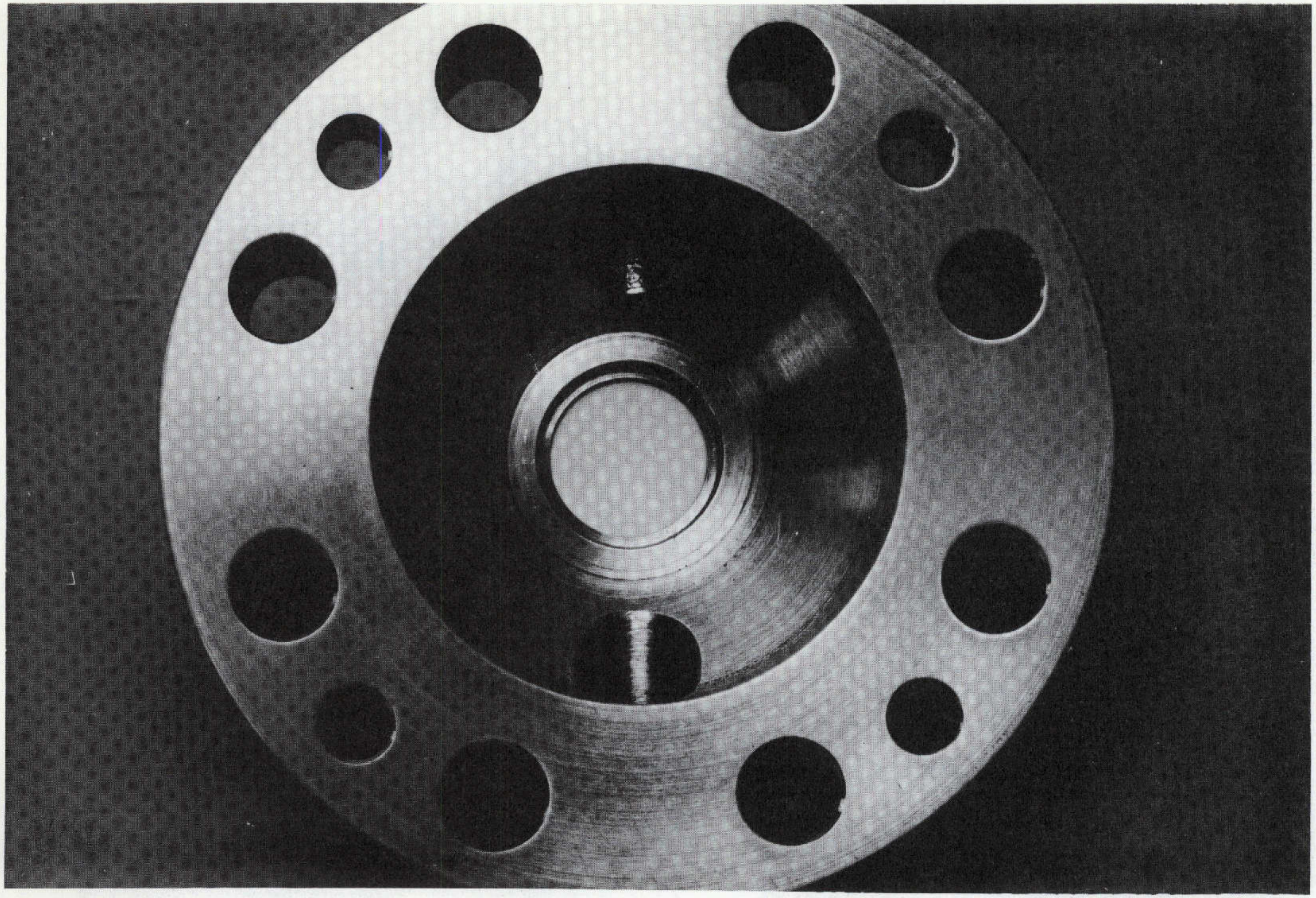

5AA34-1/7/72-S1E

Figure 3-21. Forward Closure (Aft End), R1D3488

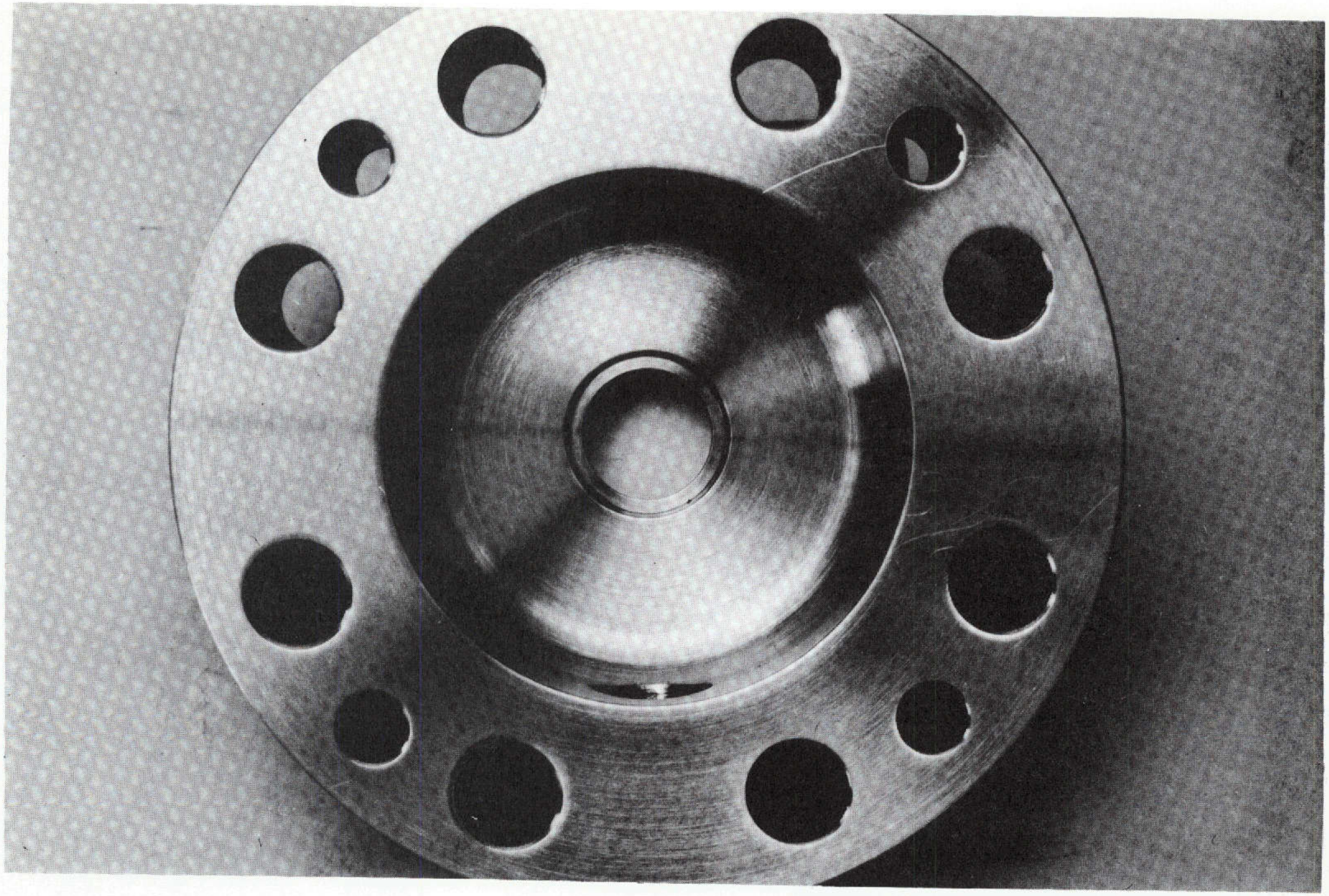

5AA34-1/7/72-S1G

Figure 3-22. Aft Closure (Forward End), R1D4272

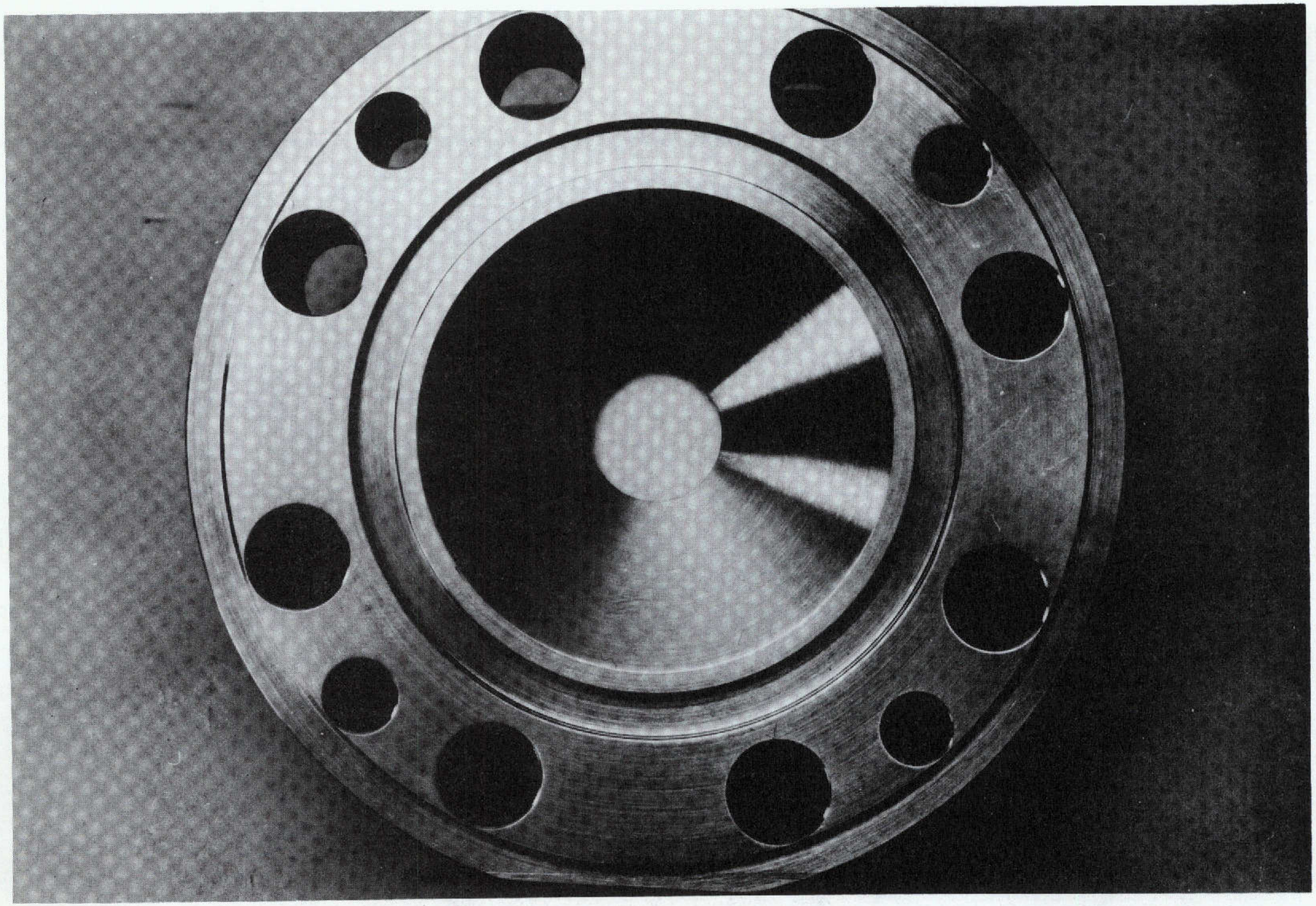

5AA34-1/7/72-S1H

Figure 3-23. Aft Closure (Aft End), R1D4272

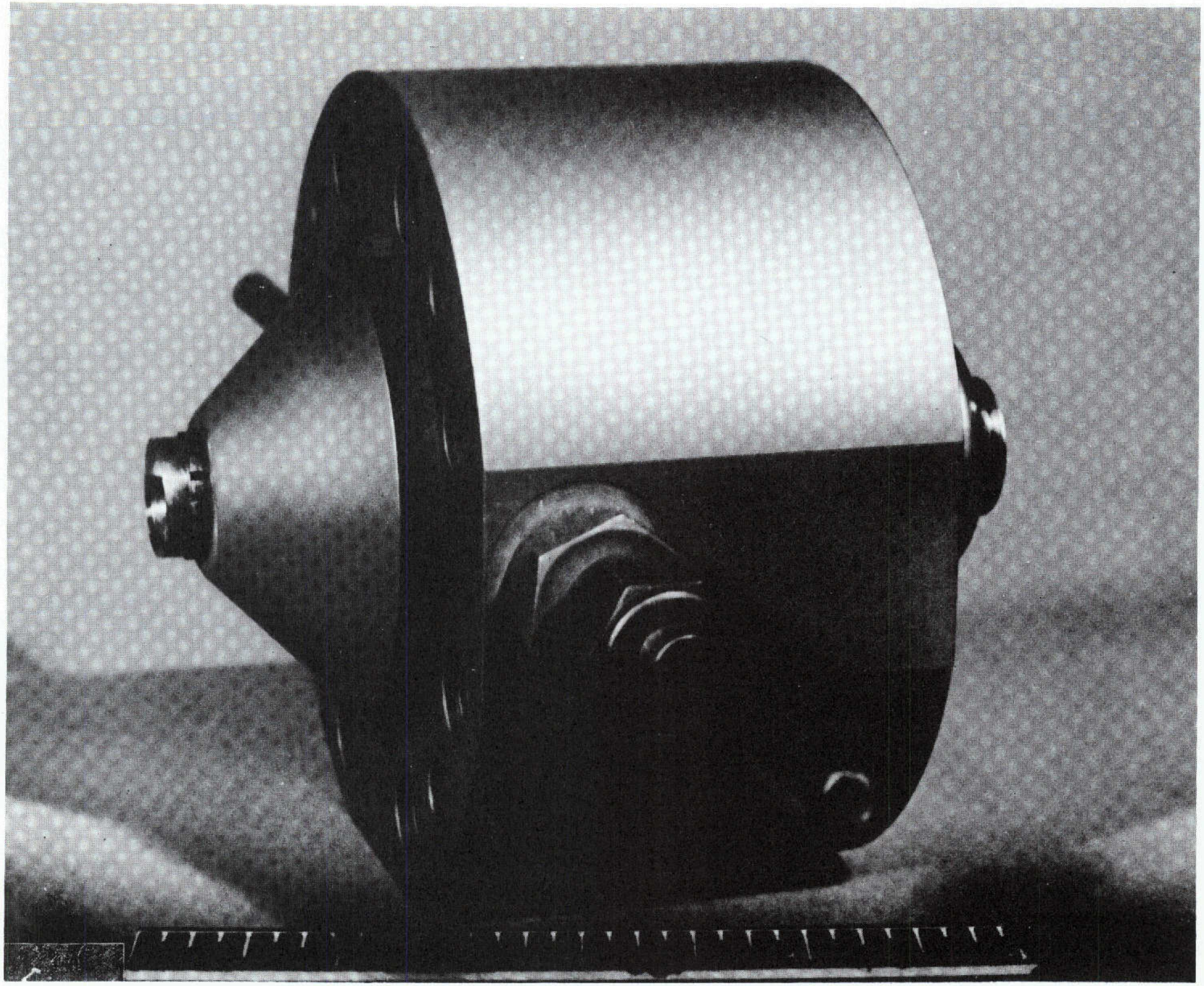

5AA34-2/3/72-S1C

Figure 3-24. Body Assembly (Side View), R1D4273

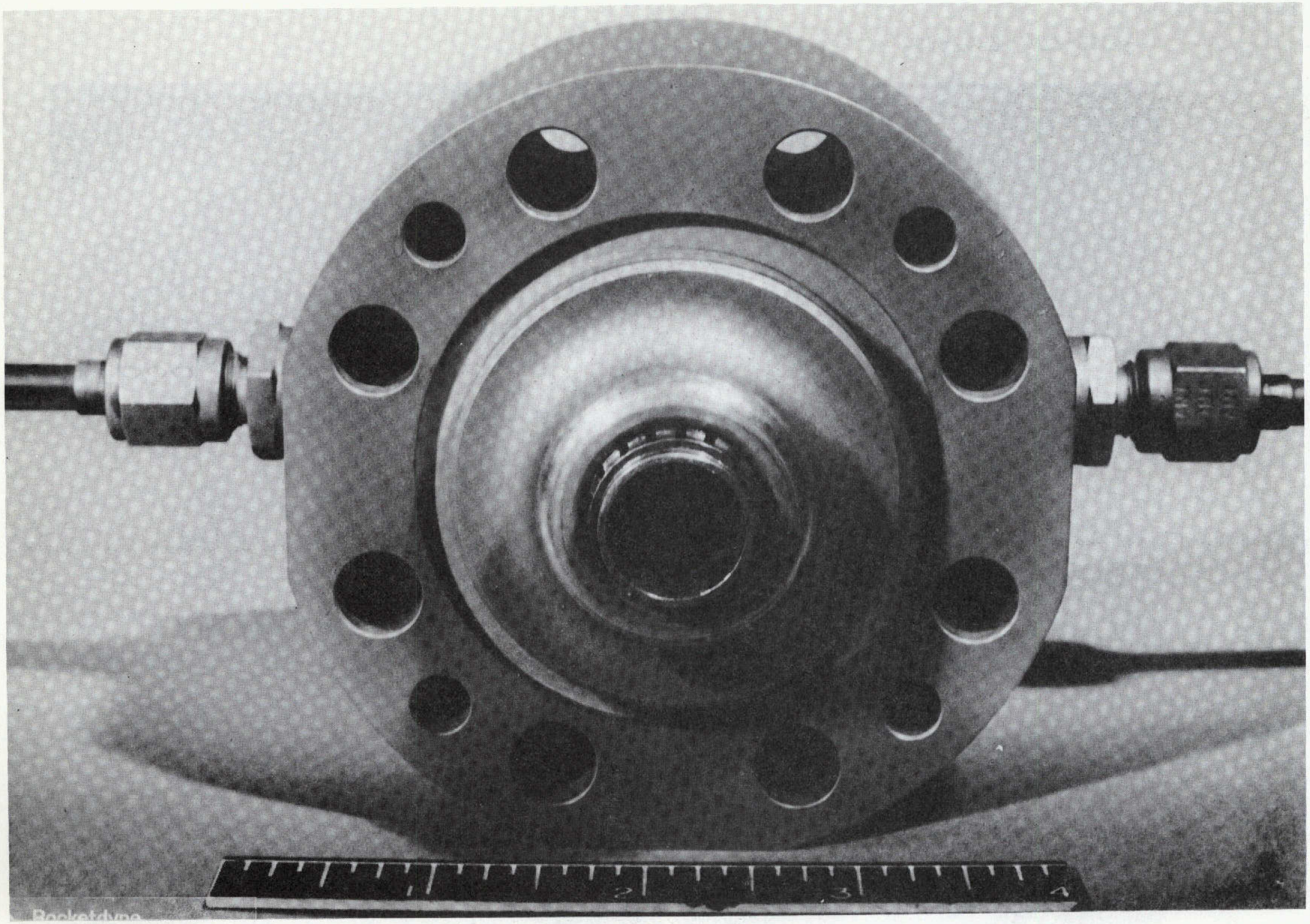

5AA34-2/3/72-S1B

Figure 3-25. Body Assembly (Looking Aft) R1D4273

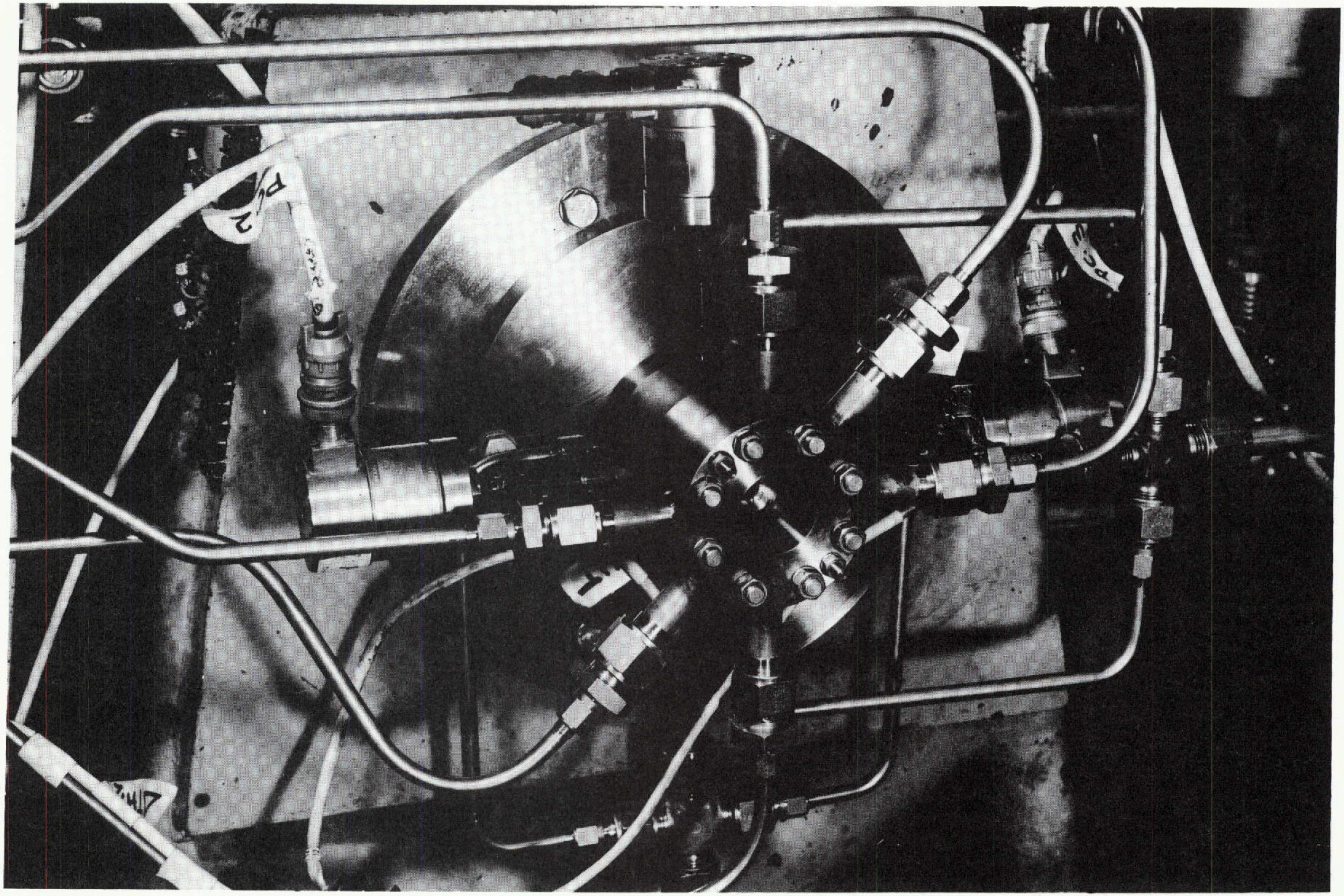

5AA24-2/22/72-S1

Figure 3-26. Chamber Assembly on Lima Stand (R1D1243)

3.4 EXPERIMENTAL RESULTS

All gas/liquid experimental results are presented in this section. These include cold-flow mixing, cold-flow atomization, and hot-fire results. Cold-flow mixing results are presented in terms of the mixture ratio uniformity parameter, E_m (Appendix F), cold-flow atomization results are presented in terms of the mass median droplet diameter, $\overline{D}$, and the hot-fire results are presented in terms of η_{c*}. In the section devoted to correlation of the results, cold-flow results are transformed from E_m and $\overline{D}$ into $\eta_{c*_{mix}}$ and $\eta_{c*_{vap}}$ by means of analytical combustion models (Appendix F).

The format of the presentation will be the same for all three sections and is listed below. (The discussion of the hot-fire results does not include a "Generalization of the Results" section.)

1. Nominal Conditions-Baseline Comparisons
2. Variations About AR = 3
3. Generalization of the Results

This format has been adopted to focus attention upon the primary objective of the the study, the determination of the effect of element shape upon injector performance at a fixed set of nominal conditons. Broad discussion of methods of generalizing the results is incoprorated in separate material at the end of each section and may either be studied or ignored and will not influence the general results of the program. These generalizations are highly interesting and important and warrant incorporation in the report, however; it is suggested that they be studied upon a second reading of the report, if desired. The nominal, or baseline conditions are listed in Table 3-4 and the element comparison scheme has been outlined in Section 3.2.2 (Fig. 3-4).

3.4.1 Mixing Studies

The objective of the mixing studies was to determine the effect of element geometry and, to some extent, operational parameters upon the mixture ratio uniformity parameter, E_m (Appendix F). The method for obtaining the experimental data is outlined in Appendix A. Mass fluxes and mixture ratios at discrete points in the flowfield produced by a given element were measured by means of a two-phase sampling probe that was positioned 2 inches downstream of the injector element exhaust plane. None of the Phase II mixing results are included in this presentation, as these data were obtained at a sampling distance of 5 inches. Since mixing efficiency varies with distance, the 2- and 5-inch results would not be expected to be comparable

All of the Phase III mixing cold-flow data are presented in Table 3-12.

3.4.1.1 Nominal Conditions--Baseline Comparison. The mixing results for four baseline injector elements are presented in Fig. 3-27. Data, E_m, are plotted with respect to actual center-post recess in Fig. 3-27a and with respect to relative recess, R/y_1, in Fig. 3-27b. The relative recess appears to offer the better representation of the results. A cross plot of Fig. 3-27b is presented as Fig. 3-28, wherein E_m is shown as a function of aspect ratio, x/y_1, for constant values of centerpost recess. (Note: Results presented at aspect ratio unity are those for a circular concentric tube element, not a rectangular element of aspect ratio unity.)

The representations of Fig. 3-28 show that the quality of mixture ratio uniformity improves dramatically with increased aspect ratio at the nominal operating conditions. This result was so interesting that a more detailed analysis of the data was undertaken in an attempt to explain exactly how the change in shape, alone, could improve the mixing to such a degree. The results of this extended analysis are presented in Fig. 3-29 and 3-30.

FOLDOUT FRAME

1

FOLDOUT FRAME

2

TABLE 3-12 NONCIRCULAR ORIFICE PROGRAM, GAS/LIQUID MIXING RESULTS (PHASE III DATA ONLY)

Test No.	Element Code No.	$\dot{w}_T$ $\frac{lbm}{sec}$	$\dot{w}_L$ $\frac{lbm}{sec}$	$\dot{w}_G$ $\frac{lbm}{sec}$	MR $\frac{\dot{w}_L}{\dot{w}_G}$	ρ_L $\frac{lbm}{ft^3}$	ρ_G $\frac{lbm}{ft^3}$	V_L $\frac{ft}{sec}$	V_G $\frac{ft}{sec}$	P_c (psia)	Recess (in.)	$\frac{R}{y_1}$	$\frac{\rho_G}{\rho_L}$	$\frac{V_G}{V_L}$	Mach No.	E_m %	η_{c^*MIX} %
4	GCR-2	0.432	0.370	0.0617	6.0	62.4	0.270	42.5	935	47.0	0.0965	1.170	0.00433	22.0	0.880	82.53	95.64
5	GCR-2	↑	↑	↑	↑	↑	↑	42.5	↑	↑	0.007	0.085	↑	22.0	↑	63.83	88.08
6	GST-1							97.2			---	---		9.62		80.40	95.38
7	GCR-2							42.5			0.0652	0.790		22.0		60.69	86.33
8	GCR-2							↑			0.0870	1.055		↑		76.52	94.45
9	GCR-2										0.1188	1.440				80.02	95.36
11	GCR-2										0.1054	1.278				79.60	95.19
12	GCR-5										0	0				65.48	89.03
15	GCR-5										0.0475	0.798				81.56	96.03
25	GCR-3	↓	↓	↓				↓	↓		0.127	1.539			↓	77.63	94.62
26	GCR-3	0.432	0.370	0.0617				42.5	935		0.105	1.273		↓	0.880	72.82	92.77
27	GCR-2	0.216	0.185	0.0309				21.3	468		0.105	1.273		22.0	0.441	74.59	91.54
30	GCR-4	0.216	0.185	0.0309				21.3	935		0	0		43.9	0.880	75.35	93.99
31	GCR-3	0.432	0.370	0.0617				42.5	935		0	0		22.0	0.880	49.33	77.05
32	GCR-2	0.216	0.185	0.0309				21.3	468		0.007	0.085		↑	0.441	59.68	84.66
33	GCR-7	0.216	0.185	0.0309				42.5	935		0.004	0.069			0.880	64.37	88.15
34	GCC-2	0.432	0.370	0.0617							0.007	0.044				48.90	76.29
35	GCC-2	↑	↑	↑				↑	↑		0.102	0.636			↑	49.62	76.49
36	GCC-2							↓			0.241	1.502		↓		59.76	85.08
37	GCC-2							42.5			0.164	1.022		22.0		53.89	80.44
38	GST-2							100.7			---	---		9.35		84.05	97.12
39	GCR-6							42.5			0	0		22.0		57.39	83.44
40	GCR-6	↓	↓	↓			↓	42.5	↓	↓	0.2375	2.039	↓	22.0	↓	75.64	92.40
41	GCR-2	0.432	0.370	0.0617			0.270	42.5	935	47.0	0.0110	0.133	0.00433	22.0	0.880	64.62	88.27
42	GCR-2	0.216	0.185	0.0309			0.136	21.2	929	23.6	0.0110	0.133	0.00218	43.8	0.876	77.66	94.52
43	GCR-3	0.324	0.278	0.0463	↓		0.197	31.9	962	34.3	0.0110	0.133	0.00316	30.2	0.905	68.04	90.35
44	GCC-2	0.432	0.370	0.0617	6.0		0.270	42.5	935	47.0	0.007	0.044	0.00433	22.0	0.880	45.65	74.95
45	↑	0.340	0.278	↑	4.51		↑	31.9	↑	↑	↑	↑	↑	29.4	↑	60.62	85.54
46		0.247	0.185		3.00			21.3						44.0		79.32	96.65
47		0.154	0.0926		1.50			10.6						88.0		81.33	98.93
48		0.189	0.127	↓	2.06			14.6	↓					64.1	↓	80.19	98.10
49		0.112	0.050	0.0617	0.810			5.74	935					163.0	0.880	76.28	99.15
50		0.278	0.0238	0.0396	6.01			27.3	600					22.0	0.564	44.19	74.10
51		0.159	0.119	0.0396	3.01			13.7	600	↓				43.8	0.564	75.29	94.85
52		0.0991	0.0595	0.0396	1.50			6.83	600	47.0				87.8	0.564	75.58	98.23
53		0.162	0.139	0.0231	6.02			15.9	350	51.0				22.0	0.316	46.18	75.21
54		0.0924	0.0693	0.0231	3.00		↓	7.96	350	51.0			↓	44.0	0.316	71.31	93.73
55		0.0577	0.0346	0.0231	1.50		0.270	3.98	350	51.0			0.00433	88.0	0.316	77.19	98.40
56		1.024	0.878	0.146	6.01		0.637	100.8	935	106.0			0.0102	9.28	0.900	56.52	83.52
57		0.518	0.372	↑	2.55		↑	42.7	↑	↑			↑	22.0	↑	77.29	97.11
58	↓	0.332	0.186	↓	1.27	↓	↓	21.4	↓	↓	↓	↓	↓	43.8	↓	84.66	99.42
59	GCC-2	0.239	0.0930	0.146	0.637	62.4	0.637	10.7	935	106.0	0.007	0.044	0.0102	87.6	0.900	82.48	99.60

FOLDOUT FRAME
1

FOLDOUT FRAME
2

TABLE 3-12 (Concluded)

Test No.	Element Code No.	$\dot{w}_T$ $\frac{lbm}{sec}$	$\dot{w}_L$ $\frac{lbm}{sec}$	$\dot{w}_G$ $\frac{lbm}{sec}$	MR $\frac{\dot{w}_L}{\dot{w}_G}$	ρ_L $\frac{lbm}{ft^3}$	ρ_G $\frac{lbm}{ft^3}$	V_L $\frac{ft}{sec}$	V_G $\frac{ft}{sec}$	P_c (psia)	Recess (in.)	$\frac{R}{y_1}$	$\frac{\rho_G}{\rho_L}$	$\frac{V_G}{V_L}$	Mach No.	E_m %	η_{c^*MIX} %
60	GCC-2	0.269	0.140	0.129	1.09	62.4	1.50	16.0	350	284.0	0.007	0.044	0.0240	21.9	0.316	86.40	99.59
61	↑	0.199	0.0697	0.129	0.540	↑	1.50	8.00	350	284.0	↑	↑	0.0240	43.8	0.316	83.78	99.83
62		0.164	0.0348	0.129	0.270		1.50	4.00	350	284.0			0.0240	87.5	0.316	89.45	99.97
63		0.333	0.239	0.0939	2.55		0.637	27.4	600	116.0			0.0102	21.9	0.552	75.62	96.21
64		0.213	0.119	0.0939	1.27		↑	13.7	600	116.0			↑	43.8	0.552	85.04	99.45
65		0.154	0.0597	0.0939	0.636			6.85	600	116.0				87.6	0.552	81.63	99.62
66		0.194	0.139	0.0548	2.54			15.9	350	121.0				22.0	0.316	77.90	96.86
67		0.124	0.0696	0.0548	1.27		↓	7.95	↑	121.0			↓	44.0	↑	85.36	99.47
68		0.0896	0.0348	0.0548	0.635		0.637	3.98		121.0			0.0102	88.0		80.18	99.57
69		0.164	0.0348	0.129	0.270		1.50	3.98		284.0			0.0240	88.0		90.93	99.96
70		0.149	0.0204	0.129	0.158		1.50	2.33	↓	284.0			0.0240	150.0	↓	89.50	100.03
71		0.435	0.306	0.129	2.37		1.50	35.0	350	284.0			0.0240	10.0	0.316	79.05	98.09
72		0.217	0.186	0.0310	6.00		0.135	21.3	935	22.0			0.00216	44.0	0.909	49.22	75.80
73		0.124	0.0930	0.0310	3.00		↑	10.6	935	22.0			↑	88.0	0.909	68.23	92.09
74		0.0775	0.0465	0.0310	1.50			5.31	935	22.0				176.0	0.909	67.56	96.98
75		0.139	0.119	0.0199	5.98			13.6	600	25.0				44.0	0.548	51.59	77.26
76		0.0796	0.0597	0.0199	3.00			6.82	600	25.0				88.0	0.548	71.98	94.06
77		0.0498	0.0299	0.0199	1.50			3.41	600	25.0				176.0	0.548	70.83	93.91
78		0.0812	0.0696	0.0116	6.00			7.95	350	26.0				44.0	0.314	71.00	92.18
79		0.0464	0.0348	0.0116	3.00		↓	3.98	350	26.0			↓	88.0	0.314	64.04	92.43
80		0.0290	0.0174	0.0116	1.50		0.135	1.99	350	26.0			0.00216	176.0	0.314	67.67	97.39
81	↓	0.119	0.0248	0.0939	0.264	↓	0.637	2.84	600	116.0	↓	↓	0.0102	211.0	0.552	90.81	99.97
82	GCC-2	0.199	0.0697	0.129	0.540	62.4	1.50	7.95	350	284.0	0.007	0.044	0.0240	44.0	0.316	85.11	99.86

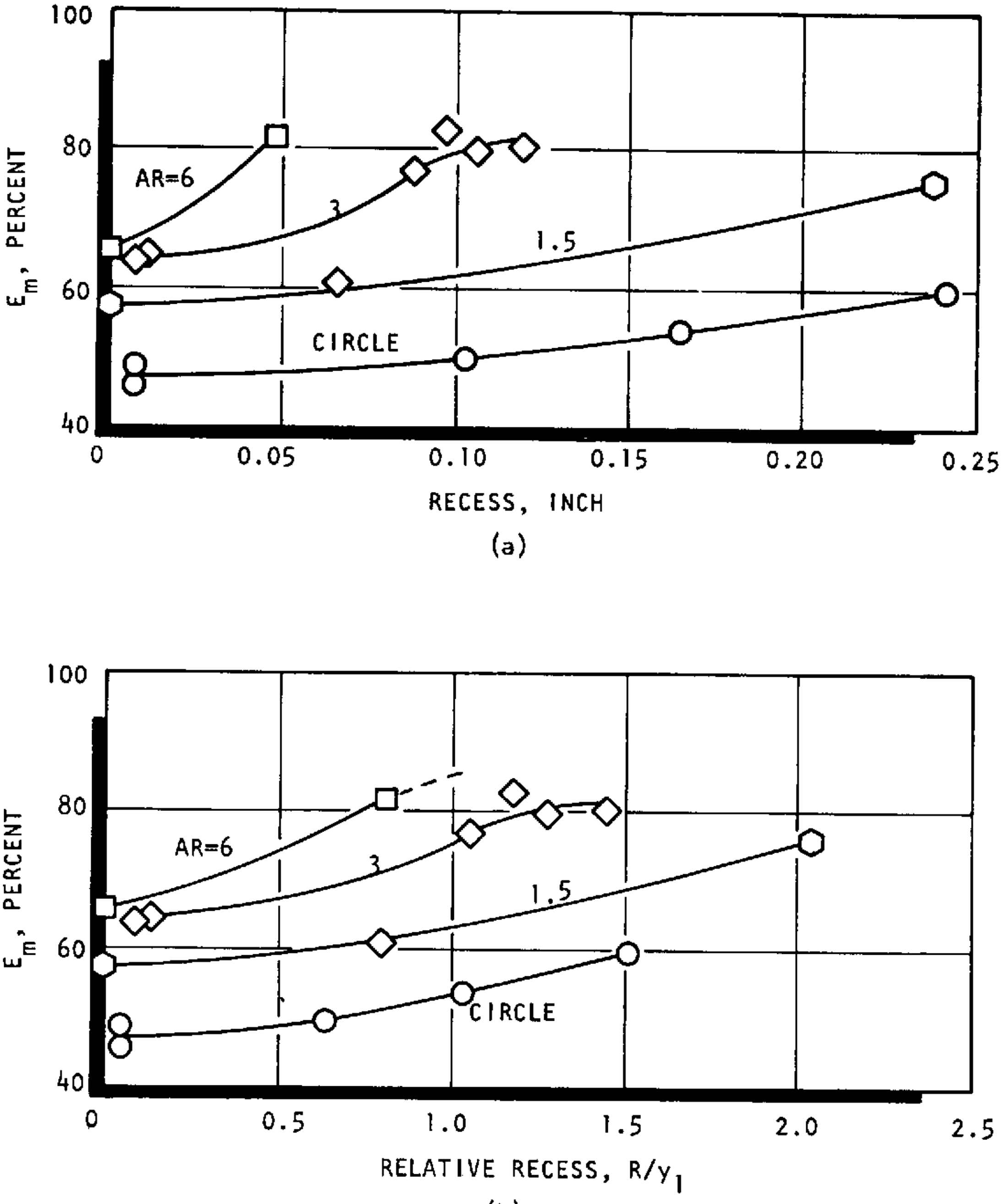

Figure 3-27. Mixture Ratio Uniformity Comparison of the Four Baseline Elements (at Nominal Conditions) as a Function of Center-Post Recess

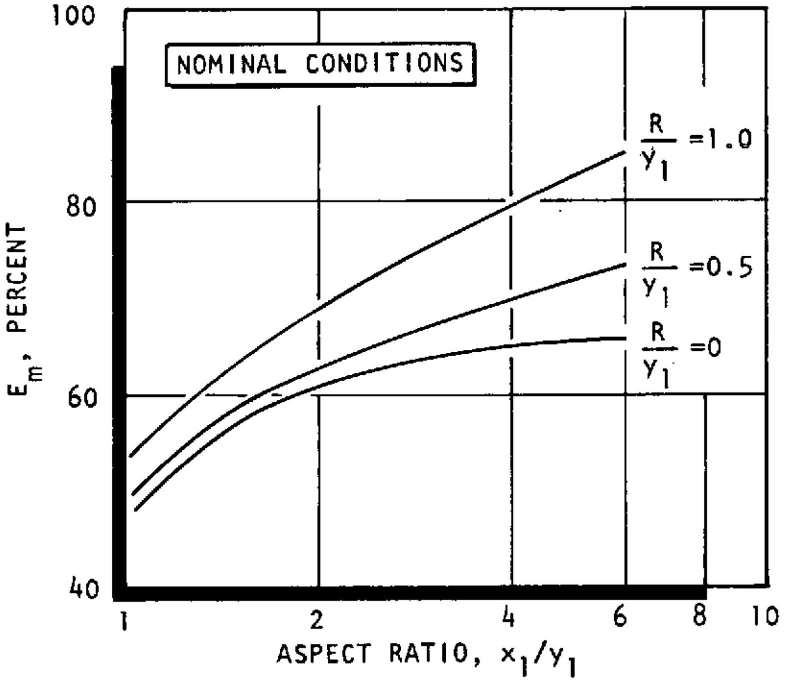

Figure 3-28. Mixture Ratio Uniformity Comparison as a Function of Aspect Ratio (nominal conditions)

In these two figures, mass fraction flux (mass fraction per unit area) mff contours for the liquid and the gas component are shown for each of the four elements at zero recess. The mass fraction flux is computed by dividing the local value of the mass flux of the i^{th} component, $\dot{w}_i/A$, (liquid or gas) by the total injected mass flow of the i^{th} component, $\dot{w}_{Ti}$. At a point in the flowfield where the local mixture ratio, $\dot{w}_L/\dot{w}_G$ is equal to the injected mixture ratio, $\dot{w}_{LT}/\dot{w}_{GT}$, the values of the mass fraction flux for the liquid and gas components would be equal. Thus, for an element which could produce perfect mixing, E_m = 100 percent, the liquid and gas mass fraction flux contours would be, everywhere, superimposed, one upon the other. In Fig. 3-29 constant mff contours $\left[(\dot{w}_i/A) \; / \; w_{Ti} = 0.5\right]$ are presented for the liquid and gas components. (The value mff = 0.5 was selected arbitrarily and the comparison could have been made at other values. Only one contour value was selected to avoid confusion.) These contours are obtained by plotting the distance from the centerline of the element, in polar coordinates, at which the given value of mff is found in the sampling plane (which is normal to the element centerline). Here again, if the elements had produced perfect mixing, the two contours would lie directly upon one another. For the circular element, the value of 0.5 for the mff is achieved much closer to the element centerline than that of the gas component. There are no points in the flowfield that are "on mixture ratio" for this value of mff. Physically this means that the liquid is "coring" or remaining in the center of the flowfield and has not been spread out in the radial direction by the gas.

This is a classic problem for circular concentric tube elements operating at high mixture ratios (>4:1) and having relatively low gas-to-liquid velocity ratios.

The influence of element shape is quite evident in Fig. 3-29. The "warping" of the flowfield causes contours to approach each other or intermingle, and thus, the degree of mixing is increased without the necessity of increasing the gas velocity or decreasing the liquid velocity.

Exactly the same result can be noted in Fig. 3-30, wherein the value of mff for the liquid and gas component is plotted as a function of the radial distance from the element centerline along a fixed ray in the collection plane (i.e., mff = f(r),

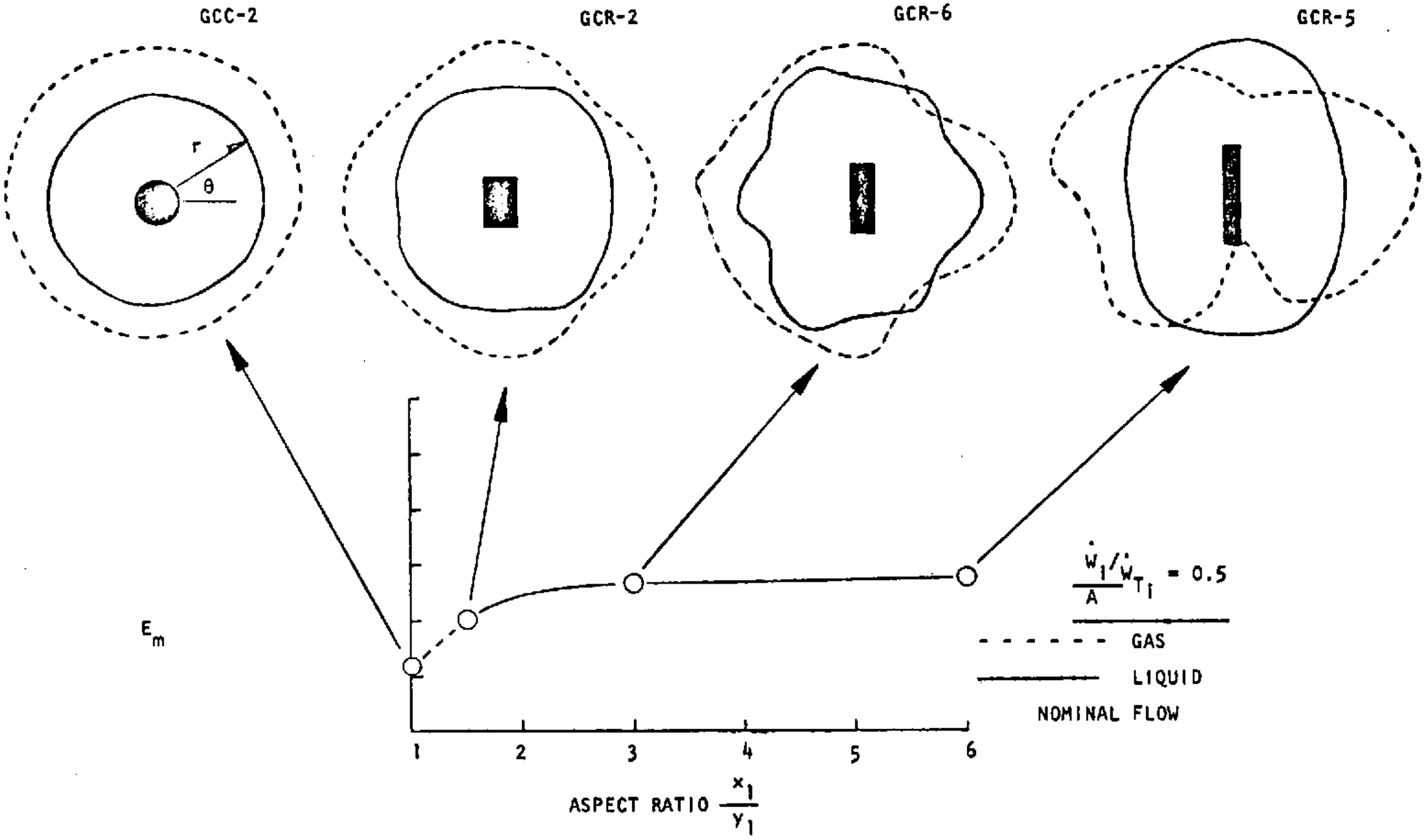

Figure 3-29. Effect of Liquid Port Aspect Ratio Upon Flowfield, $R/y_1 = 0$ (Constant mff Contours)

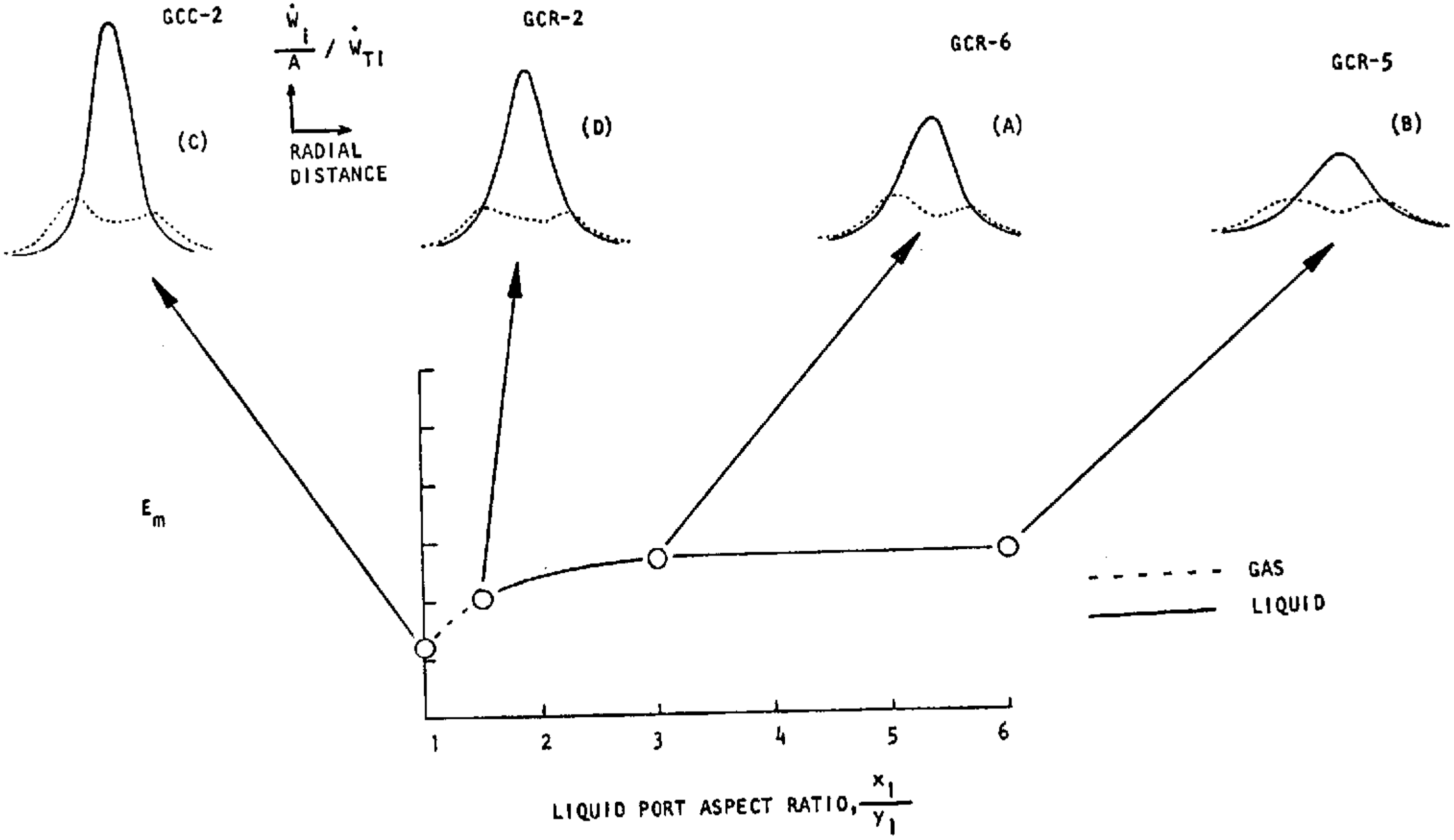

Figure 3-30. Effect of Liquid Port Aspect Ratio Upon Flowfield (mff Variable)

θ = constant). Here, the coring problem encountered by the circular element can be seen plainly. The increased aspect ratio systematically reduces the "coring."

There is another interesting potential advantage of RCTE's that can be deduced from Fig. 3-29. The mff contours for the highest aspect ratio element (GCR-5) suggest that the flowfield can be "tailored" to provide "fuel-rich" and "oxidizer-rich" zones that can be employed to ensure thrust chamber/injector compatibility in the outer zone of the chamber wall.

Centerpost recess produces approximately the same change in the character of the contour plots as does increased aspect ratio. Recess has the ability to reduce coring.

3.4.1.2 Variations About AR = 3. Continuing with the investigation of the effect of shape as outlined in Fig. 3-4, the next task was to study the influence of element area ratio, element scale, and deviation from uniform gas annulus gap with aspect ratio, x_1/y_1, equal to 3.0.

The effect of a reduction in the gas annulus area (with uniform gap) is presented in Fig. 3-31. This comparison could not be made at the nominal flowrates due to the fact that the gaseous nitrogen employed as a fuel simulant was already at a velocity of 950 ft/sec in the baseline element. A reduction in the gas area at the nominal conditons would have caused the nitrogen to choke. The comparison was made, therefore, at one-half the nominal total flowrate. The mixture ratio and gas density were held at nominal values, 6.0 and 0.27 lbm/ft^3, respectively.

The value of E_m dropped off for the baseline AR = 3 element (GCR-2) as the total flow was reduced. At one-half nominal flowrate, the liquid velocity was 21 ft/sec and the gas velocity was reduced from 935 to 468 ft/sec. At these flow conditions, the element with reduced gas area (GCR-4) was operating with the same liquid velocity but with a gas velocity of 935 ft/sec. It can be seen that this increase in gas-to-liquid velocity ratio produced a significant increase in E_m. This change in E_m is ascribed totally to the change in gas velocity, as the density and mixture ratio were held constant.

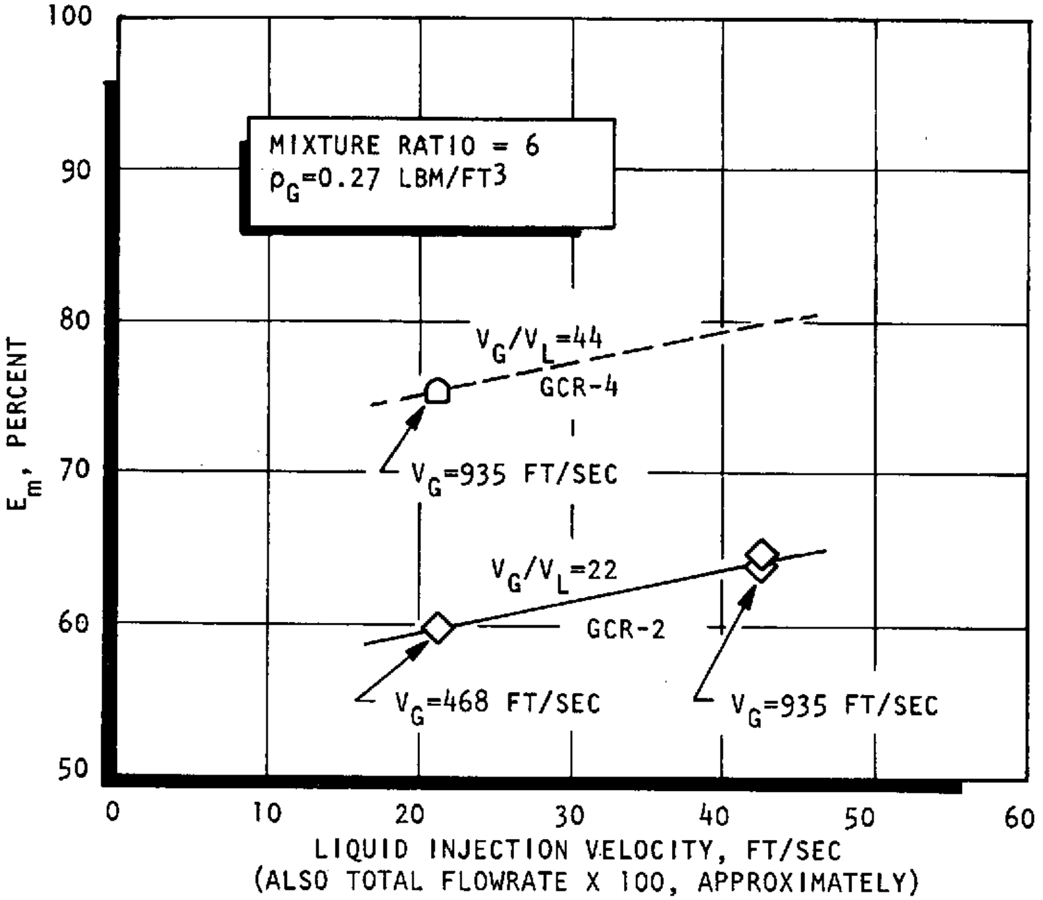

Figure 3-31. Effect of Variation of Gas to Liquid Velocity Ratio at Constant Mixture Ratio and Constant Gas Density (GCR-2 and GCR-4)

The effect of element size is shown in Fig. 3-32. Here, again, the comparison was not made at the nominal flowrate. The scaled-down model, GCR-7 ($\frac{1}{\sqrt{2}}$ reduction of GCR-2), had liquid and gas area exactly one-half those of the large element. Comparison was made at nominal mixture ratio, density, and velocities, thus the total flow in GCR-7 was exactly one-half that in GCR-2. This meant that the mass fluxes ($\dot{w}_i/A_i$) for both elements were identical. The curve of E_m for GCR-2 is shown as a function of liquid velocity. This curve is reproduced from Fig. 3-31. The data point for GCR-7 is plotted on the same scale. It can be seen that the value of E_m is unaffected by size as long as the mass flows per unit area are preserved along with densities, velocities, and mixture ratio. This is a highly important result and suggests, at least at this scale, that thrust per element has no effect upon mixing of an individual element. This is not to say, however, that improved interelement mixing cannot be improved with lower thrust per element and thus the mixing of the injector improved overall (i.e., more elements).

The effect of variation of the gas port aspect ratio (change of x_3/y_3 with gas annulus area and centerpost configuration held constant) is shown in Fig. 3-33. This change produces a nonuniform gas gap. Here, values of E_m for GCR-2 and GCR-3 are plotted as functions of centerpost recess. This result, alone is relatively uninteresting in that it merely says that the level of mixing dropped when the gas port aspect ratio was changed from 1.86 to 2.347. The more interesting aspects of this experiment are presented in Fig. 3-34. Here, again, mff contours are employed to tell the story. Gas and liquid contours for mff = 0.5 are presented for GCR-2 and GCR-3 at their respective points of centerpost recess at which maximum mixing level was encountered. These points are marked by arrows in Fig. 3-33.

The contours for element GCR-2 (Fig. 3-34) suggest that there is "too much" gas concentration in the y direction and that a redistribution of some of the gas to the X direction should tend to cause the contour lines to more closely coincide. As a matter of fact, the design of GCR-3 was based upon analysis of these contours and its objective was exactly that stated. What happened is obvious.

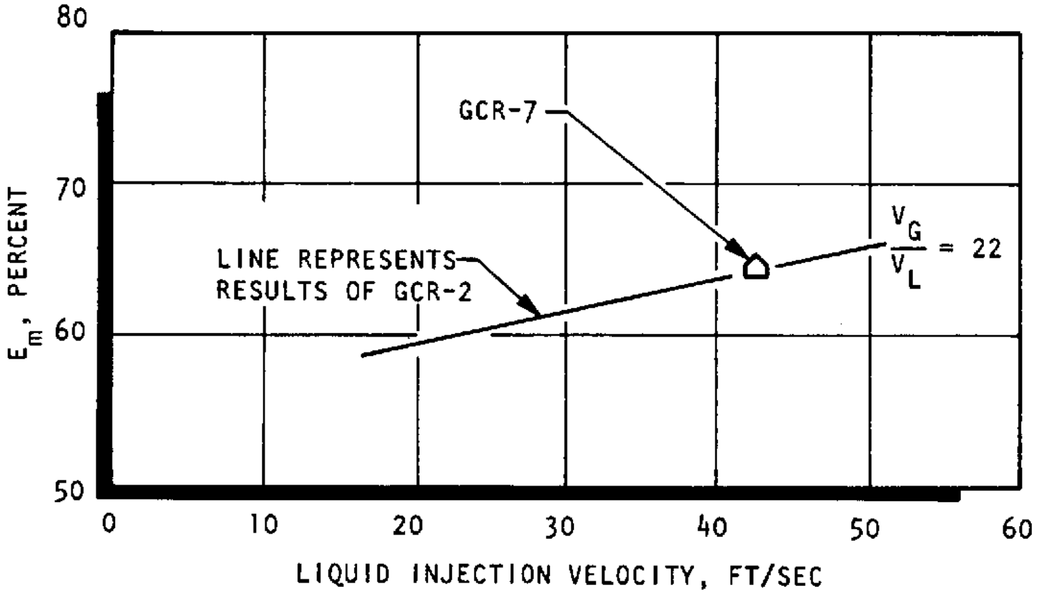

Figure 3-32. Effect of Element Size at Constant Density and Mixture Ratio (GCR-2 and GCR-7)

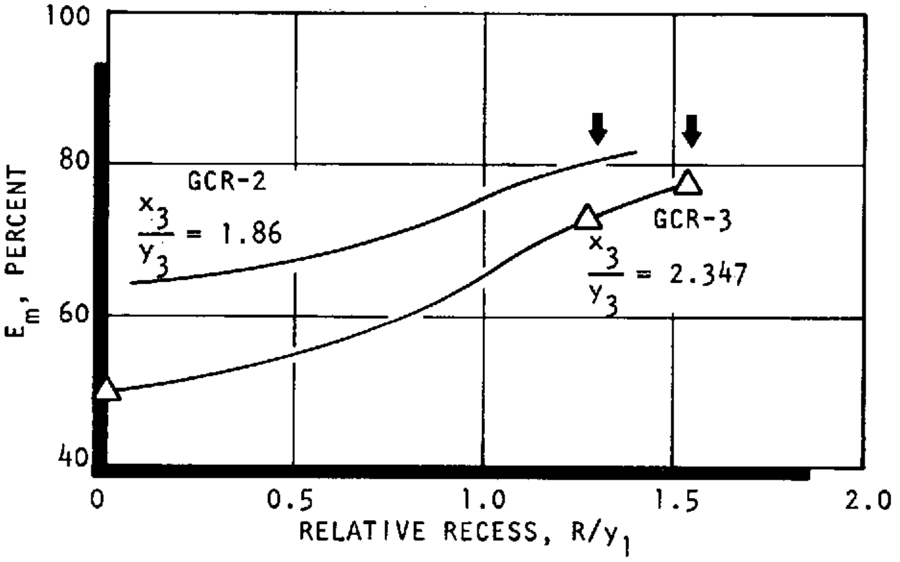

Figure 3-33. Effect of Variation of Gas Port Aspect Ratio Upon Mixing at Nominal Conditions (GCR-2 and GCR-3)

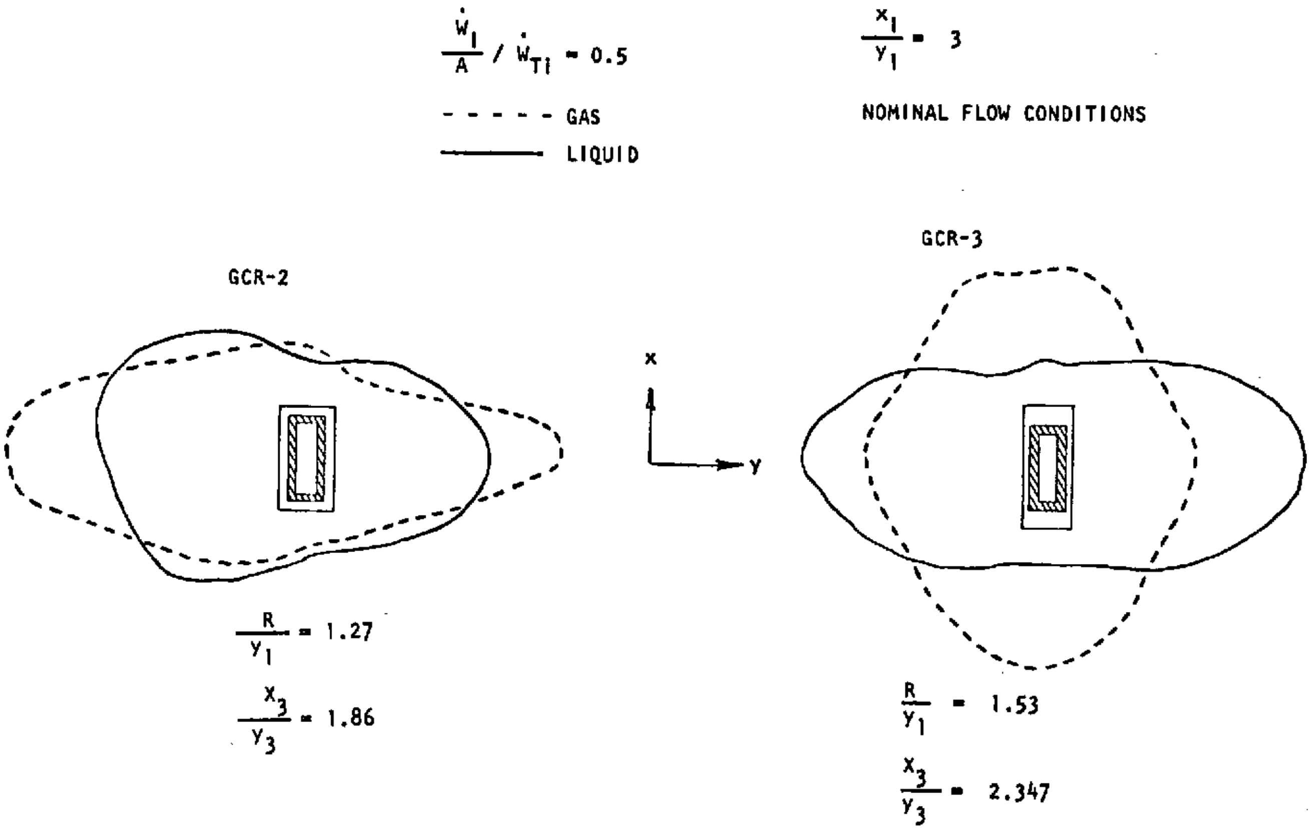

Figure 3-34. Effect of Gas Port Aspect Ratio on Flowfield Development

The redistribution of the gas component from y to x was greatly overdone. As a result, the mixing uniformity dropped; however, the character of the flowfield was changed. This result suggests that an optimum value of X_3/y_3 must exist between the values that were tested. The inferences of these data are presented in Fig. 3-35, which is highly speculative, but interesting. If the trends suggested in Fig. 3-35 are correct, then RCTE's offer yet another degree of freedom to the injector designer to aid in improving mixing with element geometry.

3.4.1.3 Generalization of the Results. Mixing uniformity cold-flow tests conducted with RCTE's proved to be relatively time consuming and, therefore, costly. This was due to the fact that the flowfields were highly nonaxisymmetric and a great number of sampling points had to be incorporated to obtain accurate results. On the other hand, cold-flow tests with the circular concentric tube element (GCC-2) proved to be quite economical due to the axisymmetric nature of the flowfield. Therefore, it was decided that an appreciation of the influence of the flow parameters upon the mixing characteristics of G/L CTE's could best be obtained with the CCTE. An extensive set of data was obtained with element GCC-2 covering a broad range of gas velocity (350 to 935 ft/sec), gas density (0.135 to 1.5 $\frac{\text{lbm}}{\text{ft}^3}$), and liquid velocity (2 to 100 ft/sec). This test matrix was in keeping with the statement made in Section 3.2.1, that the most practical variables of the cold-flow facilities were V_G, ρ_G, and V_L. The results of this parametric study are presented in Fig. 3-36 through 3-39. It must be pointed out that even this extensive parametric variation does not show the independent effects of velocity ratio and mixture ratio. This is due to the fact that the entire set of results was obtained with one element and, thus, the area ratio, A_G/A_L, was not a variable. As a result, the mixture ratio was a dependent variable as shown in Eq. 3-8.

$$MR = K \left(\frac{V_L}{\rho_G V_G} \right) \tag{3-8}$$

where K is a constant. It has been shown (Fig. 3-31) that a variation of velocity ratio (by variation of area ratio) produces a change in mixing with constant density and constant mixture ratio. This type of comparison is not allowed by the restrictions of Eq. 3-8.

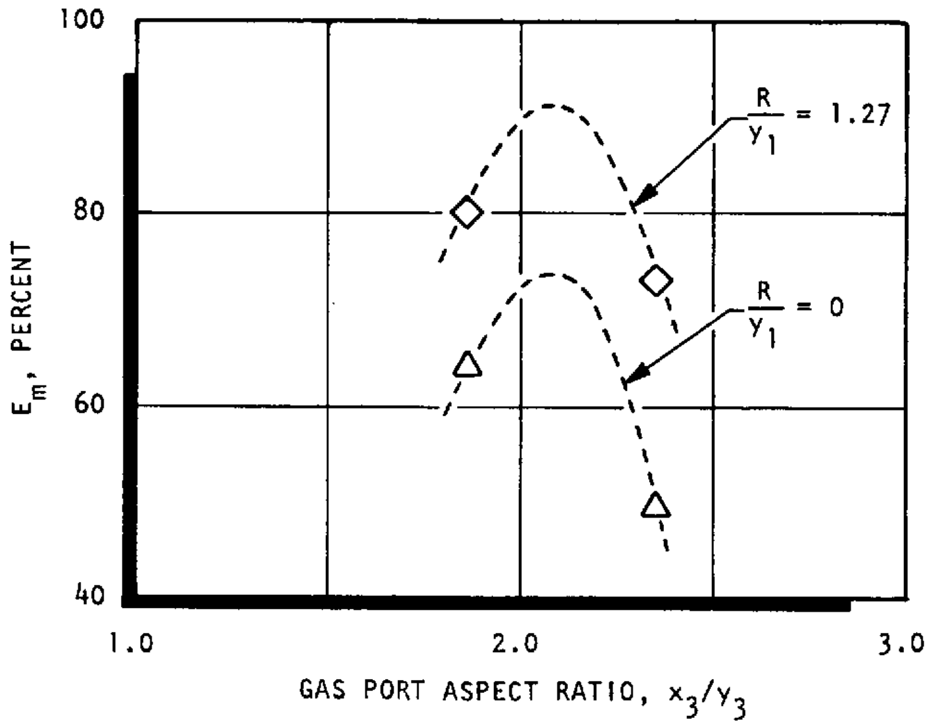

Figure 3-35. Mixture Ratio Uniformity Trends Inferred From Analysis of the Effects of Gas Port Aspect Ratio, x_3/y_3

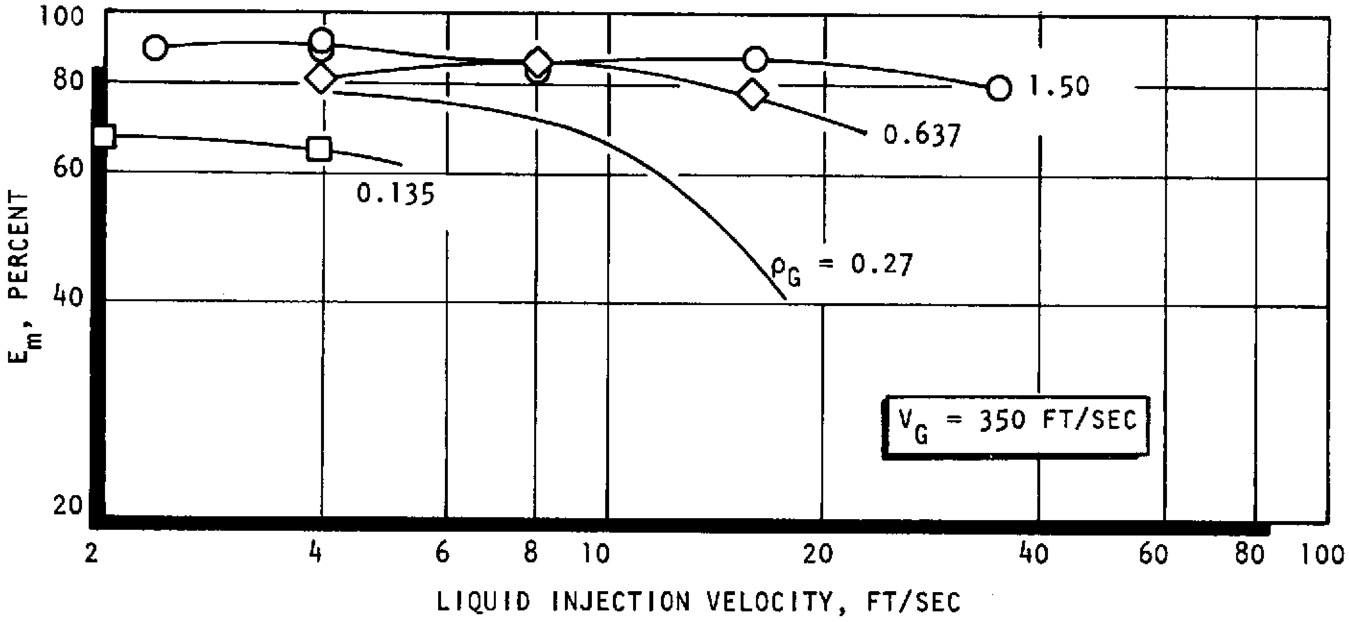

Figure 3-36. E_m as a Function of V_L Along Lines of Constant ρ_G. Circular Concentric Tube Element. (Limited data points shown for reference; curves are "best fit" of actual data)

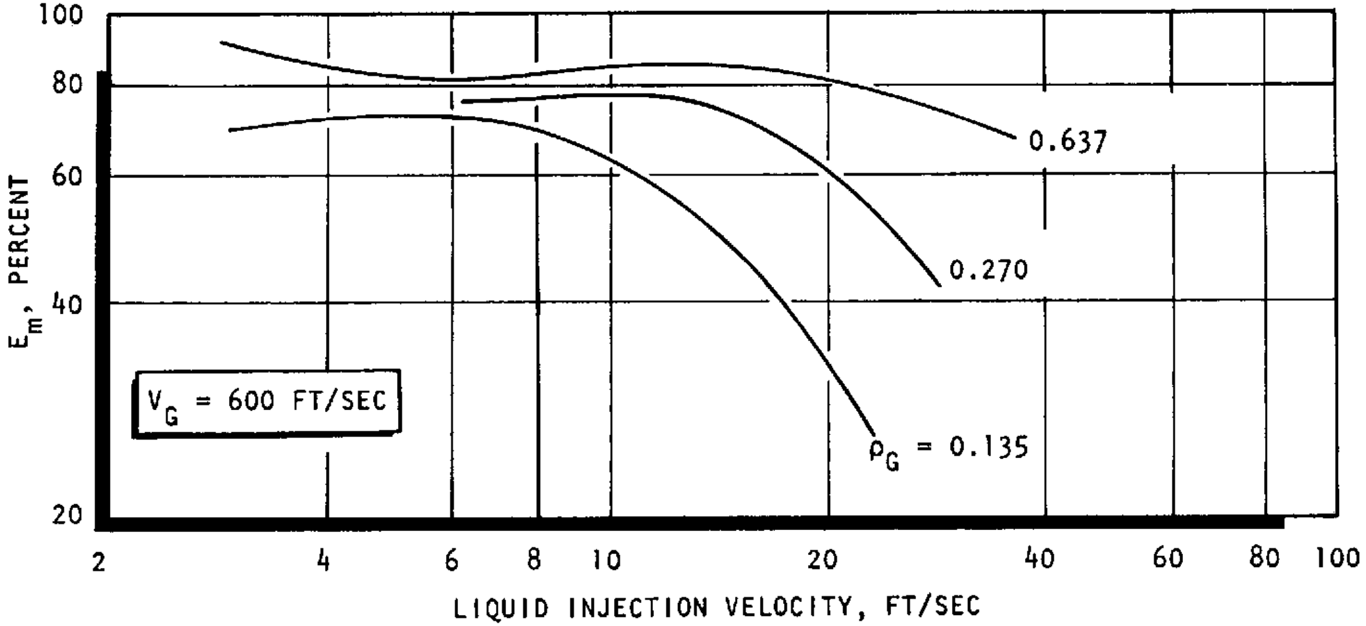

Figure 3-37. E_m as a Function of V_L Along Lines of Constant ρ_G. Circular Concentric Tube Element (data points not shown)

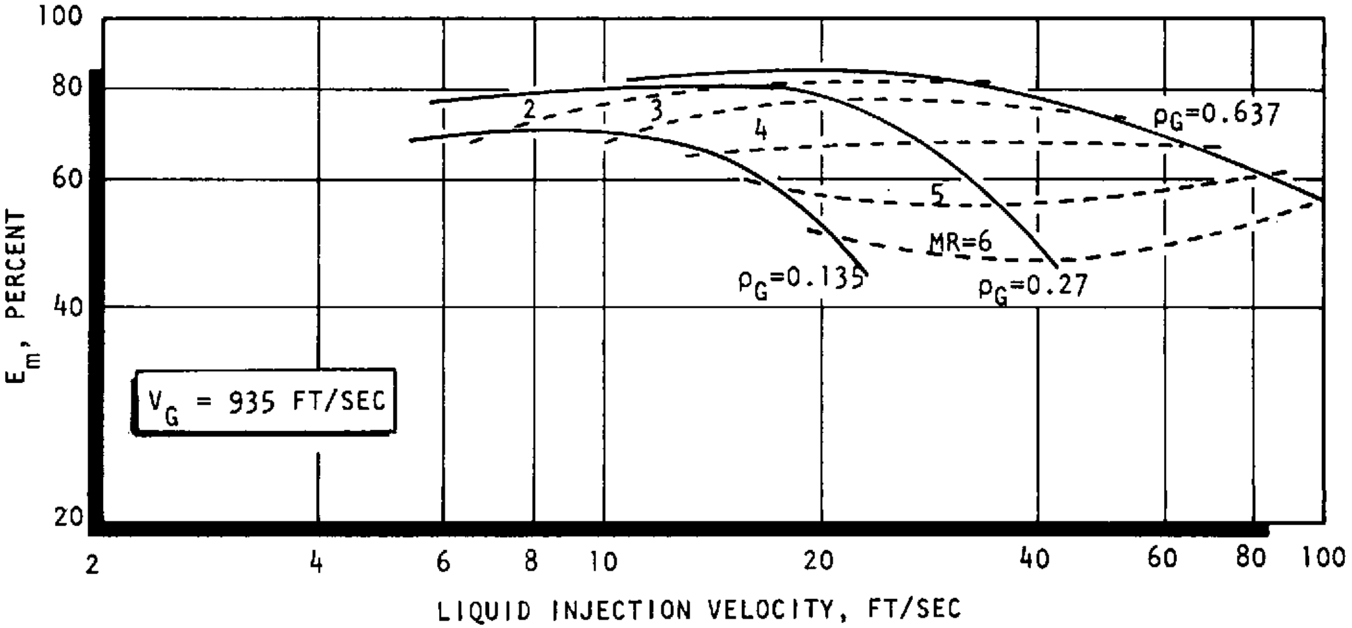

Figure 3-38. E_m as a Function of V_L Along Lines of Constant ρ_G and Mixture Ratio. Circular Concentric Tube Element (data points not shown)

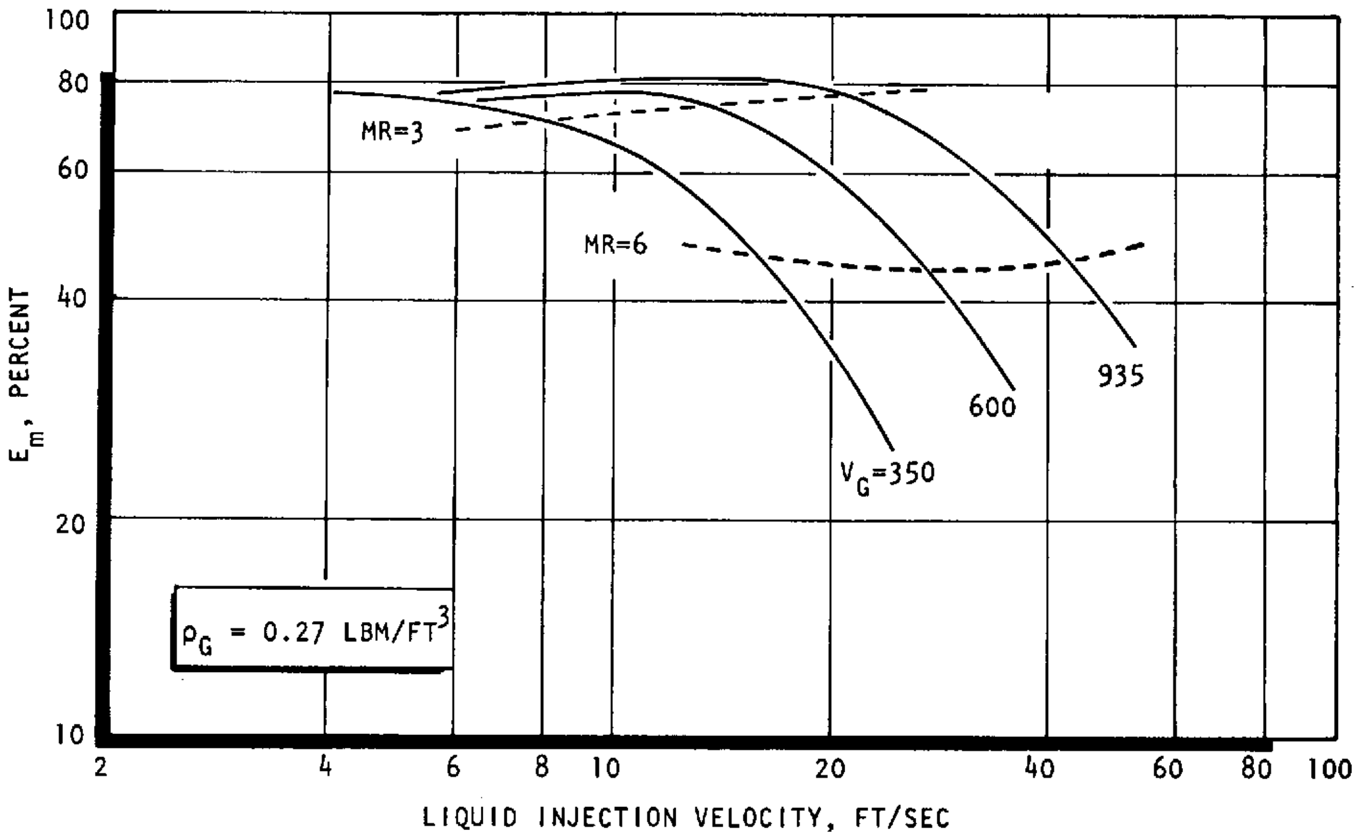

Figure 3-39. E_m as a Function of V_L Along Lines of Constant V_G and Mixture Ratio. Circular Concentric Tube Element (data points not shown)

Figures 3-36 through 3-38 show the variation of E_m with liquid velocity along lines of constant density with gas velocity a constant in each figure. One of the many possible cross plots is presented in Fig. 3-39, wherein the variation of E_m with liquid velocity is shown along lines of constant gas velocity with gas density everywhere constant. Lines of constant mixture ratio have been included in Fig. 3-38 and 3-39 to illustrate the fact that this quantity is dependent upon the other variables, and also to show that although the parametric roles of V_G, ρ_G, and V_L are quite clear, the interpretation of performance variations with constant mixture ratio throttling (V_G = const) are not straightforward.

Figures 3-36 through 3-39 show clearly that the liquid velocity is the parameter which most influences the mixing performance of a concentric tube element. In addition, the lines of constant mixture ratio in Fig. 3-38 and 3-29 show that for this particular element, no combination of variables can produce high levels of mixing as long as the mixture ratio is maintained at high values. However, based upon the results shown in Fig. 3-31 for a RCTE, it can be expected that a change in area ratio that increased the velocity ratio V_G/V_L at high mixture ratio will produce a higher mixing level. Great care must be taken not to associate directly the effects of changes in velocity ratio shown by these data with a change i velocity ratio at constant mixture ratio. These additional data are required to complete the study.

These data do, however, provide certain broad design criteria. In general, one can conclude that "good" mixing, with zero post recess may be achieved with high gas velocity, high gas density, and low liquid velocity. The most important of these being low liquid velocity.

3.4.2 Atomization Studies

Results of the atomization studies are presented with the same format that was employed for the mixing results. Methods for obtaining data, atomization faciliti descriptions, and methods for dropsize analysis may be found in the Appendixes. The data are presented in Table 3-13.

FOLDOUT FRAME
1

FOLDOUT FRAME
2

TABLE 3-13 NONCIRCULAR ORIFICE PROGRAM, ATOMIZATION DATA (PHASE II RESULTS)

Test No.	Element Code No.	$\dot{w}_T$ $\frac{\text{lbm}}{\text{sec}}$	$\dot{w}_L$ $\frac{\text{lbm}}{\text{sec}}$	$\dot{w}_G$ $\frac{\text{lbm}}{\text{sec}}$	$\frac{\dot{w}_L}{\dot{w}_G}$	ρ_L $\frac{\text{lbm}}{\text{ft}^3}$	ρ_G $\frac{\text{lbm}}{\text{ft}^3}$	V_L $\frac{\text{ft}}{\text{sec}}$	V_G $\frac{\text{ft}}{\text{sec}}$	P_c (psia)	Recess (in.)	$\frac{R}{y_1}$	$\frac{\rho_G}{\rho_L}$	$\frac{V_G}{V_L}$	Mach No.	$\rho_G V_G^2$ (psia)	$\bar{D}$ (microns)	$\bar{D}/y_1$
1	GCC-1	0.0384	0.0285	0.00990	2.88	47.7	0.0555	4.28	618	13.8	0	0	0.00116	144.0	0.486	4.57	157	0.0386
2	↑	0.0714	0.0615	0.00990	6.21	↑	0.0555	9.24	618	↑	↑	↑	0.00116	66.9	0.486	4.57	374	0.0920
4		0.0599	0.0450	0.0149	3.02		0.0584	6.76	884				0.00122	131.0	0.714	9.84	133	0.0327
5		0.106	0.0915	0.0149	6.14		0.0584	13.7	884				0.00122	64.3	0.714	9.84	268	0.0659
8		0.139	0.119	0.0200	5.95		0.0621	17.9	1110				0.00130	62.4	0.929	16.7	297	0.0731
9	↓	0.0805	0.0605	0.0200	3.02		0.0621	9.09	1110				0.00130	122.0	0.929	16.7	166	0.0408
10	GCC-1	0.153	0.133	0.0200	6.65		0.0621	20.0	1110				0.00130	55.8	0.929	16.7	393	0.0967
11	GCR-1	0.0399	0.0300	0.00990	3.03		0.0564	4.51	720				0.00118	160.0	0.572	6.31	108	0.0733
12	↑	0.0679	0.0580	0.00990	5.86		0.0564	8.71	720				0.00118	82.6	0.572	6.31	151	0.102
13		0.0609	0.0460	0.0149	3.09		0.0603	6.91	1010				0.00126	147.0	0.832	13.4	107	0.0726
14		0.105	0.0905	0.0149	6.07		0.0603	13.6	1010				0.00126	74.6	0.832	13.4	126	0.0855
15	↓	0.0778	0.0580	0.0198	2.93		0.0650	8.71	1250		↓	↓	0.00136	144.0	1.06	21.9	120	0.0815
16	GCR-1	0.136	0.116	0.0198	5.86		0.0650	17.4	1250		0	0	0.00136	71.8	1.06	21.9	156	0.105
18	GCC-1	0.0405	0.0300	0.0105	2.86		0.0558	4.51	652		0.160	1.00	0.00116	145.0	0.514	5.11	167	0.0411
19	↑	0.0705	0.0600	0.0105	5.71		0.0558	9.01	652		↑	↑	0.00116	72.3	0.514	5.11	197	0.0485
20		0.0608	0.0450	0.0158	2.85		0.0590	6.76	928				0.00123	137.0	0.753	10.9	152	0.0374
21		0.104	0.0890	0.0155	5.74		0.0588	13.4	913				0.00123	68.3	0.740	10.5	183	0.0450
22	↓	0.0808	0.0600	0.0208	2.88		0.0627	9.01	1140		↓		0.00132	127.0	0.961	17.8	134	0.0330
23	GCC-1	0.140	0.120	0.0200	6.00		0.0621	18.0	1110		0.160		0.00130	61.9	0.929	16.7	188	0.0463
25	GCR-1	0.0400	0.0300	0.0100	3.00		0.0565	4.51	726		0.0580		0.00118	161.0	0.577	6.43	123	0.0835
26	↑	0.0685	0.0585	0.0100	5.85		0.0565	8.79	726		↑		0.00118	82.7	0.577	6.43	186	0.126
27		0.0590	0.0440	0.0150	2.93		0.0604	6.61	1010				0.00127	154.0	0.837	13.5	119	0.0808
28	↓	0.105	0.0900	0.0150	6.00	↓	0.0604	13.5	1010	↓	↓	↓	0.00127	75.4	0.837	13.5	152	0.103
29	GCR-1	0.0810	0.0610	0.0200	3.05	47.7	0.0652	9.16	1260	13.8	0.0580	1.00	0.00137	137.0	1.07	22.3	124	0.0842

(PHASE III RESULTS)

1	GCR-2	0.432	0.370	0.0616	6.01	47.7	0.265	55.3	958	61.0	0	0	0.00556	17.3	0.785	52.6	490	0.234
2	↑	0.280	0.240	0.0396	6.07	↑	0.265	35.9	617	65.2	↑	↑	0.00555	17.2	0.488	21.7	520	0.248
3		0.140	0.120	0.0198	6.06		0.263	17.9	311	67.5			0.00551	17.3	0.241	5.48	700	0.334
4		0.279	0.240	0.0393	6.10		0.171	35.9	949	39.5			0.00358	26.5	0.775	33.2	420	0.200
5		0.140	0.120	0.0197	6.08		0.0852	17.9	956	19.8			0.00179	53.3	0.780	16.8	205	0.0978
6		0.279	0.210	0.0694	3.03		0.265	31.4	1080	58.9			0.00555	34.5	0.900	66.8	210	0.100
7		0.280	0.249	0.0307	8.11		0.260	37.2	487	66.4			0.00545	13.1	0.378	13.3	490	0.234
8		0.140	0.120	0.0198	6.07		0.132	17.9	619	32.6			0.00276	34.5	0.489	10.9	420	0.200
9		0.431	0.370	0.0610	6.07		0.409	55.3	615	100.0			0.00858	11.1	0.487	33.4	545	0.260
10	↓	0.279	0.240	0.0394	6.08	↓	0.521	35.9	312	135.0	↓	↓	0.0109	8.71	0.241	10.9	615	0.293
11	GCR-2	0.431	0.370	0.0615	6.02	47.7	0.808	55.3	314	208.0	0	0	0.0169	5.68	0.243	17.2	610	0.291

A

B

FOLDOUT FRAME

1

FOLDOUT FRAME

2

TABLE 3-13 (Continued)

Test No.	Element Code No.	$\dot{w}_T$ lbm/sec	$\dot{w}_L$ lbm/sec	$\dot{w}_G$ lbm/sec	$\dot{w}_L/\dot{w}_G$	ρ_L lbm/ft^3	ρ_G lbm/ft^3	V_L ft/sec	V_G ft/sec	P_c (psia)	Recess (in.)	R/y_1	ρ_G/ρ_L	V_G/V_L	Mach No.	$\rho_G V_G^2$ (psia)	$\bar{D}$ (microns)	$\bar{D}/y_1$
12	GCR-5	0.434	0.370	0.0635	5.82	47.7	0.273	53.7	948	61.0	0	0	0.00572	17.6	0.787	52.9	505	0.334
13	↑	0.279	0.240	0.0392	6.12	↑	0.259	34.8	616	65.2	↑	↑	0.00543	17.7	0.482	21.2	460	0.304
14		0.140	0.120	0.0200	5.99		0.275	17.4	296	67.5			0.00576	17.0	0.235	5.21	540	0.357
15		0.279	0.240	0.0393	6.11		0.169	34.8	945	39.5			0.00355	27.1	0.768	32.6	345	0.228
16		0.140	0.120	0.0201	5.96		0.090	17.4	908	19.8			0.00189	52.1	0.762	16.1	178	0.117
17	↓	0.279	0.210	0.0690	3.04		0.263	30.5	1060	58.9			0.00551	35.0	0.885	64.7	202	0.134
18	GCR-5	0.279	0.249	0.0306	8.14		0.264	36.1	471	66.4			0.00553	13.0	0.369	12.6	655	0.433
19	GCR-6	0.431	0.370	0.0615	6.02		0.266	55.3	979	61.0			0.00557	17.7	0.803	55.0	400	0.135
20	↑	0.279	0.240	0.0394	6.08		0.262	35.9	638	65.2			0.00549	17.8	0.502	23.0	460	0.155
21		0.140	0.120	0.0195	6.14		0.258	17.9	321	67.5			0.00540	17.9	0.246	5.73	478	0.162
22		0.279	0.240	0.0394	6.09		0.173	35.9	963	39.5			0.00363	26.8	0.791	34.7	395	0.133
23		0.140	0.120	0.0195	6.15		0.085	17.9	971	19.8			0.00178	54.2	0.791	17.3	190	0.0642
24	↓	0.279	0.210	0.0688	3.05		0.267	31.4	1090	58.9	↓	↓	0.00560	34.8	0.913	68.7	200	0.0676
25	GCR-6	0.280	0.249	0.0307	8.11		0.271	37.2	480	66.4	0	0	0.00567	12.9	0.380	13.5	498	0.168
26	GCR-2	0.431	0.370	0.0606	6.11		0.261	55.3	958	61.0	0.189	2.29	0.00547	17.3	0.778	51.7	284	0.136
27	GCR-2	0.280	0.240	0.0396	6.07		0.268	35.9	610	65.2	0.189	2.29	0.00561	17.0	0.485	21.5	300	0.143
28	GCR-2	0.140	0.120	0.0199	6.02		0.274	17.9	301	67.5	0.189	2.29	0.00574	16.8	0.238	5.34	313	0.149
29	GST-1	0.431	0.370	0.0609	6.07		0.267	127.0	934	61.0	0	0	0.00559	7.36	0.767	50.3	425	0.203
30	↑	0.279	0.240	0.0392	6.12		0.267	82.3	602	65.2	↑	↑	0.00559	7.31	0.478	20.9	415	0.198
31		0.140	0.120	0.0199	6.04		0.274	41.2	296	67.5			0.00574	7.20	0.234	5.20	410	0.196
32		0.279	0.240	0.0394	6.09		0.175	82.3	922	39.5			0.00366	11.1	0.761	32.0	385	0.184
33		0.140	0.120	0.0198	6.05		0.877	41.2	925	19.8			0.00184	22.5	0.765	16.2	280	0.134
34	↓	0.279	0.210	0.0689	3.05		0.270	72.0	1040	58.9	↓	↓	0.00567	14.5	0.877	63.5	335	0.160
35	GST-1	0.280	0.249	0.0308	8.09		0.271	85.4	465	66.4	0	0	0.00567	5.45	0.369	12.6	270	0.129
36	GCR-2	0.431	0.370	0.0610	6.06		0.269	55.3	937	61.0	0.0324	0.393	0.00563	16.9	0.772	50.9	425	0.203
37	↑	↑	↑	0.0610	6.06		0.268	↑	938	↑	0.0324	0.393	0.00563	17.0	0.773	51.0	415	0.198
38				0.0610	6.07		0.268		938		0.0625	0.758	0.00563	17.0	0.772	50.9	410	0.196
39				0.0607	6.10		0.267		937		0.0625	0.758	0.00561	16.9	0.770	50.6	385	0.184
40				0.0608	6.08		0.267		940		0.0965	1.17	0.00560	17.0	0.772	50.9	280	0.134
41				0.0613	6.03		0.268		945		0.0965	1.17	0.00562	17.1	0.777	51.6	335	0.160
42	↓			0.0608	6.08		0.270	↓	931		0.126	1.53	0.00565	16.8	0.768	50.4	270	0.129
43	GCR-2	↓		0.0609	6.08		0.272	55.3	925		0.126	1.53	0.00569	16.7	0.766	50.1	333	0.159
44	GCR-5	0.431		0.0608	6.09		0.265	53.7	933		0.0233	0.392	0.00555	17.4	0.764	49.8	375	0.248
45	↑	0.430		0.0600	6.17		0.250	↑	975		0.0552	0.928	0.00525	18.1	0.775	51.3	325	0.215
46		0.430		0.0598	6.19		0.250		971		0.0552	0.928	0.00525	18.1	0.772	51.0	330	0.218
47		0.430	↓	0.0601	6.16		0.253	↓	966	↓	0.0844	1.42	0.00531	18.0	0.772	51.0	273	0.181
48		0.430	0.370	0.0601	6.15		0.257	53.7	950	61.0	0	0	0.00540	17.7	0.766	50.2	350	0.232
49		0.179	0.120	0.0585	2.05		0.252	17.4	944	62.4	↑	↑	0.00529	54.2	0.745	48.5	145	0.0959
50	↓	0.118	0.060	0.0586	1.02		0.253	8.71	942	62.4			0.00530	108.0	0.745	48.4	150	0.0993
51	GCR-5	0.148	0.090	0.0585	1.54		0.251	13.1	947	62.4	↓	↓	0.00526	72.5	0.746	48.6	140	0.0926
52	GCR-2	0.139	0.120	0.0191	6.27		0.247	17.9	315	67.5	0	0	0.00518	17.6	0.236	5.29	609	0.291
53	↑	0.429	0.370	0.0590	6.27		0.250	55.3	959	61.0	0.105	1.27	0.00525	17.3	0.763	49.7	311	0.148
54	↓	0.278	0.240	0.0379	6.33	↓	0.152	35.9	1010	39.5	0.105	1.27	0.00319	28.3	0.781	33.7	212	0.101
55	GCR-2	0.139	0.120	0.0193	6.22	47.7	0.082	17.9	953	19.8	0.105	1.27	0.00173	53.1	0.764	16.1	175	0.0835

A

B

TABLE 3-13 (Concluded)

Test No.	Element Code No.	$\dot{w}_T$ $\frac{lbm}{sec}$	$\dot{w}_L$ $\frac{lbm}{sec}$	$\dot{w}_G$ $\frac{lbm}{sec}$	$\frac{\dot{w}_L}{\dot{w}_G}$	ρ_L $\frac{lbm}{ft^3}$	ρ_G $\frac{lbm}{ft^3}$	V_L $\frac{ft}{sec}$	V_G $\frac{ft}{sec}$	P_c (psia)	Recess (in.)	$\frac{R}{y_1}$	$\frac{\rho_G}{\rho_L}$	$\frac{V_G}{V_L}$	Mach No.	$\rho_G V_G^2$ (psia)	$\overline{D}$ (microns)	$\overline{D}/y_1$
56	GCR-2	0.277	0.210	0.0668	3.14	47.7	0.250	31.4	1080	58.9	0.105	1.27	0.00524	34.7	0.880	63.9	171	0.0816
57	GCR-2	0.279	0.249	0.0299	8.33	↑	0.252	27.2	482	66.4	0.105	1.27	0.00528	13.0	0.369	12.7	555	0.265
58	GCC-2	0.432	0.370	0.0616	6.01		0.267	55.3	938	61.0	0.00750	0.0468	0.00560	17.0	0.771	50.7	381	0.0935
59	GCC-2	0.431	↑	0.0610	6.07		0.260	↑	954	↑	0.0540	0.337	0.00545	17.3	0.773	51.1	372	0.0913
60	GCC-2	0.431		0.0614	6.02		0.271		923		0.101	0.632	0.00568	16.7	0.764	49.8	320	0.0785
61	GCC-2	0.431		0.0610	6.07		0.262		947		0.156	0.971	0.00549	17.1	0.771	50.7	332	0.0815
62	GCR-3	0.432		0.0619	5.98		0.274		933		0.00230	0.0279	0.00574	16.9	0.776	51.4	326	0.156
63	GCR-3	0.432		0.0619	5.98		0.271		944		0.0488	0.592	0.00567	17.1	0.780	52.0	402	0.192
64	GCR-3	0.432	↓	0.0619	5.98		0.271		944		0.101	1.22	0.00567	17.1	0.780	52.0	330	0.157
65	GCR-3	0.432	0.370	0.0617	6.00		0.269		947		0.151	1.83	0.00563	17.1	0.780	52.0	392	0.187
66	GCR-7	0.216	0.185	0.0312	5.93		0.268		941		0.00300	0.0517	0.00562	17.0	0.775	51.3	288	0.195
67	GCR-7	0.216	0.185	0.0313	5.92		0.272		931		0.0353	0.609	0.00569	16.8	0.771	50.8	270	0.183
68	GCR-7	0.216	0.185	0.0312	5.94		0.264		953		0.0645	1.11	0.00554	17.2	0.779	51.9	284	0.193
69	GCR-7	0.216	0.185	0.0312	5.93		0.268		943		0.104	1.81	0.00561	17.0	0.776	51.4	182	0.123
70	GCR-6	0.432	0.370	0.0616	6.01		0.271	↓	964	↓	0.0550	0.567	0.00567	17.4	0.797	54.3	370	0.125
71	GCR-6	0.431	0.370	0.0610	6.07		0.266	55.3	972	61.0	0.0550	0.472	0.00557	17.6	0.796	54.2	338	0.114
72	GST-2	0.140	0.120	0.0197	6.10	↓	0.259	41.2	311	67.5	0	0	0.00543	7.55	0.239	5.40	400	0.525
73	GST-2	0.140	0.120	0.0196	6.11	47.7	0.0845	41.2	950	20.0	0	0	0.00177	23.1	0.767	16.5	177	0.232

A

B

Atomization results are interpreted in terms of the mass median droplet diameter, $\overline{D}$, obtained from a given sample of "frozen" wax droplets. The value of $\overline{D}$ is merely a shorthand method of evaluating the atomization characteristics of an injector element. Unfortunately, $\overline{D}$ by itself does not completely describe the nature of a given droplet sample. The droplet size distribution function is required in addition to $\overline{D}$ to perform a complete vaporization limited performance calculation (see Appendix F). A typical droplet diameter distribution is shown in Fig. 3-40, wherein the cumulative weight fraction of the wax droplet sample is shown as a function of the normalized droplet diameter, $D/\overline{D}$. By definition, these distribution functions pass through the value of 0.5 for cumulative weight fraction when $D/\overline{D} = 1$. The data shown in Fig. 3-40 represent the results of three different atomization experiments conducted with two different RCTE's (see tests 5, 24, and 54 in Table 3-13). One distribution function fits the data for these three tests quite well. This distribution function was employed for all performance analysis throughout the remainder of the study.

Phase II atomization data have been incorporated into this discussion.

3.4.2.1 Nominal Conditions--Baseline Comparison. The nominal conditions--baseline comparison is shown in Fig. 3-41. Here the droplet mass median diameters normalized with respect to the characteristic size of the element are plotted as a function of the relative recess, R/y_1, of the liquid centerpost. Two basic conclusions can be drawn from these results: (1) droplet diameter is reduced with increased centerpost recess, and (2) relative droplet diameter increases with increased aspect ratio. The effect of recess is well known and has been documented many times in the past. The effect of aspect ratio, however, is quite surprising and warrants further discussion.

A cross plot of these data is presented in Fig. 3-42, wherein the relative dropsize is shown as a function of aspect ratio along lines of constant relative recess. Two important items concerning Fig. 3-42 must be kept in mind when evaluating the data: (1) relative dropsize is shown, not dropsize, and the value of y_1 is continually decreasing with increased aspect ratio; and (2) although these curves are drawn to the aspect ratio unity, the data at unity were obtained with a circular

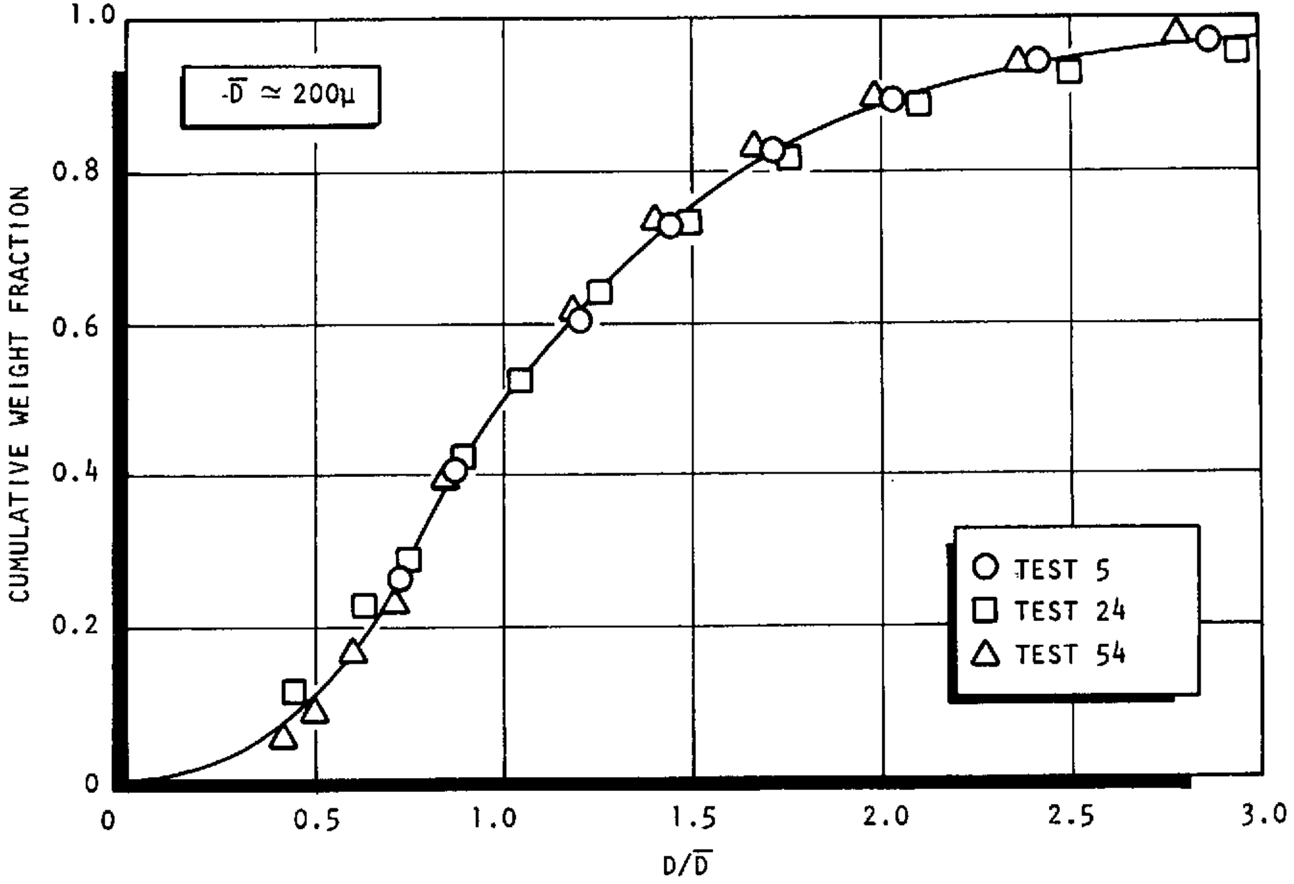

Figure 3-40. Typical Dropsize Distribution Function. Gas/Liquid Rectangular Concentric Tube Element (GCR-2), and Circular Concentric

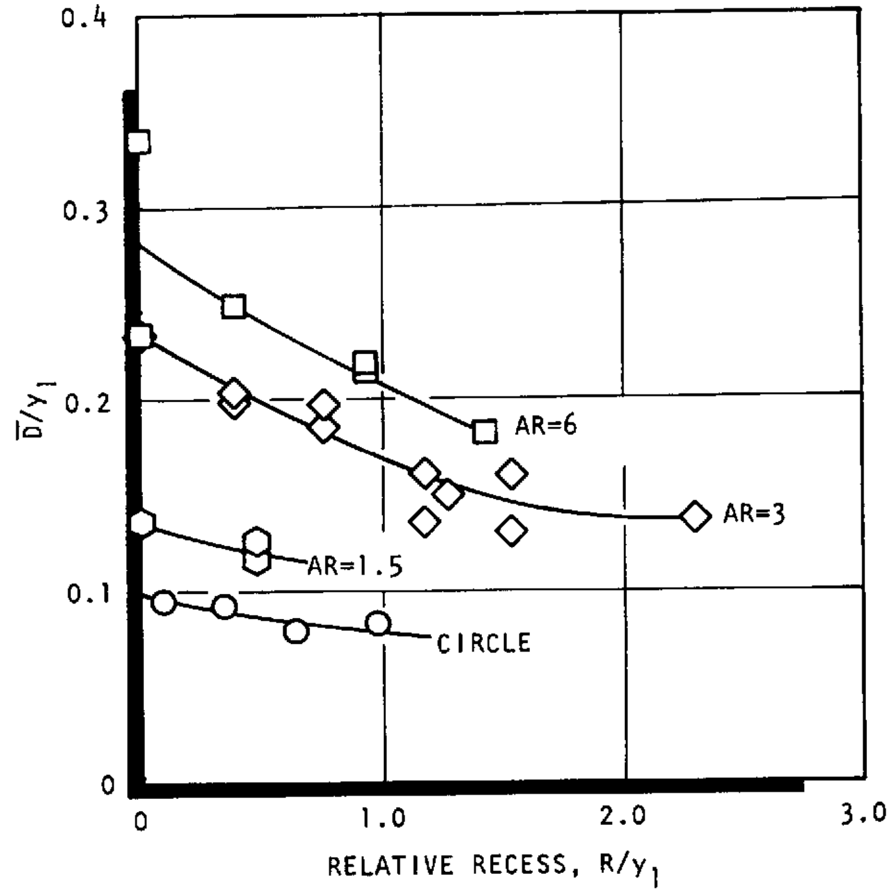

Figure 3-41. Normalized Droplet Diameter as a Function of Center-Post Relative Recess for the Four Baseline Elements at Nominal Conditions

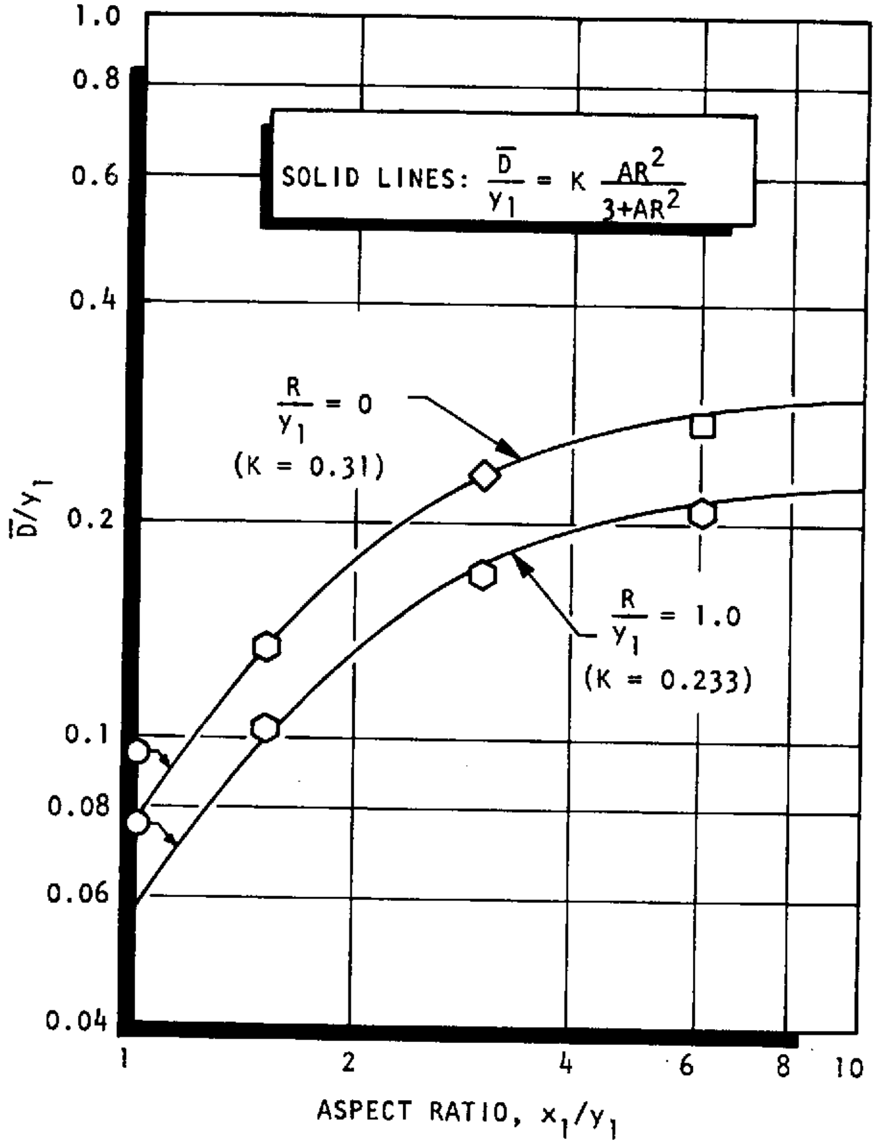

Figure 3-42. Normalized Droplet Diameter as a Function of Aspect Ratio for Constant Values of Relative Recess (baseline elements at nominal conditions)

element, not a RCTE with aspect ratio unity, and should not be expected to fall on the curves.

It was found that a relatively simple algebraic function could be employed to correlate the RCTE dropsize results. This function is presented as Eq. 3-9:

$$\frac{\overline{D}}{y_1} = K \left[\frac{AR^2}{3 + AR^2}\right] \tag{3-9}$$

where K = f(recess).

The curves that are drawn through the data in Fig. 3-42 were generated with Eq. 3-9. The implication that these curves fall below the CCTE data at aspect ratio unity is purely speculation and has not been shown. It is interesting to note that Eq. 3-9 states that, geometrically, dropsize is a function of the term:

$$\overline{D} = f\left\{ y_1 \left[\frac{AR^2}{3 + AR^2}\right]\right\} \tag{3-10}$$

(Note: It must be remembered that the liquid port area, X_1y_1, was held constant as aspect ratio was varied.)

It is interesting to speculate upon what a correlation of droplet diameter based upon the hydraulic diameter of the liquid orifice would yield as a functional relationship. If it had been assumed that the correlating parameter was $\overline{D}/D_H$ where $D_H \equiv$ hydraulic diameter, the following would have been the result:

$$\overline{D} = f\left\{ y_1 \left[\frac{AR}{1 + AR}\right]\right\} \tag{3-11}$$

The similarity between this function and Eq. 3-10 is striking. However, hydraulic diameter alone is not sufficient to describe the data. The difference between

Eq. 3-10 and 3-11 also point out the danger of adopting complex combinations of variables as correlating parameters early in an experimental study.

The variation of actual dropsize with aspect ratio is shown as a function of aspect ratio in Fig. 3-43. The curve through these data was obtained from Eq. 3-10 by adding the additional restriction that the product $X_1 y_1$ is a constant and is equal to the liquid area, A_L. This restriction adds the additional relation:

$$y_1 = \sqrt{\frac{A_L}{AR}} \qquad (3\text{-}12)$$

Combination of Eq. 3-9 and 3-11 yields:

$$\overline{D} = K\sqrt{\frac{A_L}{AR}} \left[\frac{AR^2}{3 + AR^2}\right] \qquad (3\text{-}13)$$

where

$K = 0.310$

$\sqrt{A_L} = 513$ microns

$AR = X_1/y_1$

These results can be interpreted quite simply from the implications of Eq. 3-10. This relation states that the characteristic dimension for atomization is a complex quantity at low aspect ratios and approaches y_1 as $AR \to \infty$. Physically, this is reasonable. At low aspect ratios, although y_1 is reduced by an increase in aspect ratio, X_1 is increased. Evidently, the increase in the X dimension is more detrimental to atomization than the decrease in y_1 is beneficial for atomization. As the aspect ratio increases to larger and larger values, the characteristic thickness of the liquid jet quite naturally approaches the value of y_1.

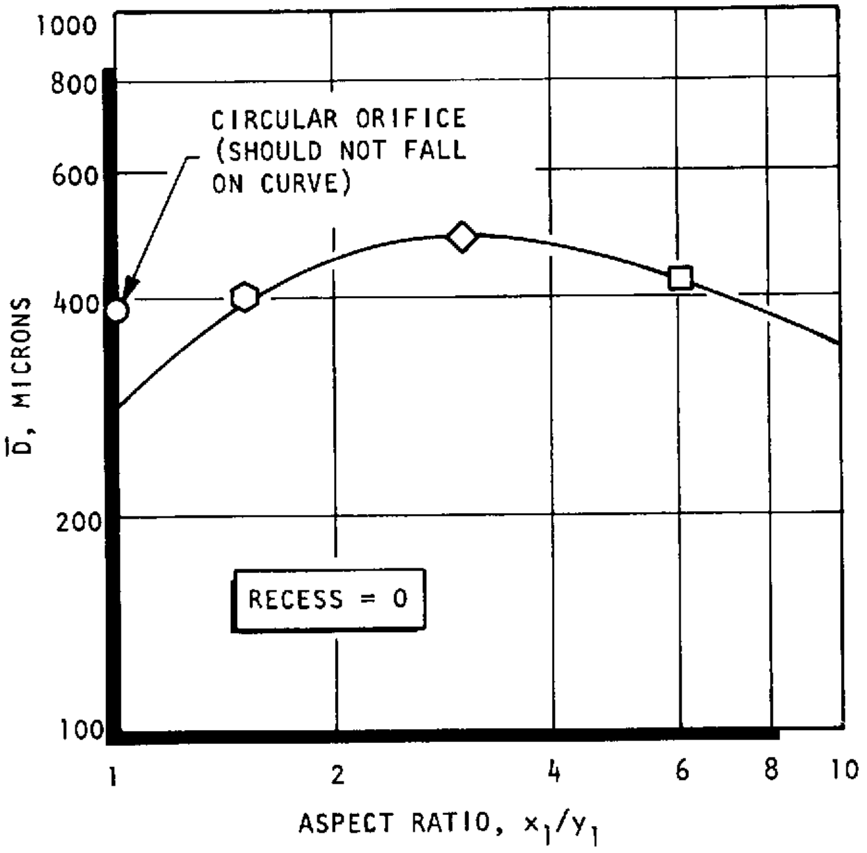

Figure 3-43. Variation of Wax Droplet Diameter With Aspect Ratio (baseline elements, nominal conditions)

3.4.2.2 Variations About AR = 3.

Only two of the three variations about the aspect ratio three baseline element were investigated during the atomization study (element scale and nonuniform gas gap). (Atomization experiments with element GCR-4, one-half baseline gas area, were not conducted due to exhaustion of the budget allocated to cold-flow atomization testing before completion of this element).

The effects of variation of element size and gas port aspect ratio are presented in Fig. 3-44. The effect of size is shown in Fig. 3-44a, wherein the relative dropsize is presented as a function of actual recess for both GCR-2 (the larger element) and GCR-7 (the smaller element). What is shown in this figure is the reduction in dropsize produced by a $\sqrt{2}$ reduction in the characteristic size of the element. If the characteristic dimension, y_1, had been sufficient to describe the droplet variation the points for GCR-7 would have fallen directly on the curve for GCR-2. At zero recess the GCR-7 element actually provided a dropsize reduction of roughly $1.2 \sqrt{2}$.

This result suggests that the effect of element size upon dropsize is stronger than the first power of a characteristic dimension. However, the limited amount of data plus the fairly large degree of uncertainty associated with dropsize data preclude any valid speculation as to the second-order effects of element size.

The effect of the gas port aspect ratio is shown in Fig. 3-44b. At zero recess, the element having a nonuniform gas gap (GCR-3) produced a $\overline{D}$ significantly smaller than the baseline element. However, the dropsizes for the two elements approach one another at moderate recess. There appears to be considerable scatter in these data such that a firm conclusion as to the gas gap effect cannot be drawn. The results seem quite rational except for the data point at the greatest recess for element GCR-3.

Atomization experiements with element GCR-4 (1.2 nominal gas area) were not conducted as discussed earlier. However, it can be postulated that an improvement in atomization would have been realized with this element at the nominal flowrate and mixture ratio. This improvement would be attributable to the doubling of the

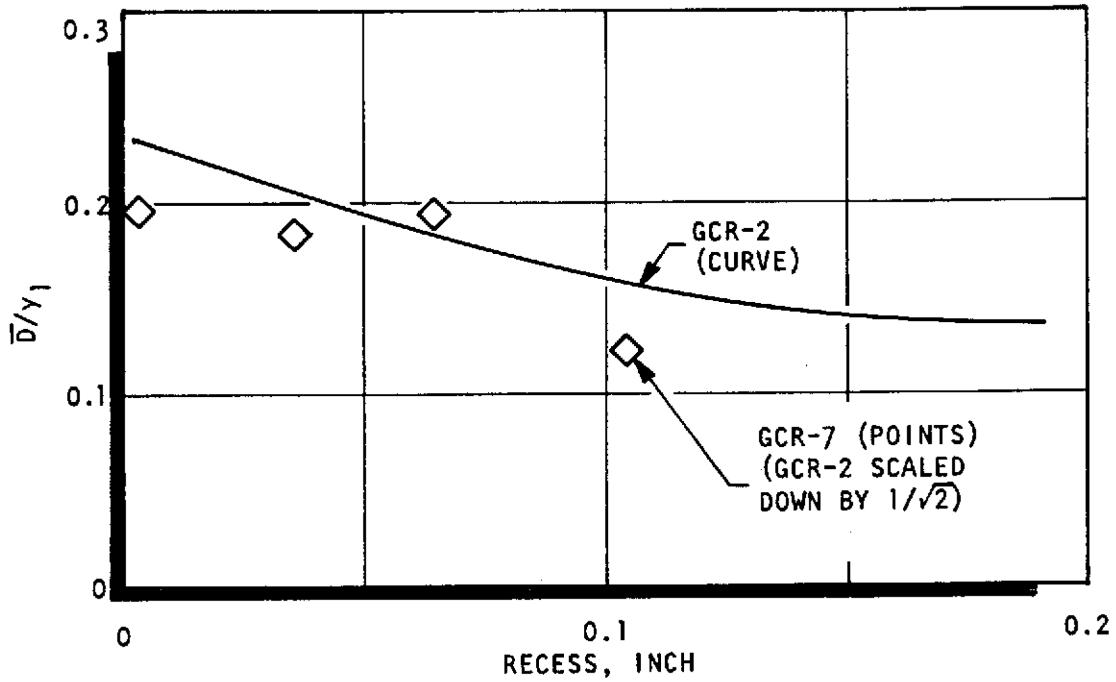

(a) EFFECT OF ELEMENT SIZE

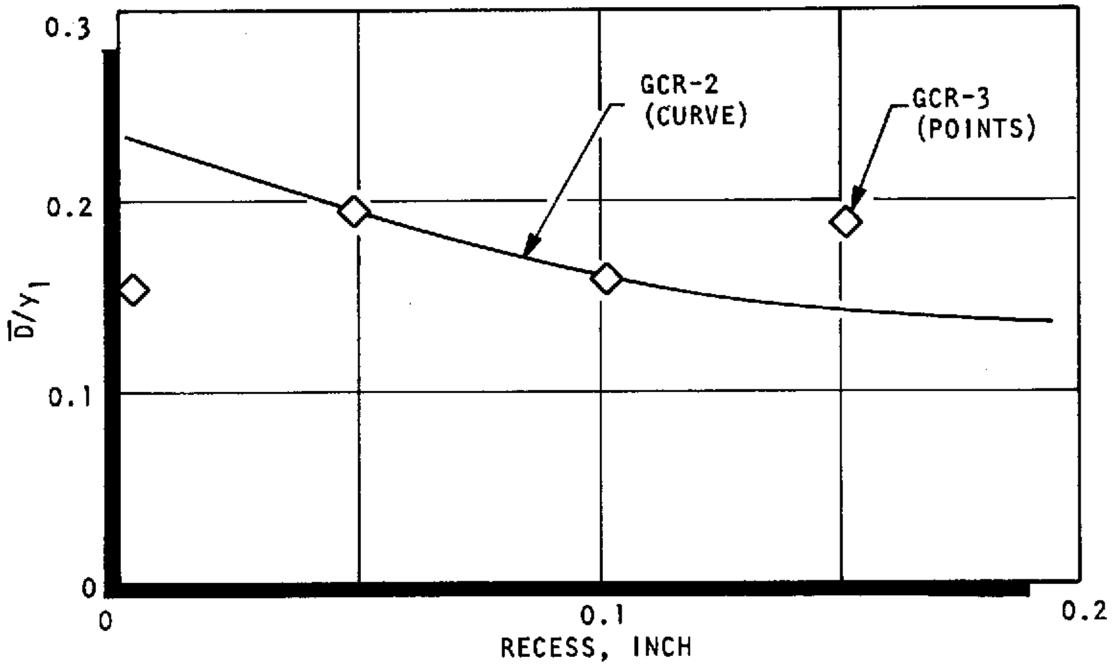

(b) EFFECT OF NONUNIFORM GAS GAP

Figure 3-44. Effect of Element Size Reduction and Nonuniform Gas Gap Upon Atomization (AR = 3, MR = 6, ρ_G = 0.27 lbm/ft^3, V_G = 950 ft/sec) gas velocity at constant liquid velocity and gas density. The magnitude of the improvement, however, is unknown for these elements (see Ref. 7 for other elements).

3.4.2.3 Generalization of the Results. The bulk of the parametric atomization data was obtained with the baseline AR = 3 element (GCR-2). As a result, these data were employed in an attempt to generalize the results to operating conditions other than the nominal set. The influence of a parametric variation of gas velocity, gas density, and liquid velocity at mixture ratio equal to 6.0, is depicted in Fig. 3-45. In this figure, the relative dropsize, $\overline{D}/y_1$, is shown as a function of liquid injection velocity along lines of constant density and constant gas velocity. The parametric variations of V_L, V_G, and ρ_G are not independent and are subject to the restrictions of Eq. 3-8 with mixture ratio a constant. It was found through further analysis of data at other mixture ratios that the effect of mixture ratio could be incorporated by casting the results shown in Fig. 3-45 into the form shown in Fig. 3-46. Here, $\overline{D}/y_1$ is plotted as a function of $\rho_G V_G^2$ along lines of constant liquid velocity.

The restrictions of Eq. 3-8 still apply here; however, the mixture ratio is allowed to vary in addition to the other parameters. A physical interpretation of the data in this form is quite clear. With a fixed liquid velocity, the droplet size is significantly reduced by increasing $\rho_G V_G^2$. However, as the liquid velocity is increased, the value of $\rho_G V_G^2$ required to produce the same droplet diameters is increased. The fact that the product $\rho_G V_G^2$ improves the correlation of the data suggests strongly that the Weber number is a key parameter for the description of the atomization process (see Table 3-3).

This method of presentation is extended to the other baseline elements in Fig. 3-47 through 3-49. In Fig. 3-47, the atomization results for both the Phase II (GCC-1) and the Phase III (GCC-2) CCTE's are presented. This figure is significant in that the direct correlation between low density, "open-air" atomization and high-density atomization can be accomplished. These data (Table 3-13) incorporate large variations in gas density (0.055 to 0.27 lb/ft^3), liquid velocity (4 to 55 ft/sec), and gas velocity (300 to 1000 ft/sec).

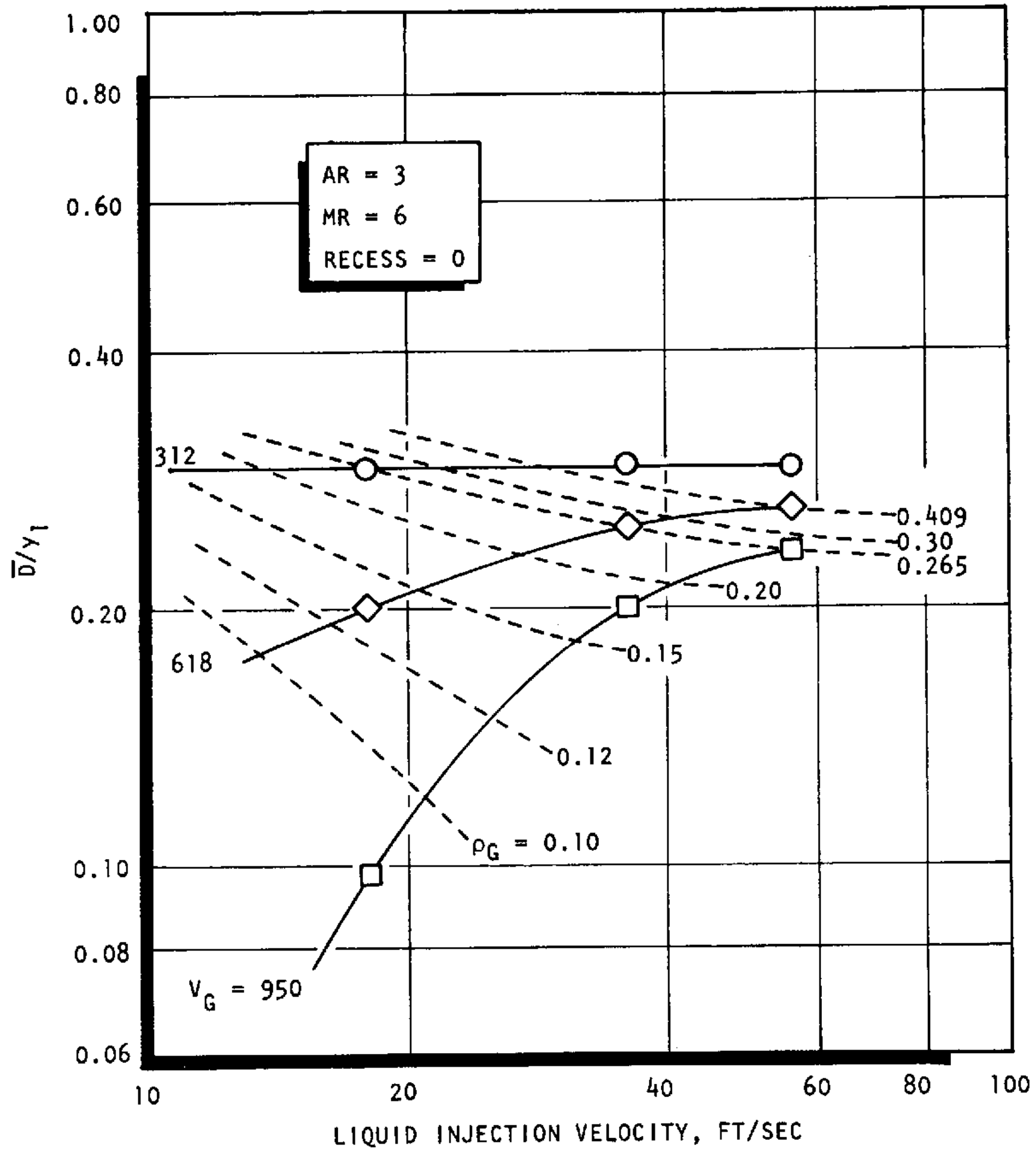

Figure 3-45. Effect of V_L, V_G, and ρ_G Upon Dropsize at Constant Mixture Ratio for the Baseline AR=3 RCTE (GCR-2)

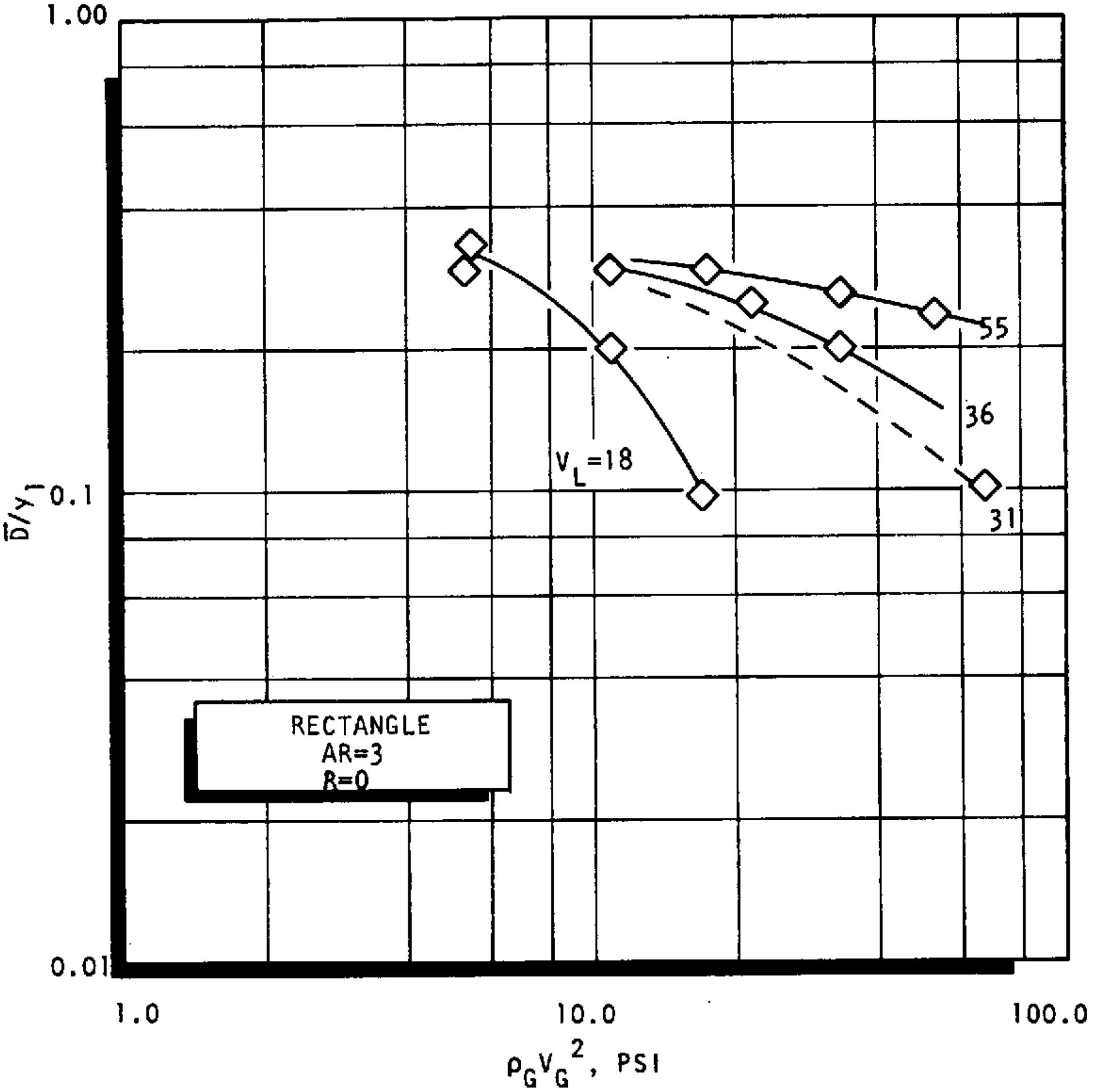

Figure 3-46. Variation of Dropsize With $\rho_G V_G^2$ and V_L. Baseline AR=3 Element (GCR-2)

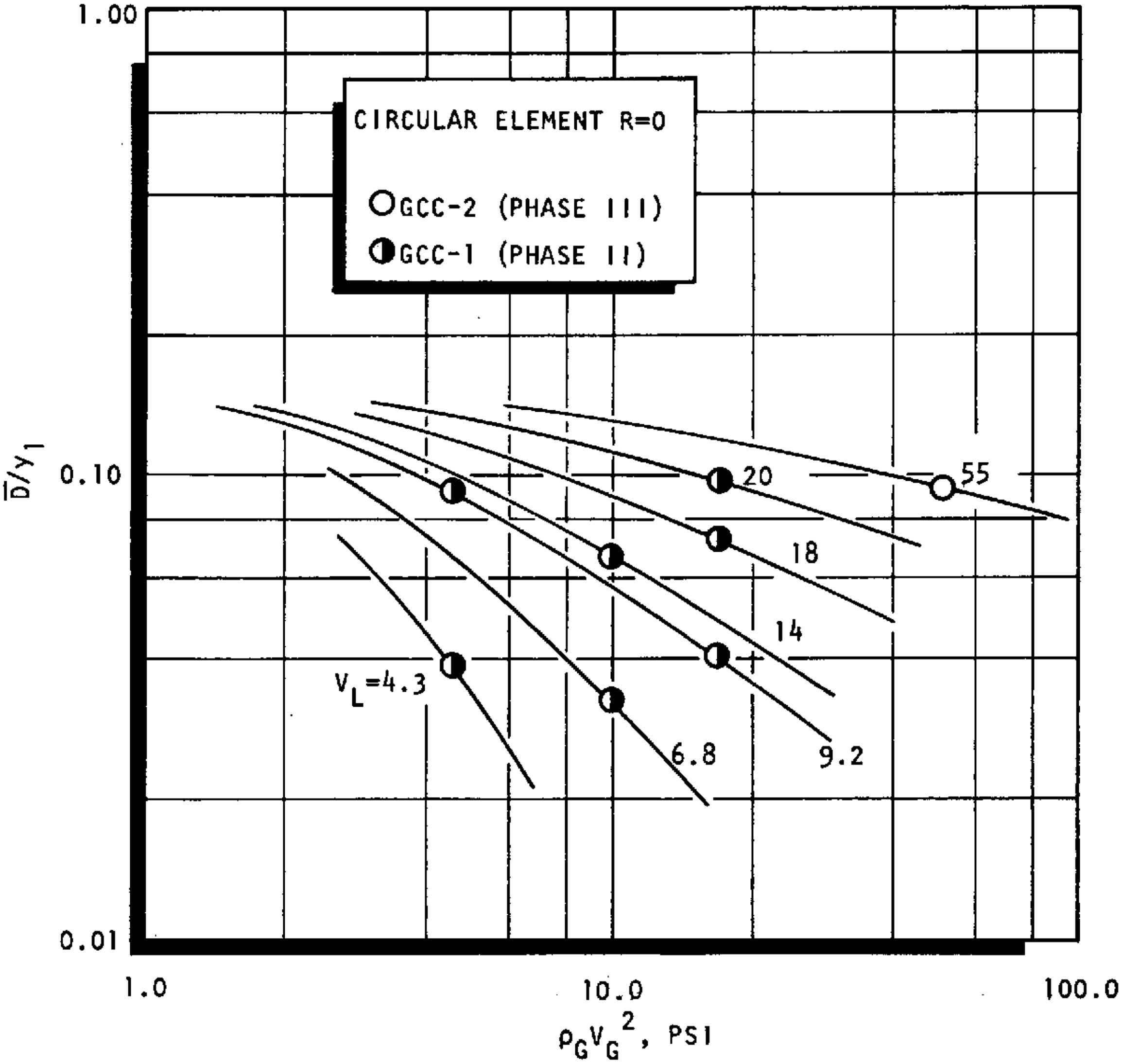

Figure 3-47. Variation of Dropsize With $\rho_G V_G^2$ and V_L. Baseline Circular Element. (Note: Solid lines are estimates based upon the limited data shown)

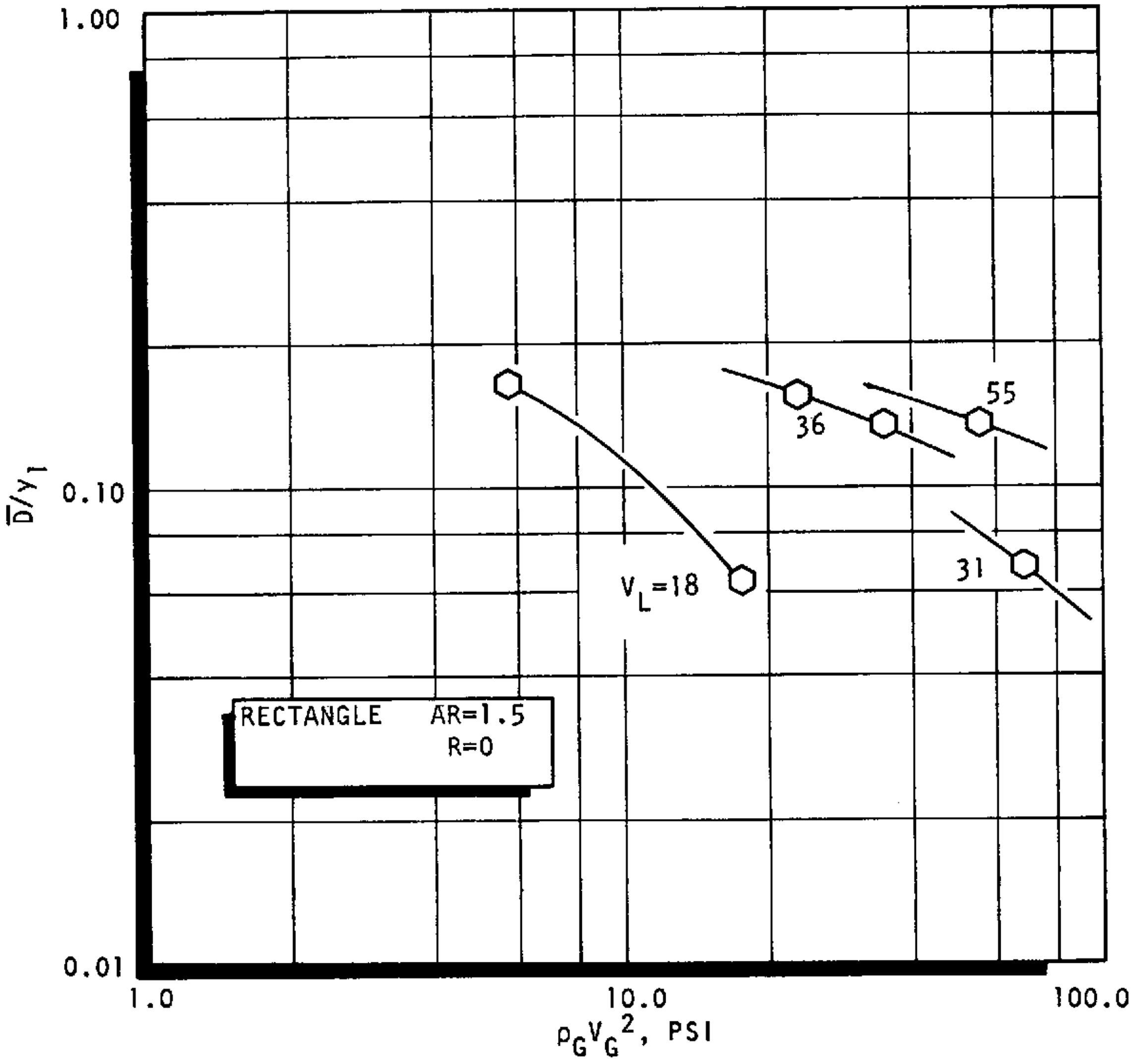

Figure 3-48. Variation of Dropsize With $\rho_G V_G^2$ and V_L. Baseline AR=1.5 Element (GCR-6)

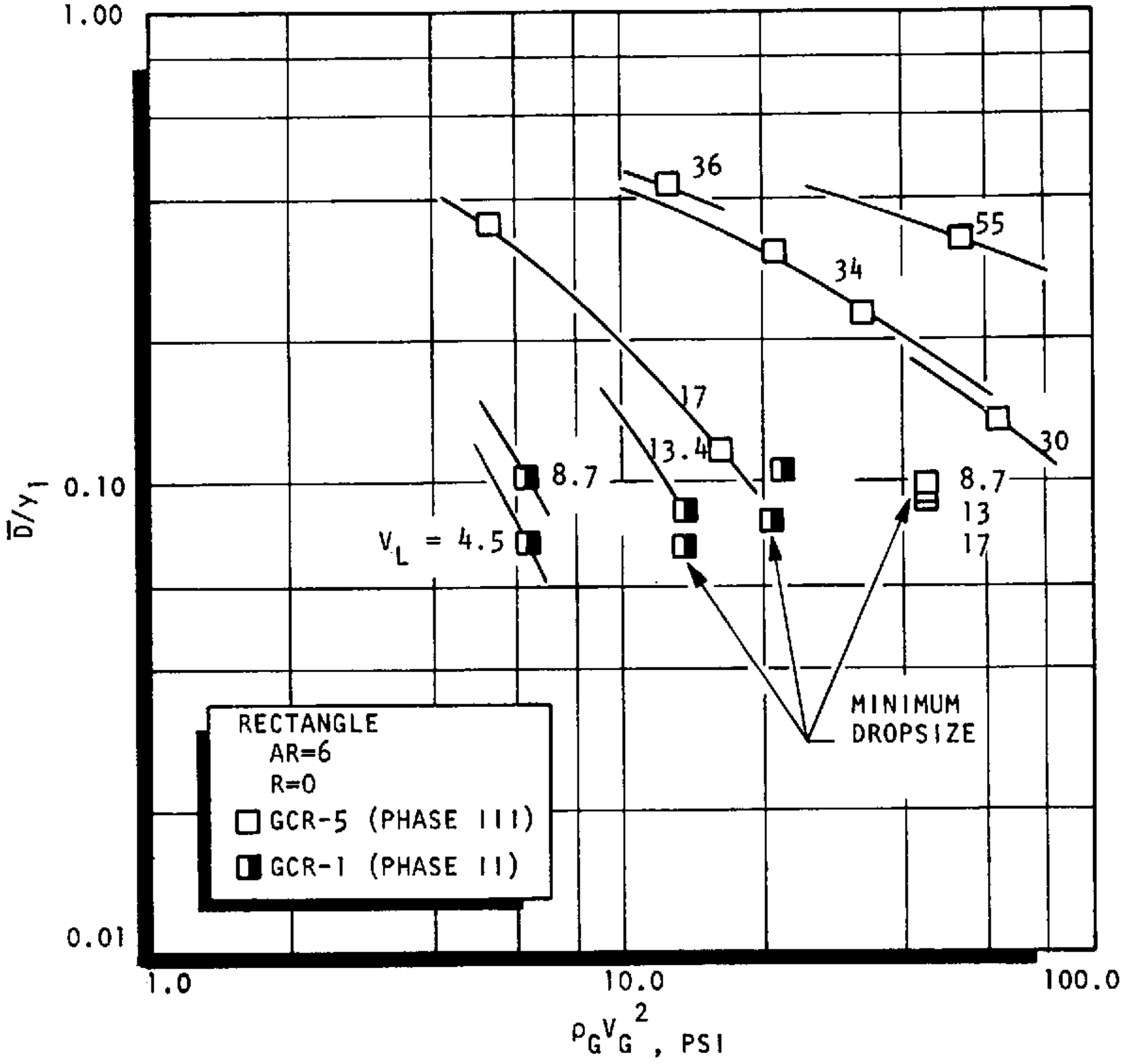

Figure 3-49. Variation of Dropsize With $\rho_G V_G^2$ and V_L Baseline AR=6 Element

A very interesting result is shown in Fig. 3-49 in which the dropsize data from both the Phase II (GCR-1) and the Phase III (GCR-5) AR = 6 elements are presented. Here again, the Phase II and III data correlate well except for a set of points which has been pointed out in the figure. It is believed that these points constitute limiting dropsizes. That is to say that a dropsize can be achieved, regardless of how low the liquid velocity is or how high the value of $\rho_G V_G^2$ is, such that a smaller droplet cannot be realized. The smallest dropsizes shown in Fig. 3-49 are on the order of 100 to 110 microns. It is reasonable to suppose that such a limit does exist. As the droplets become smaller and smaller, they are more easily accelerated by the gas stream (the acceleration is proportional to 1/D). If the droplets are accelerated rapidly to the gas velocity, the ΔV between the droplets and the gas goes rapidly to zero and further droplet breakup is halted. This would not be the case, however, if the droplet were held in place until breakup occurred. In that case, smaller droplets could be obtained from droplets less than 100μ with increased gas velocity.

Further dropsize comparisons for the baseline elements are presented in Fig. 3-50 through 3-52 as functions of $\rho_G V_G^2$ for three different liquid velocities.

Finally, the effect of liquid velocity variation upon dropsizes with centerpost recess is shown in Fig. 3-53. Once again, the limiting dropsize phenomenon appears in these data. Actually, the dropsize at the breakoff point is approximately 200μ. This is a rather large dropsize and smaller droplets should have been achieved for this element. The premature breakoff at this point has not been explained.

3.4.3 Multi-Showerhead Triplet Results

The basic multi-showerhead triplet (MST) element mixing and atomization results are discussed briefly in this section (for data see Tables 3-12 and 3-13). The specification for the two MST elements tested (GST-1 and GST-2) is presented in Table 3-5. A discussion of the geometry of these elements may be found in Section 3.3.1.

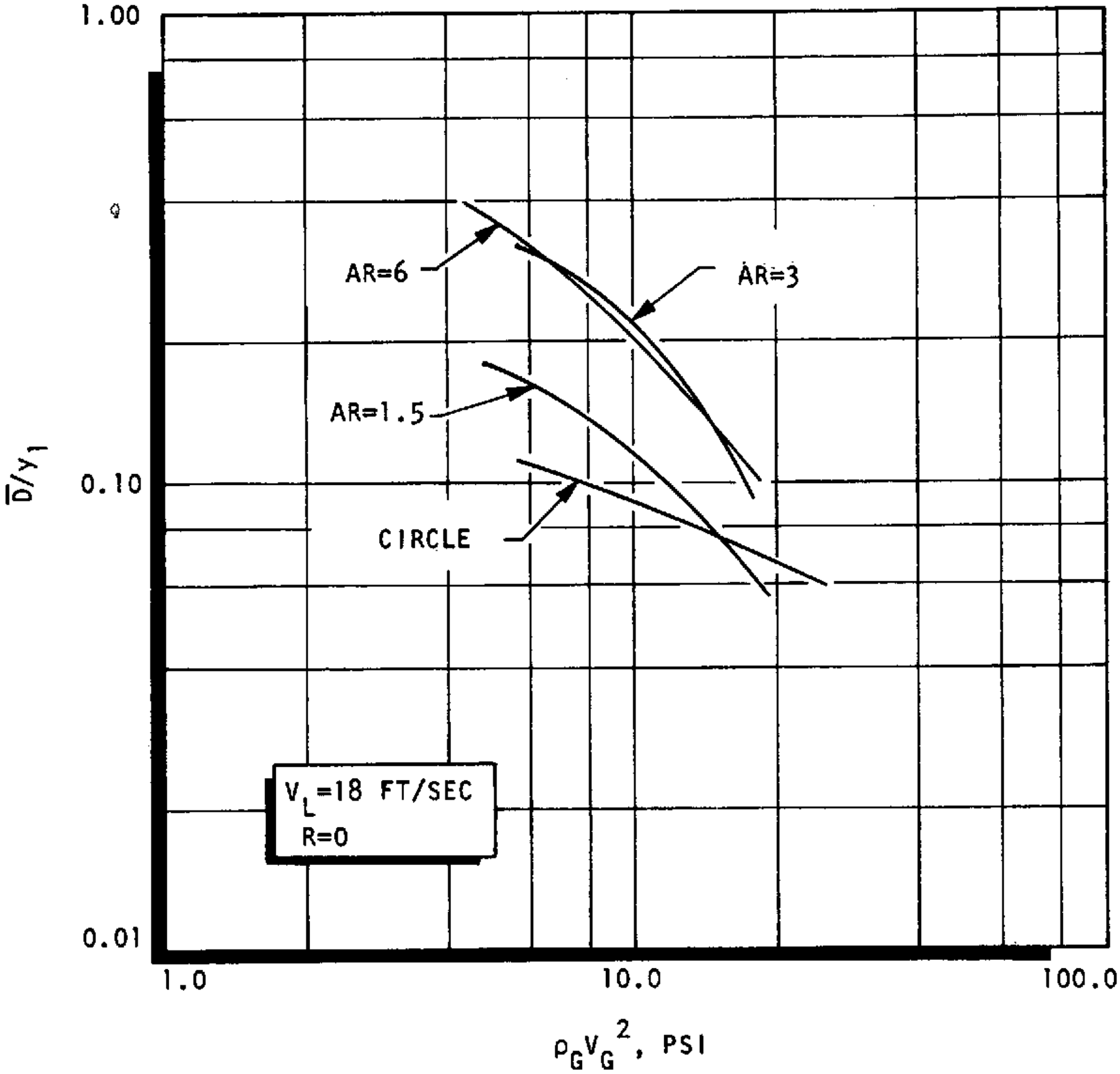

Figure 3-50. Baseline Element Dropsize Comparison

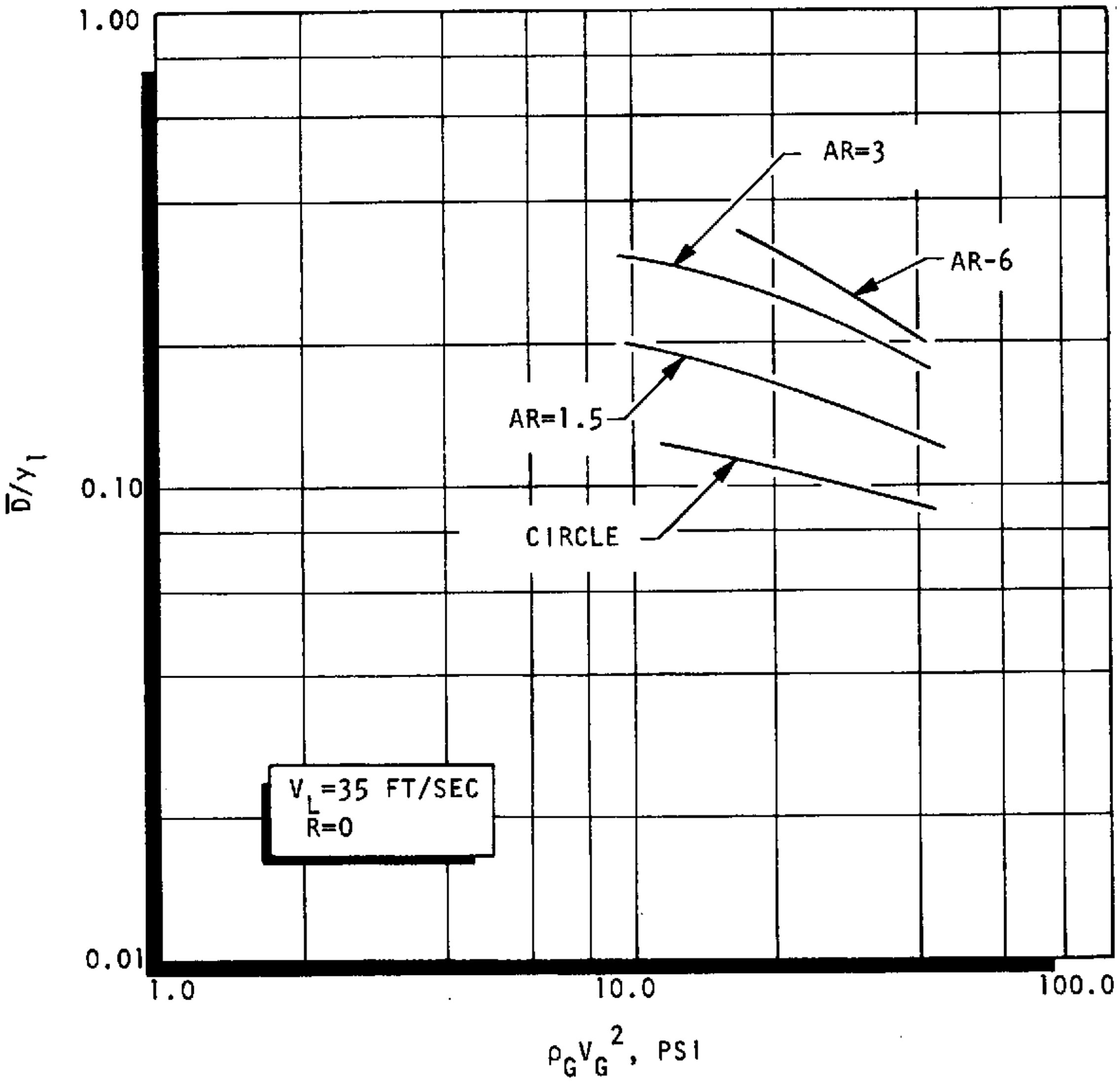

Figure 3-51. Baseline Element Atomization Comparison

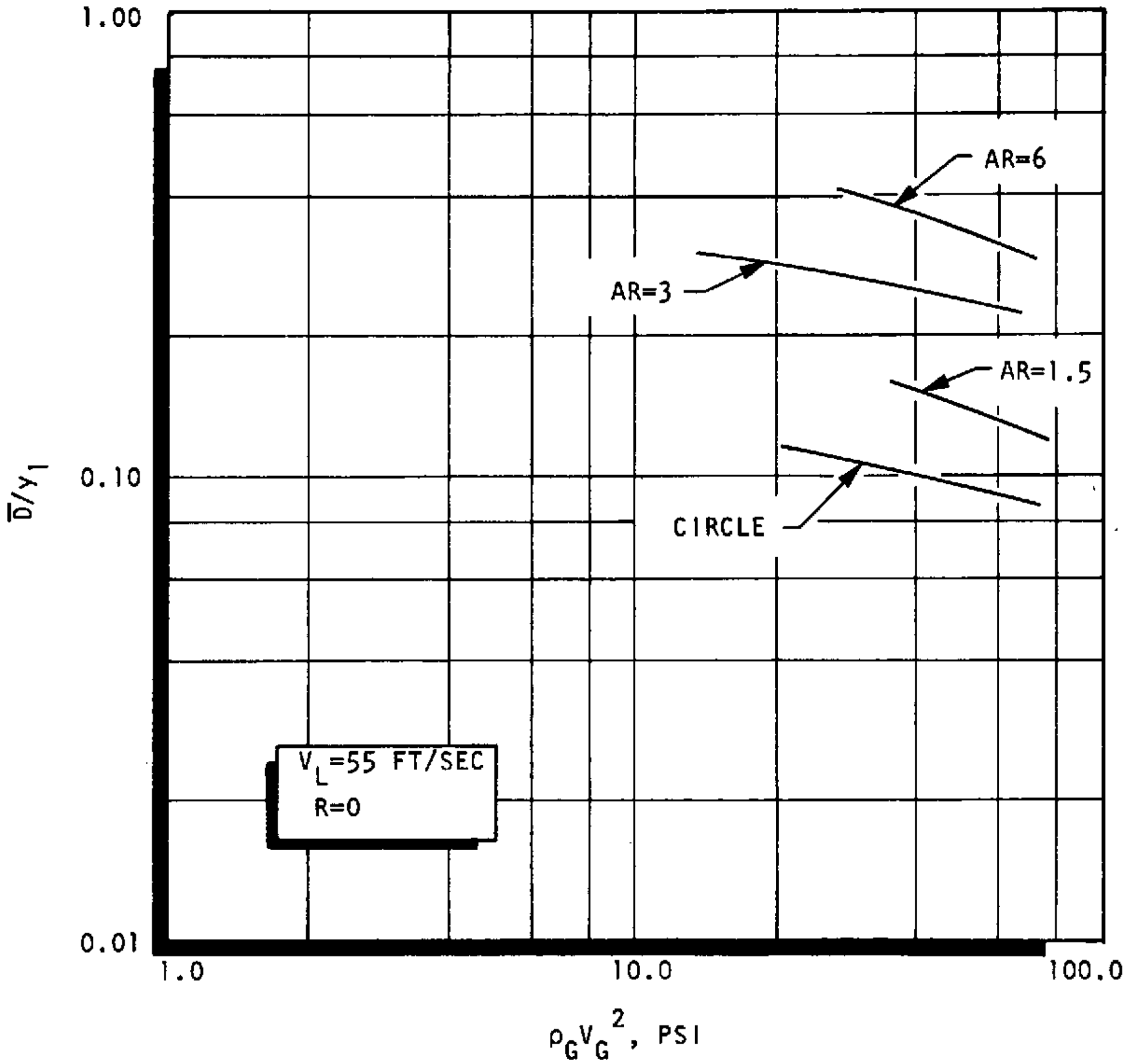

Figure 3-52. Baseline Element Atomization Comparison

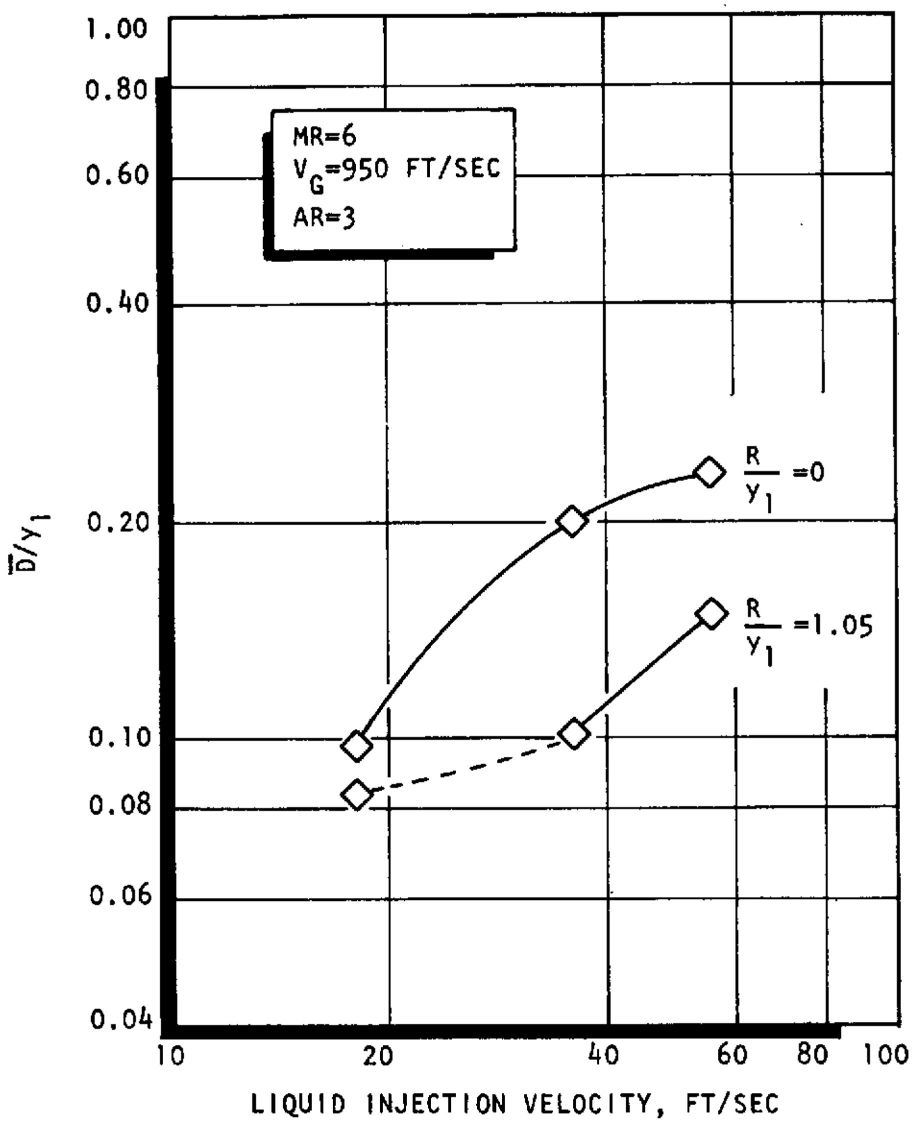

Figure 3.53. Dropsize Variation With V_L Showing the Effect of Center-Post Recess (GCR-2)

A face pattern view of the two MST elements is shown in Fig. 3-54. In each case, two rectangular gas jets are impinged at an included angle of 60 degrees upon a set of showerhead liquid orifices. The total gas and liquid areas are equal, respectively, for the two elements.

The objective of the test series was to determine the effect of the size and number of the liquid jets upon mixing and atomization. The basic results are presented in Fig. 3-55. It can be seen that the number of orifices had little effect on the mixing characteristics of the element. However, dropsize was greatly improved with the larger number of orifices (smaller jets) at low gas velocity. At high gas velocity the jet size had no effect.

The truly interesting aspect of these data is that the mixing uniformity is relatively high and the droplet diameters are quite small. Further atomication characteristics of the 28-oridice element (GST-1) are presented in Fig. 3-56. Dropsize is shown as a function of liquid velocity along lines of constant gas velocity and gas density. The trend with constant gas density suggests that there is an optimum operating point for atomization. This is logical in view of the fact that this element is subject to agglomeration of the liquid jets if the gas velocity is not high enough. The diameter of each jet is already 500 microns. This is as small as some of the droplets produced by the concentric tube elements. Evidently, below the optimum operating point the benefit of reduced liquid velocity is overcome by the agglomeration produced by the "pushing together" of the liquid jet by a low gas velocity.

In all, these are very interesting elements and should be investigated in more detail. The brief mention of their results in this report stems not from a lack of technical interest but rather from limitations dictated by the scope of the program.

These elements were not included in the hot-fire experiments under this study.

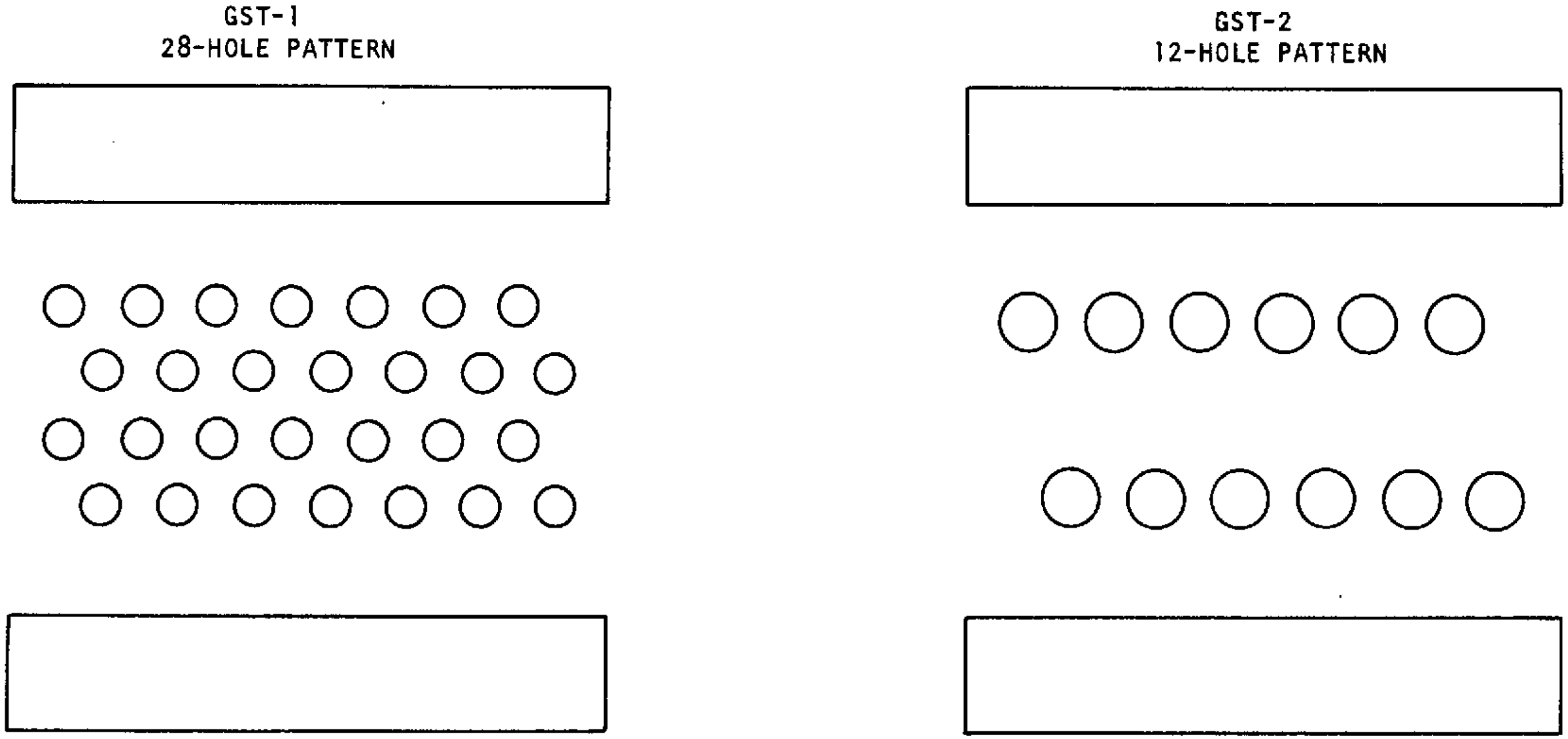

Figure 3-54. Multi-Showerhead Triplet Element Face Patterns

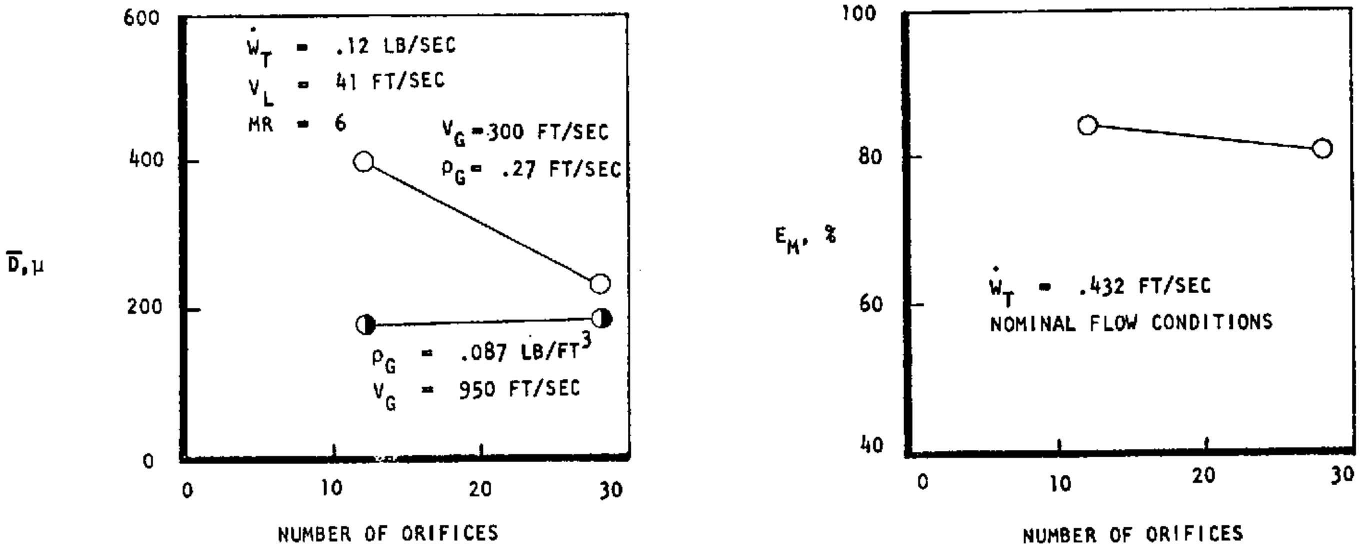

Figure 3-55. Atomization and Mixing Results for the Multi-Showerhead Triplet Elements (GST-1 and GST-2)

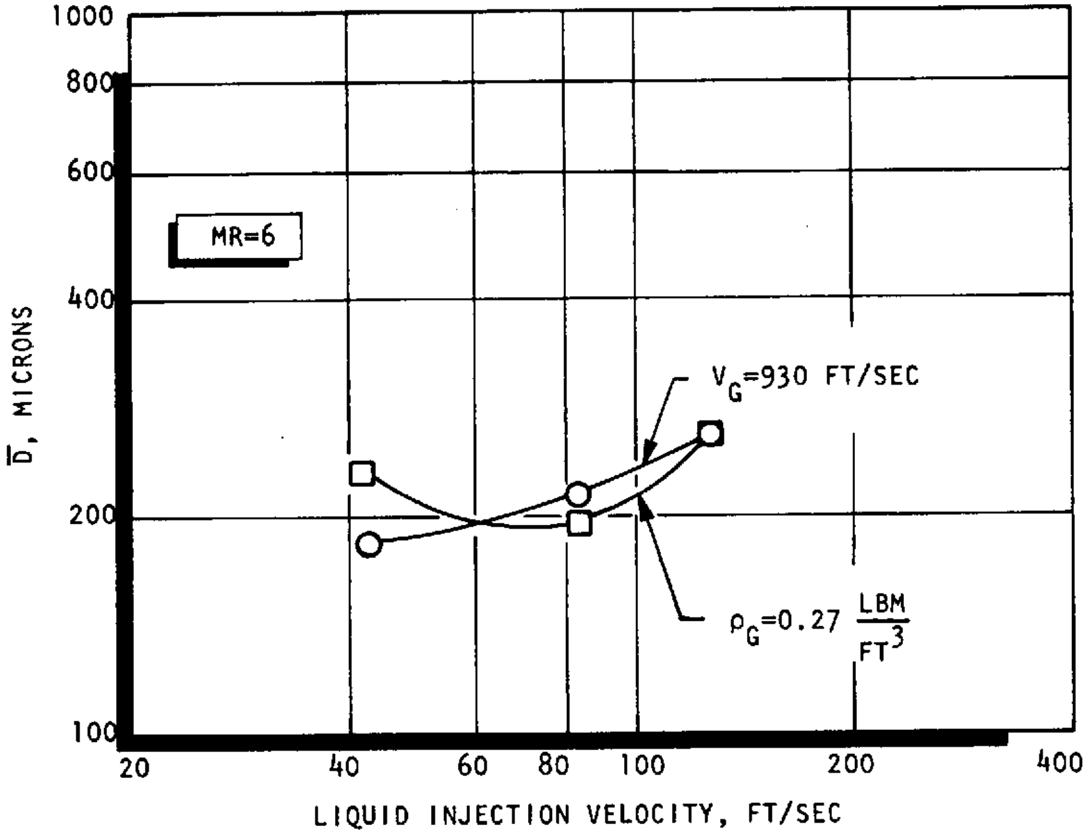

Figure 3-56. Variation of Dropsize for the GST-1 Element as a Function of Liquid Velocity Along Lines of Constant V_G and ρ_G

3.4.4 Hot-Fire Studies

Results of the hot-fire studies are presented in Table 3-14. Two characteristic velocity efficiency values are presented ($\eta_{c^*_{RAW}}$, was obtained directly from the test data with the only correction being an adjustment of static chamber pressure to throat stagnation pressure under the assumption of isentropic flow from the static pressure tap to the throat). For the contraction ratio 2.3:1 chamber employed, this correction was:

$$P_{o_{TS}} = P_{c_{STATIC}} \times (1.0418) \qquad (3\text{-}14)$$

The value of C* efficiency labeled $\eta_{c^*_{corr}}$ has been corrected for bulk heat loss according to the following relationship:

$$\eta_{c^*_{corr}} = \eta_{c^*_{RAW}} \times f_{HL} \qquad (3\text{-}15)$$

where

$$f_{HL} = \sqrt{1 + \frac{1}{\eta^2_{c^*_{RAW}}} \left[\frac{\Delta Q}{\dot{W}_T \; C_{p_s} \; T_c} \right]} \qquad (3\text{-}16)$$

where

ΔQ ≡ total heat loss, Btu/sec

$\dot{W}_T$ ≡ total chamber flowrate

C_{p_s} ≡ chamber gas specific heat, Btu/lbm-R (shifting)

T_c ≡ theoretical combustion flame temperature, R.

In general, a bulk heat loss correction is inappropriate for most large rocket engine applications. However, in this case, the chamber diameter is extremely small and the chamber length-to-diameter ratio is quite large ($L/D \simeq 6.7$). Therefore, it was assumed that the bulk heat loss was a valid, first-order correction.

FOLDOUT FRAME

1

FOLDOUT FRAME

2

TABLE 3-14 NONCIRCULAR ORIFICE PROGRAM GAS/LIQUID HOT-FIRE RESULTS (PHASE IV)

Test No.	Element Code No.	$\dot{w}_T$ $\frac{lbm}{sec}$	$\dot{w}_L$ $\frac{lbm}{sec}$	$\dot{w}_G$ $\frac{lbm}{sec}$	MR $\frac{\dot{w}_L}{\dot{w}_G}$	ρ_L $\frac{lbm}{ft^3}$	ρ_G $\frac{lbm}{ft^3}$	V_L $\frac{ft}{sec}$	V_G $\frac{ft}{sec}$	P_c (psia) Static	Recess (in.)	T Oxid Inj. (°F)	T Fuel Inj. (°F)	$\frac{R}{y_1}$	$\frac{\rho_G}{\rho_L}$	$\frac{V_G}{V_L}$	Mach No.	$\overline{\dot{Q}/A}$ $\frac{BTU}{in^2\text{-sec}}$	η_{c^*} RAW (%)	f_{HL}	η_{c^*} CORR.
3	GCC-2	0.350	0.292	0.0579	5.05	69.5	0.191	30.0	1235	534.7	0	-284.2	71.2	0	0.00275	41.2	0.290	7.90	76.1	1.0117	77.0
4	↑	0.463	0.406	0.0574	7.07	73.7	0.231	39.3	1011	651.8	↑	-309.0	71.1	↑	0.00313	25.8	0.237	8.23	75.4	1.0067	75.9
5		0.397	0.340	0.0569	5.98	73.3	0.206	33.1	1121	583.0		-307.0	73.3		0.00281	33.9	0.262	7.07	75.6	1.0075	76.1
6		0.488	0.419	0.0689	6.08	73.3	0.250	40.8	1122	707.5		-305.8	74.7		0.00341	27.5	0.262	8.26	74.8	1.0073	75.3
7	↓	0.539	0.469	0.0700	6.70	73.2	0.271	45.7	1051	769.4		-304.7	75.1		0.00370	23.0	0.245	9.09	75.4	1.0067	75.9
8	GCC-2	0.587	0.508	0.0785	6.48	72.8	0.300	49.8	1063	851.9		-301.7	74.7		0.00412	21.3	0.248	9.53	75.9	1.0066	76.4
11	GCR-8	0.370	0.321	0.0490	6.55	69.3	0.214	33.2	933	617.8		-282.5	83.1		0.00309	28.1	0.216	10.7	87.8	1.0083	88.5
12	↑	0.351	0.301	0.0496	6.07	71.4	0.205	30.2	984	594.1		-295.1	84.7		0.00287	32.6	0.227	10.5	87.5	1.0092	88.3
13		0.382	0.332	0.0495	6.71	71.6	0.219	33.2	921	635.7		-296.1	86.0		0.00306	27.7	0.212	11.0	88.1	1.0082	88.8
14		0.503	0.434	0.0693	6.26	72.0	0.290	43.2	974	839.7		-296.8	85.7		0.00403	22.6	0.225	12.8	86.5	1.0082	87.2
15		0.363	0.278	0.0853	3.26	71.5	0.239	27.9	1454	682.6		-295.2	84.6		0.00334	52.2	0.338	11.2	89.4	1.0196	91.2
16		0.364	0.301	0.0626	4.81	72.0	0.225	30.0	1132	650.7	↓	-298.2	85.9	↓	0.00313	37.8	0.261	11.0	88.3	1.0127	89.4
17		0.224	0.195	0.0298	6.54	70.0	0.128	19.9	943	372.5	0	-288.0	85.2	0	0.00183	47.3	0.218	7.66	87.7	1.0093	88.5
18		0.494	0.424	0.0699	6.08	71.9	0.293	42.3	972	841.0	0.0779	-295.9	80.9	0.9442	0.00408	23.0	0.225	13.4	87.7	1.0088	88.4
19		0.216	0.185	0.0305	6.08	69.0	0.132	19.2	939	381.1	0.0779	-282.7	82.4	0.9442	0.00191	48.9	0.217	10.9	91.7	1.0132	92.9
20		0.248	0.197	0.0505	3.91	68.2	0.165	20.7	1246	472.4	0.0779	-277.3	82.5	0.9442	0.00242	60.1	0.289	14.5	91.9	1.0282	94.5
21		0.377	0.327	0.0505	6.47	70.5	0.215	33.2	958	618.1	0.1164	-289.4	82.0	1.411	0.00305	28.9	0.222	11.2	85.9	1.0090	86.7
22		0.209	0.179	0.0304	5.88	69.3	0.133	18.5	928	385.0	0.1164	-284.2	82.3	1.411	0.00192	50.2	0.214	12.4	94.7	1.0150	96.1
23		0.351	0.301	0.0501	6.01	70.3	0.220	30.7	927	635.8	0.1164	-288.2	83.4	1.411	0.00313	30.2	0.214	17.8	93.3	1.0141	94.6
24	↓	0.449	0.385	0.0639	6.03	71.2	0.285	38.8	914	821.3	0.1164	-292.0	82.3	1.411	0.00400	23.6	0.211	21.6	94.0	1.0135	95.3
27	GCR-8	0.399	0.331	0.0688	4.80	71.4	0.263	33.2	1066	756.9	0.1641	-293.6	82.8	1.989	0.00368	32.1	0.247	22.7	92.0	1.0225	94.1
30	GCR-4	0.307	0.268	0.0396	6.75	71.1	0.180	26.8	1778	516.0	0	-293.8	91.2	0	0.00253	66.3	0.413	12.6	87.4	1.0115	88.4
31	↑	0.276	0.237	0.0396	5.98	71.1	0.167	23.7	1919	473.8	↑	-293.9	90.1	↑	0.00235	80.9	0.447	12.3	86.7	1.0138	87.9
32	↓	0.400	0.345	0.0553	6.23	70.8	0.244	34.7	1834	694.7		-290.6	89.5		0.00345	52.8	0.427	14.9	88.2	1.0112	89.2
33	GCR-4	0.491	0.424	0.0668	6.36	71.1	0.298	42.6	1813	847.0		-291.0	88.4		0.00419	42.6	0.422	16.7	87.9	1.0104	88.8
34	GCR-7	0.273	0.233	0.0399	5.85	71.5	0.172	46.5	1872	486.0		-296.4	85.6		0.00241	40.3	0.438	11.0	89.5	1.0121	90.6
35	↑	0.368	0.317	0.0509	6.23	71.9	0.226	62.9	1824	637.8		-297.5	85.1		0.00314	29.0	0.426	13.0	88.1	1.0105	89.0
36		0.500	0.431	0.0693	6.22	71.6	0.300	85.8	1871	844.2	↓	-294.3	84.5	↓	0.00419	21.8	0.438	13.8	85.5	1.0092	86.3
37		0.439	0.378	0.0606	6.24	71.3	0.267	75.7	1838	751.7	0	-292.8	84.3	0	0.00374	24.3	0.430	13.8	87.0	1.0099	87.9
38		0.304	0.262	0.0419	6.26	71.6	0.189	52.3	1797	526.1	0.0536	-296.4	77.8	0.9241	0.00264	34.4	0.423	12.5	88.2	1.0120	89.3
39		0.400	0.346	0.0539	6.42	71.8	0.245	68.7	1777	683.7	0.0536	-296.7	77.5	0.9241	0.00341	25.9	0.418	14.8	87.6	1.0110	88.6
41	↓	0.271	0.228	0.0436	5.22	63.3	6.188	51.3	1874	528.0	0.104	-250.2	82.6	1.793	0.00297	36.6	0.440	18.7	95.4	1.0215	97.5
42	GCR-7	0.327	0.282	0.0449	6.29	65.7	0.219	61.3	1662	616.1	0.104	-261.1	81.1	1.793	0.00333	27.1	0.389	19.1	95.9	1.0146	97.3
45	GCR-10	0.290	0.238	0.0521	4.57	63.9	0.183	26.7	1179	516.2	0	-254.4	74.7	0	0.00286	44.1	0.275	12.2	85.3	1.0198	87.0
46	GCR-10	0.406	0.354	0.0524	6.75	63.2	0.225	40.1	965	638.7	0	-250.0	74.8	0	0.00356	24.1	0.225	13.7	81.4	1.0111	82.3
48	GCR-10	0.330	0.288	0.0425	6.80	58.9	0.183	34.0	940	513.7	0.0123	-232.3	69.3	0.2067	0.00311	27.6	0.220	9.24	81.2	1.0091	81.9
52	GCR-9	0.309	0.267	0.0422	6.33	60.6	0.173	31.6	1033	497.5	0.0110	-239.5	82.1	0.0944	0.00285	32.7	0.239	9.05	82.5	1.0096	83.3
53	GCR-9	0.411	0.356	0.0550	6.47	60.4	0.229	42.3	1018	659.0	0.0110	-236.9	82.6	0.0944	0.00379	24.1	0.236	11.3	82.4	1.0091	83.2
55	GCR-9	0.550	0.480	0.0704	6.81	63.8	0.298	53.9	999	860.5	0.0110	-251.2	83.3	0.0944	0.00467	18.6	0.231	13.0	81.2	1.0081	81.9
56	GCR-9	0.490	0.426	0.0633	6.74	63.6	0.265	48.1	1010	764.0	0.0110	-250.8	82.4	0.0944	0.00417	21.0	0.234	12.1	80.9	1.0085	81.6

A

B

FOLDOUT FRAME
1

FOLDOUT FRAME
2

TABLE 3-14 (Concluded)

Test No.	Element Code No.	$\dot{w}_T$ $\frac{lbm}{sec}$	$\dot{w}_L$ $\frac{lbm}{sec}$	$\dot{w}_G$ $\frac{lbm}{sec}$	MR $\frac{\dot{w}_L}{\dot{w}_G}$	ρ_L $\frac{lbm}{ft^3}$	ρ_G $\frac{lbm}{ft^3}$	V_L $\frac{ft}{sec}$	V_G $\frac{ft}{sec}$	P_c (psia) Static	Recess (in.)	T Oxid Inj. (°F)	T Fuel Inj. (°F)	$\frac{R}{y_1}$	$\frac{\rho_G}{\rho_L}$	$\frac{V_G}{V_L}$	Mach No.	$\frac{\overline{\dot{Q}/A}\ BTU}{in^2\text{-}sec}$	η_{c*} RAW (%)	f_{HL}	η_{c*} CORR.
60	GCC-2	0.362	0.313	0.0492	6.36	63.1	0.214	35.4	934	619.0	0.153	-249.8	82.6	0.9539	0.00339	26.4	0.216	9.17	87.8	1.0075	88.5
61	↑	0.446	0.386	0.0594	6.50	65.6	0.255	42.0	948	736.4	0.153	-261.7	83.2	0.9539	0.00389	22.6	0.219	12.6	85.2	1.0089	86.0
62		0.530	0.459	0.0707	6.49	65.3	0.299	50.1	963	861.1	0.153	-258.9	82.5	0.9539	0.00458	19.2	0.223	13.5	83.7	1.0085	84.4
63		0.524	0.453	0.0709	6.39	66.3	0.298	48.7	969	858.1	0.153	-264.1	82.0	0.9539	0.00449	19.9	0.224	13.7	84.1	1.0088	84.8
65		0.443	0.383	0.0599	6.39	66.7	0.264	40.9	926	753.3	0.2156	-267.3	77.3	1.344	0.00396	22.6	0.215	14.7	87.4	1.0102	88.3
66	↓	0.517	0.448	0.0688	6.51	67.3	0.298	47.5	942	852.2	0.2156	-269.8	78.7	1.344	0.00443	19.8	0.219	14.5	84.9	1.0090	85.7
67	GCC-2	0.532	0.461	0.0704	6.55	67.2	0.289	48.9	993	834.1	0.0905	-269.5	84.1	0.5642	0.00430	20.3	0.229	11.7	80.8	1.0078	81.4
68	GCR-10	0.432	0.376	0.0564	6.66	63.1	0.235	41.5	968	683.5	0.0123	-249.2	86.9	0.2067	0.00372	23.3	0.223	11.3	81.9	1.0087	82.6
69	GCR-10	0.555	0.477	0.0783	6.08	66.2	0.299	50.1	1057	889.6	0.0123	-263.3	100.3	0.2067	0.00452	21.1	0.241	13.7	80.9	1.0094	81.7
70	GCR-10	0.465	0.404	0.0619	6.52	65.2	0.251	43.1	998	749.2	0.0123	-259.0	102.3	0.2067	0.00385	23.1	0.227	13.0	82.8	1.0093	83.6
71	GCR-3	0.447	0.389	0.0585	6.64	51.6	0.222	53.7	1087	663.1	0.0033	-205.5	103.1	0.0400	0.00426	20.3	0.247	9.43	76.7	1.0080	77.3
72	GCR-3	0.503	0.434	0.0688	6.31	58.9	0.254	52.5	1119	757.7	0.0033	-229.5	103.9	0.0400	0.00431	21.3	0.254	11.5	77.0	1.0091	77.7
73	GCR-3	0.573	0.497	0.0751	6.62	56.6	0.272	62.7	1139	810.9	0.0033	-219.1	102.5	0.0400	0.00481	18.2	0.259	11.6	73.2	1.0087	73.8

B

A

3.4.4.1 Nominal Conditions--Baseline Comparison. Hot-fire c* efficiency results for the four baseline elements are presented in Fig. 3-57. Values of η_{c*} are shown as functions of the operating static pressure (not the computed throat stagnation pressure). The elements were throttled over a range of chamber pressure to ensure that a valid interpolation to the baseline 800 psia could be made. Data obtained at several values of center-post recess are presented for the baseline circular element and the baseline AR = 3 element.

In general, the perforamnce dropped off slightly with increased chamber pressure (throttling up). This is due to the fact that the gas velocity remains roughly constant while the liquid velocity increases, thus reducing V_G/V_L. This is detrimental to both mixing and atomization. For the two elements fired with center-post recess, the performance was improved substantially as recess was increased.

The variation of c* efficiency with aspect ratio, at zero recess and nominal conditions, is presented in Fig. 3-58. The performance first improved markedly with aspect ratio and then suddenly fell off again at the highest aspect ratio.

The effect of center-post recess upon η_{c*} is shown in Fig. 3-59 for the circular and the AR = 3 baseline elements at nominal conditions. For both elements, the performance was significantly improved with recess. However, the difference in performance between the elements was maintained, approximately. The performance of the recessed (R/y_1 = 1.411) AR= 3 rectangular concentric tube element was notably high for a single-element injector (η_{c*} = 95 percent).

3.4.4.2 Variations About AR = 3. Characteristic velocity efficiency for the three variations about the aspect ratio 3.0 baseline element is presented in Fig. 3-60. Detailed comparison of the data with those obtained with the baseline AR = 3 element are presented in the next section in which the cold-flow and hot-fire results are correlated. One trend of note that is evident in these results is that the scaled down model of the baseline AR = 3 element (GCR-7) appears to be more sensitive to throttling than its larger counterpart. This is actually an indication that the smaller element is following the slopes predicted from

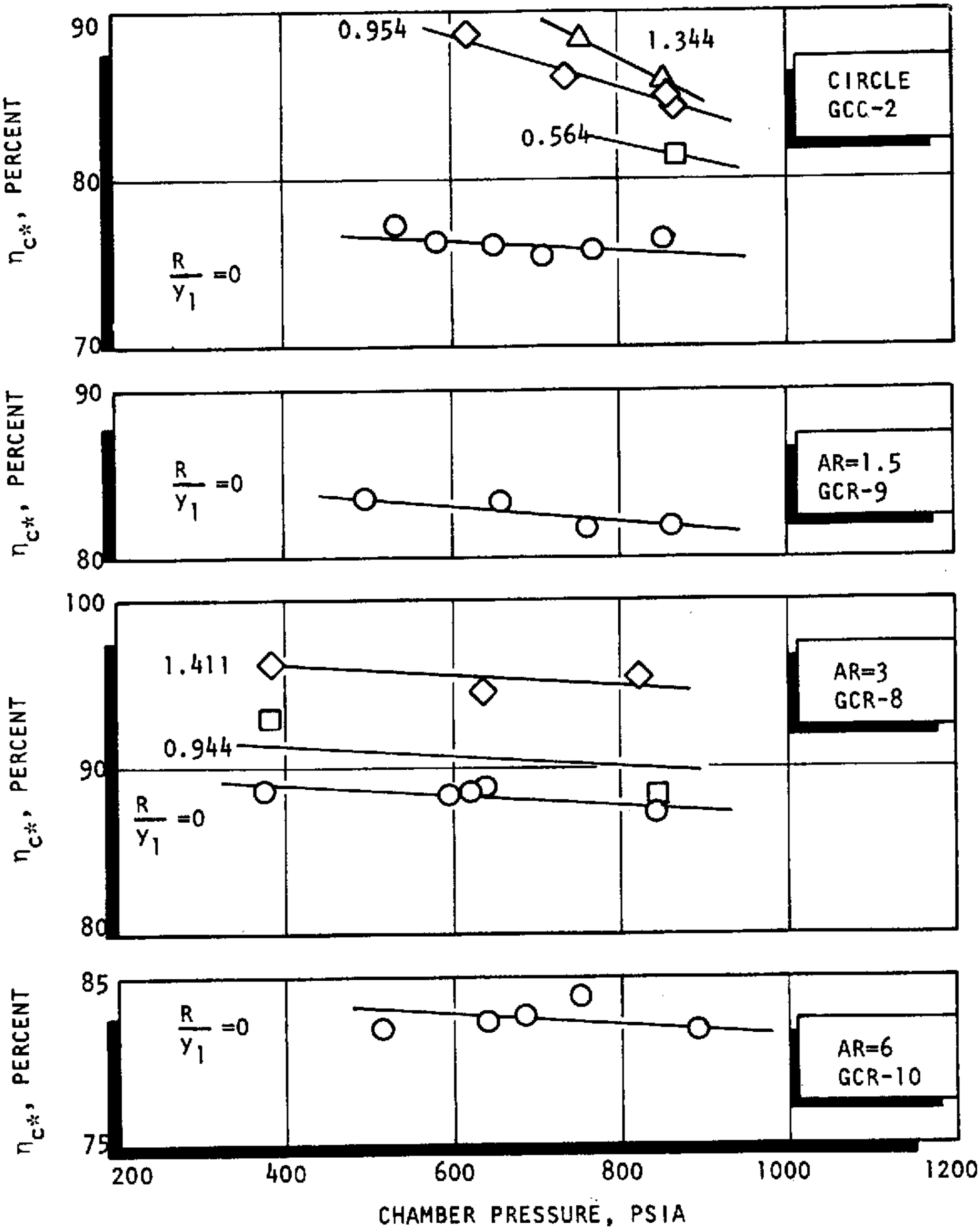

Figure 3-57. Characteristic Velocity Efficiency as a Function of Chamber Pressure (Baseline Elements)

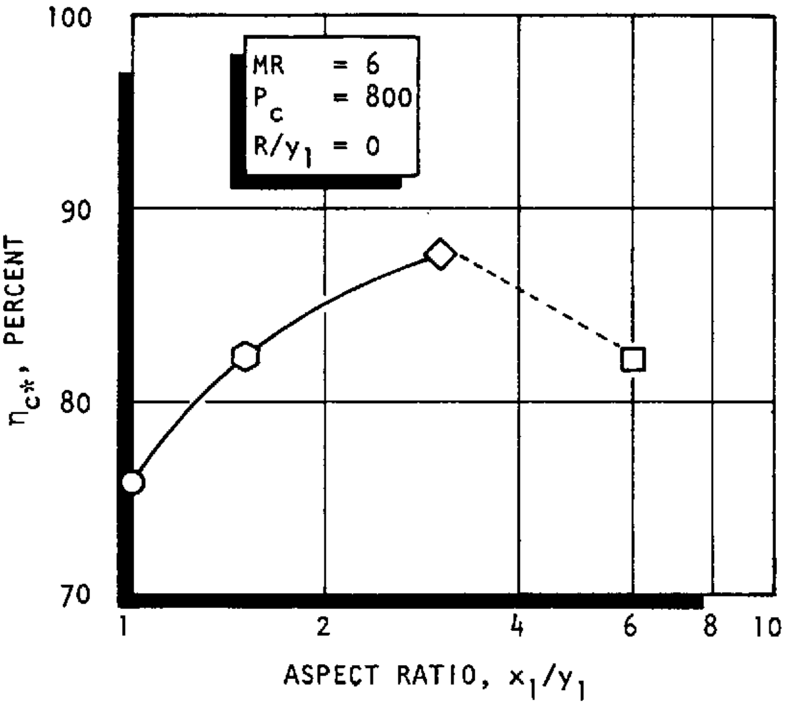

Figure 3-58. Variation of c* Efficiency With Aspect Ratio (baseline elements, nominal conditions)

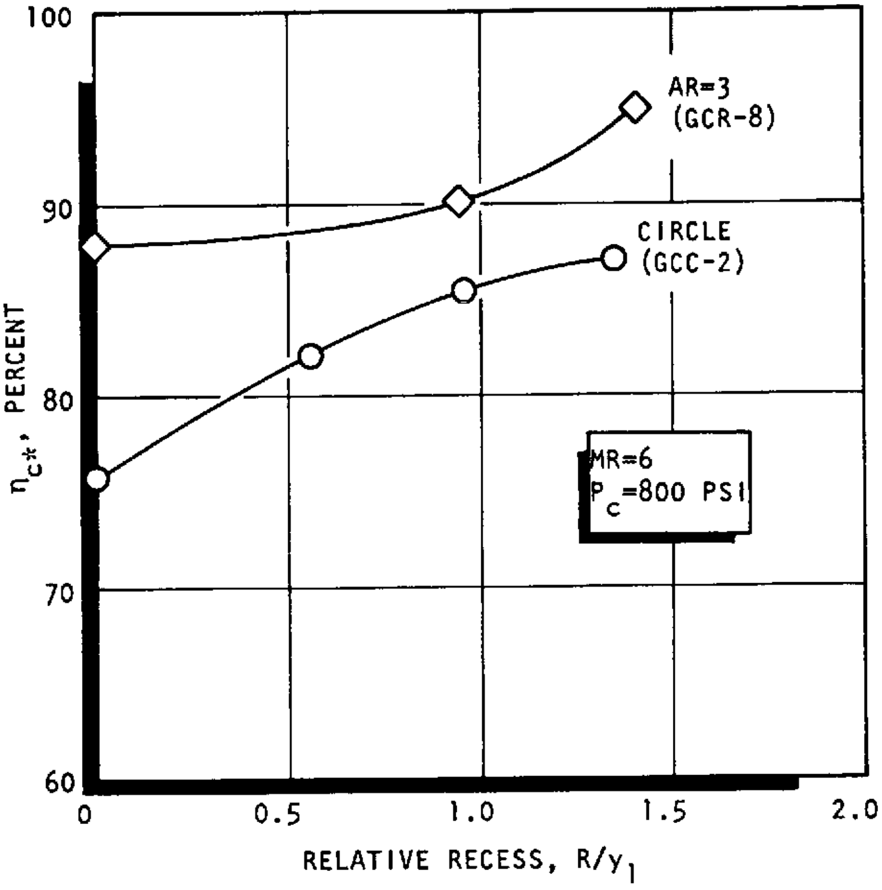

Figure 3-59. Characteristic Velocity Efficiency as a Function of Center-Post Recess (nominal conditions)

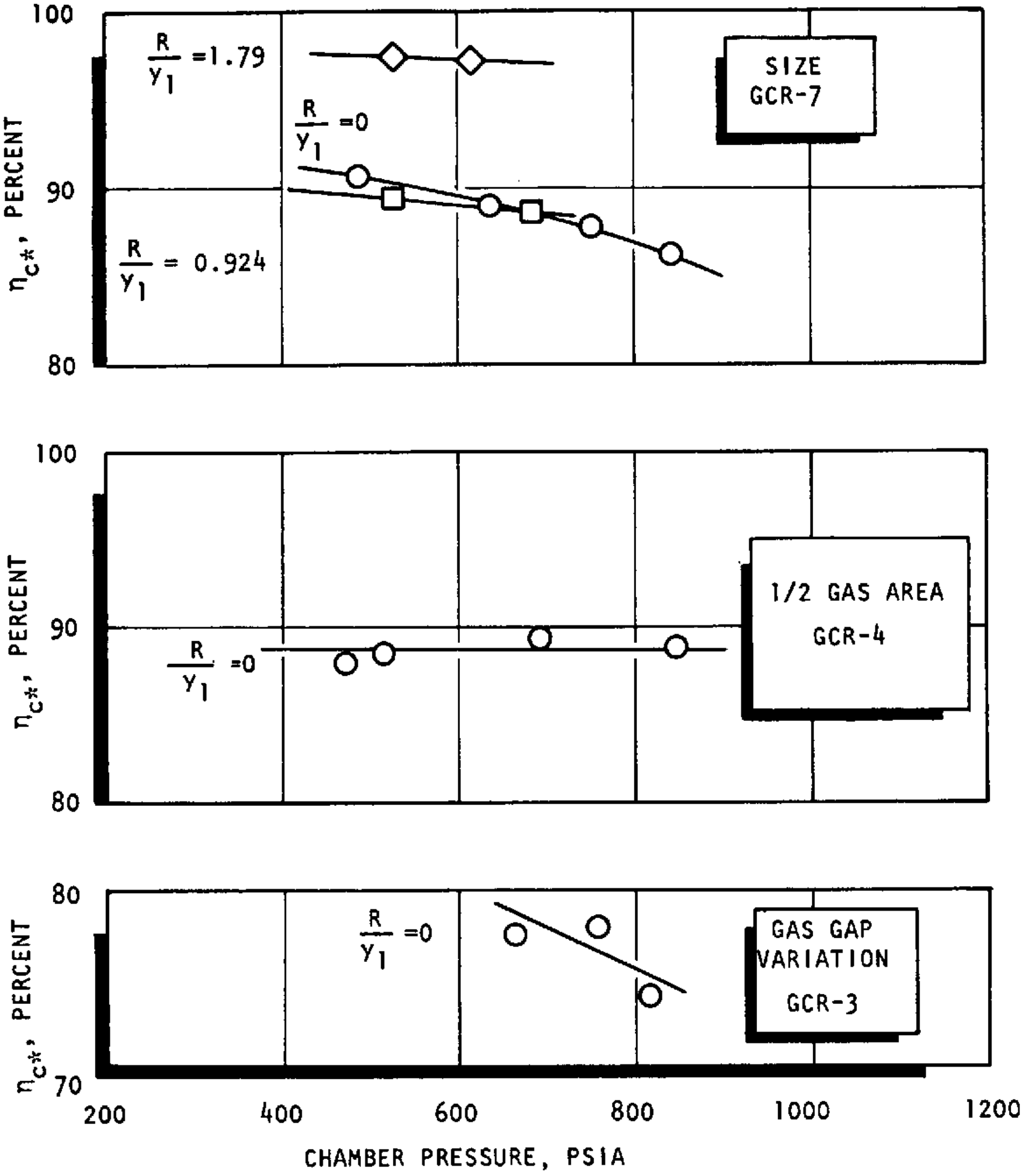

Figure 3-60. Variation About AR=3 Comparisons, c* Efficiency as a Function of Chamber Pressure

cold flow more closely than the large element. The effect could be attributable to the interference of the chamber walls in the mixing and atomization process. The smaller element is "farther" from the walls and its flowfield would be affected to a lesser degree.

3.5 CORRELATION OF THE TEST RESULTS

This section contains a comparison of the gas/liquid cold-flow and hot-fire results. The approach to this comparison was discussed, briefly, in Section 3.1. Basically, the cold-flow results have been transformed into mixing limited ($\eta_{c*_{mix}}$) and vaporization limited ($\eta_{c*_{vap}}$) c* efficiency values and these values employed as the primary basis of comparison with hot-fire c* efficiency trends.

The methods employed to compute the values of $\eta_{c*_{vap}}$ and $\eta_{c*_{mix}}$ are summarized in Appendix F. The results of these computations are presented in Fig. 3-61 and 3-62.

The mixing limited c* efficiency, $\eta_{c*_{mix}}$, is presented in Fig. 3-61 as a function of E_m for all of the injector elements of Phase III. It can be seen that one curve describes these data quite well. This curve, however, is only valid for mixture ratio 6.0. Other mixture ratios will yield separate curves. This points to the fact that E_m and $\eta_{c*_{mix}}$ are not uniquely related.

The vaporization limited efficiency results presented in Fig. 3-62, wherein the value of $\eta_{c*_{vap}}$ is shown as a function of the mass median liquid oxygen droplet diameter. The droplet distribution function employed to compute these results was shown in Fig. 3-40.

Comparisons between cold-flow and hot-fire are made at the nominal conditions. A list of these conditions is presented in Table 3-4. The results of the calculations of mixing limited and vaporixation limited efficiency are summarized in Table 3-15. For each element, the values of E_m, $\eta_{c*_{mix}}$, $\bar{D}_{wax}$, $\bar{D}_{LOX}$, $\eta_{c*_{vap}}$, and the product of $\eta_{c*_{mix}}$ and $\eta_{c*_{vap}}$ ($\eta_{c*_{C.F.}}$) are presented.

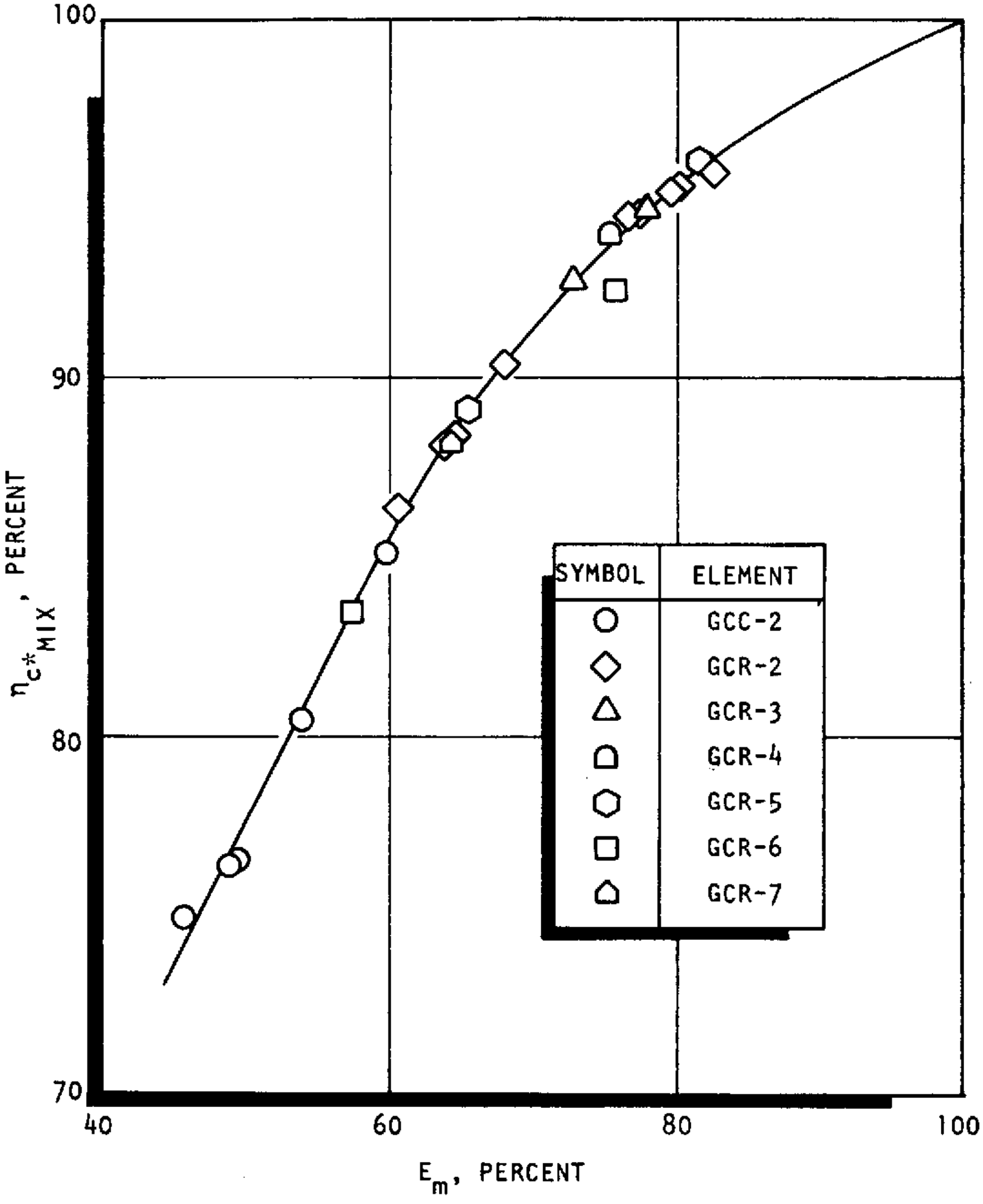

Figure 3-61. Mixing Limited c* Efficiency as a Function of E_m, for LOX/GH_2 at a Mixture Ratio 6.0:1 (all injector elements)

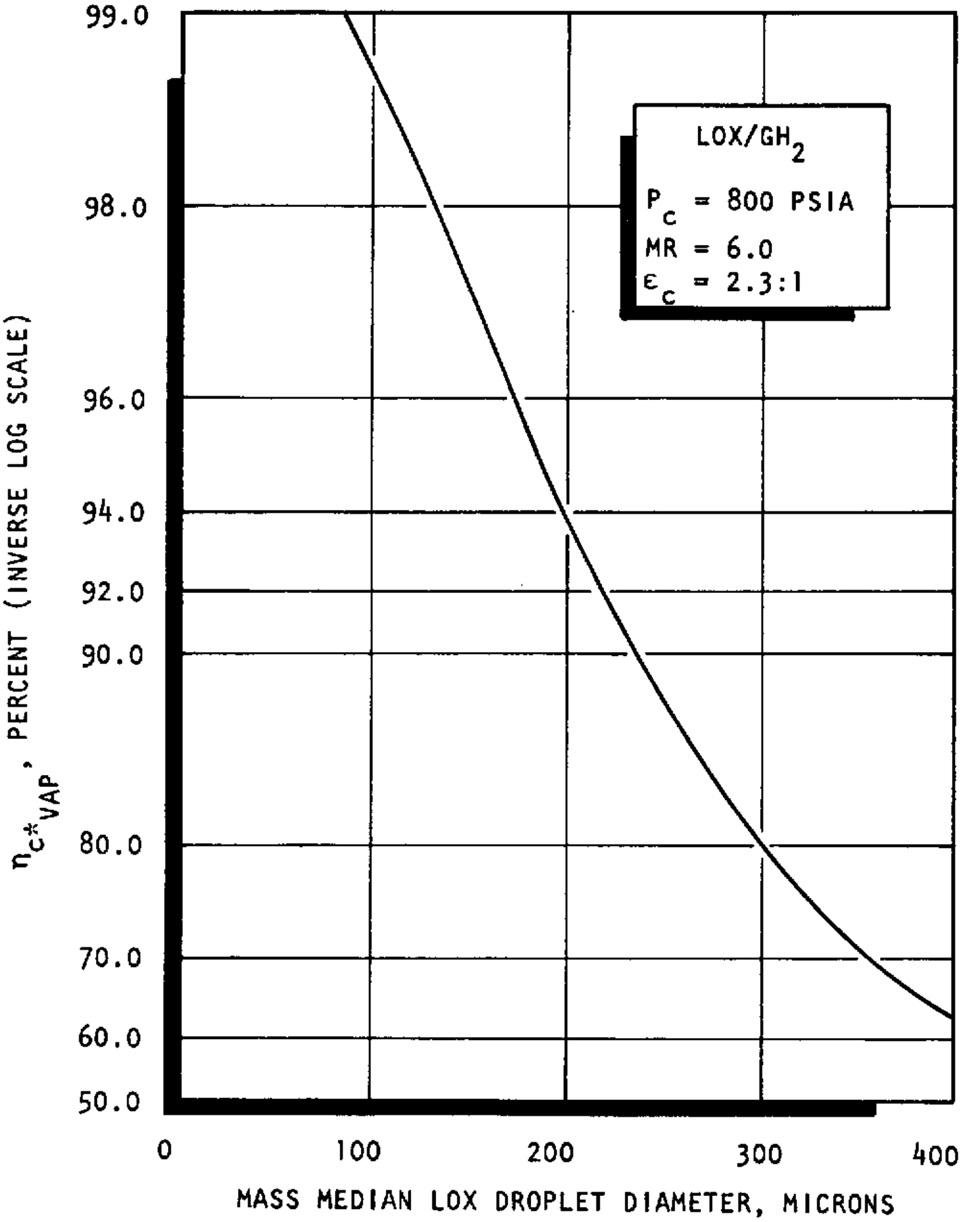

Figure 3-62. Vaporization Limited c* Efficiency for LOX/GH$_2$ at Mixture Ratio 6.0:1 for P_c = 800 psia and Contraction Ratio 2.3:1

TABLE 3-15 RESULTS OF MIXING LIMITED AND VAPORIZATION LIMITED C* EFFICIENCY CALCULATIONS BASED UPON COLD-FLOW DATA (NOMINAL CONDITIONS)

Element Code No.	Element Type	Relative Recess R/y_1	E_m, %	η_{c^*} mix	$\bar{D}_{wax}$ microns	$\bar{D}_{LOX}$ microns	η_{c^*} vap	η_{c^*} C.F.
GCC-2	Circle	0	47.0	75.1	395	150	97.3	73.1
		0.564	49.0	76.7	342	130	98.0	75.2
		0.954	52.8	79.8	310	118	98.4	78.5
		1.344	57.2	83.3	281	107	98.6	82.1
GCR-9	AR = 1.5	0	57.2	83.3	399	152	97.2	81.0
GCR-8	AR = 3	0	64.0	88.0	488	186	94.8	83.4
		0.564	67.5	90.2	413	157	96.9	87.4
		0.944	74.5	93.4	363	138	97.8	91.3
		1.411	81.0	95.6	314	120	98.3	94.0
GCR-10	AR = 6	0	65.8	89.2	428	163	96.6	86.2
GCR-7	Size	0	64.4	88.3	287	109	98.6	87.1
GCR-3	Gas gap	0	49.5	77.2	321	122	98.3	75.9

The conversion from wax droplet diameter to liquid oxygen droplet diameter was based upon a property correction for gas/liquid atomization developed by Ingebo. This correction has been employed for gas/liquid concentric tube results in a FLOX/methane injector study at Rocketdyne (Ref. 7). The value of the correction was computed with Eq. 3-17:

$$\frac{\overline{D}_{LOX}}{\overline{D}_{WAX}} = \frac{\left(\frac{\sigma\mu}{\rho}\right)_{LOX}}{\left(\frac{\sigma\mu}{\rho}\right)_{WAX}} = 0.381 \qquad (3\text{-}17)$$

where

$\sigma \equiv$ surface tension

$\mu \equiv$ viscosity

$\rho \equiv$ density

The physical properties of the various fluids employed in this program are presented in Appendix G.

Comparisons between the cold-flow and hot-fire c* efficiencies are presented in Fig. 3-63 through 3-66 for the baseline elements and two of the variations about AR = 3. In each figure curves for both the cold-flow c* efficiency ($\eta_{c^*_{C.F.}} = \eta_{c^*_{mix}} \times \eta_{c^*_{vap}}$) and the mixing limited c* efficiency, $\eta_{c^*_{mix}}$, are presented, (i.e., curves for $\eta_{c^*_{vap}}$ = 100 percent). Examination of Fig . 3-63 through 3-66 will show that the curves representing mixing limited performance are much more representative of the hot-fire results than the curves that include a vaporization limited component. This result is quite reasonable since no account of secondary droplet breakup has been taken in the calculation of the liquid oxygen droplet diameters.

In this thrust chamber (with a contraction ratio of 2.3.:1) the combustion gas can be expected to reach a velocity of 1400 ft/sec in the chamber and 5000 ft/sec

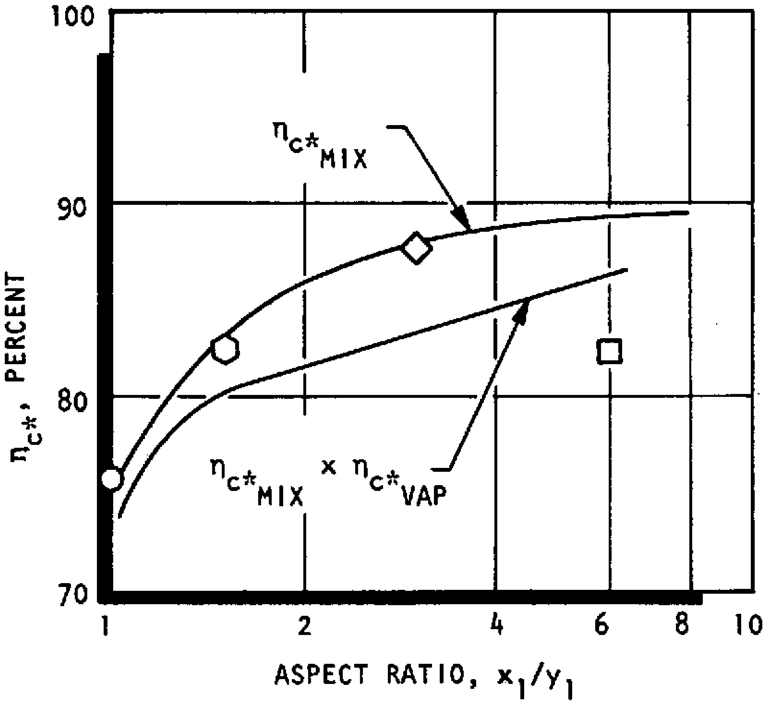

Figure 3-63. Comparison of Hot-Fire and Cold-Flow c* Efficiencies for the Baseline Elements at Zero Recess

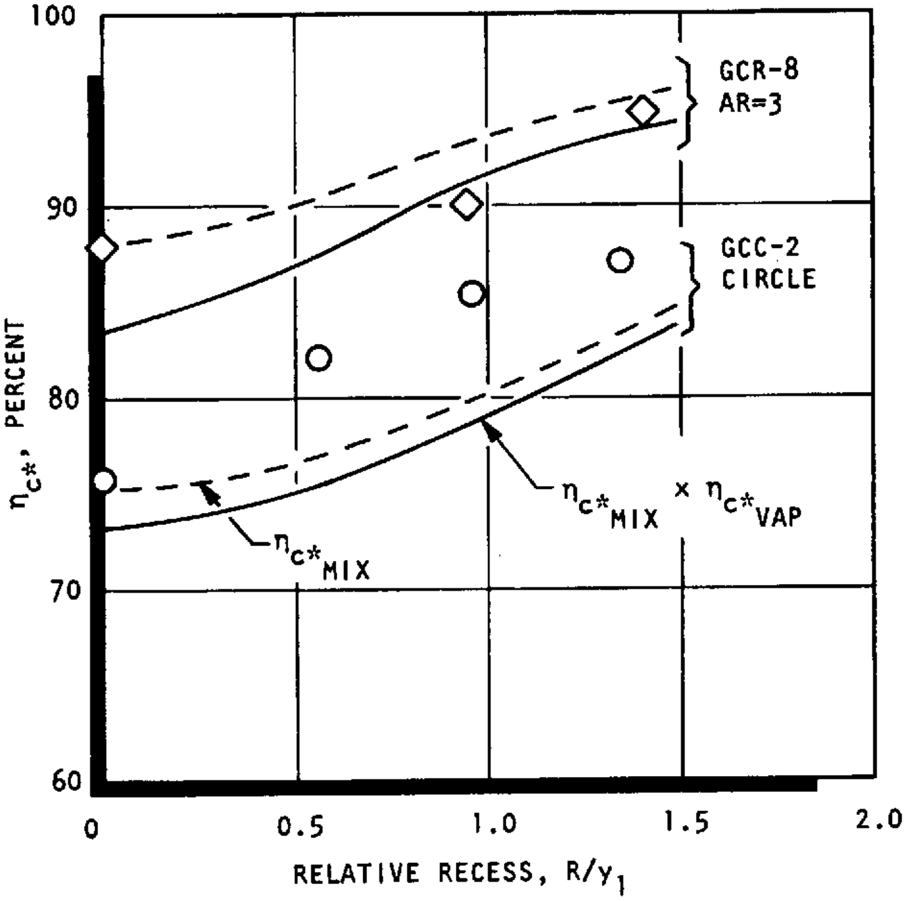

Figure 3-64. Comparison of Cold-Flow and Hot-Fire c* Efficiencies for the CCTE (GCC-2) and the RCTE (AR=3, GCR-8) Presented as a Function of Center-Post Recess

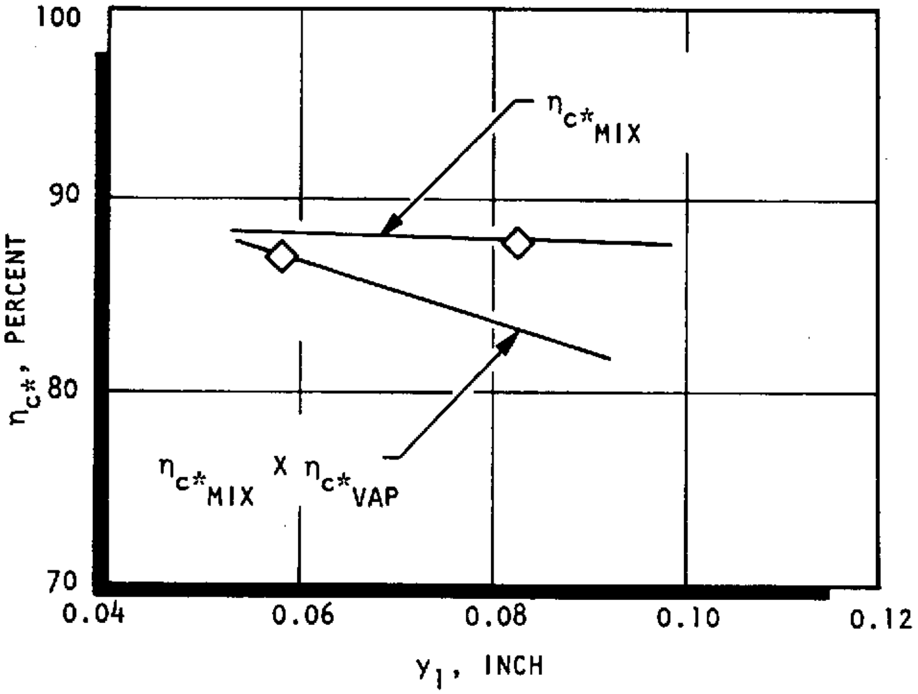

Figure 3-65. Comparison of Cold-Flow and Hot-Fire c* Efficiencies Showing the Effect of Element Size

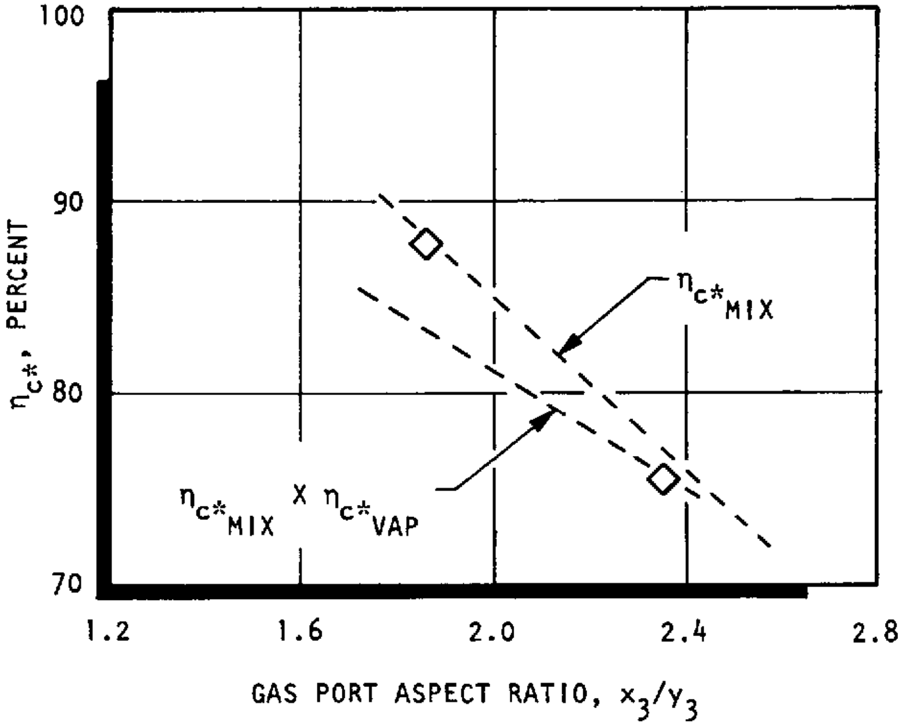

Figure 3-66. Comparison of Cold-Flow and Hot-Fire c* Efficiencies Showing the Effect of Gas Port Aspect Ratio, x_3/y_3

at the throat. These velocities are more than adequate to produce substantial secondary droplet breakup. Rocketdyne is presently initiating a program (Ref. 8) to investigate the effect of secondary atomization with G/L circular concentric tube injector elements.

No attempt was made to correct for the influence of secondary breakup in this report due to the fact that there were no experimental data available for G/L secondary breakup at the time of publication. Sufficient basic data have been presented in this document to allow corrections to be made at such time that these complementary data become available. However, the mixing limited c* results approximate the hot-fire data so well that, even with a more sophisticated droplet size correction, it appears that the values of $\eta_{c^*_{vap}}$ must approach 100 percent in most cases.

The nominal conditions--baseline element comparison presented in Fig. 3-63 shows that three of the four elements follow the mixing limited c* trend almost exactly. The highest aspect ratio element does not fall on this curve. One possible explanation for this deviation is the following. As the aspect ratio is increased, relative distortion of the flowfield increases (see Figure 3-29). The aspect ratio 6:1 element is the only element for which the liquid component significantly "breaks through" the gas component to the outer portions of the flowfield (see Fig. 3-29). This could mean that a significant portion of the liquid oxygen may have impinged upon the chamber wall forming a liquid film that would significantly interfere with both the mixing and vaporization mechanisms. This effect would only be associated with extremely small diameter chambers. In large chambers, the higher aspect ratio elements would be oriented with respect to the chamber wall in such a manner that the gas (fuel) component would be next to the wall, not the liquid component.

A comparison of cold-flow and hot-fire c* efficiencies for the baseline CCTE and the AR = 3 RCTE is presented in Fig. 3-64 as a function of center-post recess. Here again, the mixing limited cold-flow curves are more representative of the hot-fire performance. The level and increase of performance with recess are quite closely approximated in the case of the RCTE. The performance of the CCTE increased to a greater degree than was estimated from cold flow.

Two of the variations about aspect ratio 3:1 are compared on the basis of c* efficiency in Fig. 3-65 and 3-66. In Fig. 3-65, the effect of element size clearly demonstrates the "mixing limited" nature of the hot-fire results. Reference to Fig. 3-32 and 3-44a will recall that the cold-flow results showed no change in level of mixing with size. However, a significant reduction of primary dropsize was suggested as element size was reduced. The hot-fire results show no significant change in performance with size.

The effect of gas port aspect ratio is shown in Fig. 3-66. The trends suggested by the cold-flow results are drawn only to represent the change from one aspect ratio to the other, and are not representative of the true curves that should connect these two points (see Fig. 3-35). The change in level of performance, and indeed the actual value of performance, are represented by the mixing limited cold-flow results.

In summary, it may be concluded that the correlation between the mixing limited cold-flow c* efficiencies and the hot-fire performance values is excellent. It may be assumed, therefore, that the mixing trends suggested by the cold-flow data are truly representative of the processes encountered in hot fire and that the cold-flow design guidelines may be employed in the formulation of injector designs for hot fire.

Due to the mixing limited nature of the hot-fire results, the trends in concentric tube atomization characteristics have neither been confirmed nor denied. Other studies, however, have clearly confirmed the validity of the cold-flow atomization representation (Ref. 7).

4.0 LIQUID/LIQUID STUDIES

Although Phases III and IV of the subject program were primarily dedicated to the investigation of gas/liquid injector elements, two significant liquid/liquid injector studies were undertaken. These studies were conducted during Phase IV, and included a mixing and atomization study of unlike triplet elements with circular orifices and a mixing study of unlike-doublet elements with rectangular orifices having rounded entrances.

The triplet studies were conducted to gain a better appreciation of the mixing and atomization levels achievable with triplet elements. This was to serve as a basis for comparison of the performance of triplet injector elements with the performance of unlike-doublet elements.

The unlike-doublet studies were conducted to obtain mixing data for rectangular unlike-doublet elements having orifices with rounded inlets. These results complement the rectangular unlike-doublet mixing results of Phase I which were obtained with sharp entranced orifices.

No attempt has been made in this document to give the background for the liquid/liquid studies nor the interrelationship and correlation of these data with other liquid/liquid results obtained during Phase I. A detailed discussion of all of the liquid/liquid results is presented in the Comprehensive Program Summary Report (Ref. 3). A full appreciation for these data and their implication for injector design can only be obtained by reading Ref. 3. The results obtained during Phase IV are presented in this report for completeness of documentation, only. It was decided that a comprehensive discussion of the liquid/liquid results in both the Program Summary and this document would be unwarranted.

The mixing results for both the triplets and the unlike doublets are presented in terms of the "centerline momentum ratio," ϕ. (See Appendix H and Ref. 3 for background.) The physical basis for the parameter is identical for the different element types. However, the computation of this parameter is dependent upon the element type. The equations for the definition of the centerline momentum ratio are presented below for triplet and unlike-doublet elements:

- triplet

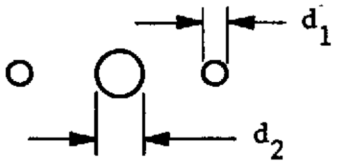

$$\phi \equiv \frac{\rho_1 V_1^2 d_1}{\rho_2 V_2^2 d_2/2} \quad . \; . \; . \; . \tag{4-1}$$

- rectangular unlike doublet

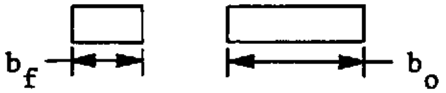

$$\phi \equiv \frac{\rho_f V_f^2 b_f}{\rho_o V_o^2 b_o} \tag{4-2}$$

In the case of the triplet elements, the outer orifices are denoted by the subscript 1 and the central orifice by the subscript 2. For the unlike doublets, the larger orifice (area) is denoted by the subscript o (oxidizer) and the smaller orifice by the subscript f (fuel). For this particular study, the widths of the o and the f orifices were the same.

4.1 TEST HARDWARE

The design specifications for circular triplet elements and the rectangular unlike-doublet elements are presented in Table 4-1. The nomenclature employed here are defined in Fig. 4-1.

TABLE 4-1. NONCIRCULAR ORIFICE PROGRAM--PHASE IV LIQUID/LIQUID STUDIES HARDWARE SUMMARY

Element Code No.	d_1 (in.)	d_2 (in.)	d_1/d_2	b_o (in.)	b_f (in.)	b_f/b_o	w (in.)	b_o/w AR_o	A_1 (in.^{2})	A_2 (in.^{2})	A_o (in.^{2})	A_f (in.^{2})	$(\frac{L}{D})_1$	$(\frac{L}{D})_2$	$(\frac{L}{D})_o$	$(\frac{L}{D})_f$	
UT-1	0.0300	0.0300	1.000	----	----	---	----	---	0.001414	0.000707	----	----	13.5	15.0	--	--	Triplets
UT-2	0.0300	0.0430	0.698	----	----	---	----	---	0.001414	0.00145	----	----	13.5	10.5	--	--	
UT-3	0.0300	0.0575	0.522	----	----	---	----	---	0.001414	0.00260	----	----	13.5	7.83	--	--	
UT-4	0.0200	0.0200	1.000	----	----	---	----	---	0.000628	0.000314	----	----	13.5	15.0	--	--	
UT-5*	0.0670	0.0670	1.000	----	----	---	----	---	0.00706	0.00353	----	----	50.0	50.0	--	--	
UD-1	----	----	---	0.0490	0.0490	1.000	0.0490	1.000	----	----	0.00240	0.00240	--	--	10	10	Unlike Doublets
UD-2	----	----	---	0.0930	0.0930	1.000	0.0258	3.600	----	----	0.00240	0.00240	--	--	↑	↑	
UD-3	----	----	---	0.1200	0.1200	1.000	0.0200	6.000	----	----	0.00240	0.00240	--	--			
UD-4	----	----	---	0.0327	0.0204	0.625	0.1175	0.278	----	----	0.00384	0.00240	--	--			
UD-5	----	----	---	0.0620	0.0388	0.625	0.0620	1.000	----	----	0.00384	0.00240	--	--			
UD-6	----	----	---	0.0736	0.0736	0.625	0.0327	3.600	----	----	0.00384	0.00240	--	--			
UD-7	----	----	---	0.1518	0.0949	0.625	0.0253	6.000	----	----	0.00384	0.00240	--	--			
UD-8	----	----	---	0.0783	0.0306	0.391	0.0783	1.000	----	----	0.00614	0.00240	--	--			
UD-9	----	----	---	0.1487	0.0581	0.391	0.0413	3.600	----	----	0.00614	0.00240	--	--	↓	↓	
UD-10	----	----	---	0.1920	0.0751	0.391	0.0320	6.000	----	----	0.00614	0.00240	--	--	10	10	

*Results for this element were obtained under NASA Contract No. NAS7-726 and are included here for completeness.

- TRIPLET ELEMENTS

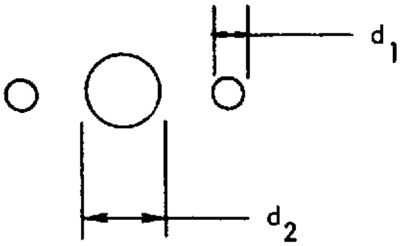

$$A_1 = 2\ (\pi d_1^2/4)$$

$$A_2 = \pi d_2^2/4$$

- UNLIKE DOUBLETS

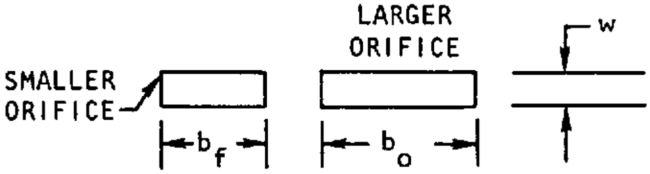

$$A_f = b_f w$$

$$A_o = b_o w$$

$$A_f/A_o = b_f/b_o$$

Figure 4-1. Triplet and Unlike-Doublet Nomenclature

The model hardware assemblies for the two element types were quite similar. A schematic cross section of a typical triplet model is presented in Fig. 4-2 and that for a typical unlike-doublet model in Fig. 4-3.

The triplet model configuration (Fig. 4-2) is typical for the two elements having a diameter ratio unity, $d_2/d_1 = 1.0$. The elements are labeled UT-1 and UT-4. The diameter ratios 1.433 (UT-2) and 1.917 (UT-3) were obtained by drilling out the central orifice of element UT-1 (see Table 4-1). Element UT-5 was not fabricated or tested under this contract. This element was tested under NASA contract NAS7-726, and is documented in Ref. 9. Atomization results from UT-5 were incorporated in the discussion of triplet atomization in this report for completeness. All triplet elements incorporated circular orifices with rounded inlets. The outer orifices were canted toward the central orifice with an included angle of 60 degrees.

The rectangular unlike doublets (Fig. 4-3) were configured with a face orifice spacing of 0.26 inch, rounded inlets, orifice length-to-hydraulic diameter ratio 10:1, and an included impingement angle of 60 degrees.

The model element injector body design was similar for the triplet and doublet elements. The only difference being the number of orifice inlet fittings--two for the doublets and three for the triplets. A typical injector body is shown in Fig. 4-4 (unlike doublet shown).

Face patterns for three unlike-doublet models (UD-1, UD-2, UD-3 - see Table 4-1) are shown in Fig. 4-5. The orifices for the rectangular unlike-doublet models were fabricated by the electrical discharge machining (EDM) method.

4.2 EXPERIMENTAL RESULTS

The liquid/liquid experimental results are presented in two parts; triplet results and unlike-doublet results. The triplet results discussion has a mixing and an atomization section, while the discussion of unlike-doublet results has only a mixing section.

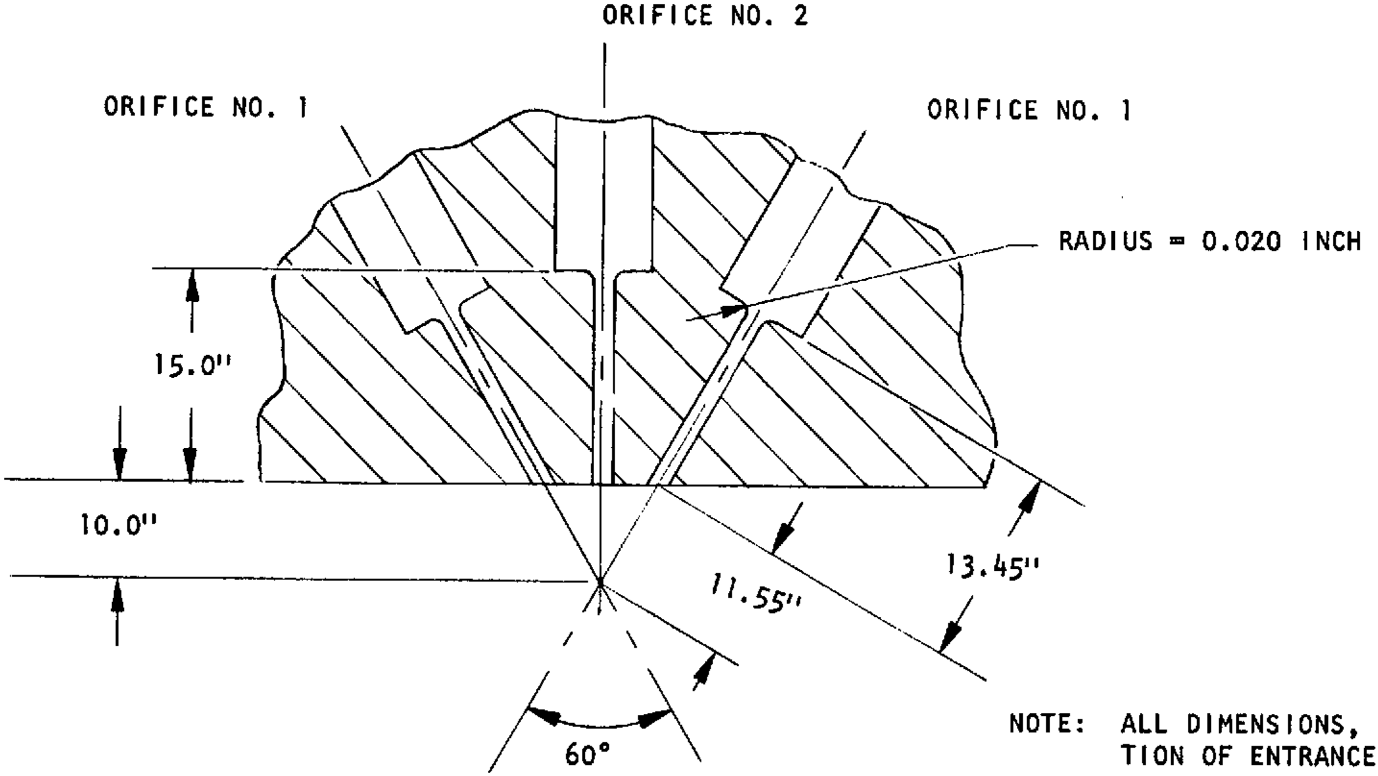

NOTE: ALL DIMENSIONS, WITH THE EXCEPTION OF ENTRANCE RADIUS, ARE GIVEN IN MULTIPLES OF ORIFICE DIAMETER

Figure 4-2. Schematic of Triplet Element Geometry (Typical for Models With $d_2/d_1 = 1$, see Table 4-1)

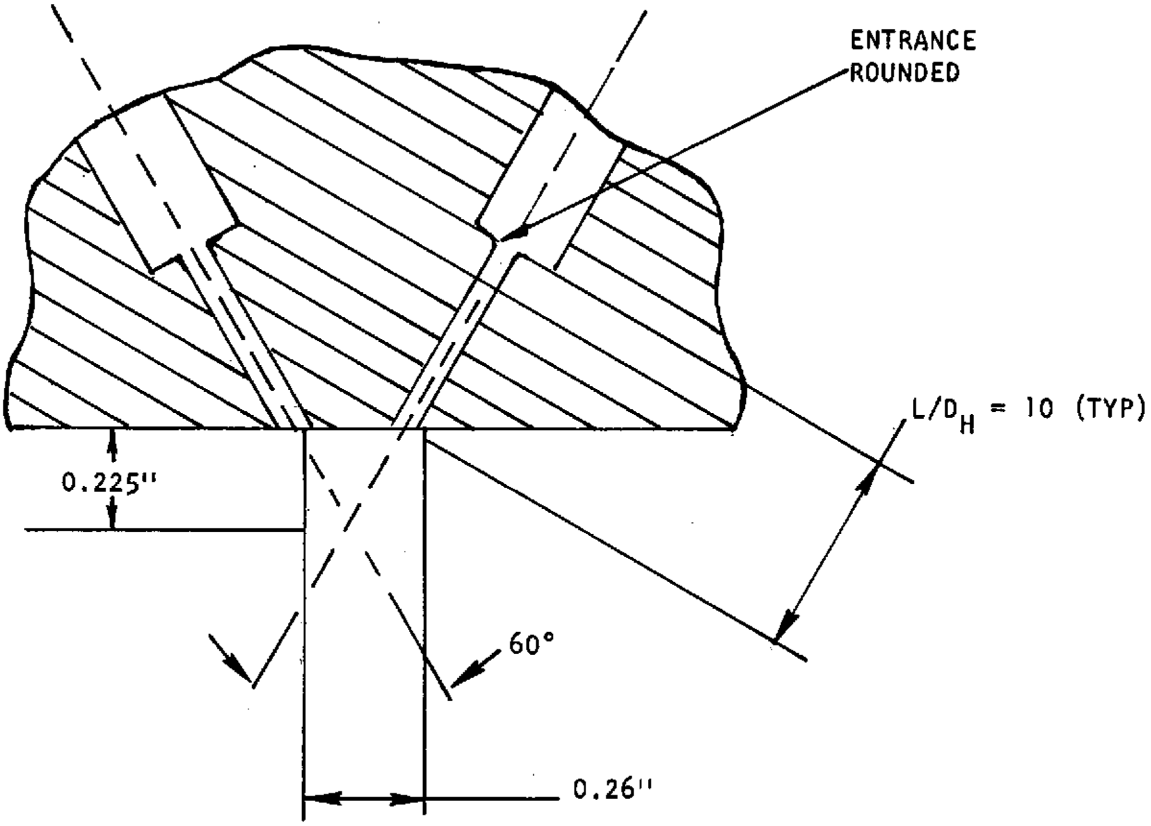

Figure 4-3. Rectangular Unlike-Doublet Model Format Typical for all 10 Models

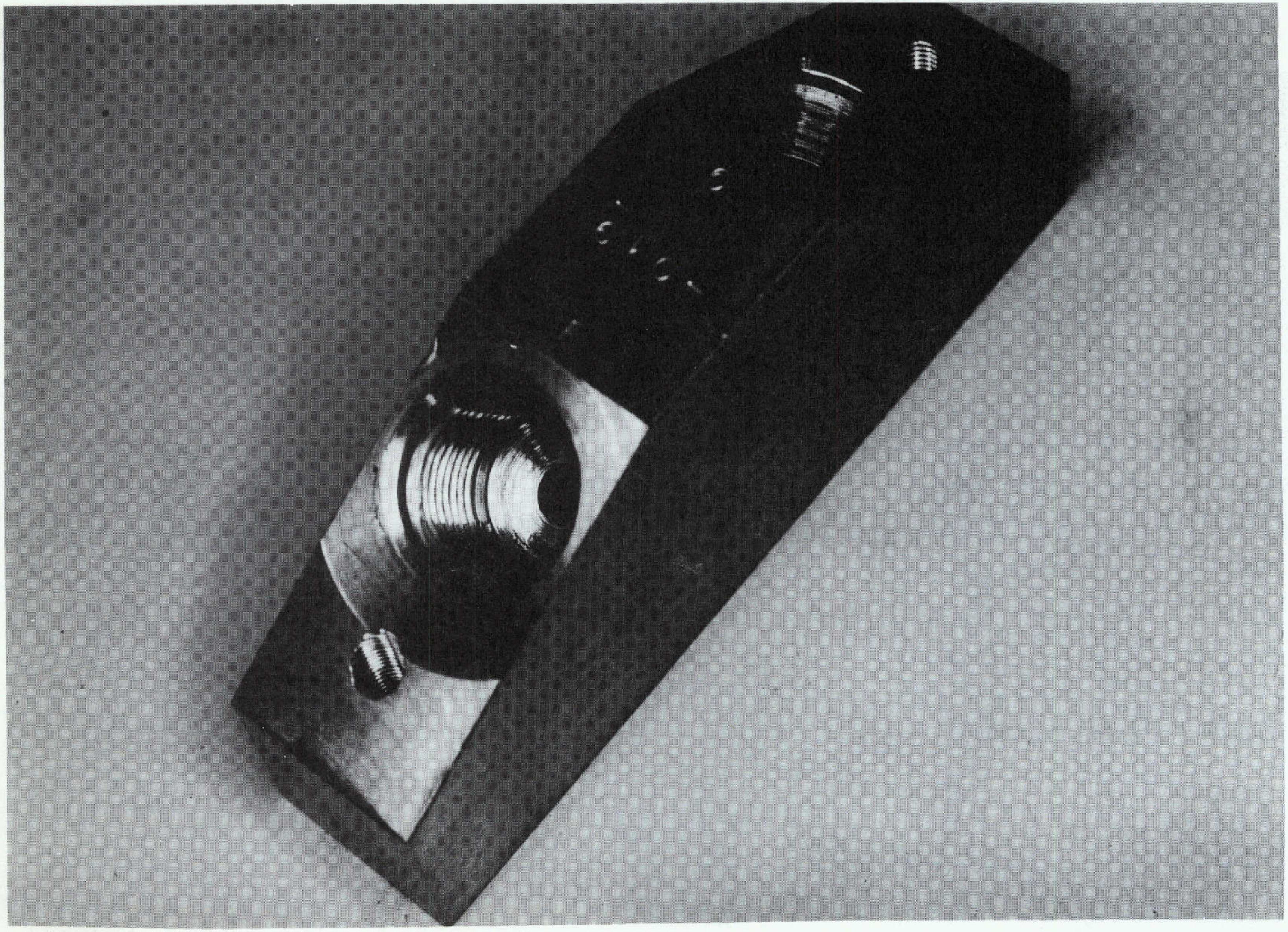

5AA34-5/21/73-S1A

Figure 4-4. Model Injector Element Body

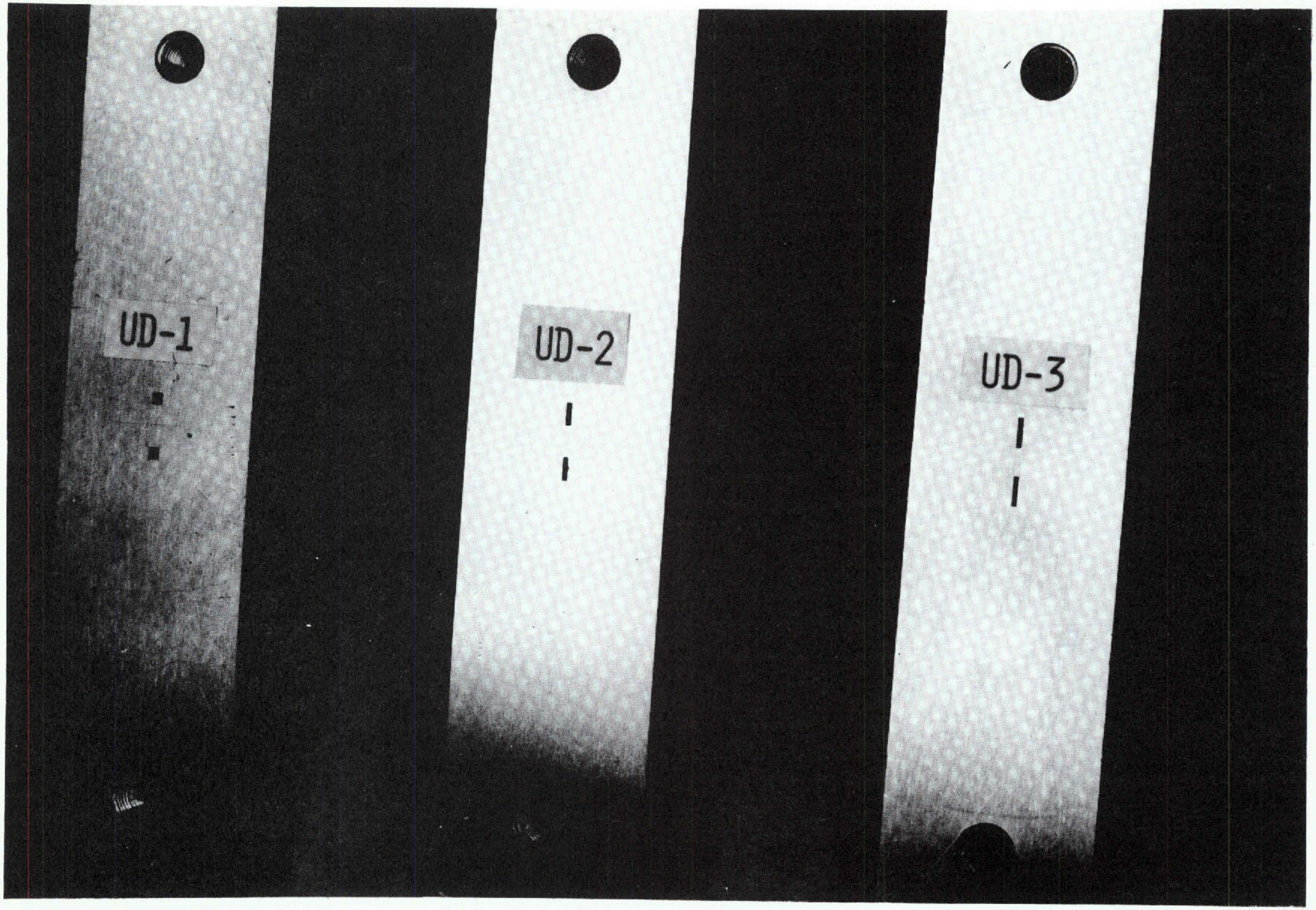

5AA34-5/21/73-S1B

Figure 4-5. Typical Rectangular Unlike Doublet Face Patterns

4.2.1 Triplet Results (Circular Orifices)

4.2.1.1 Triplet Mixing Results. The triplet mixture ratio uniformity results are presented in Table 4-2. Reference may be made to Table 4-1 for model configuration descriptions. The results are interpreted in terms of the mixture ratio uniformity parameter, E_m (see Appendix F), and the centerline momentum ratio, ϕ (see Eq. 4-2 and Appendix H).

The effects of orifice diameter, diameter ratio, and centerline momentum upon the mixing of the triplet elements tested are shown in Fig. 4-6. It is quite evident that the mixing level achieves a maximum value for values of ϕ near unity. Actually, for the elements having $d_1/d_2 = 1.00$, the optimum E_m was achieved for $\phi = 1.00$, while for the elements having $d_1/d_2 < 1.0$, the optimum values of E_m were obtained at a value of $\phi = 0.714$. This suggests that, for triplets, the specification of both ϕ and d_1/d_2 is required to ensure optimum mixing. That is to say:

$$E_{m_{opt}} = f(\phi, d_1/d_2) \tag{4-3}$$

The effect of orifice diameter is shown in Fig. 4-6a for $d_1/d_2 = 1.00$. The results were obtained with elements having 0.020- and 0.030-inch diameter orifices. It can be seen that at least for this magnitude of size variation, E_m is relatively insensitive to the orifice diameter, especially at the optimum point, $\phi = 1.0$.

The effect of diameter ratio is shown in Fig. 4-6b. Two effects are evident: (1) the value of ϕ for optimum mixing moves with diameter ratio, and (2) the level of mixing drops with decreasing diameter ratio, d_1/d_2. This latter influence is highlighted in the cross plot of the data presented in Fig. 4-6c. (The dashed curve in Fig. 4-6 represents a correction of the results to equal total flowrate--correction obtained from Fig. 4-7.) Here, the maximum values of E_m are plotted with respect to diameter ratio. (Note: Values of $d_1/d_2 < 1.0$ represent triplet elements with the central orifice larger than the outer orifices.)

TABLE 4-2. TRIPLET MIXING RESULTS

TEST NO.	ELEMENT CODE NO.	$\dot{W}_T$ (lbm/sec)	$\dot{W}_2$ (lbm/sec)	$\dot{W}_1$ (lbm/sec)	W_2/W_1	V_2	V_1	ϕ	Em,%
1	UT-1	0.0777	0.0348	0.0429	0.811	77.7	70.0	1.109	93.2
2			0.0273	0.0504	0.542	70.0	82.2	2.483	76.7
3			0.0427	0.0350	1.220	95.4	57.1	0.490	83.3
4			0.0502	0.0275	1.825	112.0	44.9	0.219	69.6
5	UT-1	0.0777	0.0206	0.0571	0.361	46.0	93.2	5.596	45.2
6	UT-4	0.0345	0.0154	0.0191	0.811	77.7	70.0	1.109	91.9
7			0.0121	0.0224	0.542	61.0	82.2	2.483	71.4
8	UT-4	0.0345	0.0190	0.0155	1.220	95.3	57.1	0.490	79.4
9	UT-2	0.108	0.0652	0.0428	1.522	71.0	69.9	0.917	86.5
10			0.0751	0.0329	2.283	81.8	53.7	0.408	81.2
11			0.0544	0.0536	1.015	59.2	87.5	2.062	54.6
12			0.0835	0.0245	3.416	91.0	39.9	0.182	58.8
13			0.0435	0.0645	0.675	47.4	105.0	4.660	28.0
14			0.0681	0.0399	1.709	74.2	65.1	0.727	90.4
15			0.0652	0.0428	1.522	71.0	69.9	0.917	88.4
16		0.144	0.0908	0.0532	1.709	98.9	86.8	0.727	87.3
18	UT-2	0.0811	0.0512	0.0299	1.709	55.7	48.9	0.727	90.7
19	UT-3	0.165	0.1251	0.0399	3.133	76.0	65.2	0.523	80.0
20			0.1187	0.0463	2.562	72.1	75.6	0.782	82.3
21			0.1213	0.0437	2.773	73.6	71.4	0.668	82.2
22			0.1136	0.0514	2.208	69.0	83.9	1.053	81.0
23			0.1301	0.0349	3.725	79.0	57.0	0.360	71.2
24	UT-3	0.165	0.1074	0.0576	1.863	65.2	94.1	1.479	78.6

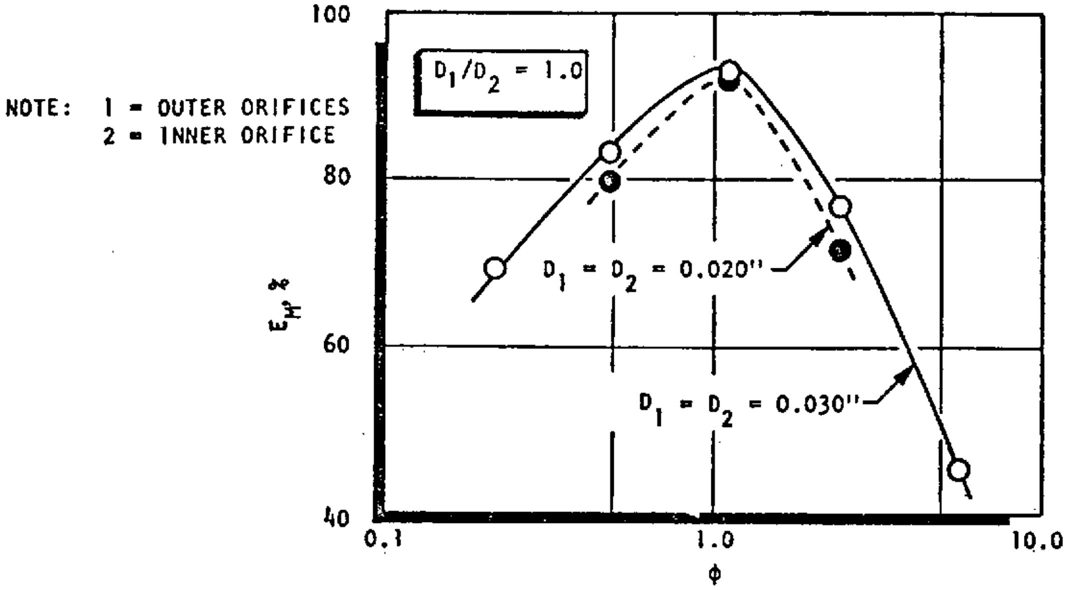

(a) EFFECT OF ORIFICE SIZE AS A FUNCTION OF ϕ

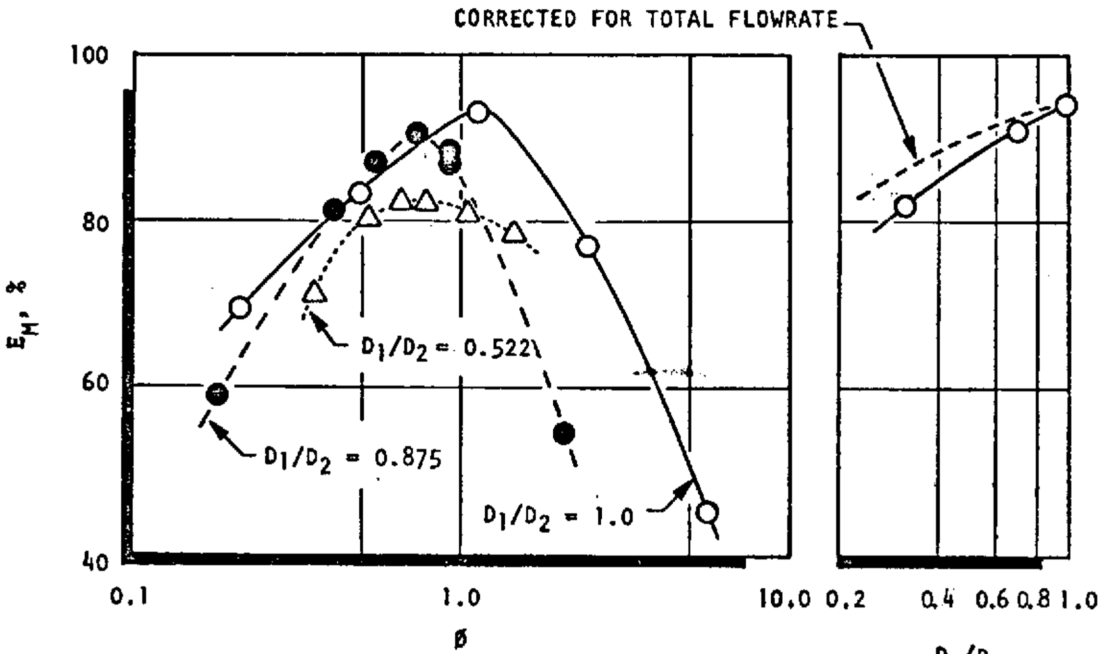

(b) EFFECT OF DIAMETER RATIO AS A FUNCTION OF ø

(c) EFFECT OF DIAMETER RATIO AT OPTIMUM MIXING LEVEL

Figure 4-6. Effect of Oxidizer Diameter and Diameter Ratio Upon Unlike Triplet Mixing, Presented as a Function of ϕ

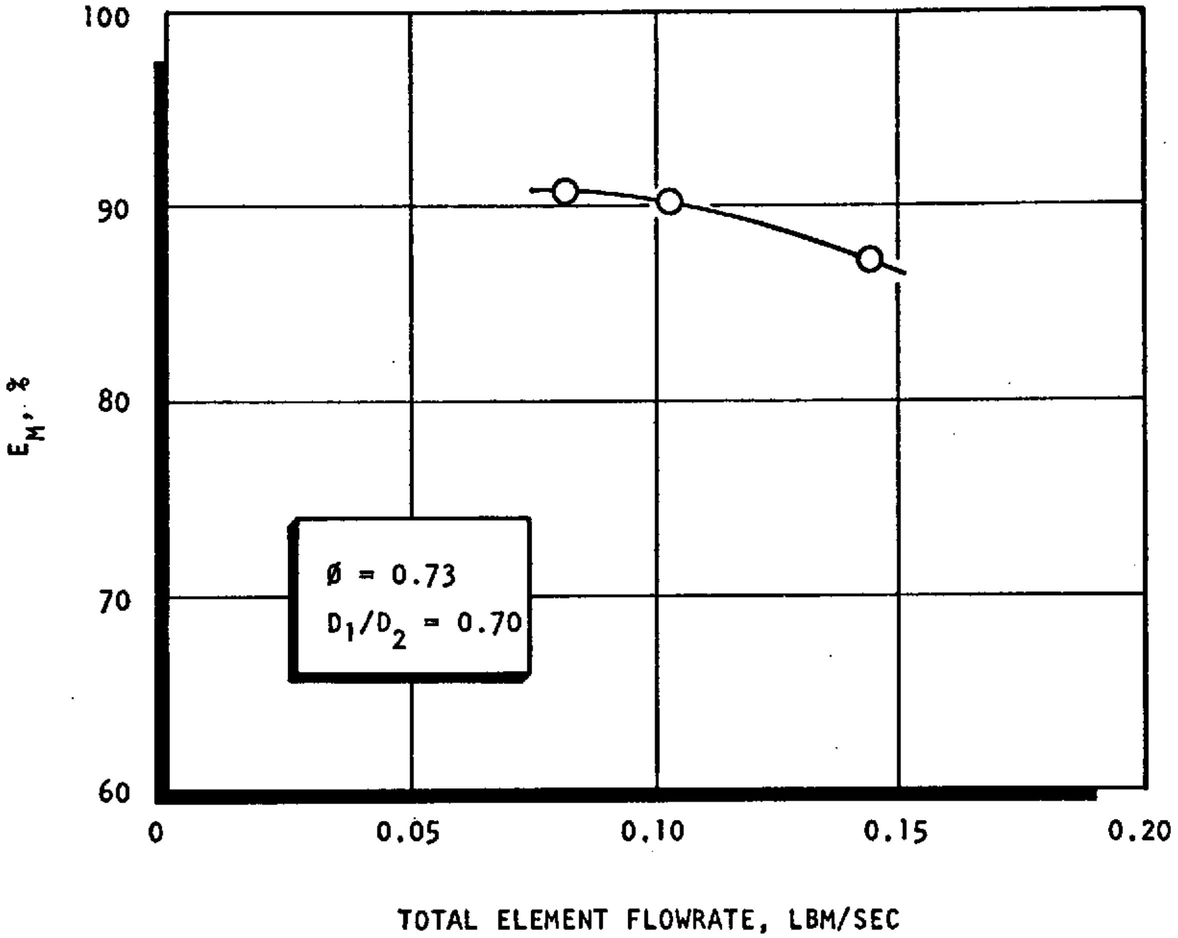

Figure 4-7. Effect of Total Flowrate Level Upon Unlike Triplet Mixing

The effect of total element flowrate upon triplet mixture ratio uniformity is shown in Fig. 4-7. A 4 to 5 percentage point reduction in E_m was encountered for a factor of two increase in total flow.

4.2.1.2 Triplet Atomization Results. The results of the triplet atomization experiments are summarized in Table 4-3 for the outer orifices and Table 4-4 for the central orifices. All of the atomization tests were conducted at the value of centerline momentum ratio, ϕ, which was found to yield optimum mixing for each individual element.

Results in Tables 4-3 and 4-4 are presented in terms of the mass median droplet diameter, $\overline{D}$, and the relative droplet diameter, $\overline{D}/D_j$ (droplet diameter to orifice diameter ratio).

A detailed analysis of these results suggested that only the dropsize data obtained for wax jet Reynolds numbers less than 10^4 (laminar jets) could be correlated. The results for Reynolds numbers above this value indicated a great deal of scatter due to the fact that the jets were in transition from laminar to turbulent flow (Ref. 3 and 4).

The best correlation of the laminar jet atomization data was found to be of the form:

$$\overline{D}/D_j = f\ (W_e,\ L/D,\ R_e) \tag{4-4}$$

where

W_e = Weber number = $\rho V_j^2 D_j/\sigma$
R_e = Reynolds number = $\rho V_j D_j/\mu$
L/D = orifice length to diameter ratio
V_j = wax jet velocity
ρ = wax density
μ = wax viscosity
σ = wax surface tension

TABLE 4-3. TRIPLET ATOMIZATION RESULTS, WAX IN OUTER ORIFICES, NO. 1

TEST NO.	ELEMENT CODE NO.	$\dot{W}_T$ (lbm/sec)	$\dot{W}_2$ (lbm/sec)	$\dot{W}_1$ (lbm/sec)	$\dot{W}_2/\dot{W}_1$	WAX REYNOLDS NO.	WAX VELOCITY (ft/sec)	$\bar{D}, \mu$	$\bar{D}/D_j$
1	UT-4	0.01080	0.00465	0.00615	0.756	1175	30	640	1.260
2		0.01794	0.00774	0.0102	0.759	1959	50	341	0.671
3		0.0360	0.0155	0.0205	0.756	3917	100	205	0.404
4		0.0541	0.0233	0.0308	0.756	5876	150	157	0.309
5	UT-4	0.0720	0.0310	0.0410	0.756	7834	200	123	0.242
6	UT-1	0.0243	0.0105	0.0138	0.761	1763	30	620	0.814
7		0.0405	0.0174	0.0231	0.753	2938	50	428	0.562
8		0.0810	0.0349	0.0461	0.757	5876	100	240	0.315
9		0.1215	0.0523	0.0692	0.756	8813	150	136	0.178
10	UT-1	0.1621	0.0698	0.0923	0.756	11000	187	148	0.194
29	UT-2	0.0610	0.0379	0.0231	1.641	2938	50	515	0.676
30		0.1218	0.0757	0.0461	1.642	5876	100	291	0.382
31		0.1829	0.1137	0.0692	1.643	8813	150	197	0.259
32		0.2438	0.1515	0.0923	1.641	11752	200	175	0.230
33	UT-2	0.3657	0.2273	0.1384	1.642	17628	300	175	0.230
34	UT-3	0.0819	0.0588	0.0231	2.545	2938	50	490	0.643
35		0.1638	0.1177	0.0461	2.553	5876	100	200	0.263
36	UT-3	0.2457	0.1765	0.0692	2.551	8813	150	200	0.263
DATA FROM NAS7-726 (Ref. 9)									
185	UT-5	0.1081	0.0457	0.0624	0.732	3504	27	583	0.343
186		0.1636	0.0700	0.0936	0.748	5250	40	470	0.276
187		0.2186	0.0943	0.1243	0.759	6969	53	412	0.242
188		0.3269	0.1408	0.1861	0.757	10434	80	307	0.180
189		0.4292	0.1853	0.2439	0.760	13689	104	266	0.156
190		0.5603	0.2393	0.3210	0.745	18007	137	190	0.112
191	UT-5	0.6123	0.2583	0.3540	0.730	19857	151	195	0.115

TABLE 4-4. TRIPLET ATOMIZATION RESULTS, WAX IN CENTRAL ORIFICE, NO. 2

TEST NO.	ELEMENT CODE NO.	$\dot{W}_T$ (lbm/sec)	$\dot{W}_2$ (lbm/sec)	$\dot{W}_1$ (lbm/sec)	$\dot{W}_2/\dot{W}_1$	WAX REYNOLDS NO.	WAX VELOCITY (ft/sec)	$\bar{D}$, μ	$\bar{D}/D_j$
12	UT-1	0.01852	0.00692	0.0116	0.597	1763	30	820	1.076
13		0.0309	0.0115	0.0194	0.593	2938	50	405	0.532
14		0.0618	0.0231	0.0387	0.597	5876	100	208	0.273
15		0.0927	0.0346	0.0581	0.596	8813	150	155	0.203
16		0.1235	0.0461	0.0774	0.596	11751	200	108	0.142
17	UT-1	0.1853	0.0692	0.1161	0.596	17627	300	96	0.126
18	UT-4	0.00825	0.00308	0.00517	0.596	1175	30	840	1.654
19		0.01373	0.00513	0.00860	0.597	1959	50	355	0.699
20		0.0275	0.0103	0.0172	0.599	3917	100	172	0.339
21		0.0412	0.0154	0.0258	0.597	5876	150	140	0.276
22		0.0549	0.0205	0.0344	0.596	7834	200	114	0.224
23	UT-4	0.0824	0.0308	0.0516	0.597	11751	300	112	0.221
24	UT-2	0.0433	0.0241	0.0192	1.255	4212	50	611	0.559
25		0.0864	0.0481	0.0383	1.256	8422	100	307	0.281
26		0.1297	0.0722	0.0575	1.256	12633	150	190	0.174
27		0.1728	0.0962	0.0766	1.256	16843	200	154	0.141
28	UT-2	0.2593	0.1443	0.1150	1.255	25265	300	149	0.136
39	UT-3	0.0643	0.0424	0.0219	1.936	5631	50	800	0.548
40		0.1286	0.0848	0.0438	1.936	11262	100	372	0.255
41		0.1929	0.1271	0.0658	1.932	16892	150	209	0.143
42		0.2572	0.1695	0.0877	1.933	22523	200	220	0.151
43	UT-3	0.3859	0.2543	0.1316	1.932	33777	300	173	0.119
DATA FROM NAS7-726 (Ref. 9)									
192	UT-5	0.0843	0.0315	0.0528	0.597	3530	27	606	0.356
193		0.1258	0.0465	0.0793	0.586	5223	40	484	0.284
194		0.1650	0.0629	0.1021	0.616	7060	54	425	0.250
195		0.2477	0.0935	0.1542	0.606	10498	80	333	0.196
196		0.3294	0.1201	0.2093	0.574	13477	103	297	0.175
197	UT-5	0.4155	0.1572	0.2583	0.609	17636	134	238	0.140

(It must be noted that the values of ρ, μ, and σ were not varied and thus the general specification of Weber number and Reynolds number as independent parameters is speculative.)

Equation 4-4 states that dropsize for triplet elements in laminar flow is a function of Weber number and orifice L/D. The Weber number describes the dynamic aspects of the atomization process while the L/D and Reynolds number describe the degree of jet velocity profile development for laminar flow in orifices with rounded entrances.

Atomization results are presented in Fig. 4-8 for the outer orifices and in Fig. 4-9 for the central orifices. The dropsizes are presented in terms of Weber number and L/D only, while the effect of Reynolds number has been neglected. The following argument is presented to show that the Reynolds number effect is truly second order, at least over the range of variables tested.

Due to the fact that the physical properties of the fluids (ρ, μ, σ) were not varied, the Reynolds number, Weber number, and jet diameter are related, uniquely:

$$R_e = \text{constant} \times \sqrt{W_e \times D_j} \qquad (4\text{-}5)$$

Thus, for a constant jet diameter, the independent effect of Reynolds number and Weber number cannot be determined. However, the results shown in Fig. 4-8 and 4-9 suggest that as long as the orifice L/D is equivalent, the data obtained with different jet diameters are well represented by a single curve. This strongly suggests that the independent effect of Reynolds number is, indeed, second order.

It must be emphasized that these representations do not imply the independent influence of fluid density, viscosity, or surface tension. Also, no account is made of the dynamic condition or physical properties of the jets opposing the wax jets. The data were obtained with hot water as a propellant simulant injected in those orifices opposing the wax (see Appendix D).

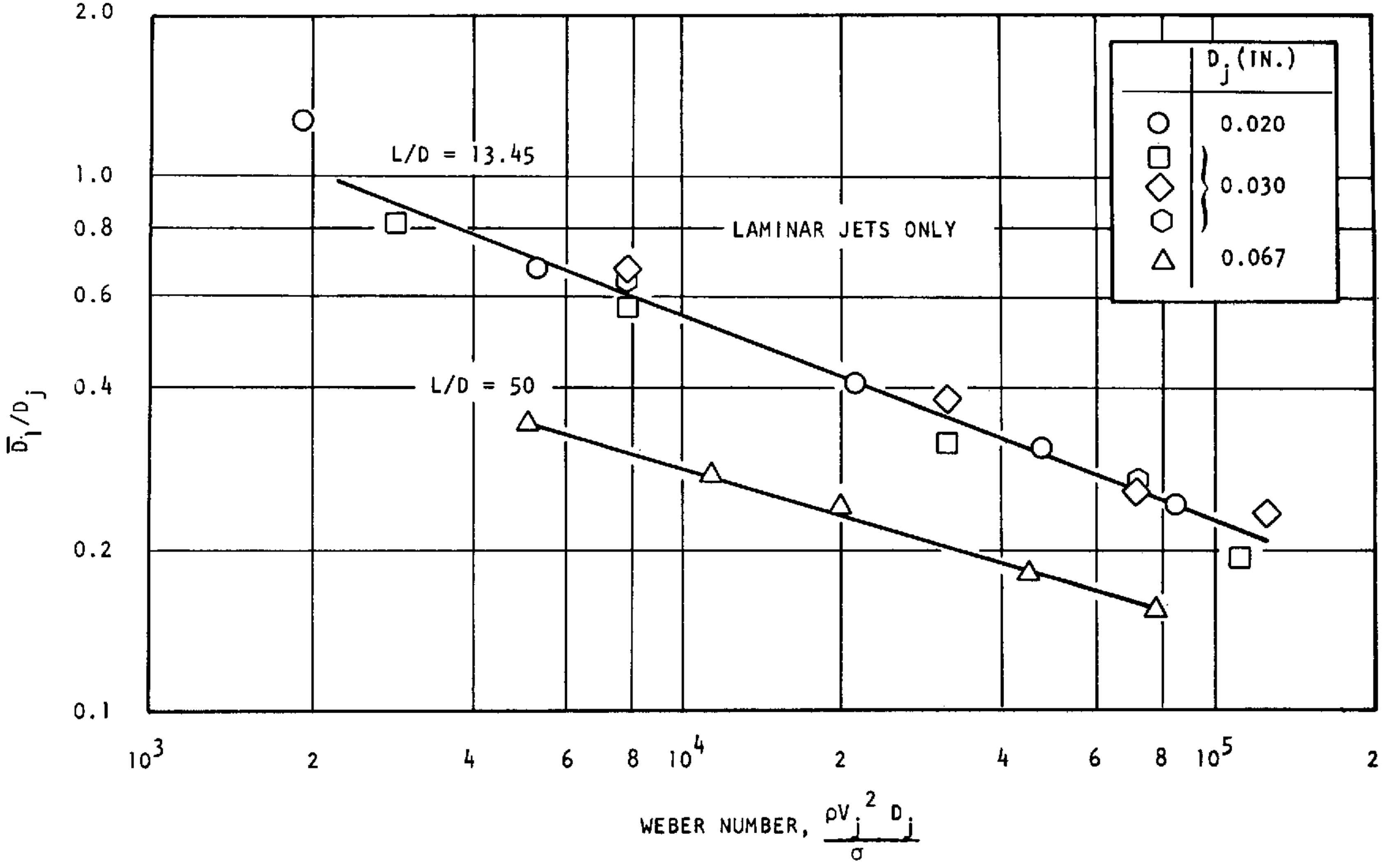

Figure 4-8. Triplet Atomization Results--Outer Orifice

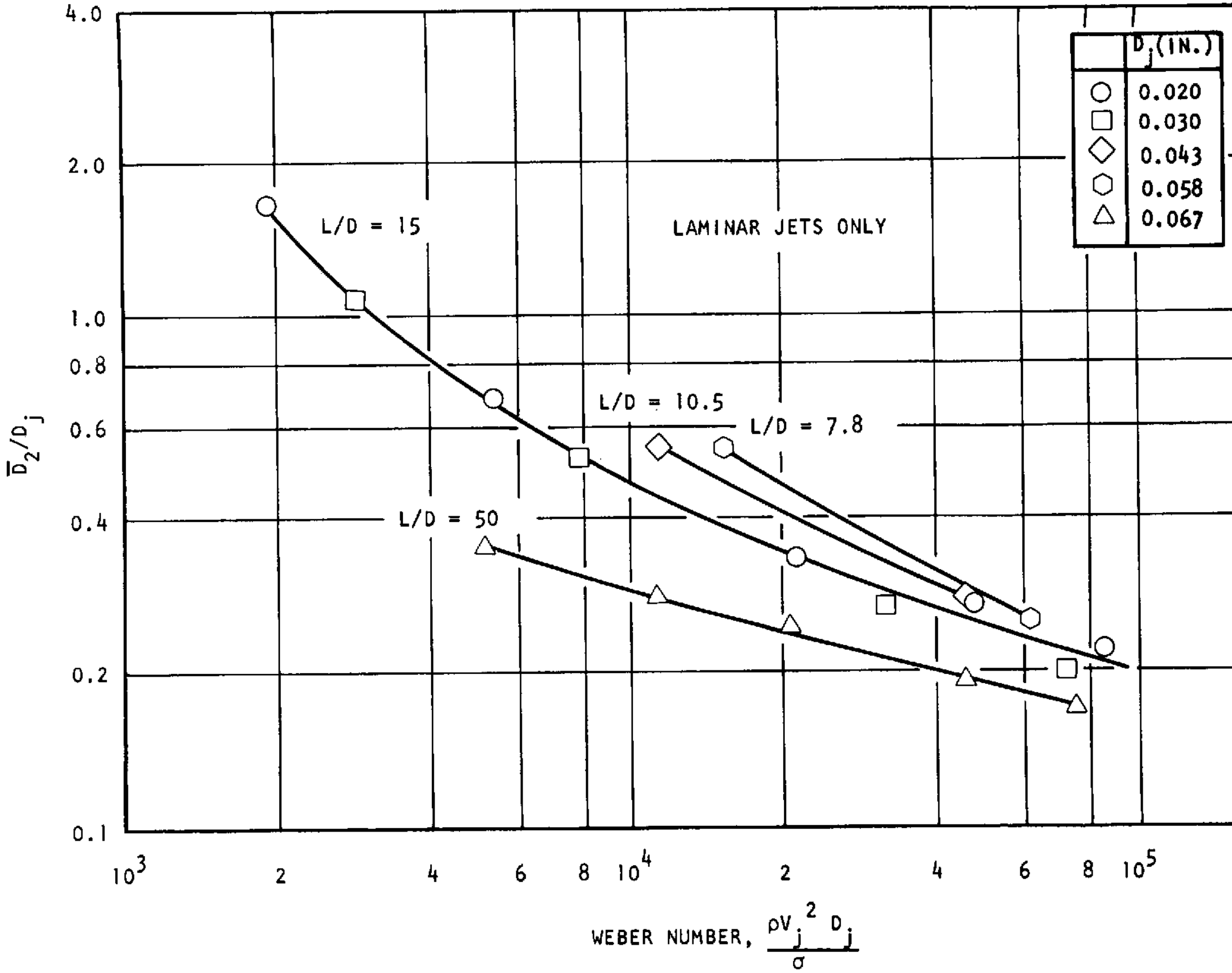
4.0
2.0
1.0
0.8
0.6
0.4
0.2
0.1
$\bar{D}_2/D_j$
10^3
2
4
6
8
10^4
2
4
6
8
10^5
2
WEBER NUMBER, $\frac{\rho V_j^2 D_j}{\sigma}$
L/D = 15
L/D = 10.5
L/D = 7.8
L/D = 50
LAMINAR JETS ONLY
D_j (IN.)
○ 0.020
□ 0.030
◇ 0.043
⬡ 0.058
△ 0.067

An interesting cross correlation of the data is presented in Fig. 4-10, wherein $\overline{D}/D_j$ is plotted as a function of the product of Weber number and orifice L/D for both central and outer jets. A single curve is representative of the data for both No. 1 and No. 2 orifices in the range $10^5 < (W_e)\ (L/D) < 3 \times 10^6$. For values of $(W_e)\ (L/D)$ below 10^5, the curves diverge. An analytical expression of the curve in the range 10^5 to 3×10^6 is:

$$\overline{D} = 2.15 \times 10^5\ V_j^{-0.77}\ (L/D)^{-0.39}\ D_j^{0.62} \tag{4-6}$$

where

V_j = ft/sec
D_j = inch
$\overline{D}$ = microns

A comparison of the atomization characteristics (laminar wax jets) of an unlike-triplet element, an unlike-doublet element and a like-doublet element is presented in Fig. 4-11. The comparison is made for the fuel orifice of each element. The orifice diameter is 0.067 inch and the L/D = 50. Dropsize values for all elements were obtained from correlations presented by Zajac (Ref. 9) for laminar jets. The diameter ratios for the triplet, the like doublet, and the unlike doublet are unity.

The like and unlike doublets produce approximately the same dropsize while the triplet produces somewhat larger sizes.

4.2.2 Unlike-Doublet Results (Rectangular Orifices)

The objective of the unlike-doublet experiments conducted during Phase IV was to obtain critical design data for rectangular doublets with rounded entrances to complement the data formerly obtained during Phase I for doublets with sharp entrances. Primary experimental effort was centered about the parametric investigation of the effect of element area ratio and orifice aspect ratio upon mixing.

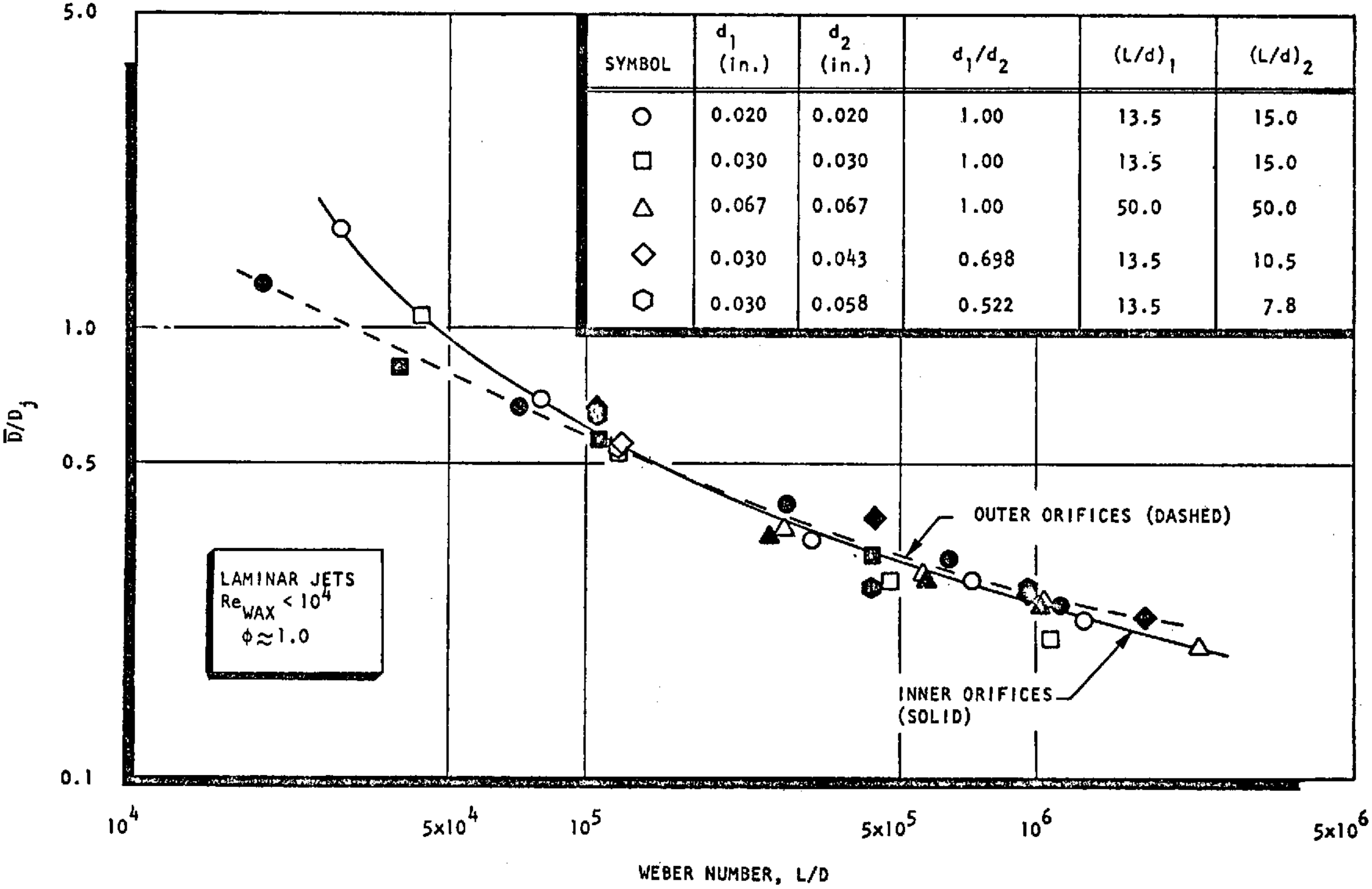

SYMBOL	d_1 (in.)	d_2 (in.)	d_1/d_2	$(L/d)_1$	$(L/d)_2$
○	0.020	0.020	1.00	13.5	15.0
□	0.030	0.030	1.00	13.5	15.0
△	0.067	0.067	1.00	50.0	50.0
◇	0.030	0.043	0.698	13.5	10.5
⬡	0.030	0.058	0.522	13.5	7.8

Figure 4-10. Correlation of Relative Droplet Diameter With Weber No. and Orifice L/D for Unlike Triplets (Both Central and Outer Orifice Results Shown)

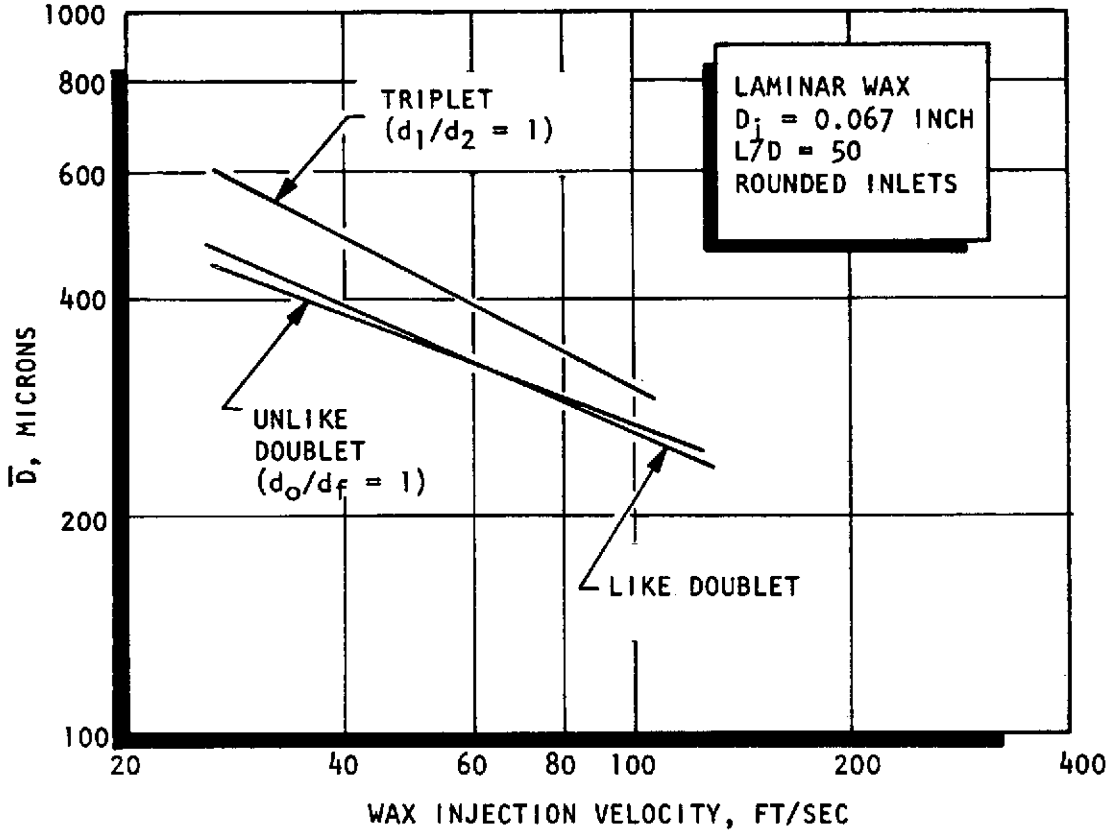

Figure 4-11. Comparison of Wax Droplet Diameters for a Triplet, an Unlike Doublet, and a Like Doublet (Laminar Wax)

The geometrical and operational parameters that were investigated are presented in Fig. 4-12.

Centerline momentum ratio, ϕ (see Appendix H), has been shown to be the most critical correlating parameter for unlike-doublet mixing. The mixing level, E_m, of single elements, optimizes normally at a value of $\phi \approx 1.0$. As a matter of fact, the expression $\phi = 1$ has, for years, served as a design criterion for unlike-doublet injectors. When a propellant combination is specified (i.e., ρ_o/ρ_f) at a given mixture ratio and the condition $w_o/w_f = 1$ is imposed, the value of b_o/b_f is defined for the case $\phi = 1$. Thus, the only independent variable remaining is the aspect ratio of one of the orifices (e.g., $b_o/w_o = AR_o$). The aspect ratio of the other orifice is functionally related to AR_o and is not an independent parameter.

The restriction of equal facing widths, $w_o/w_f = 1$ (Fig. 4-12) was imposed to limit the scope of the investigation. A logical extension of the work reported in this document would be the investigation of elements for which $w_o/w_f \neq 1$.

The test matrix that was selected for the unlike-doublet experiments is shown in qualitative form in Fig. 4-13. Three values of area ratio A_o/A_f were selected (1.00, 0.625, and 0.391). (Note: due to the restriction $w_o = w_f$, $A_o/A_f = b_o/b_f$.) For each value of area ratio, b_o/b_f, at least three values of oxidizer orifice aspect ratio b_o/w_o were selected (four values were selected for $b_o/b_f = 0.625$). The element design specifications are summarized in Table 4-1.

4.2.2.1 Unlike-Doublet Mixing Results. The rectangular unlike-doublet, cold-flow mixing data are presented in Table 4-5. The results are interpreted in terms of the mixture ratio uniformity parameter, E_m (see Appendix F), as a function of the centerline momentum ratio parameter, ϕ (see Appendix H).

The basic mixing characteristics of the 10 unlike-doublet elements are presented in Fig. 4-14 through 4-16. Each figure is reserved for results obtained at one value of area ratio, b_f/b_o. Within each figure, the data for the various oxidizer

Element Nomenclature

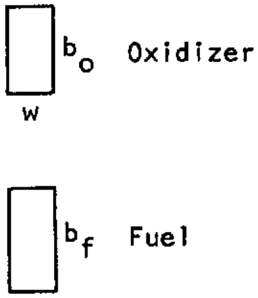

Basic Definitions and Ground Rules

$w_o = w_f = w$

$AR_o = b_o/w$

$AR_f = b_f/w$

Area Ratio $= A_f/A_o = b_f/b_o$

$\rho_o/\rho_f = \text{const} = 1.44$

θ = impingement angle = 60 degrees

Correlating Parameter

Centerline Momentum Ratio

$$\phi = \frac{\rho_f \; b_f \; V_f^{\,2}}{\rho_o \; b_o \; V_o^{\,2}} = \frac{1}{MR^2} \; \frac{\rho_o}{\rho_f} \; \frac{b_o}{b_f}$$

where

$MR = \dot{w}_o/\dot{w}_f$

Figure 4-12. Definition of Nomenclature for Unlike-Doublet Cold-Flow Testing

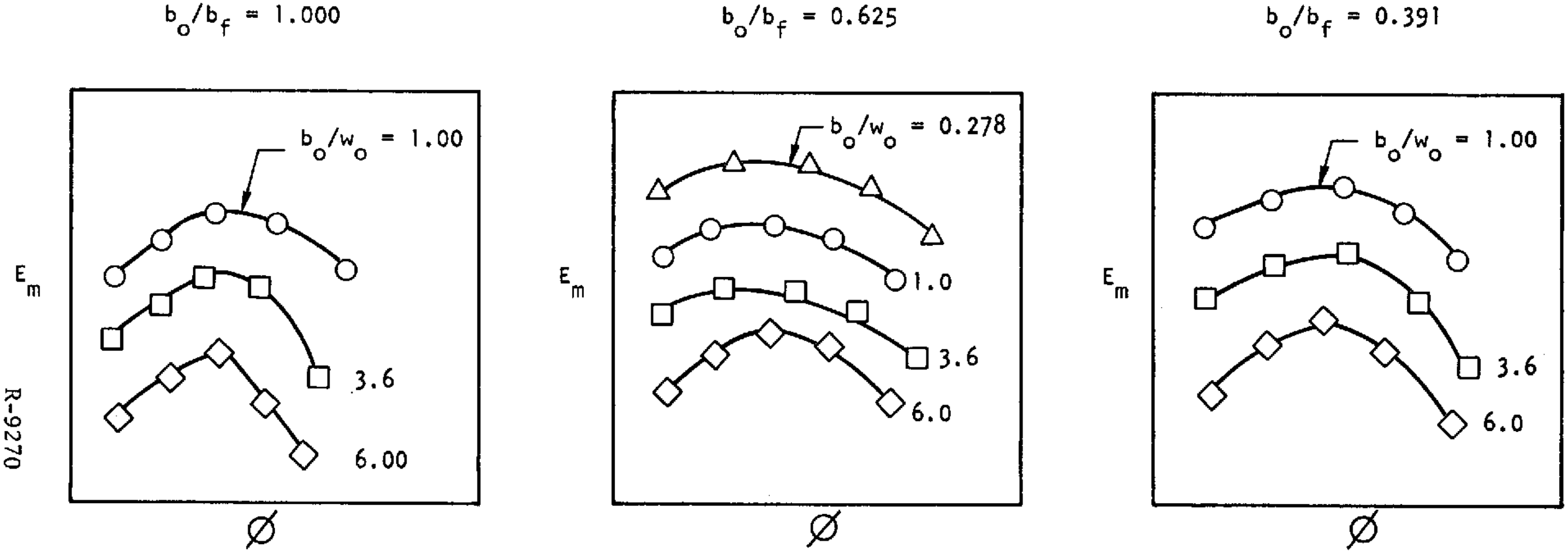

Figure 4-13. Unlike-Doublet Test Matrix

TABLE 4-5. RECTANGULAR UNLIKE-DOUBLET MIXING RESULTS, ROUNDED ENTRANCES

TEST NO.	ELEMENT CODE NO.	$\dot{W}_T$ (lbm/sec)	$\dot{W}_o$ (lbm/sec)	$\dot{W}_f$ (lbm/sec)	$\dot{W}_o/\dot{W}_f$	V_o (ft/sec)	V_f (ft/sec)	ϕ	Em,%
69	UD-1	0.180	0.094	0.086	1.09	61.8	82.7	1.25	78.3
5			0.068	0.112	0.607	44.7	107.0	3.99	60.6
4			0.083	0.097	0.856	54.6	93.3	2.01	78.5
3			0.099	0.081	1.22	65.1	77.9	0.984	78.5
2			0.118	0.062	1.90	77.6	59.6	0.406	70.6
1	UD-1	0.180	0.131	0.049	2.67	86.2	47.1	0.206	61.2
58	UD-2	0.180	0.083	0.097	0.856	54.6	93.3	2.00	75.0
57			0.091	0.089	1.02	59.9	85.6	1.41	85.7
56			0.099	0.081	1.22	65.1	77.9	1.00	83.4
55			0.106	0.074	1.43	69.7	71.2	0.707	75.0
54	UD-2	0.180	0.114	0.066	1.73	75.0	63.5	0.500	61.1
73	UD-3	0.180	0.099	0.081	1.22	65.1	77.9	1.00	86.8
72			0.101	0.079	1.28	66.4	76.0	0.900	84.4
63			0.083	0.097	0.856	54.6	93.3	2.00	72.4
62			0.091	0.089	1.02	59.9	85.6	1.41	84.2
61			0.099	0.081	1.22	65.1	77.9	1.00	88.8
60			0.106	0.074	1.43	69.7	71.2	0.707	80.0
59	UD-3	0.180	0.114	0.066	1.73	75.0	63.5	0.500	68.8
68	UD-4	0.180	0.111	0.069	1.61	45.6	66.3	0.900	79.0
67			0.109	0.071	1.54	44.8	68.3	1.00	79.6
66			0.128	0.052	2.46	52.6	50.0	0.380	77.1
65			0.105	0.075	1.40	43.2	72.1	1.18	75.8
64			0.120	0.060	2.00	49.3	57.7	0.580	74.0
10			0.078	0.102	0.765	32.1	98.1	4.14	79.8
9			0.094	0.086	1.09	38.7	82.7	1.93	77.1
8			0.110	0.070	1.57	45.2	67.3	0.934	78.9
7			0.130	0.050	2.60	53.5	48.1	0.341	68.2
6	UD-4	0.180	0.142	0.038	3.74	57.6	36.5	0.164	69.7
27	UD-5	0.180	0.094	0.086	1.09	38.7	82.7	1.97	80.4
26		0.183	0.104	0.079	1.32	42.8	76.0	1.36	85.0
25		0.180	0.109	0.071	1.54	44.8	68.3	0.998	85.8
24			0.116	0.064	1.81	47.7	61.5	0.716	80.2
23	UD-5	0.180	0.123	0.057	2.16	50.6	54.8	0.505	67.8

TABLE 4-5. (Continued)

TEST NO.	ELEMENT CODE NO.	$\dot{W}_T$ (lbm/sec)	$\dot{W}_o$ (lbm/sec)	$\dot{W}_f$ (lbm/sec)	$\dot{W}_o/\dot{W}_f$	V_o (ft/sec)	V_f (ft/sec)	ϕ	Em, %
22	UD-6	0.180	0.117	0.063	1.86	48.1	60.6	0.670	68.4
21			0.102	0.078	1.31	41.9	75.0	1.37	82.6
20			0.094	0.086	1.09	38.7	82.7	1.97	70.6
19			0.130	0.050	2.60	53.5	48.1	0.348	48.6
18			0.110	0.070	1.57	45.2	67.3	0.950	86.6
17			0.110	0.070	1.57	45.2	67.3	0.950	87.9
16			0.110	0.070	1.57	45.2	67.3	0.950	79.1
15			0.078	0.102	0.765	32.1	98.1	4.02	42.8
14			0.094	0.086	1.09	38.7	82.7	1.97	61.2
13			0.110	0.070	1.57	45.2	67.3	0.953	86.2
12			0.130	0.050	2.60	53.5	48.1	0.348	53.0
11	UD-6	0.180	0.142	0.038	3.74	58.4	36.5	0.169	36.0
38	UD-7	0.180	0.109	0.071	1.54	44.8	68.3	1.00	82.9
37			0.111	0.069	1.61	45.6	66.3	0.900	86.1
36			0.114	0.066	1.73	46.9	63.5	0.800	85.2
35			0.126	0.054	2.33	51.8	51.9	0.432	63.9
34			0.130	0.050	2.60	53.5	48.1	0.348	55.9
33			0.134	0.046	2.91	55.1	44.2	0.277	50.0
32			0.094	0.086	1.09	38.7	82.7	2.00	57.4
31			0.101	0.079	1.28	41.5	76.0	1.41	68.0
30			0.109	0.071	1.54	44.8	68.3	1.00	78.8
29			0.116	0.064	1.82	47.7	61.5	0.707	85.3
28	UD-7	0.180	0.123	0.057	2.16	50.6	54.8	0.500	76.9
70	UD-8	0.180	0.123	0.057	2.16	31.6	54.8	0.800	86.9
43			0.104	0.076	1.37	26.7	73.1	2.00	69.3
42			0.112	0.068	1.65	28.8	65.4	1.41	75.2
41			0.119	0.061	1.95	30.6	58.7	1.00	82.8
40			0.126	0.054	2.33	32.4	51.9	0.707	84.7
39	UD-8	0.180	0.132	0.048	2.75	33.9	46.2	0.500	72.2

TABLE 4-5. (Concluded)

TEST NO.	ELEMENT CODE NO.	$\dot{W}_T$ (lbm/sec)	$\dot{W}_o$ (lbm/sec)	$\dot{W}_f$ (lbm/sec)	$\dot{W}_o/\dot{W}_f$	V_o (ft/sec)	V_f (ft/sec)	ϕ	Em, %
74	UD-9	0.180	0.119	0.061	1.95	30.6	58.7	1.00	81.9
71			0.112	0.068	1.65	28.8	65.4	1.36	83.4
48			0.104	0.076	1.37	26.7	73.1	2.00	81.1
47			0.112	0.068	1.65	28.8	65.4	1.36	74.2
46			0.119	0.061	1.95	30.6	58.7	1.00	83.7
45			0.126	0.054	2.33	32.4	51.9	0.680	85.8
44	UD-9	0.180	0.132	0.048	2.75	33.9	46.2	0.500	74.4
53	UD-10	0.180	0.104	0.076	1.37	26.7	73.1	2.00	72.2
52			0.112	0.068	1.65	28.8	65.4	1.41	82.1
51			0.119	0.068	1.75	30.6	65.4	1.00	80.5
50			0.126	0.054	2.33	32.4	51.9	0.707	69.3
49	UD-10	0.180	0.132	0.048	2.75	33.9	46.2	0.500	54.1

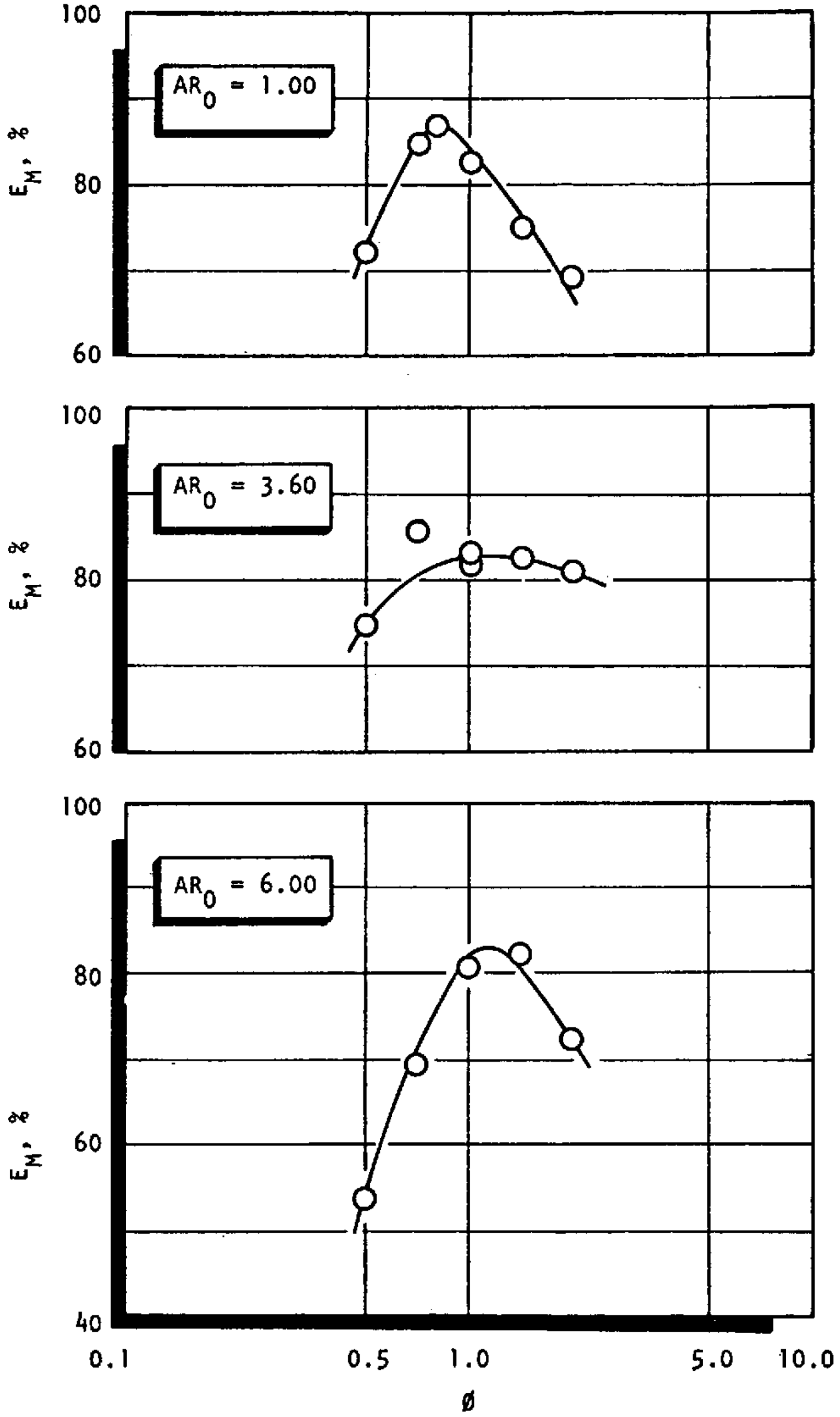

Figure 4-14. Rectangular Unlike-Doublet Mixing, E_m, as a Function of Ø and AR_o for b_f/b_o = 0.391 (Rounded Entrances)

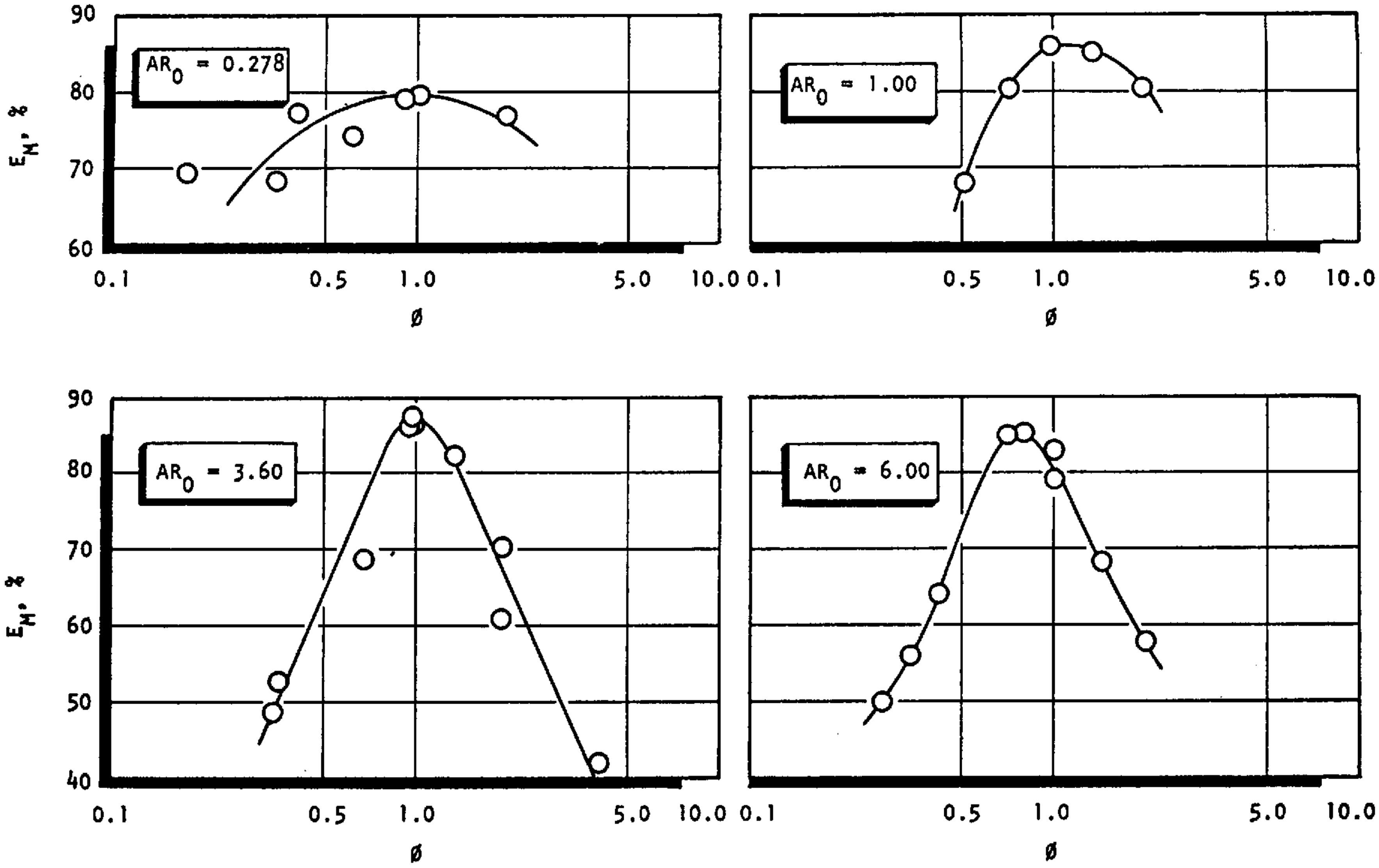

Figure 4-15. Rectangular Unlike-Doublet Mixing, E_m, as a Function of Ø and AR_o for $b_f/b_o = 0.625$ (Rounded Entrances)

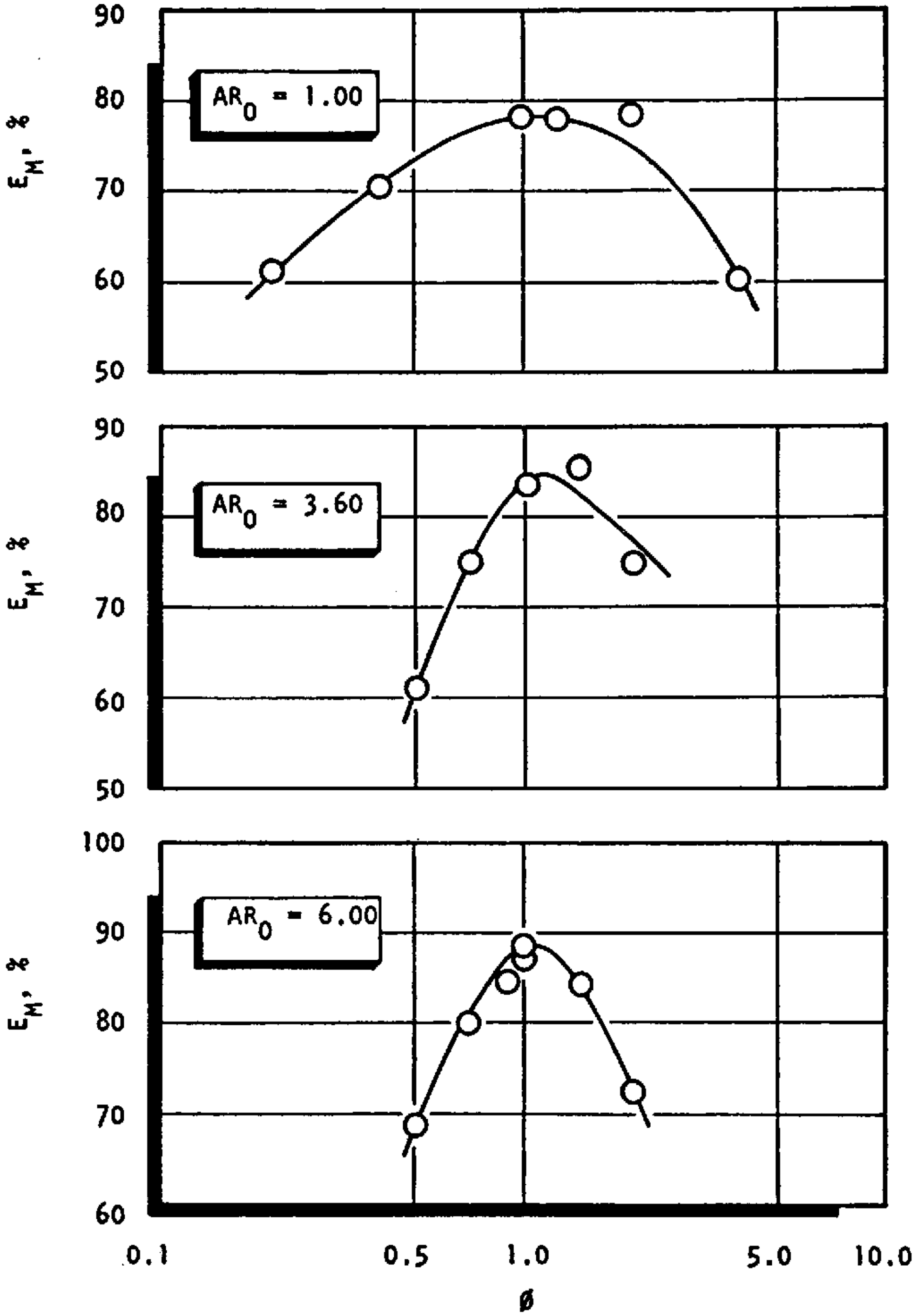

Figure 4-16. Rectangular Unlike-Doublet Mixing, E_m, as a Function of Ø and AR_o for b_f/b_o = 1.00 (Rounded Entrances)

orifice aspect ratios are presented in separate plots. In all cases, it may be noted that the mixing level for a given element optimized at a value of ϕ near unity. The value of the maximum level of mixing varies with both b_f/b_o and b_o/w, however.

A cross plot of the data is presented in Fig. 4-17, wherein the maximum E_m is shown as a function of AR_o along lines of constant b_f/b_o. It is clear from the results that the optimum value of AR_o is functionally related to the value of b_f/b_o. A correlation of all of the data is presented in Fig. 4-18, which suggests the analytical form of this relationship. Here, the maximum values of E_m are plotted as a function of $AR_o/(b_f/b_o)^3$. This presentation allows a single curve to be drawn through the data. Mixing results previously obtained with rectangular unlike doublets with sharp-edged entrances (see Ref. 1 and 3) are also presented in Fig. 4-18. For both rounded and sharp-edged entrances, the maximum levels of mixing are achieved for a value of $AR_o/(b_f/b_o)^3 \approx 8$.

The results, as depicted in Fig. 4-18, can be formulated into a design criteria for rectangular unlike doublets for optimum mixing. These criteria are embodied in the following equations:

Design for optimum mixing level

$$\phi = 1.0 \tag{4-7}$$

and

$$AR_o/(b_f/b_o)^3 = 8 \tag{4-8}$$

for $w_o = w_f$ only

Of the two criteria, Eq. 4-7 is by far the most stringent. Deviations from $\phi = 1$ can produce large reductions in the level of mixing. It can be seen from Fig. 4-18, however, that for rounded entrance rectangular unlike doublets there is a great degree of latitude in the value of the constant assigned to Eq. 4-8. This constant can vary from 3 to 50 with no significant reduction in level of mixing. With sharp orifice entrances, the maximum obtainable mixing level is only a few percent lower, but the sensitivity of off-optimum values of $AR_o/(b_f/b_o)^3$ is substantially greater.

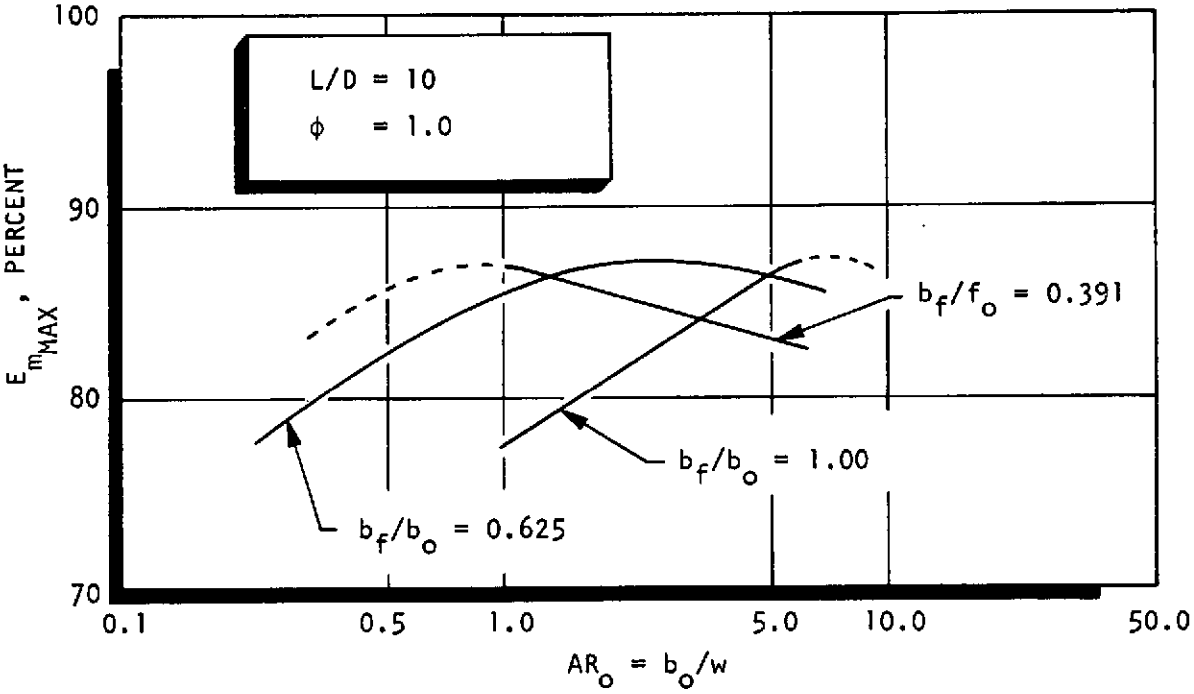

Figure 4-17. Rectangular Unlike-Doublet Mixing as a Function of b_f/b_o and AR_o for ϕ = 1.00

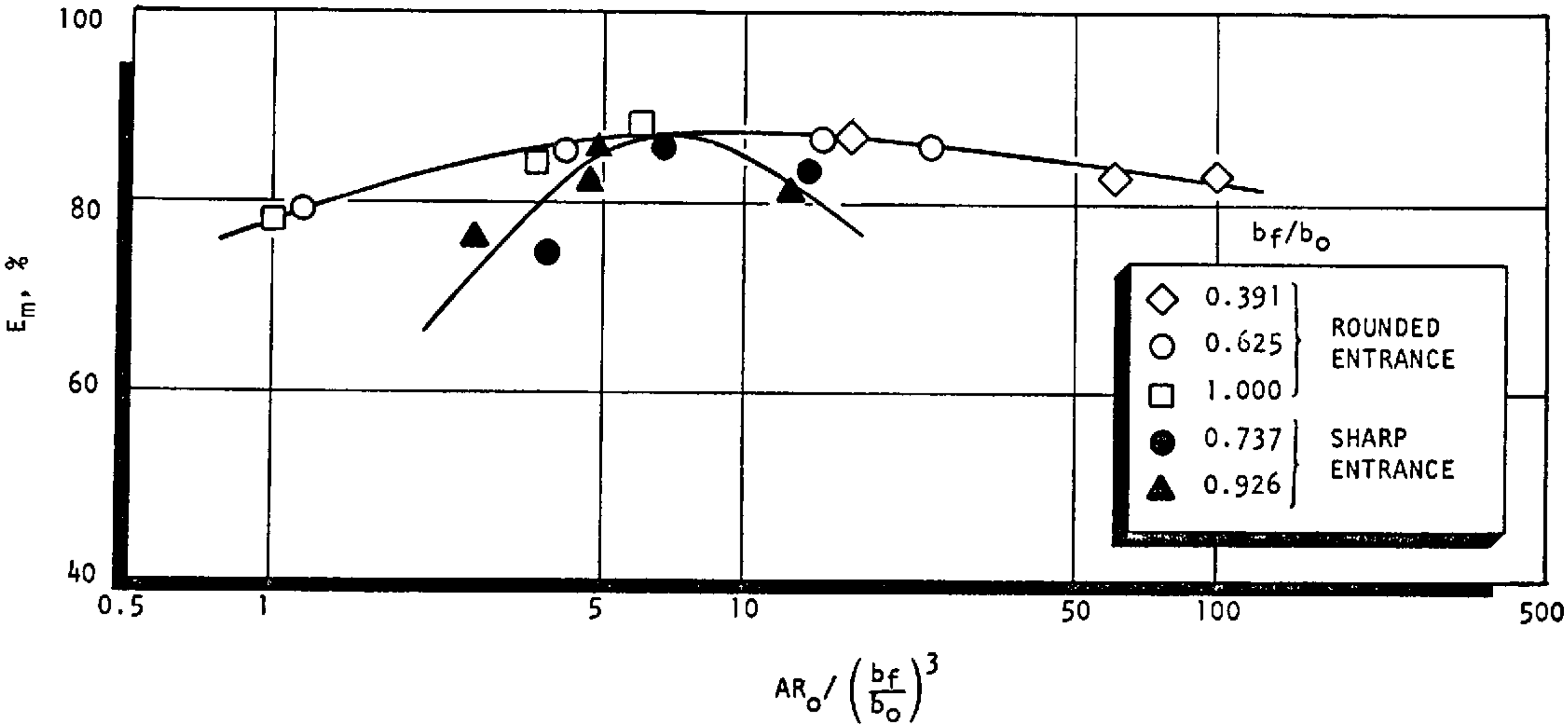

Figure 4-18. Mixing Uniformity for Rectangular Unlike Doublets as a Function of $AR_o/(b_f/b_o)^3$ (Sharp and Rounded Entrance Data Shown)

5.0 APPLICATION OF RESULTS TO INJECTOR DESIGN AND GENERAL CONCLUSIONS

5.1 GAS/LIQUID ELEMENTS

The results that have been presented for the gas/liquid rectangular concentric tube injector elements suggest that the introduction of rectangular shape for injector design would be most beneficial for those applications in which high mixture ratio (MR > 4) and/or low gas momentum ($\rho_G V^2_G < 50$ psi) are imposed.* For these applications, the rectangular shape can be employed to significantly improve mixing. However, care must be taken to ensure that the particular thrust chamber is not vaporization performance limited. (It has been shown that an increased aspect ratio produced an increased droplet diameter--see Fig. 3-43. An aspect ratio of at least 6:1 must be employed to achieve dropsizes that are comparable to a circular element of equivalent injection areas.)

In general, no significant additional mixing advantage is achieved for aspect ratios greater than 3:1 for zero center-post recess. However, higher aspect ratios do appear to offer added mixing quality with recessed center-posts (see Fig. 3-28).

Aspect ratios greater than 6:1 are probably not practical from a fabrication standpoint. However, aspect ratios on the order of 6:1 are attractive as they provide the desirable mixing advantages and, at the same time, offer no apparent atomization penalty (see Fig. 3-43).

The limited data obtained under this study suggest the guidelines listed in this section (see Table 5-1).

---

*A rocket engine that operates with gaseous hydrogen at 800 psi will produce a value of $\rho_G V_G^2 = 58$ for $V_G = 1000$ ft/sec.

TABLE 5-1. SUGGESTED DESIGN GUIDELINES FOR APPLICATION OF RECTANGULAR CONCENTRIC TUBE INJECTOR ELEMENTS

Quantity	Target Valves
Range of Application	$\dot{w}_L/\dot{w}_G > 4.0$
Liquid Port Aspect Ratio	$x_1/y_1 \approx 3{:}1$ (mixing limited)
	$x_1/y_1 \approx 6{:}1$ (mixing and vaporization limited)
Center-Post Recess	$r/y_1 \approx 1.0$
Gas Port Aspect Ratio	$x_3/y_3 \approx 2.1$ for $x_1/y_1 = 3.0$
	x_3/y_3 Unknown for $x_1/y_1 = 6$

5.2 LIQUID/LIQUID ELEMENTS

Design guidelines and conclusions concerning optimum mixing for unlike triplets and doublets as well as some guidelines for triplet atomization design are presented in this section. The mixing guidelines may be employed directly to injector design. However, caution must be exercised with the atomization criteria. The triplet atomization criteria obtained in this study are applicable to laminar flow only in orifices with rounded entrances. In addition, property corrections from wax to the desired propellant must be employed. It is interesting to note that for the fuel component (UDMH), velocities up to 30 ft/sec (in a 0.070-inch-diameter orifice) or 50 ft/sec (in a 0.020-inch-diameter orifice) produce Reynolds numbers less than 10^4. Thus, actual rocket applications will be concerned with laminar jets if the entrances to the orifices are rounded.

5.2.1 Triplet Mixing Design Guidelines

The design guidelines for triplet elements having circular orifices are quite simple. Basically, the element design should be configured such that the following criteria are met (see Table 5-2).

TABLE 5-2. TRIPLET INJECTOR DESIGN CRITERIA FOR MIXING

For $d_1/d_2 \geq 1.0$	$\phi = 1.00$
For $d_1/d_2 < 1.0$	$\phi = 0.714$

For a given propellant combination and specified mixture ratio, the value of ϕ may be computed with the following relationship:

Given

ρ_1 and ρ_2

and mixture ratio = $\dot{w}_2/\dot{w}_1$

$$\phi = \frac{1}{2} \frac{\rho_2}{\rho_1} \left(\frac{d_2}{d_1}\right)^3 \frac{1}{MR^2} \tag{5-1}$$

Since the value of ϕ is specified for optimum mixing, the following equation represents the design criteria for triplets:

$$\frac{d_1}{d_2} = \sqrt[3]{\frac{1}{2} \frac{\rho_2/\rho_1}{\phi\ MR^2}} \tag{5-2}$$

Once the value of $\frac{d_1}{d_2}$ has been established (iteration may be required to fix the appropriate value of ϕ), the maximum level of mixing is determined (see Fig. 4-6C).

5.1.1. Unlike-Doublet Mixing Design Guidelines

The design guidelines for optimum mixing are essentially identical for both circular and noncircular orifice unlike doublets. That is:

$$\phi = 1$$

However, the noncircular orifices provide an additional degree of design flexibility. The importance of this additional flexibility is illustrated in the following discussion.

The specification of a propellant combination and an operational mixture ratio, when combined with the criterion, $\phi = 1$, yields the following relationships:

- for circular orifices

$$\left(\frac{d_f}{d_o}\right)_{opt} = \sqrt[3]{\frac{\rho_o/\rho_f}{MR^2}} \qquad (5\text{-}4)$$

- for rectangular orifices

$$\left(\frac{b_f}{b_o}\right)_{opt} = \sqrt[3]{\frac{\rho_o/\rho_f}{MR^2}} \qquad (5\text{-}5)$$

For the circular orifice, this is the end of the line. The mixing level associated with the particular orifice diameter ratio must be accepted (see, for example, Ref. 3). This limitation is due to the fact that the aspect ratio for a circle is unity and does not provide an additional degree of freedom.

However, for the rectangular elements, the value of the aspect ratio of the oxidizer remains a free variable, even after the ratio b_f/b_o has been stipulated according to Eq. 5-5. The optimum value of this variable can be computed from the following relationship to achieve a design capable of the maximum levels of mixture ratio uniformity.

$$(AR_o)_{opt} = \left(\frac{b_o}{w}\right)_{opt} = 8\left(\frac{b_f}{b_o}\right)^3 = 8\,\frac{(\rho_o/\rho_f)}{MR^2} \qquad (5\text{-}6)$$

5.2.3 Triplet Atomization Design Guidelines

An approximate dropsize relationship has been presented for triplet elements with circular (rounded entrance) orifices:

$$\bar{D} = 2.15 \times 10^5 \, V_j^{-.77} \left(\frac{L}{D}\right)^{-.39} D_j^{.62} \tag{5-7}$$

where

V_j = ft/sec

D_j = inches

$\bar{D}$ = microns

This relationship may be employed to compute the approximate mass median wax droplet diameter produced by either the central orifice or the outer orifices for laminar flow. However, there is a strong property correction that must be applied to the wax droplet diameter. This correction has not been established for laminar jet flow with triplet elements. Yet, some appreciation for the relative importance of the changes of the injector design variable can be realized. The relationship for droplet diameter can be employed to test the sensitivity of dropsize to injection velocity (Δp), orifice length, and jet diameter. For example, the relationship suggests that V_j and D_j are of equal import while the orifice length $(\frac{L}{D})$ is less important (or influential).

6.0 RECOMMENDATIONS FOR FUTURE WORK

6.1 GAS/LIQUID WORK

In the areas of gas/liquid rectangular and circular concentric tube mixing and atomization, further cold-flow experimentation is required with variation of area ratio. This will aid in generalizing the results that are presently restricted according to Eq. 3-8. Some work in this area has been reported in Ref. 7. However, these results were limited to a specific application. More general parametric data are needed.

Further data concerning the effect of gas port aspect ratio, x_3/y_3, upon the mixing characteristics for rectangular concentric tube elements (RCTE), are required. The results presented in this report show this to be a potentially valuable parameter for the optimization of mixing, and also for control of the spatial mixture ratio distribution produced by injector elements. The latter feature could have valuable application with regard to injector/thrust chamber compatibility.

The work with RCTE's should be carried to its natural conclusion--the design and hot-fire demonstrations of a large-scale injector designed for high mixture ratio (e.g., LOX/GH_2 at MR = 6) and low gas injection momentum. This type of study could also include a variation of the orientation of the peripheral elements to evaluate the advantage of RCTE's for improved injector/chamber compatibility, and perhaps stability.

6.2 LIQUID/LIQUID WORK

An evaluation of the mixing characteristics of rectangular unlike doublets with unequal facing widths (i.e., $w_o \neq w_f$, see Fig. 4-12) is strongly recommended. The additional flexibility of the parameter w_o/w_f, when added to Eq. 4-7 and 4-8 could, perhaps, greatly increase the maximum levels of single-element mixing available with unlike-doublet elements. This is an extremely valuable goal due to the fact that the simplicity of the unlike-doublet element makes it an attractive candidate for injector design.

In conjunction with the mixing evaluation, a detailed study of reactive stream separation ("blowapart") should be conducted. If the unlike doublet is to be employed with hypergolic propellants, this problem must be address and definitive design guidelines for the avoidance of blowapart established.

7.0 REFERENCES

1. Nurick, W. H. and R. M. McHale: Noncircular Orifice Holes and Advanced Fabrication Techniques for Liquid Rocket Injectors, Phase I Final Report, Contract NAS9-9528, NASA CR-10870, Rocketdyne Division, Rockwell International, Canoga Park, California, 15 September 1970.

2. McHale, R. M.: Noncircular Orifice Holes and Advanced Fabrication Techniques for Liquid Rocket Injectors, Phase II Final Report, Contract NAS9-9528, NASA CR-108571, Rocketdyne, 22 February 1971.

3. McHale, R. M. and W. H. Nurick: Noncircular Orifice Holes and Advanced Fabrication Techniques for Liquid Rocket Injectors, Comprehensive Program Summary Report, Contract NAS9-9528, R-9271, Rocketdyne, May 1974.

4. Streeter, V. L.: Fluid Mechanics, 4th Ed., McGraw-Hill Book Co., New York, 1966.

5. Landis, R. B.: Water Coolant Flow Requirements for J2-T, 17K, 59° Copper Chamber, LAP65-741, Rocketdyne, 17 December 1965.

6. Hines, W. S.: Turbulent Forced Convection Heat Transfer to Liquids at Very High Heat Fluxes and Flowrates, Research Report No. 61-14, Rocketdyne, 30 November 1961.

7. Burick, R. J.: Space Storable Propellant Performance Program Coaxial Injector Characterization, Contract NAS3-12051, NASA CR-120936, Rocketdyne, October 1972.

8. Zajac, L. J.: Personal communication concerning future plans to conduct secondary droplet breakup stuides for gas/liquid concentric tube elements, Rocketdyne, 1973.

9. Zajac, L. J.: Correlation of Spray Dropsize Distribution and Injector Variables, Final Report, Contract NAS7-726, R-8455, Rocketdyne, 1972.

APPENDIX A

GAS/LIQUID PRESSURIZED COLD-FLOW MIXING FACILITY*

MEASUREMENT SYSTEM

To characterize the spray fields generated by gas/liquid rocket motor injectors, a system was developed to determine local values of gas and liquid mass flux under pressurized conditions. Knowing local values of gas and liquid mass lux, the "mixedness" (i.e., E_m) of the two-phase spray field was determined.

A schematic of the complete measurement system for the characterization of dense gas/liquid spray fields is shown in Fig. A-1. Mixing experiments were performed with both single-element and multi-element gas/liquid injectors. The apparatus consisted essentially of a pressurized test section in which the deceleration probe (described in subsequent paragraphs) was positioned in r-θ coordinates. The system contained several "water traps" to ensure that water, which can accumulate during extended test periods, does not plug critical pressure lines in the system. A photograph of the system, which is located at the Combustion and Heat Transfer Laboratory, is shown in Fig. A-2.

A problem associated with the characterization of spray fields generated with single-element injectors was the suppression of the flowfield recirculation caused by the injection of high-velocity streams into a finite closed volume. High levels of recirculation within the test section precluded the accurate determination of the gas-phase flowfield. To eliminate flowfield recirculation, a low-velocity uniform "base bleed" flow surrounded the single-element injector. The values of base bleed velocity are in accord with the CrayaCurtet criterion for the elimination of recirculation (Ref. A-1).

One additional problem associated with the characterization of spray fields generated with single-element injectors was the determination of the local mass flux of the injectant gas. As the gas/liquid flow field moves through the

---

*Appendix A taken directly from Ref. A-2.

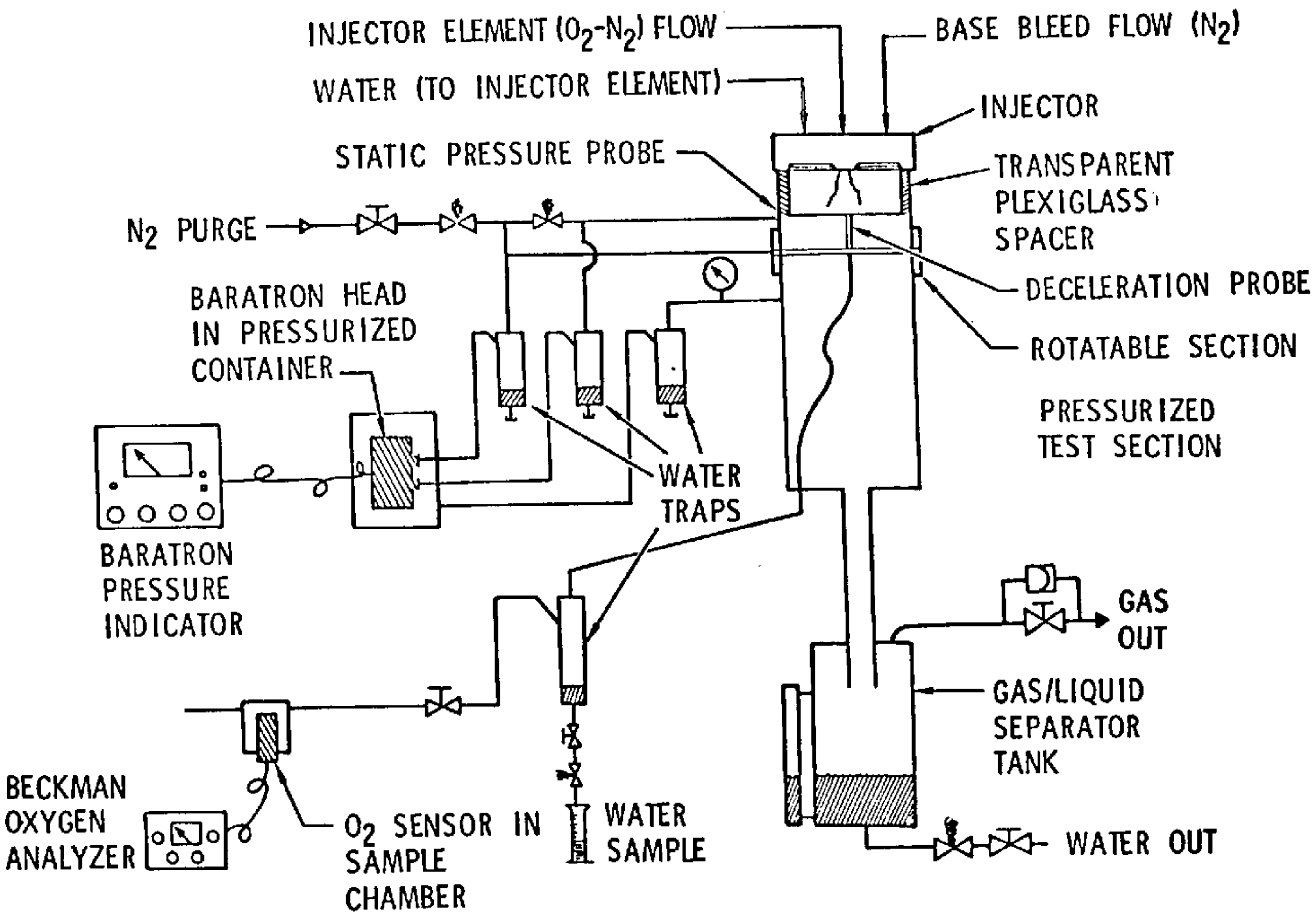

Figure A-1. Schematic of Pressurized Gas/Liquid Mixing Facility

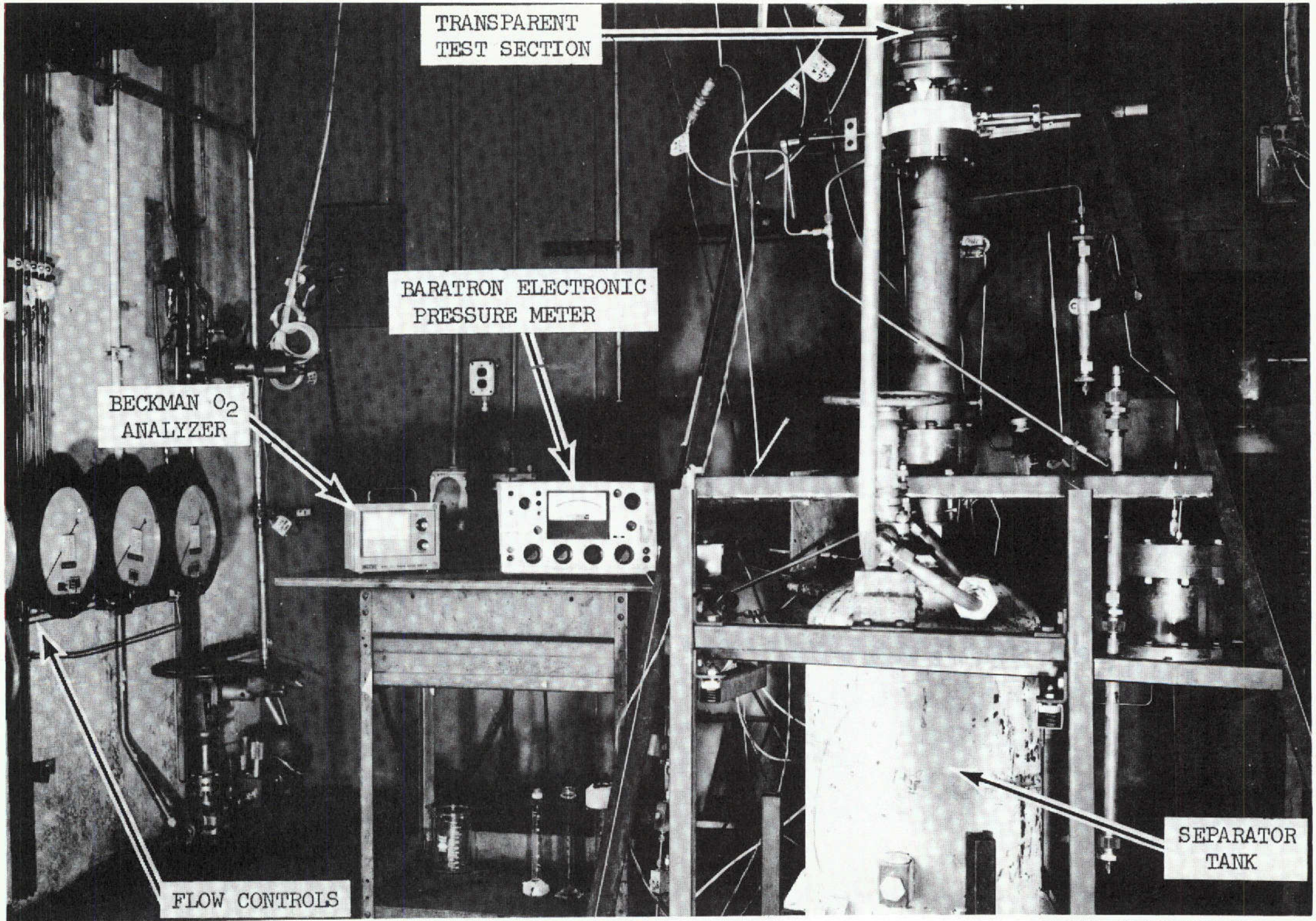

5AA21-10/27/70-S1

Figure A-2. Pressurized Gas/Liquid Mixing Facility surrounding environment on its way from the injector to the probe tip, much of the gas in the environment (base bleed) was ingested into the flowfield. Therefore, the gas flowrate measured by the probe was composed of gas that was injected and gas that was ingested. These two components were segregated to determine the injected portion (for calculation of E_m). To accomplish this, nitrogen and oxygen were mixed in known quantities and injected through the element while pure nitrogen was used as a base bleed fluid. The sample that arrived at the probe tip was processed through a Beckman oxygen analyzer (Fig. A-1). The concentration of the oxygen in the sample was then used to determine the concentration of the injected gas phase.

TWO-PHASE DECELERATION PROBE

The two-phase deceleration probe, which was used for the determination of local values of gas and liquid mass flux, was developed under Contract NAS3-12051 (see Ref. A-2). Only a brief description of the probe will be presented herein; for a more detailed description see Ref. A-3.

The concept of a deceleration probe for the measurement of gas-phase stagnation pressures, for the determination of gas velocity, in two-phase flowfields was first introduced by Dussourd and Shapiro (Ref. A-4). However, the referenced probe design was operated only in low mass flux ratio (particle flowrate/gas flowrate <0.2) flowfields. In addition, the probe design of Dussourd and Shapiro was utilized only in ambient pressure flowfields.

The deceleration probe which was developed at Rocketdyne was utilized both for the determination of gas-phase stagnation pressures and local liquid mass flux. The probe has been demonstrated to operate successfully in high mass flux ratio (liquid mass flux/gas mass flux 0.2 to 20) two-phase flowfields (Ref. A-5). In addition, measurements have been made in dense gas/liquid flowfields at static pressures up to 500 psia.

A schematic of the deceleration probe, termed the "concentric tube two-phase impact probe", is presented in Fig. A-3. The probe was constructed of two concentric tubes (A and B) with a specially designed tip attached to tube B. The tip was designed to prevent the passage of water (termed flooding) into the annulus formed by tubes A and B when the probe is utilized in high mass flux ratio flowfields. The problem of flooding is a serious limitation of the probe design described in Ref. A-4.

The operating principle for the determination of the gas-phase stagnation pressure by the concentric tube two-phase impact probe is illustrated in Fig. A-4. Basically, the intent is to decelerate the gas and measure the gas-phase stagnation pressure in a manner that minimized momentum exchange from the condensed phase upstream of the measurement location. Particles (or droplets) and gas (each at their own velocity) encounter the probe tip. The gas phase is stagnated at the probe tip where the pressure is approximately equal to the gas-phase stagnation pressure. Deviation from true gas-phase stagnation pressure is due to momentum exchange between the particles and the gas in the near flowfield of the probe tip (termed overpressure error). A particle, due to its higher inertia, passes through the probe tip and is decelerated to zero velocity in the stagnation chamber formed by tube A. However, due to momentum exchange between the particles and the stagnated gas, the particles decelerate in the probe tip to some extent over the distance X (see Fig. A-4). The gas-phase stagnation pressure $P_{o,gas}$, as measured in the probe annulus, is greater than the gas-phase stagnation pressure, $P_{o,tip}$. The difference between the two aforementioned pressures can be made small if the distance X is minimized. However, the total overpressure error (due to particle/gas momentum exchange both near and within the probe tip) can be determined by proper calibration of the probe in known two-phase flowfields (Ref. A-3).

The gas-phase stagnation pressure was measured in the 360-degree annulus at the probe tip rather than at a single point as was done on the probe described in Ref. A-4. Tests conducted with both the subject probe and one of the Ref. A-4 designs in high mass flux ratio (>3) flowfields demonstrated that the concentric

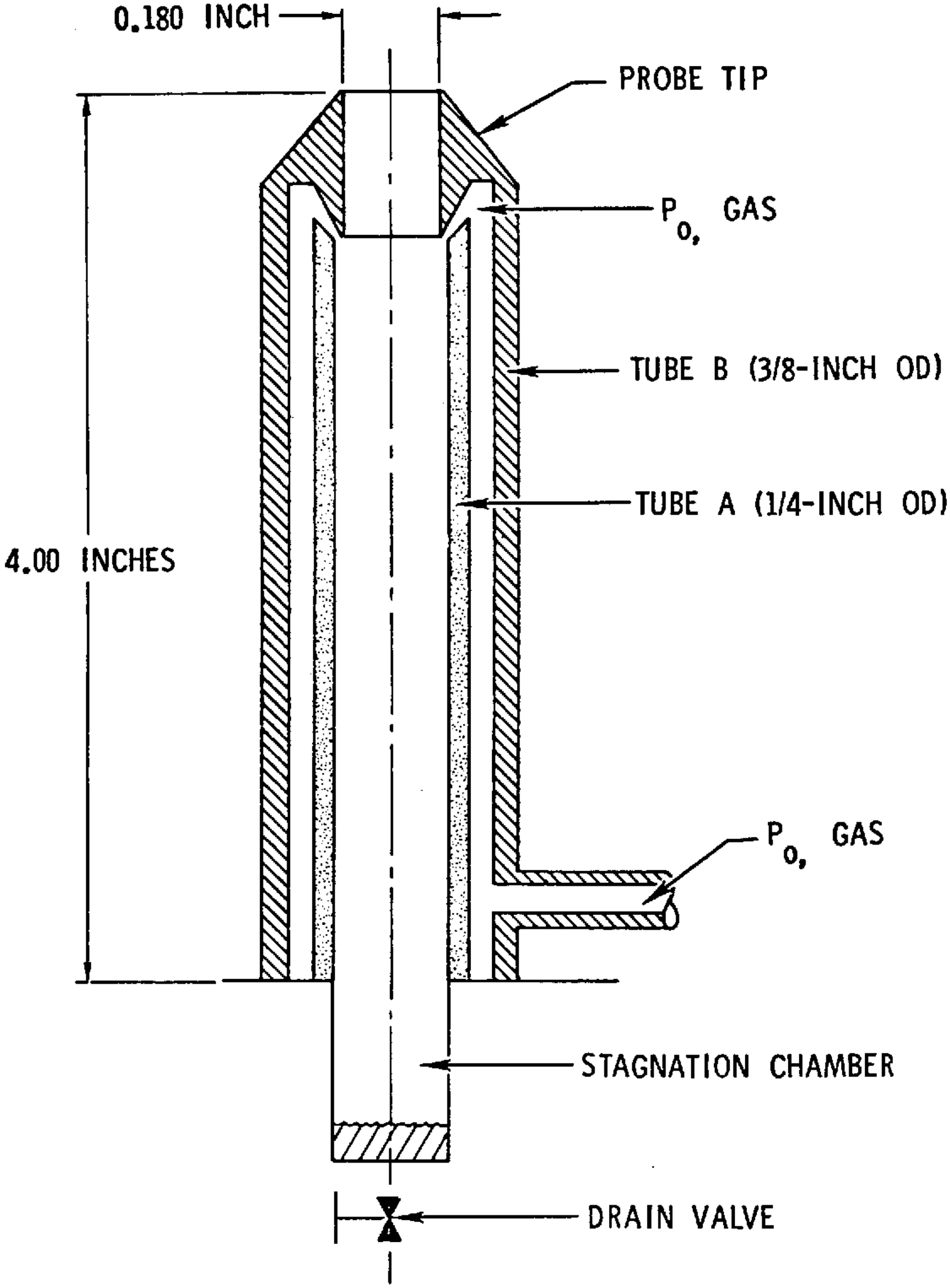

Figure A-3. Schematic of Concentric Tube Two-Phase Impact Probe

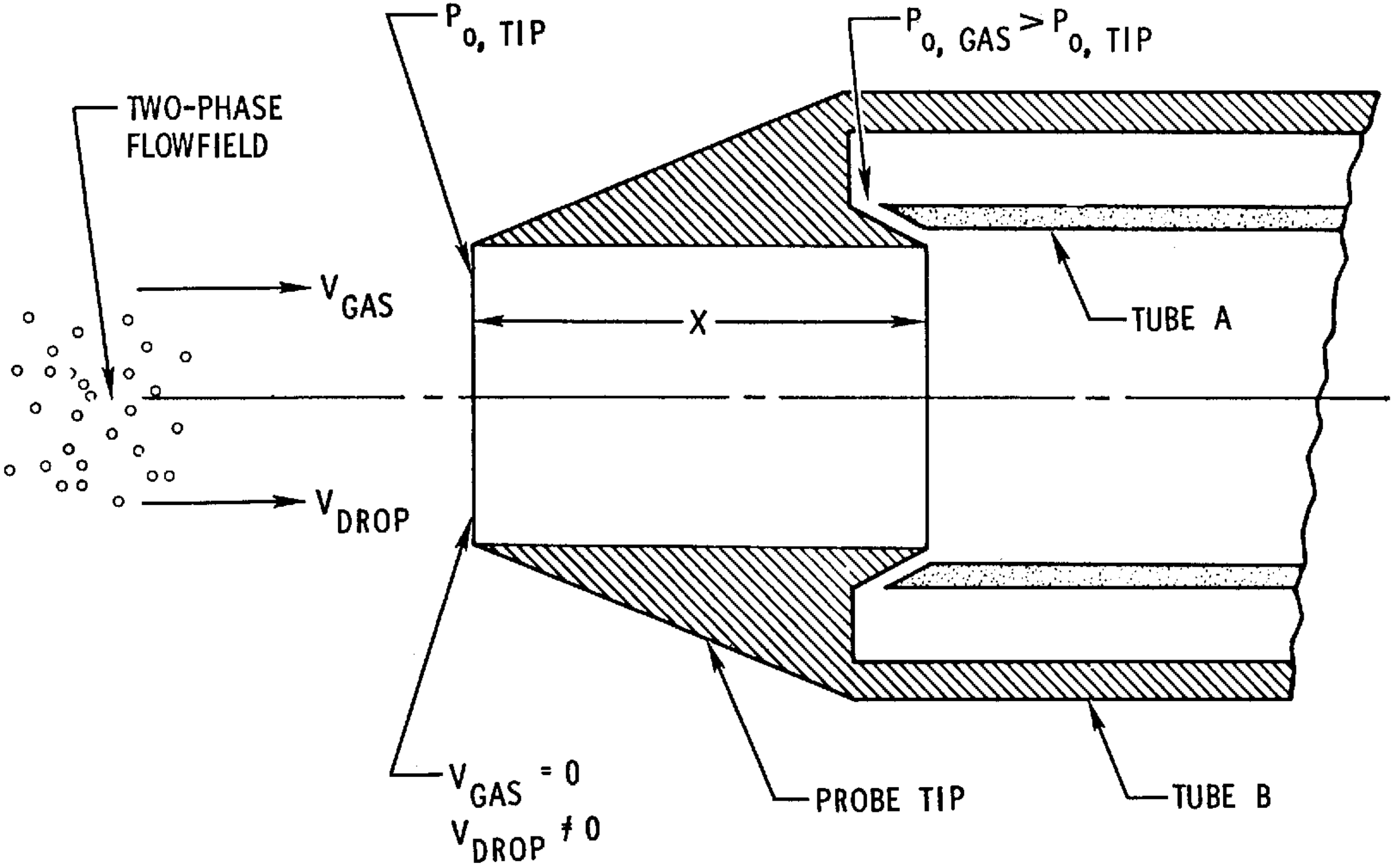

Figure A-4. Principle of Operation

tube probe eliminated the pressure oscillations encountered with a probe of Ref. A-4 design. In addition, the concentric tube probe design avoids the need for an external pressure line at the probe tip that could create flowfield disturbances. The gas-phase stagnation pressure in the probe annulus was measured with an MKS Baratron Type 77 electronic pressure meter.

Local values of liquid mass flux were determined by capturing a liquid sample in the probe stagnation chamber (Fig. A-2) for a known time interval. However, since the droplet capture efficiency of the probe design is less than 1 (≈0.95) small corrections must be made to the captured liquid mass to determine a value of local liquid mass flux. Values of the probe capture efficiency were determined by calibration of the probe in known two-phase flowfields.

A photograph of the two-phase probe and its traversing mechanism is shown in Fig. A-5. The probe is shown located in the rotatable portion of the test system.

APPENDIX A REFERENCES

A-1. Becker, H. A., H. C. Hottle, and G. C. Williams: "Mixing and Flow in Ducted Turbulent Jets," Ninth Symposium (International) on Combustion, Academic Press, 1963.

A-2. Burick, R. J.: Space Storable Propellant Performance Program Coaxial Injector Characterization, Contract NAS3-12051, NASA CR-120936, Rocketdyne, October 1972.

A-3. Burick, R. J., C. H. Scheuerman, and A. Y. Falk: "Determination of Local Values of Gas and Liquid Mass Flux in Highly Loaded Two-Phase Flow," Paper No. 1-5-21, Symposium on Flow--It's Measurement and Control in Science and Industry, 10-14 May 1971, Pittsburgh, Pa., Paper No. 1-5-21, to be published in Symposium Proceedings.

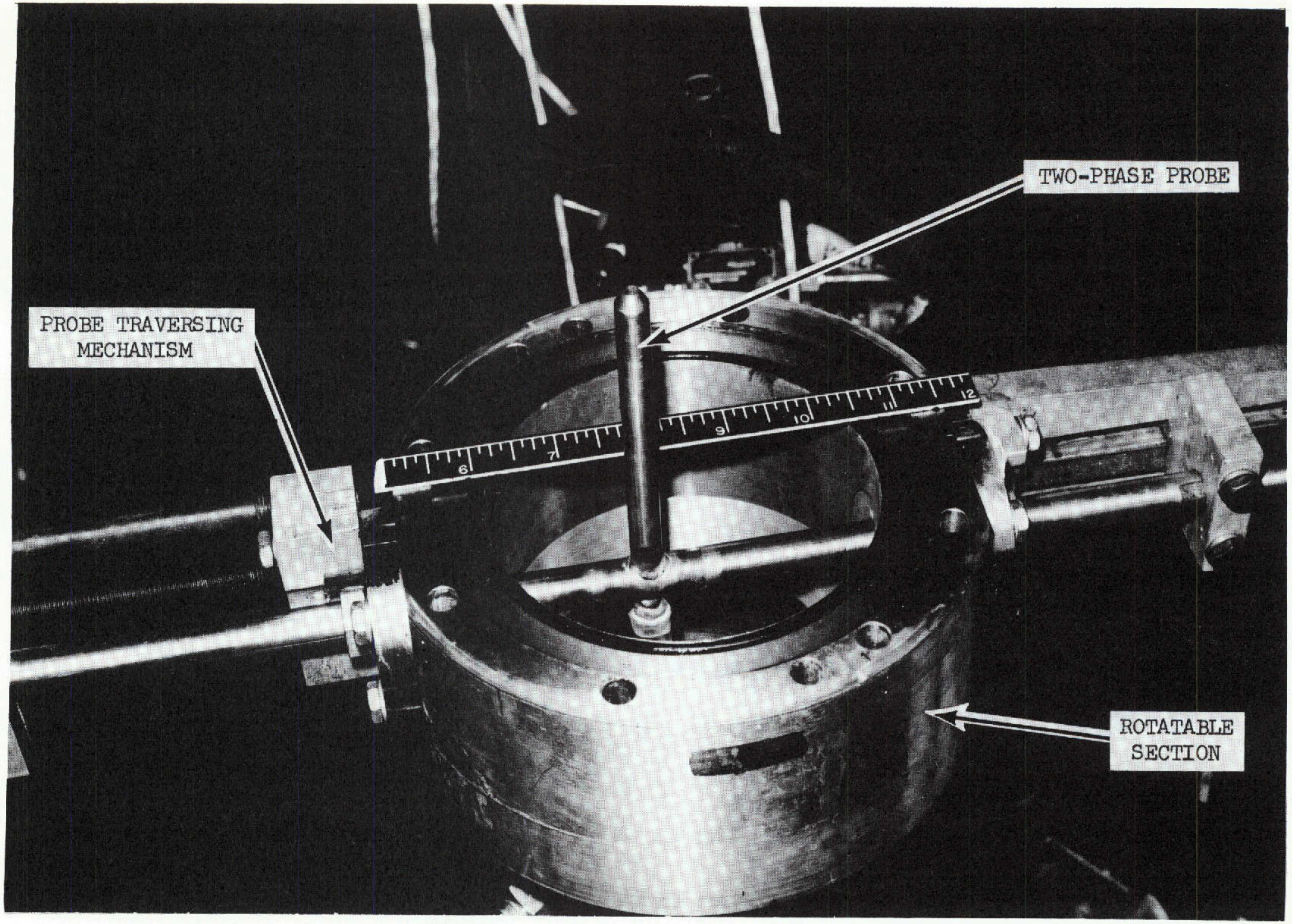

5AA36-11/19/70-S1B

Figure A-5. Two-Phase Impact Probe in Rotatable Section

A-4. Dussourd, F. L. and A. H. Shapiro: "A Deceleration Probe for Measuring Stagnation Pressure and Velocity of a Particle Laden Gas Stream: Jet Propulsion, pp 24-34, January 1958.

A-5. Mehegan, P. F. et al.: NASA CR-72703, Investigation of Gas-Augmented Injectors, Rocketdyne Division, Rockwell International, Canoga Park, California, September 1970.

APPENDIX B

GAS/LIQUID PRESSURIZED COLD-FLOW ATOMIZATION FACILITY

TECHNIQUE

To simulate the dynamic injection conditions of hot-fire propellant systems, the atomization experiments were conducted at simulated gas-phase densities. In this case, gaseous nitrogen and molten wax (Shell-270) were used as nonreactive fuel/oxidizer simulants, respectively. In this molten wax technique, the wax droplets freeze before collection and are subsequently subjected to sieve analysis after drying.

A series of 23 standard sieves ranging from 53 to 2380 microns (53 to 2380×10^{-6} meters) was available for sample sieving. For any particular sample, only 12 of the sieves were used, the particular sieve sizes that were used depended on the anticipated size range. The particular wax sample ($\approx$10 grams) was shaken on a RO-TAP automatic shaker for 30 minutes. After the sieving operation was completed, the mass of particles on each sieve was weighed on an electric balance. A total recovery of 96 to 98 percent of the mass originally introduced into the sieves was possible. The mass fraction of sample on each sieve was then plotted as a function of sieve size to determine a mass median drop size.

EXPERIMENTAL FACILITY

A schematic of the pressurized atomization facility that was employed in these studies is presented in Fig. B-1. The system consisted of a 600-gallon cylincrical tank in which a single-element injector model was mounted. Molten wax and heated GN_2 were supplied to the injector from a system that was heated with circulating hot oil. All lines and valves in the wax supply were oil jacketed to prevent wax freezing. Heated GN_2 was supplied to the injector at a temperature above the melting point of the wax ($\approx$200 F) so that the resulting wax droplets did not freeze

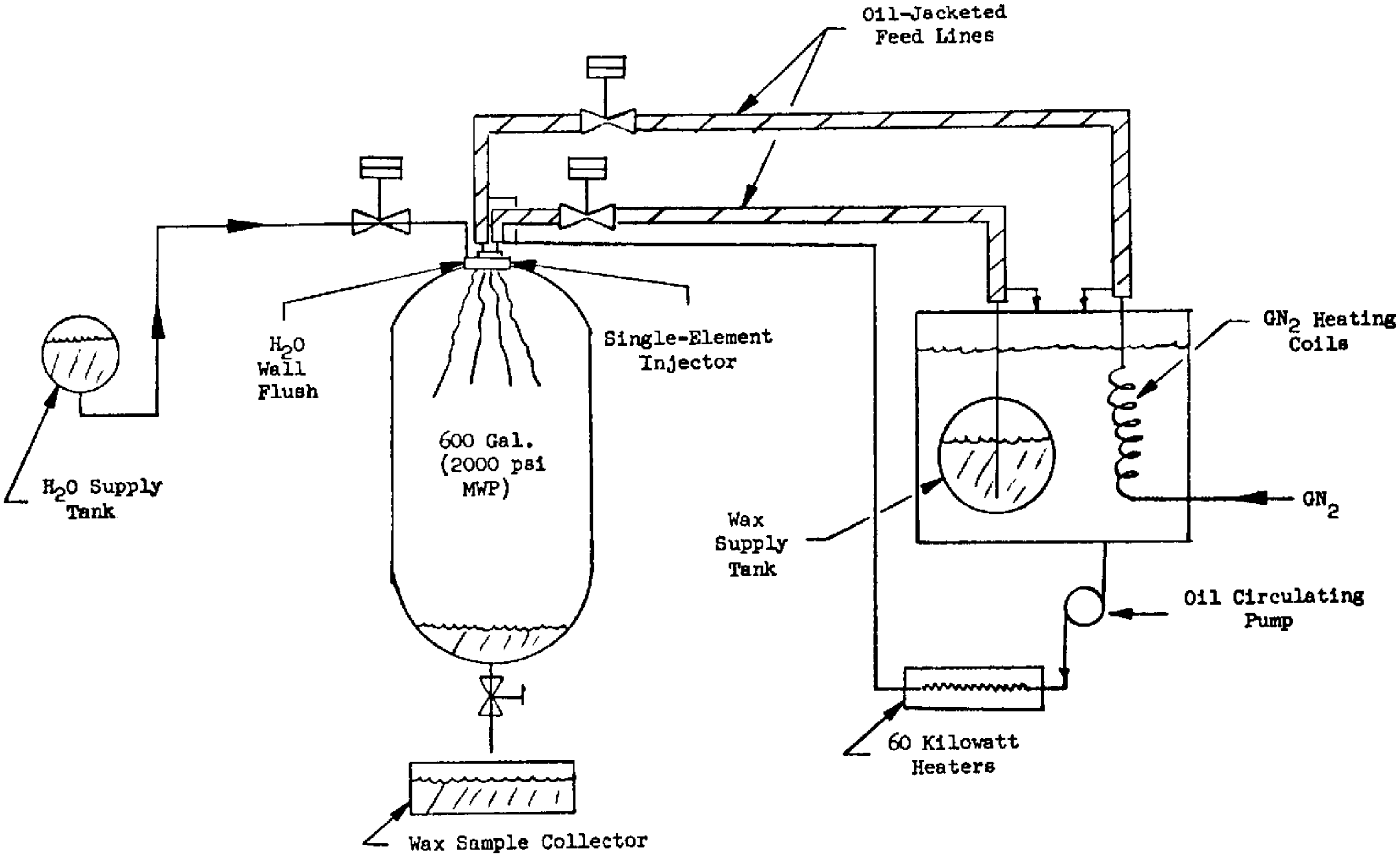

Figure B-1. Schematic of Pressurized Atomization Facility before the completion of the liquid jet breakup and atomization processes. A water flush was supplied to the inner tank walls during testing to ensure that molten wax did not adhere to the tank walls. A photograph of the pressurized atomization facility is shown in Fig. B-2.

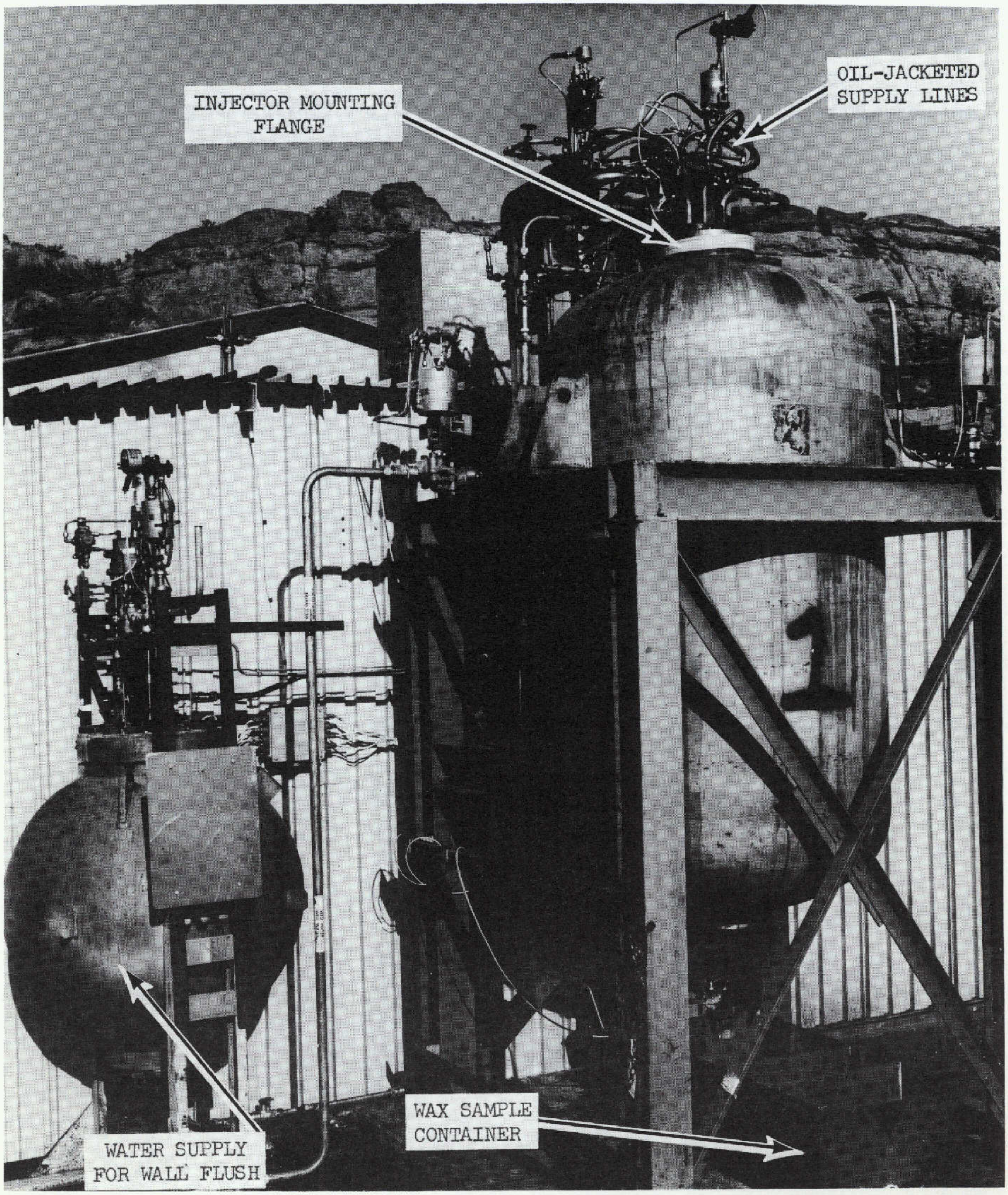

5AA36-11/20/70-S1B

Figure B-2. Pressurized Atomization Facility

APPENDIX C

LIQUID/LIQUID MIXING FACILITY

COLD-FLOW FACILITY

Flow System

The basic components of the flow system are shown in Fig. C-1. The system contains two high-pressure (1000-psia maximum rated pressure) supply tanks. Each are remotely pressurized. The propellant lines are stainless-steel tubing. Pneumatic (Annin) valves are used for tank shutoff and main valves.

Flow system instrumentation consists of four Taber "Teledyne" series-bonded strain gage pressure transducers and two Fischer-Porter turbine-type volumetric flowmeters. Measurements are made of both propellant tank pressures and propellant injection pressures. These measurements are recorded on Dynalog direct-inking graphical recorders. The volumetric flowmeter signals are recorded on a CEC multichannel oscillograph.

Cold-flow propellant simulants are trichloroethylene and water, which simulate the oxidizer and fuel, respectively. These simulants were chosen on the basis of: (1) availability, being employed on related programs at Rocketdyne using the same facility, (2) ease of handling, and (3) maintenance of the oxidizer/fuel immiscibility.

Collection System

The specific details of the collector are illustrated in Fig. C-2. As can be noted, the tubing slants outward from the collection plane to a 7- by 7-foot base. The base is 1/2-inch aluminum plate and separates the upper portion of the assembly from the Pyrex tube racks. Beneath the aluminum plate is a cart that houses the tube racks. The cart is mounted on wheels so that the entire tube matrix is easily removed from under the collector and rolled to the measurement station.

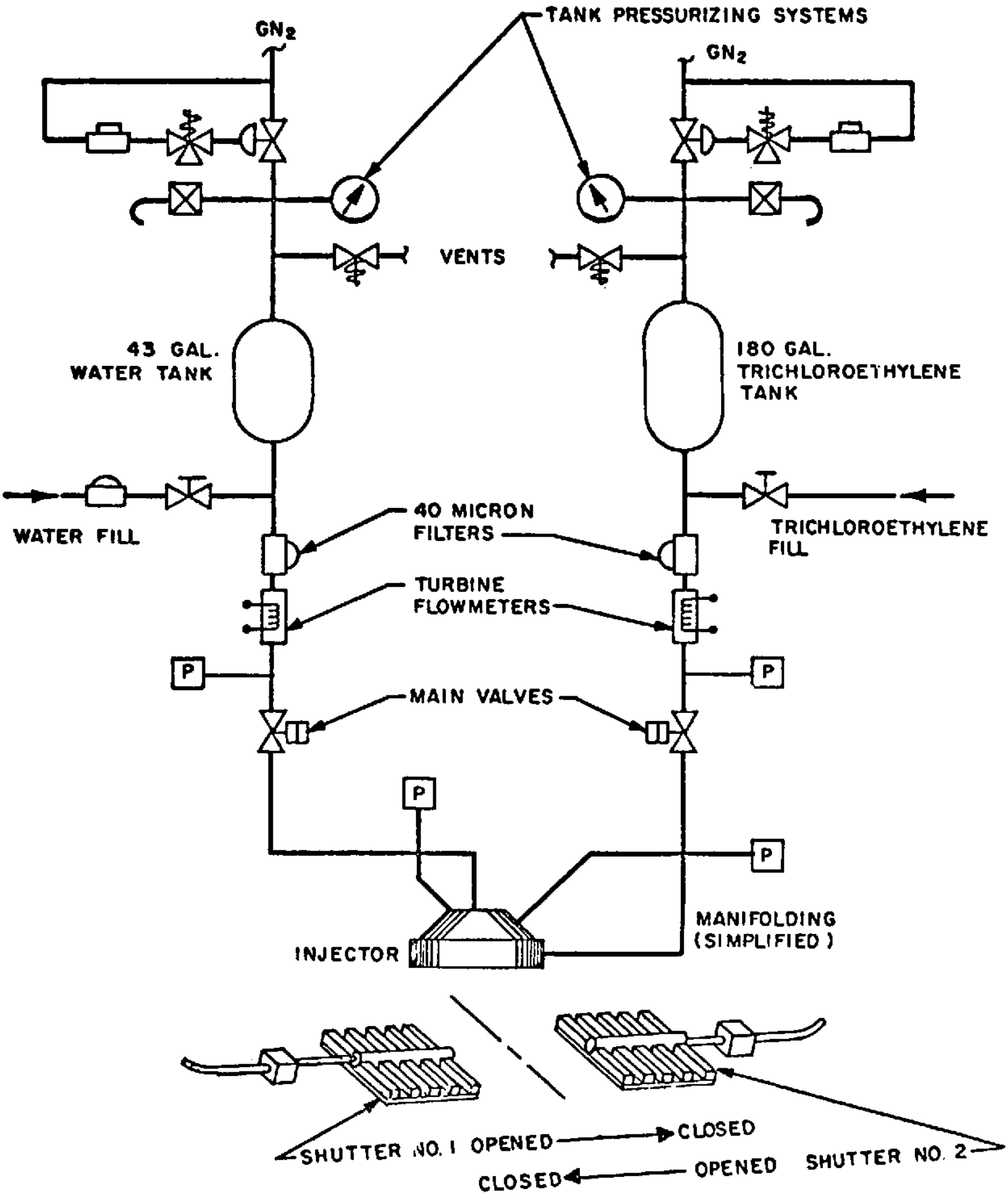

Figure C-1. Schematic Drawing of the Flow System for the Cold-Flow Mass and Mixture Ratio Distribution Study

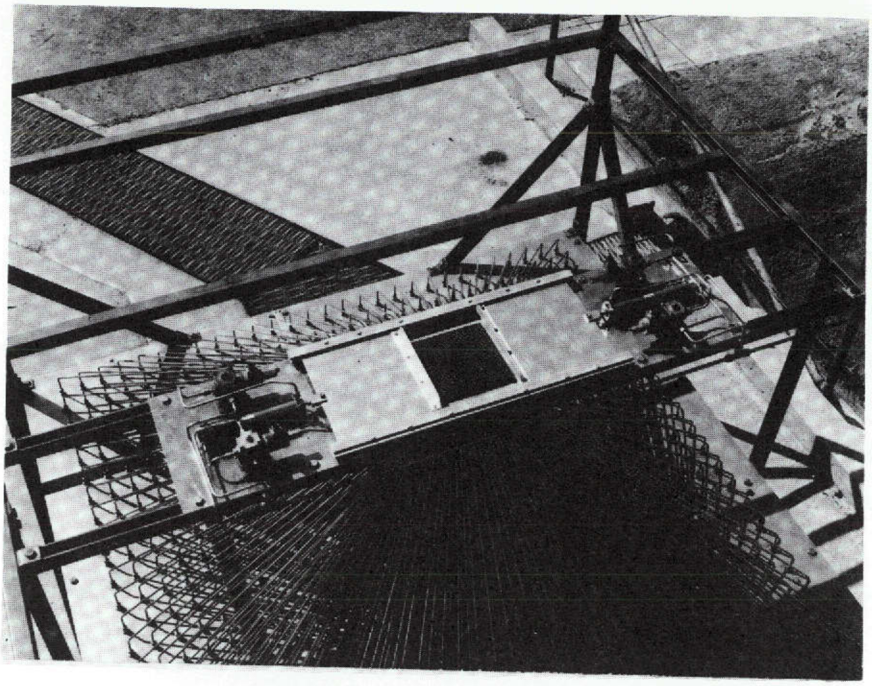

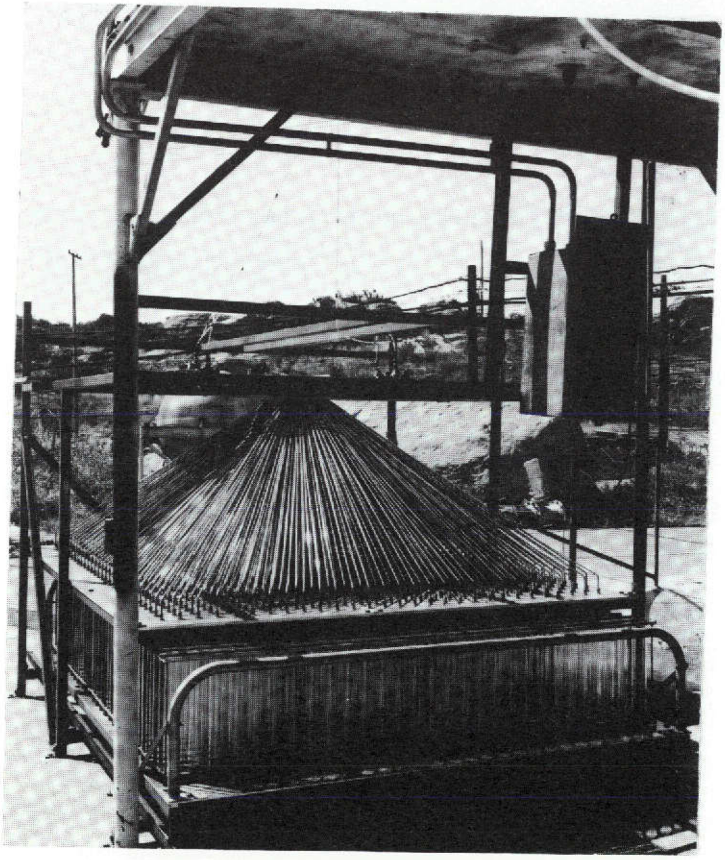

Figure C-2. Injector Spray Collection System

EXPERIMENTAL TEST PROCEDURES

The procedure for conducting a cold-flow test are as follows. The fuel and oxidizer simulant tanks are pressurized to give the desired flowrates. The main valves are opened and, after the injection pressures become steady, the shutter is opened for a selected time interval and then closed. The main valves are then closed to conclude the test run. All tests are conducted with the elements centered above the collector at a distance of approximately 3 inches. This distance was chosen since previous analytical and experimental data indicate that it represents a good approximation of the primary propellant mixing region during combustion.

The data recorded for each test included oxidizer and fuel simulant flowrates, injection pressures, flow duration, and the volume of oxidizer and fuel simulants in each of the collection tubes.

The individual volumes are determined by a volumetrically calibrated metal strip or graduated cylinders. The metal strip is a thin metal scale with a scribe mark at 10-milliliter increments. This strip is inserted into the test tube and the volume of oxidizer simulant and the volume of fuel simulant read directly. For tubes containing insufficient liquid quantities for accurate measurement, the volumetric measurements are obtained by use of graduated cylinders.

DATA ANALYSIS

The collector matrix data and the other recorded data are processed by computer to produce the following output: mass of oxidizer simulant, mass of fuel simulant, mixture ratio, and mass fraction for each tube. The mixing factor (E_m), cold flow c* efficiency ($\eta_{c^*_{mix}}$), center of collected mass (row and column), and percentage of the injected mass collected are computed.

APPENDIX D

LIQUID/LIQUID ATOMIZATION FACILITY

COLD-FLOW FACILITY

The wax flow facility used for the liquid/liquid dropsize measurements is shown in Fig. D-1 and D-2. The overall system consists of wax and water supply tanks immersed in hot oil bath container (same system employed for gas/liquid studies) and a particle collector that catches the frozen wax particles. Instrumentation requirements of pressure, flowrate, and temperature are provided by strain gage transducers, turbine flowmeters, and iron constantan thermocouples, respectively. Each wax and water tank has an independent pressurizing and vent system. Also, each product outline has three flowmeters, thermocouples, and hand shutoff valves arranged in parallel so a wide range of flowrates can be obtained. The hot oil bath (shown schematically in Fig. D-2) is heated by means of a 30-kw thermostatically controlled heater. An electrically operated pump circulates the oil from the oil bath container through the heater and back again to ensure uniform temperature. Also, hot oil is forced through jacketed run lines and valves to ensure that the wax does not freeze in the feed lines.

The particle collector (Fig. D-1) is an 18- by 50-foot, epoxy-coated, wooden platform that is located within a building. This shields the collection area from wind currents that might cause the smaller particles to be blown away. When the impact surface is washed down, the slope of the collector causes the wash water to be directed into a particle catch basin. The catch basin has several baffles to ensure that none of the wax particles are washed overboard.

Experimental Procedure

The experimental procedure for droplet size measurement is as follows:

1. The proper injector configuration is installed on the wax facility in such an orientation that the wax spray, after freezing during its ballistic trajector, strikes the particle collector.

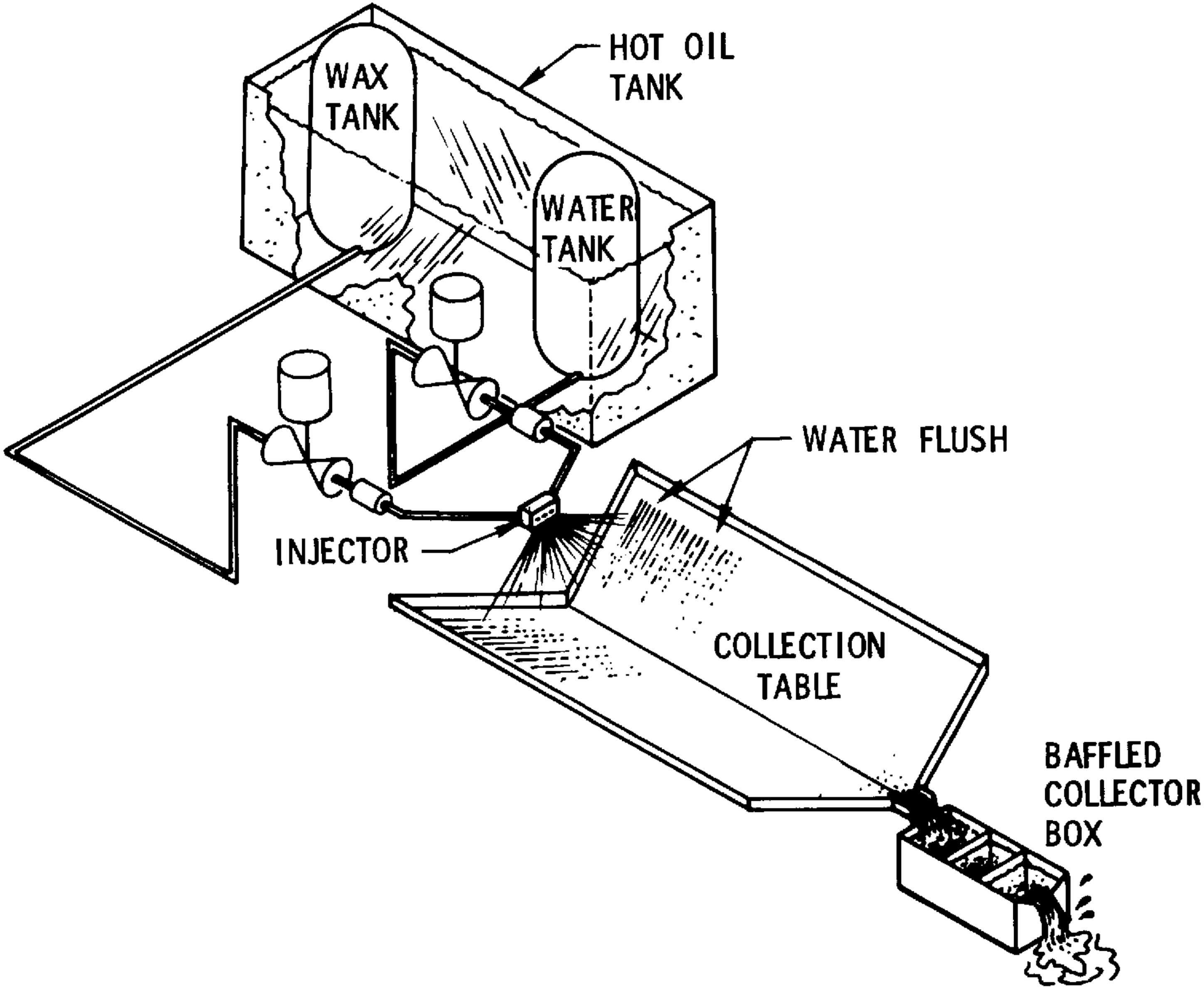

Figure D-1. Open-Air Atomization Facility

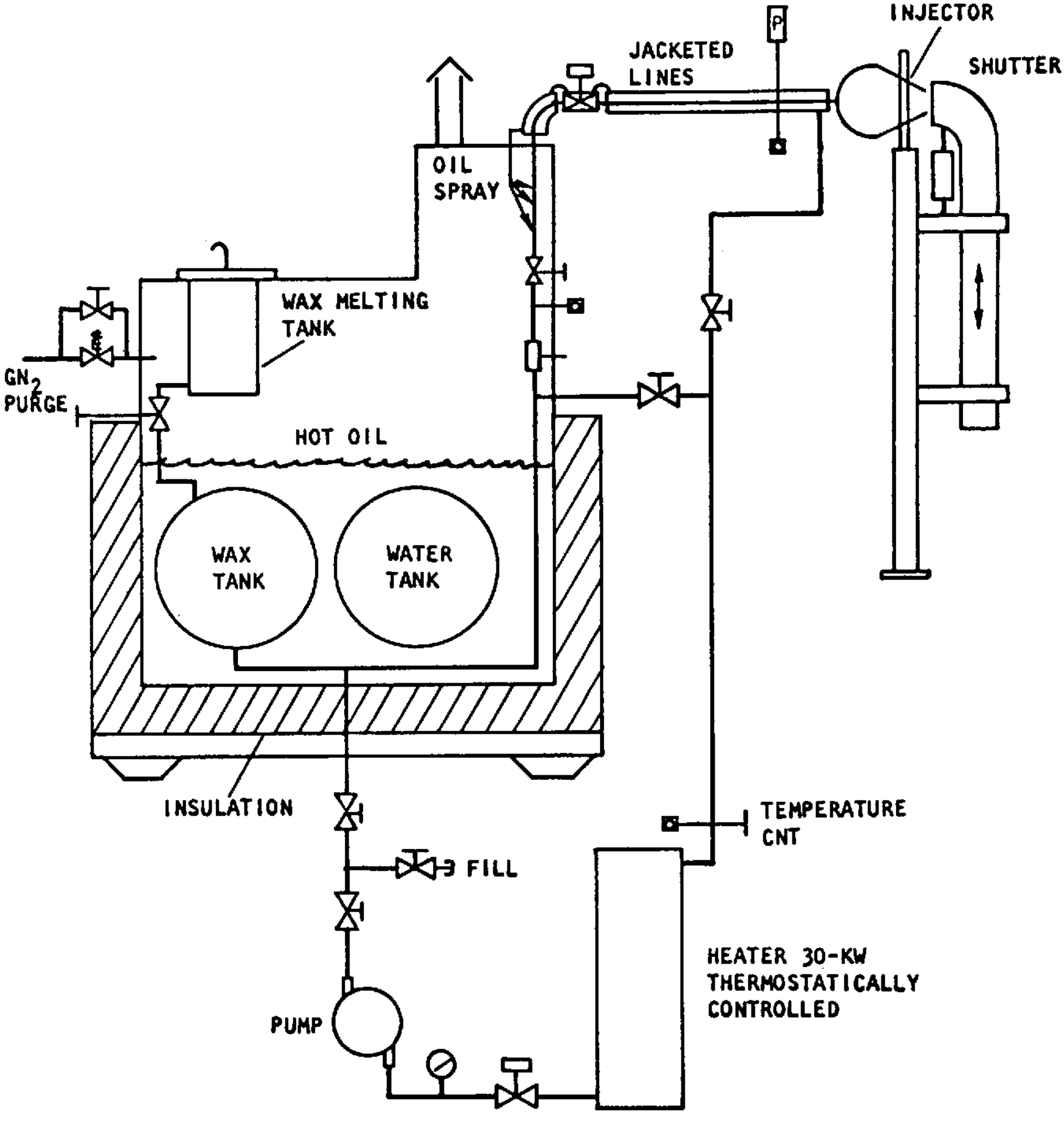

Figure D-2. Schematic of Hot-Wax Flow Facility

2. The electrical oil heater and pump are turned on to bring the propellant simulant tanks and run lines up to 210 F.
3. After all parts of the system are thoroughly heated and instrumentation requirements checked, the run tanks are pressurized.
4. With the piston-operated shutter in the up position, the test is initiated by actuating the main pneumatic shutoff valves. When the flowrates and injection pressures reach a steady condition, the shutter is actuated and the wax particles are allowed to spray onto the particle collector. The use of the shutter minimizes the influence of start and stop transients on the size distribution of the collected particles.
5. The injector flow is continued for approximately 10 seconds. The shutter is then actuated to the up position and main shutoff valves closed.
6. The tanks are then vented and systems secured.
7. The particles are then washed from the collector into the catch basin, where they are scooped from the surface of the water and placed in a plastic bag for temporary storage.

APPENDIX E

HOT-FIRE EXPERIMENTAL FACILITY

The gas/liquid hot-fire experimentation was conducted during Phase IV of this program on test stand Lima at the Propulsion Research Area (PRA) located at the Rocketdyne Santa Susana Field Laboratory Facility. A schematic of that test stand is presented in Fig. E-1 with the critical instrumentation keyed, numerically, to the instrumentation list presented in Table E-1.

The recording method for each parameter is noted in Table E-1. All of the parameters critical to performance calculation were recorded by the Beckman automatic data acquisition system.

Pressures were measured with Taber strain gage type pressure transducers. All temperatures were measured with iron-constantan thermocouples with output in millivolts. The liquid oxygen and the coolant water flowrates were measured with Fischer-Porter turbine flowmeters. The hydrogen gas flowrate was metered with a Flowdyne sonic venturi.

As shown in Fig. E-1, there were four primary systems involved in the operation of test stand Lima. There were the primary propellant systems, liquid oxygen and gaseous hydrogen, a water system for thrust chamber coolant, and a gaseous fluorine system for ignition. (GF_2 was contained in a single, 400-psi maximum commercial gas cylinder.)

All valve opening and closing was controlled by a programmed, automatic timing system. The start and shutdown sequence is listed in Table E-2.

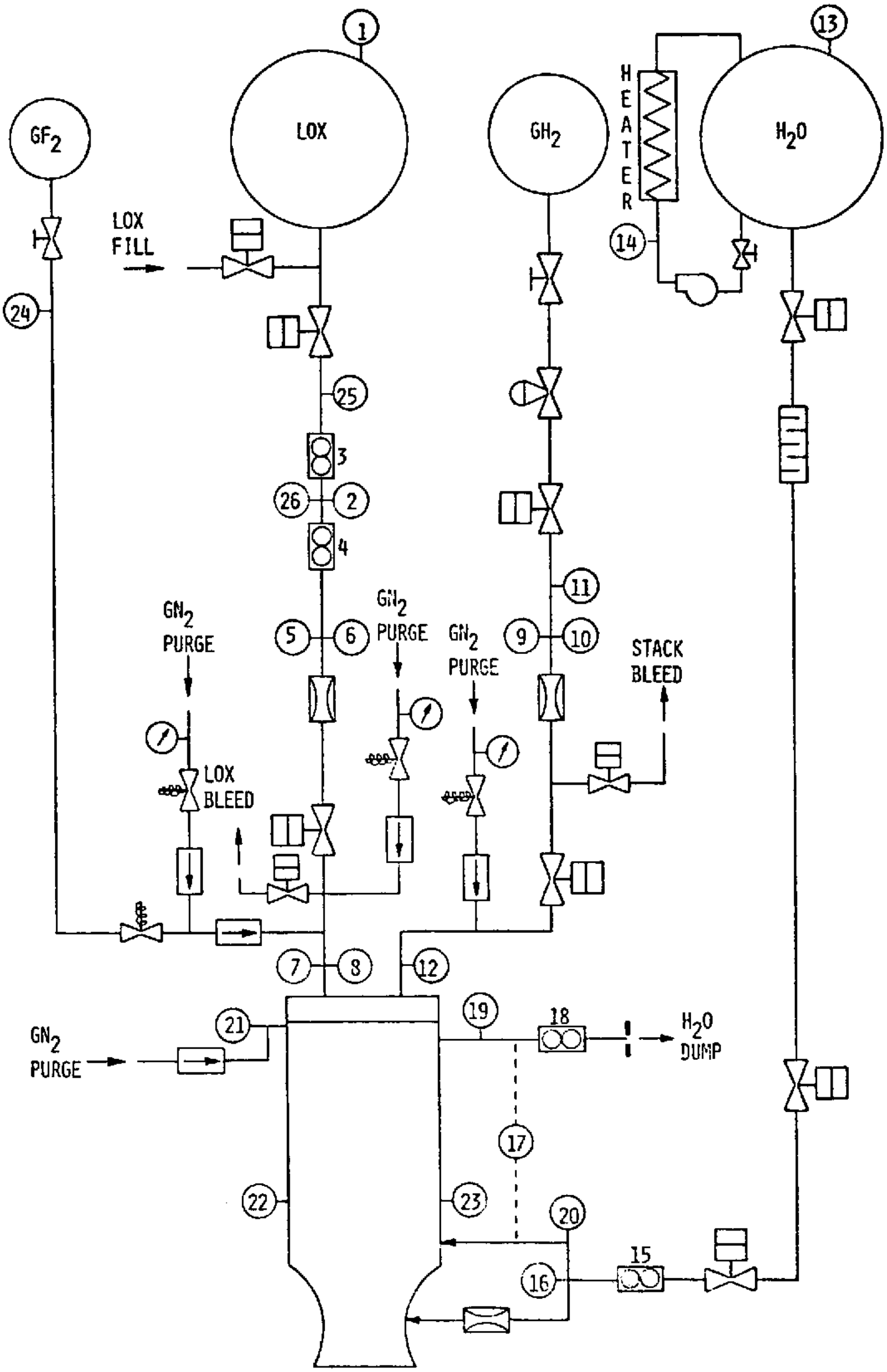

Figure E-1. Test Stand Lima Schematic, 1/2 lb/sec LOX/GH$_2$ Facility With GF$_2$ Ignition

TABLE E-1. LIMA STAND INSTRUMENTATION LIST

Parameter	Type or Range	Recording		
		Beck.	Osc.	DIGR
1. Pressure, LOX Tank	0-3000 psi			X
2. Temperature, LOX Flowmeters	I.C.	X		
3. Flowmeter 1-LOX (5806A-3173-A2)	Turbine	X	X	X
4. Flowmeter 2-LOX (5808A-3673-A2)	Turbine	X	X	X
5. Pressure, Upstream LOX Venturi	0-2000 psi	X		X
6. Temperature, Upstream LOX Venturi	I.C.	X		
7. Pressure, LOX Injection	0-2000 psi	X	X	X
8. Temperature, LOX Injection	I.C.	X		X
9. Pressure 1, Upstream GH_2 Venturi	0-2000 psi	X		X
10. Pressure 2, Upstream GH_2 Venturi	0-2000 psi	X		
11. Temperature, Upstream GH_2 Venturi	I.C.	X		
12. Pressure, GH_2 Injection	0-2000 psi	X	X	X
13. Pressure, H_2O Tank	0-3000 psi			X
14. Temperature, H_2O Heater Line	I.C.			X
15. Flowmeter 1, H_2O (Total)	Turbine	X	X	X
16. Pressure, H_2O Inlet	0-2000 psi	X		X
17. Delta Temperature, Coolant H_2O	3-Leg Thermopile	X		X
18. Flowmeter 2, H_2O (Chamber)	Turbine	X	X	X
19. Pressure, Chamber H_2O Outlet	0-2000 psi	X		
20. Temperature, H_2O Inlet	I.C.	X		X
21. P_c-1 (Injector Face)	0-1000 psi	X	X	X
22. P_c-2	0.1000 psi	X	X	X
23. P_c-3	0-1000 psi	X	X	X
24. Pressure, GF_2 Supply Line	0-1000 psi			X
25. Temperature, LOX Line	I.C.	X		
26. Pressure, LOX Flowmeters	0-2000 psi	X		

TABLE E-2. OPERATIONAL SEQUENCE FOR LIMA STAND

- Pressurize H_2O and LOX tank and pressurize GH_2 loader
- GN_2 purges on
- Water coolant main valve open
- GH_2 main open
- GF_2 main open
- LOX main open
- GF_2 main closed
- LOX main closed
- GH_2 main closed
- Coolant main closed
- GN_2 purges off
- Vent all tanks and loaders

APPENDIX F

COMBUSTION MODELS

VAPORIZATION-LIMITED COMBUSTION

The vaporization-limited combustion model formulation is based on the development of mathematical expressions for the various physical processes involved in the combustion of liquid droplet sprays in a bipropellant liquid rocket engine. The model considers propellants to be injected as sprays containing ranges of discrete droplet size groups, each possessing a given average diameter. The total spray mass is distributed among the various groups according to an experimental mass distribution function.

Of central importance in the model is the solution of the individual droplet burning rates, which are assumed to be limited by diffusion. Analysis of the dynamic behavior of single droplets is justified on the basis that the volumetric flowrate of liquid propellants into the downstream region is only about 1 to 2 percent of that of the combustion gases and, therefore, that the likelihood of droplet collisions or interference with one another is negligibly small. Under rocket conditions, in the uniform mixing zone, droplets are spaced on the order of 2 to 3 diameters apart, while the vapor film thickness is on the order of 5 to 15 percent of the droplet diameters. As a result, each droplet is considered to be immersed in an infinite combustion gas medium.

The calculation of single droplet evaporation is based on a spherically symmetric model of simultaneous heat transfer to, and mass transfer from a liquid sphere.

The liquid droplet temperature is assumed to vary with time, but to be uniform through the drop. Forced convection and resultant nonspherical transfer processes are accounted for through empirical Nusselt number correlations for both heat and mass transfer.

In evaluating the convective contribution, relative gas-to-droplet velocity is required. Droplet velocities are obtained from a drag relationship for evaporating spheres. A composite form of the drag coefficient for accelerating spheres that account for droplet flattening is employed.

Compressible gas dynamics are accounted for with area changes corresponding to chamber geometry. The droplets are treated as point sources (or sinks) of fuel (mass), oxidizer (mass), momentum, and energy with local transport rates obtained by summing the contributions of all droplets at any given location in the chamber.

The gas-phase energy equation is simplified normally by the assumption that the composition and stagnation temperature are the equilibrium values for the gas-phase oxidizer, fuel mixture ratio, and the chamber pressure. Other gas properties (static temperature, density, etc.) are evaluated from the respective stagnation values by applying the local Mach number to the frozen isentropic expansion equations.

The model is solved in numerical form by high-speed digital computers. It requires input of the "upstream boundary condition," which completely describes the initial conditions of spray (dropsize distribution, drop velocities, and temperature) and gas (composition, flowrate, and pressure) at the location where computation is started. Chamber geometry must also be specified.

Solution proceeds in a stepwise manner moving downstream to the nozzle throat. At each step, interphase transport of mass, momentum, and energy is evaluated from the transport equations previously described with subsequent solution of gas-phase equation of state and continuity, momentum, and energy balances. This results in a description of droplet group diameters, velocities, and temperatures as well as gas composition, velocity, and pressure at the new location.

This "marching technique" proceeds into the nozzle up to the geometric throat, where it is necessary to satisfy the downstream boundary condition of sonic gas velocity. If the throat Mach number deviates from unity by more than a preselected tolerance, iteration is required whereby propellant flowrates are adjusted and the entire calculation repeated. In practice, convergence of this iteration is rapid and a solution is readily obtained. The general validity of the analytical results is determined to a major extent by the accuracy of the input spray description. Vaporization rate limited c* efficiency is computed from the following equation:

$$\eta_{c^*,\mathrm{vap}} = \left[\frac{\dot{w}_B}{\dot{w}_I}\right]\left[\frac{c^*_B}{c^*_I}\right] \tag{F-1}$$

where

$\dot{w}_B$ = flowrate of burned gas at the geometric throat

$\dot{w}_I$ = injection flowrate of fuel plus oxidizer

c^*_B = theoretical c* corresponding to the composition of the burned gas at the geometric throat

c^*_I = theoretical c* corresponding to the injection mixture ratio of liquid fuel and oxidizer

MIXING LIMITED COMBUSTION

Over the past 15 years, mass and mixture ratio distribution uniformity ("mixing") has been extensively studied both analytically and experimentally. Experimental/analytical correlations demonstrate quantitatively that high combustion efficiency in rocket engine thrust chambers occurs only when the initial local mixture ratio distribution is at, or near, the target chamber mixture ratio. This implies that the injector should provide a spray field having a uniform mixture ratio over the entire flow cross section.

The sketch shown on the following page illustrates a typical curve of theoretical equilibrium c* as a function of propellant mixture ratio (oxidizer/fuel). Normally the design operating point of overall injected mixture ratio falls close to the peak, and any maldistribution of propellant mixture ratio results in a loss in overall c*. An analytical model has been developed at Rocketdyne to relate these maldistributions to an attendant loss in c* efficiency. The development of this model is outlined in the following paragraphs.

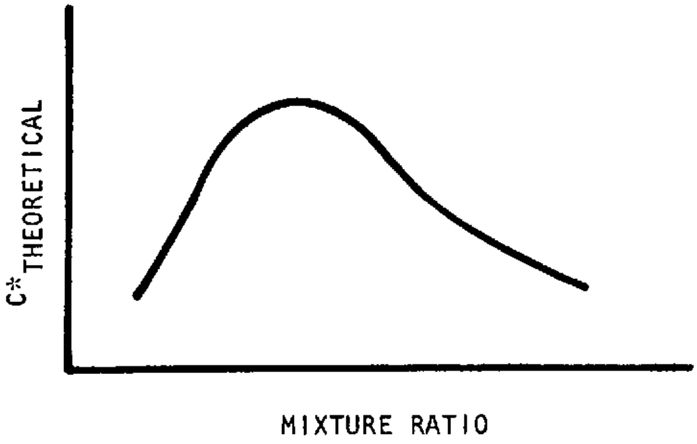

Wrubel (Ref. F-1) describes an analysis of mixing losses whereby the flow is hypothetically subdivided into "i" stream tubes, each containing propellant at some mixture ratio, which is uniform within that stream tube. No mass or energy is considered to cross stream boundaries. Propellant vaporization, mixing, and combustion are treated as being complete upstream of the start of nozzle convergence. Within the nozzle the flow is handled as being one-dimensional and isentropic. At each axial station the static pressure is considered uniform for all stream tubes. In addition, boundary layer effects are neglected. The resulting equation relating the mixing limited c* efficiency to the local mass and mixture ratio distribution is:

$$\eta_{mix} = \sum_i \left(\frac{\dot{w}_i}{\dot{w}_T} \frac{c^*_i}{c^*_{theo}} \frac{A_{t,i}}{A^*_i} \right) \qquad \text{(F-2)}$$

Here $A_{t,i}/A^*_i$ is the ratio of the cross-sectional area of the ith stream tube at the minimum chamber area to its area at the point it becomes sonic. For most cases of interest the specific heat ratios γ_i, are all of similar value so that shifts in location of the sonic condition from the geometric throat will be small and the preceding equation is closely approximated by:

$$\eta_{mix} = \sum_i \frac{\dot{w}_i}{\dot{w}_T} \frac{c^*_i}{c^*_{theo}} \qquad \text{(F-3)}$$

where the effective c* is simply a weighted average of the local c* for the individual stream tubes. For any given propellant mixture ratio distribution, Eq. F-3 provides a simple means of determining c* efficiency loss due to "mixing."

Most investigators agree that distributions developed by spray mixing near the injector will not be appreciably changed downstream by turbulent mixing of the gases. As a consequence, if the initial spray distribution formed by an injector can be experimentally determined, $(\eta_{c*})_{mix}$ can be computed by using Eq. F-3.

Rupe (Ref. F-2) introduced a term, commonly known as E_m, which is an index of mixing uniformity:

$$E_m = 1 - \sum_{i}^{N} \frac{\dot{w}_i}{\dot{w}_T} \frac{(R - r_i)}{R} - \sum_{i}^{N} \frac{\dot{w}_i}{\dot{w}_T} \frac{(R - \bar{r}_i)}{R - 1} \qquad \text{(F-4)}$$

where

E_m = mixing index

$\dot{w}_i/\dot{w}_T$ = mass fraction in the stream tube

R = ratio of total oxidizer mass to total oxidizer and fuel mass

r_i = ratio of oxidizer mass to total oxidizer and fuel mass in an individual stream tube for $r_i < R$

$\bar{r}_i$ = ratio of oxidizer mass to total oxidizer and fuel mass in an individual stream tube for $r_i > R$

The factor E_m, is not uniquely defined by $(\eta_{c*})_{mix}$. The correspondence is strongly affected by the propellant combination and the nominal mixture ratio. This term is employed to describe the average mixing uniformity of a given spray field.

APPENDIX F REFERENCES

F-1. Wrubel, J. R.: "Some Effects of Gas Stratification on Choked Nozzle Flows," AIAA Paper 64-266, 1964.

F-1. Rupe, H. J.: A correlation Between the Dynamic Properties of a Pair of Impinging Streams and the Uniformity of Mixture-Ratio Distribution in the Resulting Spray, Progress Report No. 20-209, Jet Propulsion Laboratory, Pasadena, California, 28 March 1956.

APPENDIX G

PROPERTIES OF FLUIDS EMPLOYED IN PHASES III AND IV COLD-FLOW AND HOT-FIRE PROGRAMS

The properties for the various fluids listed in Table G-1 are presented in Fig. G-1 through G-3.

TABLE G-1. KEY TO PROPERTY CHARTS
(Numbers refer to figure numbers)

	Property		
	Viscosity	Surface Tension	Acoustic Velocity
Liquid Oxygen	G-1	G-2	
Shell Wax (270)	G-1	G-2	
Water	G-1	G-2	
Gaseous Nitrogen	G-1		G-3
Gaseous Hydrogen	G-1		G-3

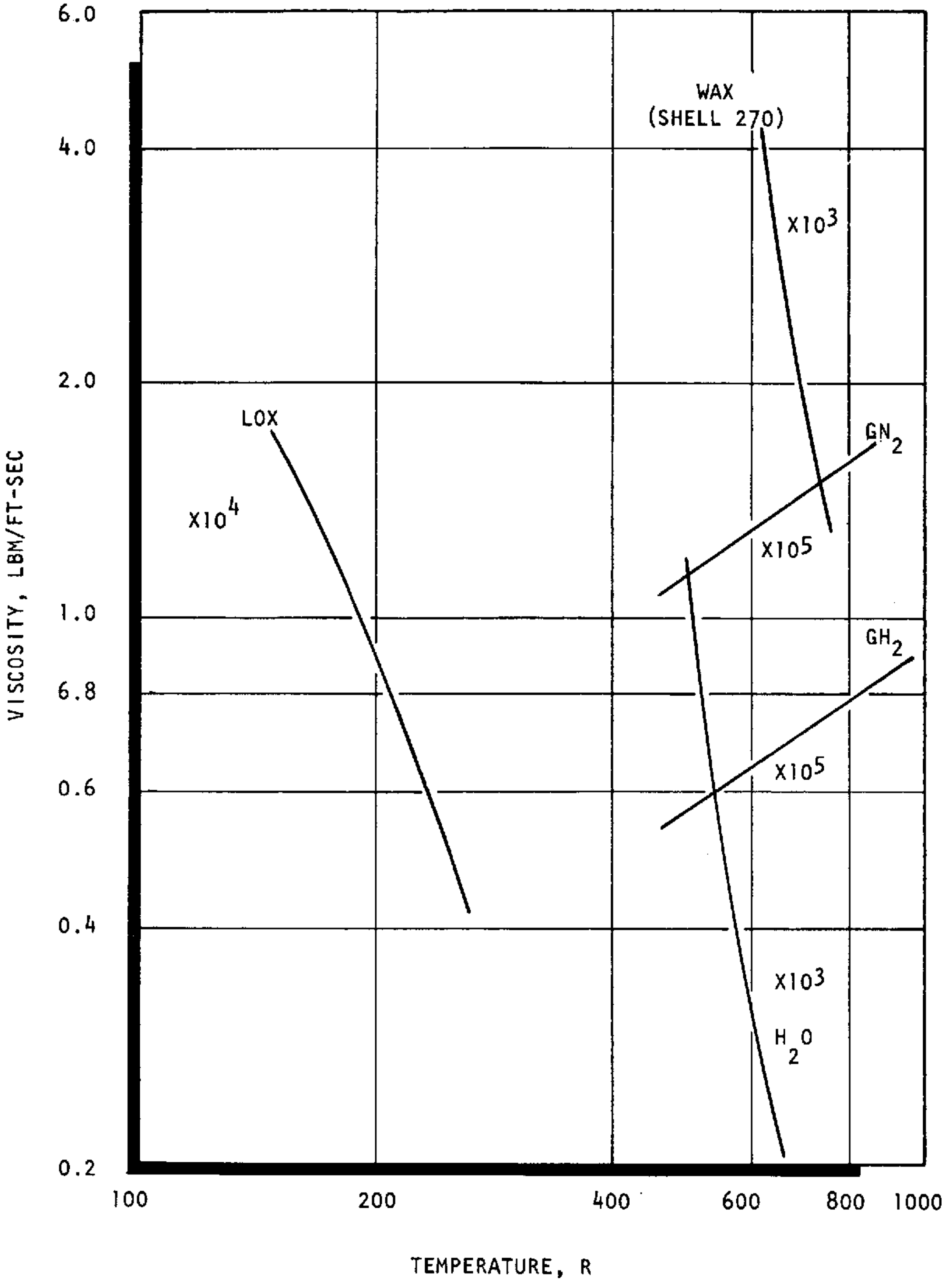

Figure G-1. Viscosity of Liquid Oxygen, Wax (Shell 270), Water, Gaseous Nitrogen, and Gaseous Hydrogen as a Function of Temperature

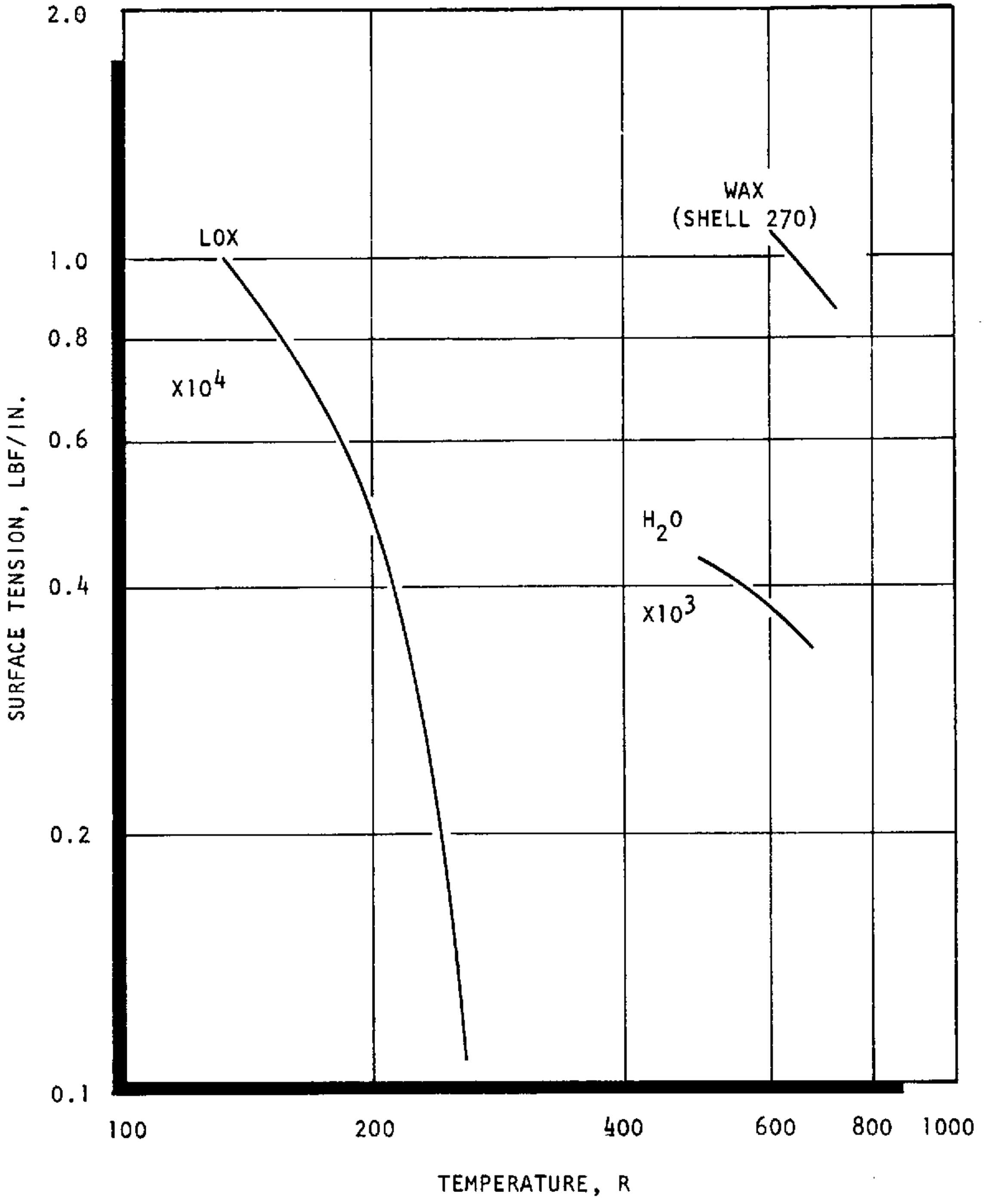

Figure G-2. Surface Tension of Liquid Oxygen, Wax (Shell 270), and Water as a Function of Temperature

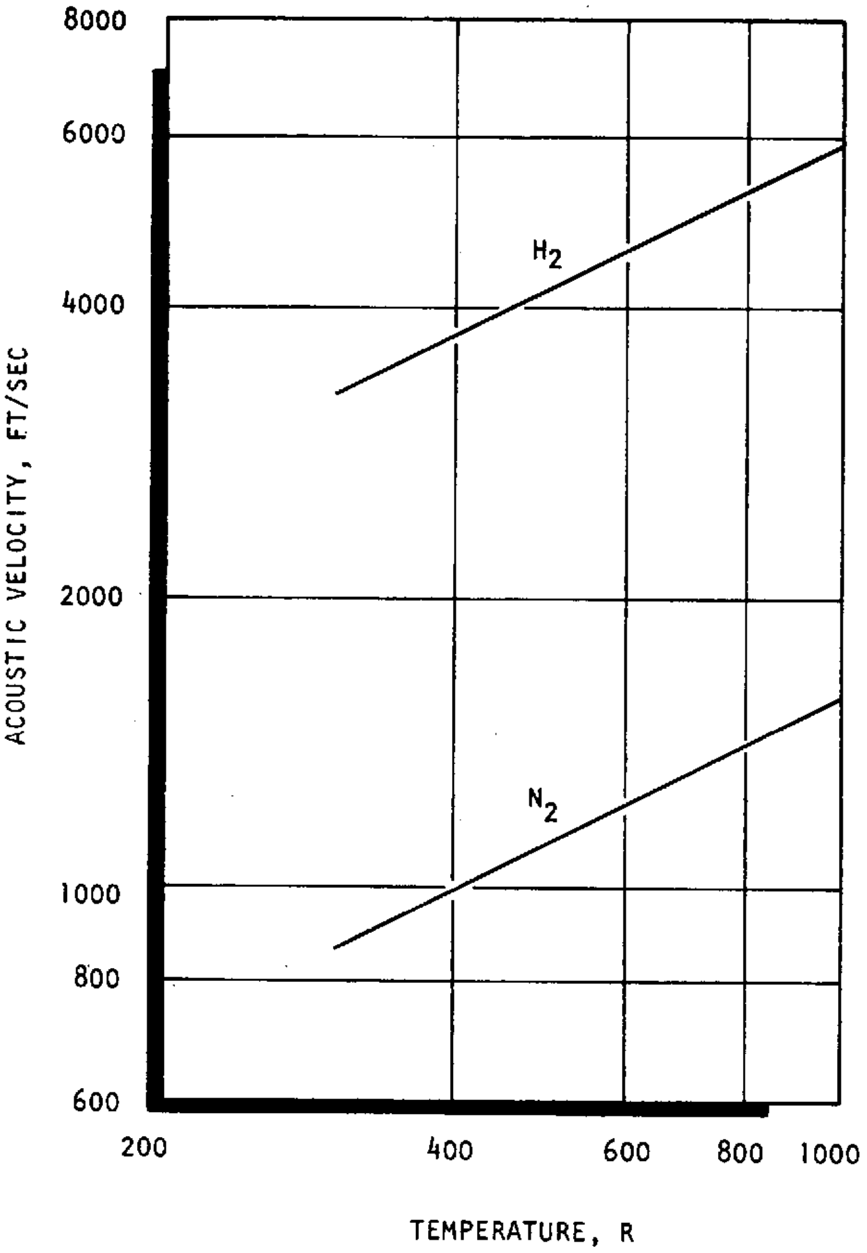

Figure G-3. Acoustic Velocity of Gaseous Nitrogen and Gaseous Hydrogen as a Function of Temperature (Low Pressure)

APPENDIX H

DISCUSSION OF THE CENTERLINE MOMENTUM RATIO PARAMETER, ϕ

INTRODUCTION

Mixing characteristics of two impinging jets of dissimilar fluids were first studied by Rupe (Ref. H-1) in 1953. Rupe evaluated the effect of density, velocity, diameter, and impingement angle on the mixing uniformity and found the resultant mixing characteristics strongly dependent upon these variables. In particular, Rupe has shown that a given unlike impinging doublet injector (circular orifice) produces optimum mixing uniformity when the product of density, velocity-squared and the diameter for each of the jets are equal, and that this optimum level is a function of geometry. It is not clear from Rupe's work whether the variables ρ, U, D, are all independent, composed of a dynamic pressure term (ρU^2) and a characteristic dimension, or a single variable($\rho U^2 D$). Over the past 15 years Rupe's result has been routinely applied to design injectors without a clear understanding of the significance of the fluid dynamics defined by his relationship. From an applications standpoint this is understandable and presented no design problems for circular orifices. However, reformulation for noncircular designs results in several possible forms of Rupe's criteria, depending upon the specification or grouping of the variables. Consequently, application of Rupe's criteria to noncircular orifice designs requires understanding of the mechanisms controlling mixing.

DISCUSSION

Based on Rupe's work, a dimensionless quantity which his experiments have shown important to mixing is:

$$\rho_1 U_1^2 D_1/\rho_2 U_2^2 D_2 \qquad \text{(H-1)}$$

Inspection of the physical significance of the variables contained in Eq. H-1 for circular geometry shows that the variables can be reformulated in terms of dynamic pressure ($\emptyset$)

$$\emptyset (D_f/D_o) = 1.0 \qquad \text{(H-2)}$$

or momentum ratio of the jets (M_f/M_o), and a diameter ratio:

$$M_f/M_1 \ (D_o/D_f) = 1.0 \qquad \text{(H-3)}$$

It becomes obvious that neither of the above physical interpretations result in a meaningful dimensionless group since they still result in two physical dimensionless ratios.

Since for circular orifices the above equations are dependent, application of either definition (Eq. H-5 or H-6) will lead to the proper design values. However, if the criteria are extended to other orifice geometries wherein the equations become independent (i.e., noncircular orifices), then the physical significance of Eq. H-1 must be known to select the proper form. As an example, a set of rectangular orifices impinging at 60 degrees, having equal widths, result in the following equations, which are equivalent to Eq. H-2 and H-3:

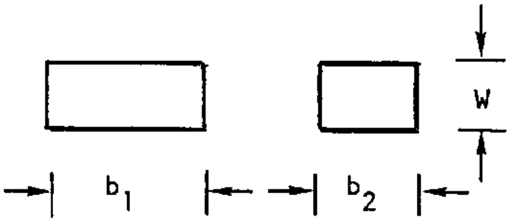

$$\emptyset (D_f/D_o)_{\text{hydraulic}} = (\rho_1 \, U_1^{\,2}/\rho_2 \, U_2^{\,2}) \ (D_f/D_o)_{\text{hydraulic}} \qquad \text{(H-4)}$$

$$(M_f/M_o)(D_o/D_f)_{hydraulic} = (\rho_1 U_1^2 A_1/\rho_2 U_2^2 A_2)\left(\frac{D_o}{D_f}\right)_{hydraulic} \qquad \text{(H-4)}$$

In this example, the hydraulic diameter ratio has been substituted for the geometric term. Note that these equations are independent and, therefore, should result in differing correlations of data. In addition, since the physical significance of the original equations is not clear, it is possible that neither of these correlations will result in a meaningful description of the mixing process.

Equation H-1 can also be formulated in terms of the centerline momentum of the jets. It is easily shown that on the basis of centerline momentum, Eq. H-1 for circular orifices is:

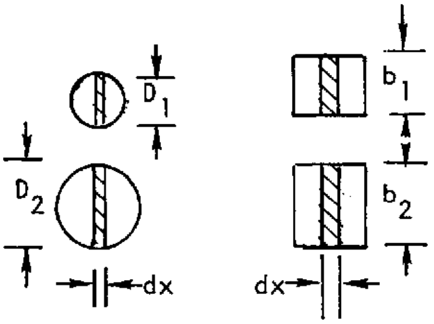

(a) CIRCULAR JETS (b) RECTANGULAR JETS

$$\emptyset = \rho_f U_f^2 D_f \, dx/\rho_o U_o^2 D_o \, dx = \rho_f U_f^2 D_f/\rho_o U_o^2 D_o \qquad \text{(H-6)}$$

and for rectangular orifices is:

$$\emptyset = \rho_1 U_1^2 b_1/\rho_2 U_2^2 b_2 \qquad \text{(H-7)}$$

Physical arguments, detailed in Ref. H-2, were employed to show that Eq. H-7 is the proper form for the parameter $\emptyset$.

APPENDIX H REFERENCES

H-1. Rupe, J. H.: A Correlation Between the Dynamic Properties of a Pair of Impinging Streams and the Uniformity of Mixture Ratio Distribution in The Resulting Spray, Progress Report No. 20-209, Jet Propulsion Laboratory, Pasadena, California, 28 March 1956.

H-2. McHale, R. M. and W. H. Nurick: Noncircular Orifice Holes and Advanced Fabrication Techniques for Liquid Rocket Injectors, Comprehensive Program Summary Report, Contract NAS9-9528, R-9271, Rocketdyne, May 1974.